

CLASSIFICATION CHANGED
UNCLASSIFIED

By Authority of ID 70-6326 Date 10-29-70

PROCEEDINGS OF THE NASA CONFERENCE ON
**COMMUNICATING
THROUGH PLASMAS OF
ATMOSPHERIC ENTRY
AND ROCKET EXHAUST**

**CASE FILE
COPY**

LANGLEY RESEARCH CENTER

JANUARY 14-15

1964

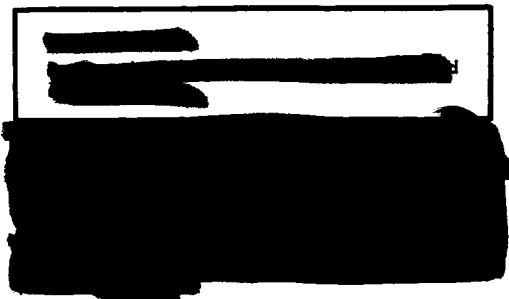


Declassified by authority of NASA
Classification Change Notices No. 211
Dated ** 31 DEC 1970



DECLASSIFIED

NASA SP-52



PROCEEDINGS OF THE NASA CONFERENCE ON

COMMUNICATING THROUGH PLASMAS OF ATMOSPHERIC ENTRY AND ROCKET EXHAUST

HELD AT LANGLEY RESEARCH CENTER, LANGLEY STATION,
HAMPTON, VIRGINIA, JANUARY 14-15, 1964



Scientific and Technical Information Division

1964

NATIONAL AERONAUTICS AND SPACE ADMINISTRATION

Washington, D.C.



DECLASSIFIED

PREFACE

This NASA conference on communicating through plasmas of atmospheric entry and rocket exhaust has been sponsored by the Electronics and Control Division of the NASA Office of Advanced Research and Technology and was held at the Langley Research Center on January 14-15, 1964. This document is a compilation of the papers presented by members of the Langley, Lewis, Goddard, Marshall, and Manned Spacecraft Centers.



CONTENTS

Preface 1

REENTRY COMMUNICATION PROBLEMS AND PREDICTIONS

1. LANGLEY REENTRY COMMUNICATIONS PROGRAM 1
By Theo E. Sims (Langley Research Center)

2. PREDICTION OF REENTRY PLASMA-SHEATH PROPERTIES 7
By Paul W. Huber and John S. Evans (Langley Research Center)

3. WAVE-PLASMA INTERACTION MODELS USEFUL FOR CALCULATION OF SIGNAL
LOSS DURING REENTRY 23
By John S. Evans and Calvin T. Swift (Langley Research Center)

4. ANTENNA RESPONSE TO A PLASMA ENVIRONMENT 33
By Francis P. Russo and Thomas G. Campbell
(Langley Research Center)

5. PRESENT PLANS FOR APOLLO COMMUNICATIONS AND TRACKING DURING REENTRY . 45
By George B. Gibson (Manned Spacecraft Center)

6. PLASMA EFFECTS ON APOLLO REENTRY COMMUNICATION 51
By Richard Lehnert and Bernard Rosenbaum
(Goddard Space Flight Center)

GROUND FACILITY STUDIES USING SIMULATED REENTRY PLASMA

7. MICROWAVE APPLICATIONS DEVELOPED AT LANGLEY RESEARCH CENTER FOR THE
REENTRY COMMUNICATIONS PROGRAM 69
By W. Linwood Jones and Bruce M. Kendall
(Langley Research Center)

8. QUALIFICATION TESTS OF A MICROWAVE REFLECTOMETER USING A GAS
DISCHARGE PLASMA 87
By Richard W. Morton (Langley Research Center)

9. PENETRATION OF DROPS INTO HIGH-VELOCITY AIRSTREAMS 95
By Robert D. Ingebo (Lewis Research Center)

10. EFFECT OF WATER ADDITION ON MICROWAVE TRANSMISSION THROUGH A
SIMULATED REENTRY PLASMA LAYER 105
By Perry W. Kuhns and Dale W. Cooper (Lewis Research Center)

11. A STUDY OF DIELECTRIC-COVERED SHUNT SLOTS IN A WAVEGUIDE 115
By William F. Croswell and Robert B. Higgins
(Langley Research Center)

12. INVESTIGATION OF THE RADIO BLACKOUT PROBLEM IN A PLASMA-SHEATH
SIMULATION FACILITY 131
By J. Kenrick Hughes (Langley Research Center)

FLIGHT EXPERIMENTS

13. SUMMARY OF RADIO-FREQUENCY FLAME EFFECTS ON MARSHALL SPACE FLIGHT
CENTER VEHICLES 143
By J. W. Harper and Olen P. Ely (George C. Marshall
Space Flight Center)

14. THE RADIO-FREQUENCY SIGNAL ATTENUATION PROBLEM OF ROCKET EXHAUSTS . . 167
By Duncan E. McIver, Jr. (Langley Research Center)

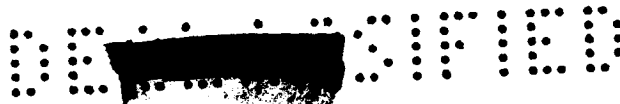
15. PROJECT RAM FLIGHT-TEST ROCKET VEHICLES 181
By James L. Raper (Langley Research Center)

16. INJECTION, DISTRIBUTION, AND EVAPORATION OF LIQUIDS IN THE FLOW
FIELDS OF HYPERSONIC VEHICLES 191
By Ivan E. Beckwith (Langley Research Center)

17. RESULTS OF THE RAM B2 MATERIALS-ADDITION FLIGHT EXPERIMENT 203
By William F. Cuddihy (Langley Research Center)

18. THE RAM B3 REFLECTOMETER EXPERIMENT 213
By William L. Grantham (Langley Research Center)

19. RAM FLIGHT-TEST RESULTS AND CONCLUSIONS 225
By Lyle C. Schroeder (Langley Research Center)



1. LANGLEY REENTRY COMMUNICATIONS PROGRAM

By Theo E. Sims
Langley Research Center

SUMMARY

The objectives of the reentry communications program at the Langley Research Center are flight verification of flow-field and signal-attenuation predictions, study of ionization effects on antennas, measurement of flow-field parameters, and development of techniques for eliminating the blackout problem. A program called Project RAM (Radio Attenuation Measurement), which includes flow-field analysis, ground facilities investigations, and flight studies, has been instituted to carry out these objectives. Some progress has been made.

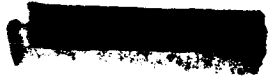
INTRODUCTION

During the critical period of atmospheric reentry, continuous maintenance of data transmission links between the spacecraft and ground stations is highly desirable. Unfortunately the ionized sheath resulting from high-temperature air in the flow field has thus far prevented this from being realized. Most missions to date involving near-orbital reentry velocities or greater have had to proceed with the certain knowledge that telemetry and communications signals and, for some flights, radar beacon tracking signals would be lost during the so-called blackout period. This loss of electromagnetic signals may be acceptable for unmanned, or even manned, ballistic reentries but it may not be acceptable for manned maneuverable spacecraft reentries. Blackout of guidance signals is definitely not acceptable for hypervelocity AICBM interceptors being developed for the nation's defense.

THE RF SIGNAL BLACKOUT PROBLEM

Figure 1, which illustrates the RF signal blackout problem, was prepared from flight data obtained from a large number of IRBM's, ICBM's, and Mercury spacecraft launched from Cape Kennedy. All these spacecraft were of the blunt-nose type. The approximate VHF blackout boundary shown in the figure was established from IRBM, ICBM, and Mercury data. Mercury flights also defined the approximate C-band blackout boundary.

The data of figure 1 are presented in terms of altitude and velocity, but many variables determine when signals from a given spacecraft will blackout and when they will recover. Some other factors are size and shape of the spacecraft, frequency of the electromagnetic signal, and signal amplitude margin of the data link. Therefore, this figure is not intended to be highly accurate and should be used for illustrative purposes only.





Nominal trajectories of several spacecraft are shown penetrating the blackout regions in the figure. Mercury, as previously stated, established the approximate C-band blackout boundary, and it can be seen that the Apollo C-band signal as well as the VHF signals will suffer extensive blackout. RAM refers to Langley probes currently being used to investigate the reentry communications problem. These probes are discussed in detail in subsequent papers.

LANGLEY PROGRAM BACKGROUND

In the middle of the 1950's the ionized flow field was recognized as a possible problem for the Langley research models program at the NASA Wallops Station. Researchers wanted to know whether models could be flown at velocities above a Mach number of 10 without jeopardizing the experiments due to blackout of telemetry signals. In 1957 in an attempt to answer this question two vehicles were flown near a Mach number of 15 over an altitude range from 70,000 feet to 90,000 feet (ref. 1). These flights confirmed that attenuation of VHF telemetry signals was a problem for the research models program at Wallops and pointed up the need for further studies. A ground plasma facility, the potassium-seeded cyanogen burner, was then developed and used for early radio transmission studies (ref. 2). This work was subsequently broadened in its scope and became the current Langley reentry communications research program referred to as Project RAM (Radio Attenuation Measurement).

LANGLEY PROGRAM OBJECTIVES

The general objective of the Langley reentry communications program is to investigate the interference of the ionized flow field with radio transmission, communications, and radar tracking for reentry vehicles at velocities from 10,000 ft/sec to 45,000 ft/sec and to develop practical methods of eliminating this data blackout phenomena. Specific objectives are as follows:

- (1) Flight verification of flow field and signal attenuation concepts developed by theory and ground tests

With this objective, it is hoped that techniques for extrapolating from accumulated ground and flight data to various spacecraft sizes and shapes and velocity-altitude regimes can be developed.

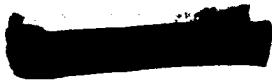
- (2) Study of ionization effects on antennas

Plasma detuning of antennas is a first-order effect in the total signal-loss problem.

- (3) Measurement of flow-field parameters

By this is meant onboard flight measurements to confirm flow-field predictions.

- (4) Development of techniques for eliminating the blackout problem





LANGLEY PROGRAM SCOPE

The scope of the Langley reentry communications program is as follows:

Flow-field analysis:

- Prediction of flow field
- Prediction of RF signal attenuation

Ground facilities investigations:

- Cyanogen burner
- 60-foot and 41-foot vacuum spheres
- Glow discharge tube
- Hypersonic tunnels
- Arc jets

Flight tests:

RAM A series	18,000 ft/sec
RAM B series	18,000 ft/sec
Scout	Rocket-exhaust studies
Fire I	37,000 ft/sec

Most of these items are covered in detail in subsequent papers. Comments in this paper are confined to general aspects only.

Flow-Field Analysis

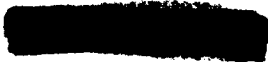
The flow-field-analysis work is in two parts: prediction of flow field and prediction of RF signal attenuation. This work is discussed in papers 2 and 3.

Ground Facilities Investigations

In the Langley program, ground facilities are fully utilized to study problem areas. When possible, existing facilities are used. The only specially developed facilities for this program are the cyanogen burner and the glow discharge tube. Investigations conducted in ground facilities have included plasma diagnostic studies, studies of antenna response to the plasma and ablation materials environment, qualification testing of flight sensors, and preflight testing of potential solutions to the blackout problem.

Cyanogen burner.- The cyanogen burner operates at a flame temperature of about 4,000° K and, when seeded with potassium, produces sufficient electron densities for application to radio transmission studies. This facility was used extensively in early communications investigations and the results obtained were reported in reference 2. Usefulness of the cyanogen burner in its present design to simulate reentry flight conditions is limited because (1) the burner operates at atmospheric pressure and the resultant plasma collision rate is higher than in flight at altitude, and (2) the flow is subsonic.

60-foot and 41-foot vacuum spheres.- In these large vacuum facilities some of the problems associated with studies at atmospheric pressure are avoided. In these facilities communications experiments can be conducted with





a full-scale nose cone immersed in a low-collision-rate plasma. The plasma is provided by the plumes of small solid-propellant rocket motors (ref. 3). These vacuum facilities have been utilized in the development of diagnostic instrumentation, in making plasma diagnostic measurements, and in testing the effectiveness of potential solutions to the blackout problem.

Glow discharge tube.- The glow discharge tube also produces a low-collision-rate plasma. This facility has been used in qualifying microwave reflectometers which will be utilized to measure electron densities in flight.

Hypersonic tunnels.- Hypersonic tunnels are used (1) to develop techniques for addition of materials to flow fields for alleviation of signal attenuation, and (2) to study spacecraft stability problems associated with rocket plumes at high altitude (refs. 4 and 5).

Arc jets.- Arc jets are used (1) to investigate ablation materials for possible use as antenna windows, and (2) to study antenna detuning and bandwidth effects.

Significant results obtained in these ground facilities are discussed in subsequent papers.

Flight Tests

In addition to the flow-field-analysis work and ground facilities investigations, several flight tests have been made.

RAM A series.- In the RAM A series there were two flights. Both flights tested the effectiveness of aerodynamic shaping (ref. 6) and one tested the effectiveness of the magnetic field in alleviating signal attenuation.

RAM B series.- In the RAM B series there have been two flights - one failure and one success. In the successful flight, water addition to the flow field was evaluated for possible use in eliminating signal attenuation (ref. 7). A multifrequency experiment from HF to X-band was also included. A third RAM B flight is being readied for launch. The primary experiment on this flight consists of microwave reflectometers to measure electron densities in the flow field.

Scout.- Scouts launched from the NASA Wallops Station have been utilized to fly some piggyback experiments to study the effects of rocket exhausts on telemetry signals and the removal of these effects by injectants (refs. 8 and 9).

Fire I.- Fire I does not contain a communications experiment, but onset of blackout and recovery from blackout of the VHF signals will be observed and correlated with predictions. Also, telemetry and signal-strength records will be studied for unusual occurrences.

These flight tests with the exception of Fire I are discussed in subsequent papers.



CONCLUDING REMARKS

The objectives of the Langley reentry communications program are to verify flow-field predictions, study antenna detuning effects, measure flow-field electron densities in flight, and develop solutions to the blackout problem. A program which includes flow-field analysis, ground facilities investigations, and flight tests has been instituted to pursue these objectives. Papers in this report give the significant progress which has been made.

REFERENCES

1. Graves, George B., Jr., and Markley, J. Thomas: Telemeter Transmission at 219.5 Megacycles From Two Rocket-Powered Models at Mach Numbers up to 15.7. NACA RM L58D18a, 1958.
2. Huber, Paul W., and Gooderum, Paul B. (With appendix A by Theo E. Sims and Duncan E. McIver, Jr., and appendix B by Joseph Burlock and William L. Grantham): Experiments With Plasmas Produced by Potassium-Seeded Cyanogen Oxygen Flames for Study of Radio Transmission at Simulated Reentry Vehicle Plasma Conditions. NASA TN D-627, 1961.
3. McIver, Duncan E., Jr.: Radio-Frequency Signal Attenuation by Plasmas of Rocket Exhaust Gases. A Compilation of Recent Research Related to the Apollo Mission. NASA TM X-890, 1963, pp. 135-144.
4. Falanga, Ralph A., Hinson, William F., and Crawford, Davis H.: Exploratory Tests of the Effects of Jet Plumes on the Flow Over Cone-Cylinder-Flare Bodies. NASA TN D-1000, 1962.
5. Hinson, William F., and Falanga, Ralph A.: Effect of Jet Plumbing on the Static Stability of Cone-Cylinder-Flare Configurations at a Mach Number of 9.65. NASA TN D-1352, 1962.
6. Sims, Theo E., and Jones, Robert F.: Flight Measurements of VHF Signal Attenuation and Antenna Impedance for the RAM A1 Slender Probe at Velocities up to 17,800 Feet Per Second. NASA TM X-760, 1963.
7. Cuddihy, William F., Beckwith, Ivan E., and Schroeder, Lyle C.: RAM B2 Flight Test of a Method for Reducing Radio Attenuation During Hypersonic Reentry. NASA TM X-902, 1963.
8. Sims, Theo E., and Jones, Robert F.: Rocket Exhaust Effects on Radio Frequency Propagation From a Scout Vehicle and Signal Recovery During the Injection of Decomposed Hydrogen Peroxide. NASA TM X-529, 1961.
9. McIver, Duncan E., Jr.: Study of the Effects of a Rocket Exhaust on Radio Frequency Signal Attenuation by the Use of a Recoverable Camera on the NASA Scout Vehicle. NASA TM X-888, 1963.



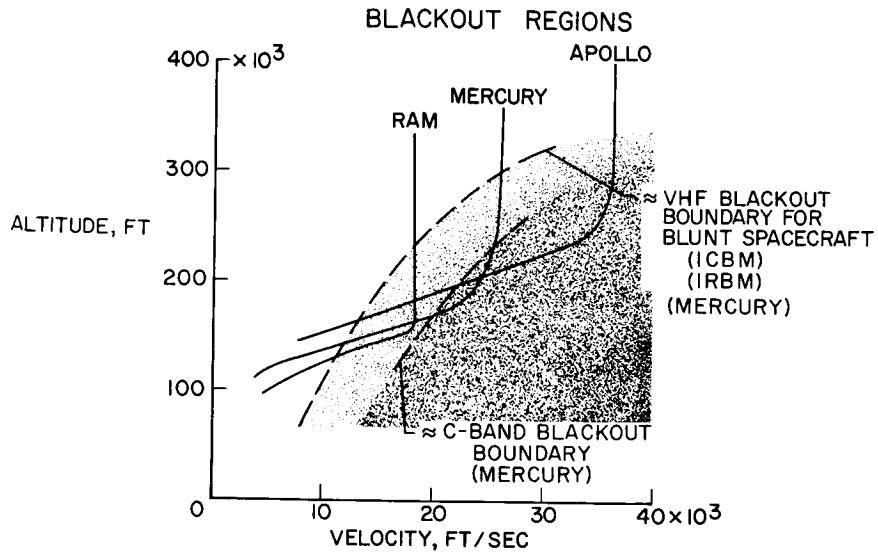
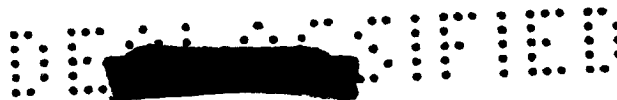


Figure 1



2. PREDICTION OF REENTRY PLASMA-SHEATH PROPERTIES

By Paul W. Huber and John S. Evans
Langley Research Center

2

SUMMARY

Methods are discussed by which the plasma properties in the flow field about a reentry vehicle can be theoretically determined for subsequent use in RF attenuation calculations. Aerodynamic properties of the flow are expediently determined first by utilizing normalized forms of equilibrium solutions, and these properties are then used as inputs to determine the chemistry and ionization in the flow by means of stream-tube methods. Multicomponent finite-rate reaction chemistry is employed to determine the distribution of electron density and electron collision frequency in the complete shock layer.

Results of these calculations for slender blunted bodies show the prime importance of nonequilibrium chemistry on the plasma properties and the strong influence of boundary layer on the distribution of properties. It also is shown that knowledge of the peak shock-layer plasma frequency at the antenna station serves, in itself, as a valuable guide in the prediction of blackout regions for large reentry bodies.

The need for additional knowledge of both the aerodynamics and the chemical-kinetics aspects of the problem is discussed in relation to the design of communications systems for advanced reentry missions. The important role of controlled flight experiments in such studies is recognized.

INTRODUCTION

The purpose of this paper and of paper 3 is to outline in as general and yet comprehensive a manner as possible the status of theoretical knowledge of the problem of attenuation and blackout of radio communications during the atmospheric entry phase of space missions. Although the companion problem of boost-phase communications degradation is a result of the same fundamental interaction (i.e., between an electromagnetic wave and a plasma), the boundary conditions and plasma-production mechanisms are quite different and, in fact, are not nearly as well understood.

Aerospace engineers, ground crews, and astronauts have been concerned with the reentry communications blackout problem for some time since it has been manifested in many different reentries from space missions including those of satellites, ICBM's, and research probes (refs. 1 to 4). In these reentries the problem did not prove to be operationally restrictive, since by the employment of careful mission programming, some additional onboard systems, and strategic location of ground stations the major goals of the missions were accomplished in spite of the compromises introduced by the blackout phenomenon. Present



knowledge, however, indicates that the extent of the blackout may be much larger for advanced missions, such as Apollo and hypervelocity Earth or Mars probes, if means are not developed to reduce the effects.

It is obvious that attempts to cope with the blackout problem must be based on a fundamental understanding of the nature of the phenomenon. It is reasonable to expect that such an understanding will evolve from a step-by-step description of the problem - starting with the simpler, or more gross, aspects. The result of even a simple understanding can be the ability to define more closely the expected blackout areas, while more refined results will include prediction of the actual amount of attenuation to be expected during the reentry period of a given advanced mission. More hopefully, however, such studies may lead to the pointing to and assessing of ways, or better ways, by which the problem may be alleviated or circumvented.

The reason that the theoretical status of the problem can be presented in two separate parts is given in the following discussion of the general theoretical procedures. The basis for the problem is that, whereas the antenna on the space vehicle is normally immersed in a "free-space" type dielectric medium, during the reentry period a plasma sheath coats the vehicle and this plasma sheath has, to some degree, the properties of a conductor. In electromagnetics literature this partial conductor is referred to as a lossy dielectric medium. The result of replacing part of the "free space" with this partial conductor is to cause some absorption and/or reflection of the communications signal at the plasma sheath.

The theoretical radio attenuation problem is determined in two independent chronological parts, each part involving an entirely different discipline. The first part involves specification of the plasma properties in the sheath, and these results in turn form the basis upon which determination of wave attenuation through this plasma can be made. Only two properties of the plasma sheath are required for determination of radio-wave attenuation although, more precisely, it is the spatial distribution of these properties in the sheath which must be known. It is significant to note from the outset that the required properties involve only those of free electrons - namely, the number per unit of volume N_e and the rate at which an average electron collides with other particles ν . The reason for concern with electrons is that they are responsive (due to their local electrostatic fields) to the rapidly oscillating electromagnetic fields of radio-frequency waves; whereas the other ions, due to their much greater mass for the same charge, will not significantly interact. Radio attenuation in the plasma is fundamentally a result of the exchange of wave electric field energy with free-electron kinetic energy wherein this electron energy increment is then dissipated in the plasma through collisions of the electrons with plasma particles and/or reradiated back in a displaced phase (i.e., absorption and/or reflection). The result can be a large decrease in the transmitted wave strength.

The role played by these plasma properties is illustrated in figure 1. The parameter f_p is known as plasma frequency and is evaluated from an expression which is proportional to the square root of the electron density N_e .



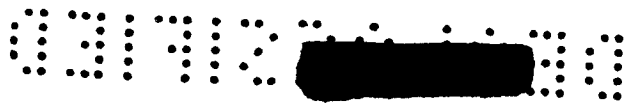
(There are constants in the expression which are not shown but include electron charge and mass and account for the dimension of frequency.) This parameter f_p is of important physical significance to the plasma (see ref. 5) and, in addition, provides a convenient yardstick with which to assess the probability of radio attenuation. For example, if the value of f_p in the plasma sheath nowhere equals or exceeds the signal-frequency value, then no attenuation - or only a negligible amount - will result. On the other hand, if, as shown in figure 1, the value of f_p does exceed the value of the signal frequency f , then the problem indeed exists and requires further study to determine its magnitude. In such a study, the spatial distributions of both the f_p and v values then become of prime importance.

The theoretical method for determination of the plasma-sheath properties is presented in this paper. This method is referred to as a stream-tube method and includes two main steps. The first step involves aerodynamic considerations wherein flow streamlines are specified in the plasma sheath as well as the pressure distributions along these streamlines. (See fig. 1.) The second step - a chemical-kinetics approach - involves determination of the flow chemistry and ionization along these streamlines, and the pressure distribution is a required input. It will be shown that nonequilibrium concepts are of prime importance in the second step. (See also ref. 6.)

The main dependencies of the plasma-sheath properties are vehicle configuration, flight parameters, and gas composition. The flight parameters - velocity, altitude, and attitude - as well as the ambient gas composition - for example, Earth atmosphere, Martian atmosphere, air with material addition or with ablation products present - primarily influence the magnitude, or value, of the plasma parameters; whereas, the vehicle configuration - size, shape, and antenna location - primarily influences the spatial distribution of the properties. Actually, this is an oversimplified representation of the problem dependency but is useful for general illustration.

SYMBOLS

D_n	nose diameter
f	signal frequency, cps
f_p	plasma frequency, cps
N_e	electron density, cm^{-3}
p	pressure
S	entropy
u	velocity, ft/sec



- x axial distance from nose
- y distance along normal from body surface
- ν electron collision frequency, sec^{-1}
- Δ shock-layer thickness along normal to body

Subscripts:

- b body
- s shock
- ∞ free stream
- ns normal shock

NORMALIZATION OF AERODYNAMIC PROPERTIES OF SHEATH

Since the starting conditions for the plasma determination are the streamline location and pressure distribution, these are discussed first. A simplifying assumption is involved - namely, these aerodynamic properties of the flow field are assumed to be unchanged from those of an equilibrium flow field at the same velocity and altitude. For slender blunted bodies, this is a reasonable assumption since the pressure distribution is only weakly influenced by real-gas effects, and the streamline location is a second-order consideration coming only into the spatial location of the streamline. This assumption can be avoided by use of subsequent iterations to the flow field, but the extra labor is not justifiable herein.

The equilibrium flow-field parameters (as well as nonequilibrium) are, however, very much dependent upon the velocity and altitude of flight. To cover adequately the combinations of velocity and altitude pertinent to the reentry phase, many such equilibrium solutions might be required, with each solution involving very time-consuming procedures. As a means of reducing much of this computational labor, a normalization procedure was found which, to a large degree, divorces the solution from its dependency on flight velocity and altitude. With such a procedure, one or two solutions will suffice, within acceptable limits of accuracy, for the complete reentry path.

Flow-Field Entropy

In equilibrium inviscid flow (neglecting any boundary layer for the moment) entropy is invariant along a streamline, or fluid flow path, and for this reason knowledge of the entropy distribution in such a flow field can be used to specify the flow paths. The equilibrium flow-field entropy is therefore normalized for this purpose. (It should be noted that the values of entropy herein



determined do not carry over to the subsequent nonequilibrium steps - only the streamline-path location is retained - so that constancy of entropy in nonequilibrium flow is not implied.) The value of entropy along the flow-field boundaries - that is, along the shock wave and the body surface - is first normalized as shown in figure 2. The increment of shock entropy above ambient entropy is normalized by the maximum, or normal shock, shock increment and is plotted as a function of the normalized axial coordinate. The body streamline is that which enters the flow field through the normal shock, so that its value is constant along the surface and equal to the normal-shock value. The variation of entropy within the shock layer at a given axial location is then normalized as shown in figure 3. In this plot the increment of flow entropy over the value at the shock, or outer boundary, is normalized by the total increment across the layer, and a family of curves each identified with axial station is the result.

The entropy normalizations illustrated in figures 2 and 3 thereby allow for complete inviscid flow-field entropy determination for a given body shape at any velocity and altitude. (The representations shown herein have been checked by comparison with solutions found in the literature for a wide range of flight conditions.) The only inputs required are the ambient entropy as a function of altitude and the normal-shock entropy as a function of altitude and velocity. Tabulations of such values are readily found in the literature (see refs. 7, 8, and 9) and it is upon reinsertion of these aerodynamic properties into the normalized flow-field representations that the strong dependency on flight parameters is again evident.

Flow-Field Pressure

The same procedure used to obtain the flow-field entropy is also applied to the determination of flow-field pressure distribution. Illustrative plots of these pressure parameters are shown in figures 4 and 5 and require no additional comments, except to point out that the values of this pressure parameter as herein determined do carry directly over as inputs to the nonequilibrium procedures. This is in contrast to the entropy parameter.

Viscous-Flow Regions

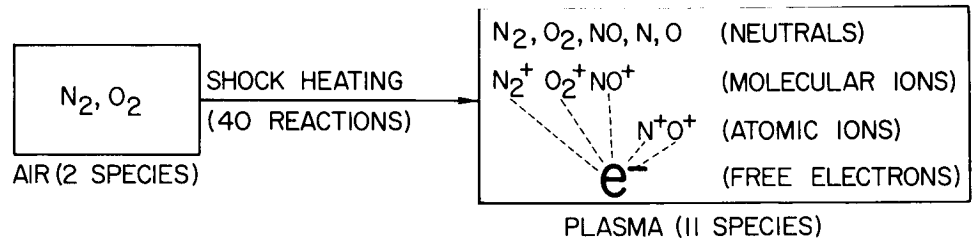
In order to complete the description of an equilibrium flow field, it is also necessary to assess the influence of viscous regions - such as the boundary layer near the body surface - on the fluid flow paths and pressure distributions. (In most radio attenuation problems, the periods of severe RF loss in reentry are those near the peak heating periods and generally occur in a continuum-type fluid-mechanics regime, in which the boundary layer is of the classical or thin type; it may thus be treated as a perturbation to the inviscid flow field. In this regime shock waves may also be considered to be thin.) The details of the boundary-layer procedure are not given herein (see ref. 6 for a more complete discussion) but the procedure involves the following general sequence: a boundary-layer calculation is made by using the "similar solutions" method of reference 10 as based on given inviscid body-surface gas properties.



The boundary-layer property profiles are then matched to the inviscid flow-field properties at the given body stations by a technique which crudely accounts for the vorticity interaction between these two flow regions. Inside the matching points (i.e., the boundary-layer region) the flow streamlines, which were previously specified from entropy considerations, are identified by a mass-flow parameter evaluated from integration of the boundary-layer properties. The pressure is assumed to be uniform across the boundary layer at a given station and equal to the inviscid surface value. (Note that the concept of streamlines inside the boundary layer is not valid but is applied to the outer reaches of the layer in lieu of a proper and expedient approach to non-equilibrium boundary layers.)

DETERMINATION OF NONEQUILIBRIUM CHEMISTRY

By using the aerodynamic properties of the flow field as an input and using also the conservation equations and chemical-kinetics relations, the plasma properties along the streamlines can be determined if some further assumptions are made - namely, that no diffusion of mass or transfer of energy occurs between streamlines and that the fluid properties appropriate to the start of the stream-tube calculations are those found behind a shock wave in which no dissociation or ionization occurs (ambient gas composition) but in which complete vibrational adjustment occurs. The details of this procedure are not discussed in this paper, but a qualitative illustration of the strong influence which nonequilibrium processes can have on the flow properties of air is given in the following block diagram (flight velocities below 30,000 ft/sec):



Note from this block diagram that in the initial stages of the stream-tube flow in the nose region, where a large energy input due to shock heating has occurred, a considerable number of chemical reactions can proceed in the dissociating and ionizing (forward) direction to produce a multicomponent mixture of species from the ambient air O_2, N_2 mixture. During the expansion process about the body and into the wake where the fluid is cooled, the reverse direction to that shown for the reactions is dominant and involves recombinations of the species to eventually become again the ambient composition.

The different species which will actually be present around the vehicle in a given problem, as well as the concentrations of these species in the mixture, depends upon a large number of factors which are generalized in the following two statements: (1) The number and types of reactions which will be significantly involved depend upon the enthalpy level, or velocity, of the flight.



For example, at velocities well below 30,000 ft/sec, as few as six reactions involving seven species will suffice to describe the chemistry; whereas, at velocities well above 30,000 ft/sec, many more reactions and species than those shown can be significant. (2) Of prime importance is the relationship between the rates at which these reactions proceed (in both the forward and reverse directions) and the rates at which flow changes take place about the vehicle. Statement (2) engulfs the nonequilibrium concept and can be simply illustrated by the following three terms:

- Chemical equilibrium
- Finite-rate nonequilibrium
- Frozen composition

If all reactions can proceed very fast in comparison with the flow rates, then the term "chemical equilibrium" applies to all the resulting conditions. If, on the other hand, one or more of the reactions is at a rate comparable with flow rates, the resulting condition is termed "finite-rate nonequilibrium." The most extreme condition of nonequilibrium is defined as one in which all reactions are so slow that no changes in composition can take place in pertinent flow times - that is, a "frozen composition." (Note that this discussion does not include the effects of vibrational relaxation, which is herein assumed to be in local equilibrium at all times.) The most difficult of these conditions to theoretically evaluate is that of finite-rate nonequilibrium, and unfortunately for problems in hypersonic air reentry this condition most generally applies since the use of some type of nonequilibrium approach is required above altitudes of approximately 100,000 feet.

In general, then, the nonequilibrium plasma problem can be briefly appraised as follows: Free electrons appear only as a trace species in most of the pertinent reentry flows, and in such flows, every reaction and reaction rate - no matter how minor an influence it may have on the thermal properties and resultant body heating problem - may conceivably have a first-order influence on this plasma property. Once these mechanisms are better understood and the reaction rates are known to a more reliable degree, some simplifications can undoubtedly be employed to reduce the complexity of the analysis. For example, some of the reactions may be found to be of negligible importance or it may be found that some of the reaction rates need not be precisely known. Each of these reaction rates has a local dependency on the gas temperature and density, and these gas properties are, in turn, dependent upon all the boundary conditions (as previously mentioned) as well as coupled to the chemistry.

The foregoing chemical-kinetics discussion has been centered about the air reentry problem in the velocity range up to about 30,000 ft/sec, but it should be pointed out that for higher entry velocities, or for other than air compositions, the problem becomes even more complex. At higher velocities additional reactions, such as those involving electron impact ionization, photo-ionization, and electronic excitation, will become important. It is obvious that ambient compositions of more than the two-component type (for example, a Martian atmosphere or air with material addition or with ablation products present) may lead to a much more complex chemistry than that indicated herein.



RESULTING PLASMA PROPERTIES

When the methods as presented are applied to a reentry problem, the plasma properties along a flow streamline are determined and typical results are illustrated by the curve labeled "Finite-rate chemistry" in figure 6. These results are for a hemispherically blunted 9° semiapex cone at a velocity of 17,700 ft/sec and an altitude of 170,000 feet. The streamline shown is one representative of flow just outside the boundary layer. For comparison, the limiting nonequilibrium properties of the streamline are given, and it is seen that a large region of uncertainty (nearly three decades) is contained within these limits. Also, for comparison, the critical electron density for VHF signals is shown.

When the procedures are followed for a number of different stream tubes and the results are cross-plotted at a given axial location (corresponding to an antenna location), the properties along a propagation path (in this case, normal incidence propagation) are found and are illustrated in figure 7. These results are for the same body and flight conditions given in figure 6, with a value of x/D_n of 5.4. The critical electron density for VHF signals is again shown for comparison. Note that there is a large variation in the electron density through the shock layer and that near the body surface there is a pronounced effect due to the boundary layer. These wall-viscous effects will generally be more important for slender bodies wherein local flow velocities are higher and shock layers thinner. It should be pointed out also that a different chemical-kinetics concept was used for the inner reaches of the boundary layer where the stream-tube concept is completely inadequate. The concept used is one of "self-limiting" reactions applied to the recombination of electrons with ions and is described in detail in reference 6.

Figure 7 is a representative output result of flow-field plasma-property determination in the form required for input to the calculation of RF attenuation. (Collision-frequency results, not shown, are also a product of these methods.) The bulk of the theoretical procedures incorporated in the plasma calculations is programed for electronic computers; the designations and status of these programs are given in table I for illustration. The notation "Programed but not checked" indicates that the procedure is working to some degree but is not yet completely satisfactory. These programs are applicable also to velocities higher than the designated value of 30,000 ft/sec, but the programs shown herein require some modification for use at higher speeds.

PREDICTION OF RF BLACKOUT REGIONS

When knowledge of the plasma properties in a reentry shock layer has been gained through the use of methods such as those described, it is possible within certain qualifications to apply this knowledge directly to the blackout problem even before quantitative attenuation calculations are made. This has been done here for large blunted bodies and the results are depicted in figure 8 wherein

predicted RF signal blackout regions appear as shaded regions below the curves for the various signal-frequency bands.

The qualifications which apply to use of these results are briefly as follows: (1) It is assumed that the body is so large that, when the plasma-frequency value anywhere in the plasma layer (through which the signal propagates) becomes equal to the signal-frequency value, an onset of attenuation, rapidly followed by a value greater than the margin of gain of the communications system, occurs. This blackout criterion in the reverse sense is assumed to apply also to the point of signal recovery in that the start of recovery occurs at this point but, because of the influence of relatively high collision frequency at the lower altitudes, the point of full recovery occurs somewhat later. (The predicted regions also have some degree of significance for smaller bodies in that the onset and recovery of attenuation - even though it may be a very small amount for small bodies - is expected also to occur at these points in the reentry.) (2) In computing the values of plasma frequency for this chart, a generalized antenna location is assumed which corresponds to an aft body station - that is, a pressure coefficient representative of such a location is employed. (3) A stream tube is selected which is believed to be generally representative of that containing peak shock-layer plasma properties. (4) A generalized concept of nonequilibrium is employed which, in essence, yields values of the plasma frequency somewhere between the limiting conditions previously discussed, but somewhat closer to the frozen limit.

It is, of course, obvious that such a generalized representation as that shown here will not exactly correspond to any specific flight problem. On the other hand, such a criterion is very useful in the conceptual stages of mission planning in which exact calculations are lacking or cannot be made with confidence. In fact, the correlation of observed signal-loss changes for the Mercury reentry is seen to be good with this criterion. If the correlation is as good for the Apollo reentries, then it is seen from figure 8 that blackout of both radio link (VHF) and tracking (S- and C-bands) signals will certainly be manifest in two extended regions for the skip trajectories shown. For nonskip braking reentries (not shown) a single, much more extended blackout region would be indicated. Good correlation has also been found to exist for the ICBM reentry attenuations observed in the Atlantic and Pacific Missile Range flights reported in references 2 and 3 and shown previously in paper no. 1. Because all these bodies are not of the very large variety, the correlation is with the points of onset of attenuation and recovery for these flights; whereas, the blackout and full-recovery points are, respectively, below and to the left of these curves. For the RAM vehicle reentries (to be described in subsequent papers) the measurable attenuation regions were well inside the regions shown, but these vehicles can be classified as very small.

A preliminary assessment of the communications problem at entry into a Martian atmosphere was made, based on concepts similar to those used herein for air, and blackout regions similar in some respects to those for Earth reentry were found.



HYPERVELOCITY ENTRY PLASMAS

It has been shown that theoretical description of reentry flow-field plasma properties can be expediently made for slender blunted axisymmetric bodies in uncontaminated air, provided the velocity is not too high. The velocity requirement follows from the lack of knowledge regarding reactions and reaction rates appropriate to the chemical kinetics at very high enthalpy. Such knowledge is fairly reliable for application to velocities up to about 20,000 ft/sec but is less reliable as velocities become progressively larger. For ablation products and/or material injection products in the flow, the knowledge is much cruder and, in fact, the phenomena are not at all well understood. This status obviously applies to the problem relating to other planetary atmospheres. The ability to describe aerodynamically the flow fields about highly blunted bodies (fairly abrupt change in contour from the nose to the afterbody shape), bodies at high angle of attack (above a few degrees), and bodies in which flow separations occur is likewise in a far less than desired status. Furthermore, supplementary test data in the hypervelocity range cannot be obtained since ground facilities are not available in which to measure such flow properties under simulated flight conditions. Also measurement in ground facilities of the required reaction rates, and so forth, is difficult for this same reason, as well as due to the problem of isolating or observing a particular rate, independent of the many others.

Since the foregoing factors may prove to be restrictive for some time to come, it is expected that in the interim, flight results may serve as indirect verifications of some of these extremely complicated concepts for application to advanced mission design. For example, carefully controlled flight experiments can be devised in which ablation, separation, and so forth, are avoided in some of the flights and pattern measurements are made at different frequencies and antenna locations, along with onboard plasma diagnostic measurements. By evaluation of such quantitative measurements and their parametric variations in terms of the known boundary conditions, a valuable insight may be gained into the fundamental plasma processes as well as obtaining engineering data. Indeed, much knowledge has been gained from these evaluations in the RAM flight program, as will be shown in a number of the subsequent papers.

CONCLUDING REMARKS

Methods have been discussed by which the plasma properties in the flow field about a reentry vehicle can be theoretically determined for subsequent use in RF attenuation calculations. The methods included aerodynamic procedures utilizing normalized forms of equilibrium flow-field solutions to expediently determine stream-tube flow properties, and procedures to determine the multicomponent finite-rate reaction chemistry along the stream tube, with the aerodynamic properties as inputs. The resulting plasma properties are distribution of electron density and electron collision frequency in the complete shock layer.



The plasma properties about slender blunted bodies have been evaluated, and the results showed the prime importance of nonequilibrium chemistry on the properties and the strong influence of boundary layer on the distribution of properties. It also was shown that knowledge of the peak shock-layer plasma frequency at the antenna station served, in itself, as a valuable guide in the prediction of blackout regions for large reentry bodies.

It was pointed out that additional knowledge of both the aerodynamics and the chemical-kinetics aspects of the problem is needed in relation to the design of communications systems for advanced reentry missions. The important role of controlled flight experiments in such studies was recognized.

REFERENCES

1. Graves, George B., Jr., and Markley, J. Thomas: Telemeter Transmission at 219.5 Megacycles From Two Rocket-Powered Models at Mach Numbers up to 15.7. NACA RM L58D18a, 1958.
2. Fetner, E. M.: Typical Effects of Shock-Layer Ionization at Telemetry and S-Band Radar Frequencies. AFMTC-TN-59-5, U.S. Air Force, Aug. 1959.
3. Anon.: Results of the First U.S. Manned Orbital Space Flight February 20, 1962. Manned Spacecraft Center, NASA.
4. Vicente, F. A.: Compilation of Blackout Re-Entry Data. Rep. TDR-169 (3153-01)-TN-1 (Contract AF-04(695)-169), Aerospace Corp. (El Segundo, Calif.), Mar. 15, 1963. (Available from DDC as AD 336 769.)
5. Huber, Paul W., and Nelson, Clifford H.: Plasma Frequency and Radio Attenuation. Proceedings of the NASA-University Conference on the Science and Technology of Space Exploration, Vol. 2, NASA SP-11, 1962, pp. 347-360. (Also available as NASA SP-25.)
6. Evans, John S., and Huber, Paul W.: Calculated Radio Attenuation Due to Plasma Sheath on Hypersonic Blunt-Nosed Cone. NASA TN D-2043, 1963.
7. Wittliff, Charles E., and Curtis, James T.: Normal Shock Wave Parameters in Equilibrium Air. Rep. No. CAL-111, Cornell Aero. Lab., Inc., Nov. 1961.
8. Marrone, Paul V.: Normal Shock Waves in Air: Equilibrium Composition and Flow Parameters for Velocities From 26,000 to 50,000 Ft/Sec. CAL Rep. No. AG-1729-A-2 (Contract NASr-119), Cornell Aero. Lab., Inc., Aug. 1962.
9. Huber, Paul W.: Hypersonic Shock-Heated Flow Parameters for Velocities to 46,000 Feet Per Second and Altitudes to 323,000 Feet. NASA TR R-163, 1963.
10. Cohen, Nathaniel B.: Boundary-Layer Similar Solutions and Correlation Equations for Laminar Heat-Transfer Distribution in Equilibrium Air at Velocities up to 41,100 Feet Per Second. NASA TR R-118, 1961.

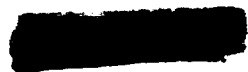


TABLE I.- LANGLEY COMPUTER PROGRAMS FOR FLOW-FIELD
PREDICTIONS TO 30,000 FT/SEC FOR AIR REENTRY

Program	Description	Status
Flow properties immediately behind shock wave	Provides starting properties for stream tube (undissociated and nonionized air; equilibrium vibration)	Working
Finite-reaction-rate flow properties along stream tube	Includes 40 reactions and 11 species	Programed but not checked
Equilibrium, real-gas boundary layer	Similar solutions	Working
Nonequilibrium boundary layer	Similar solutions; 7 reactions and 7 species	Programed but not checked

PLASMA - SHEATH PROPERTIES

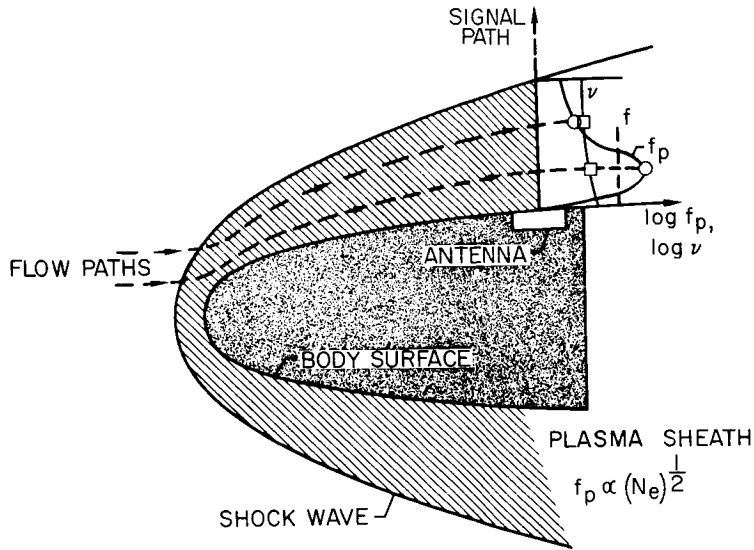


Figure 1

NORMALIZED FLOW-FIELD PARAMETERS SHOCK-WAVE ENTROPY; HEMISPHERE, 9° SEMIAPEX CONE

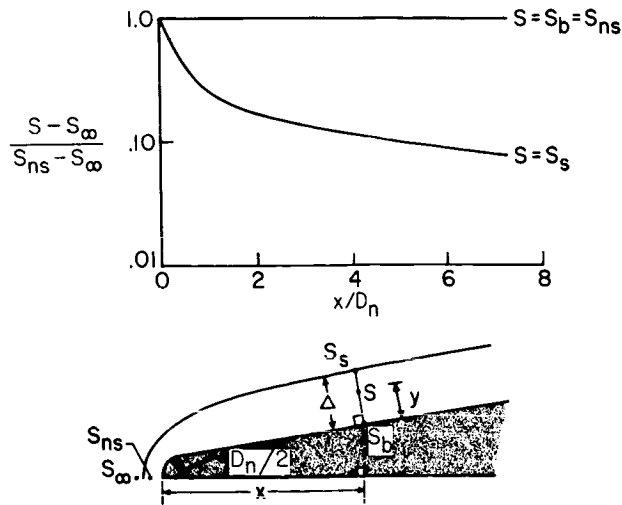


Figure 2

NORMALIZED FLOW-FIELD PARAMETERS
SHOCK-LAYER ENTROPY DISTRIBUTION; HEMISPHERE,
9° SEMIAPEX CONE

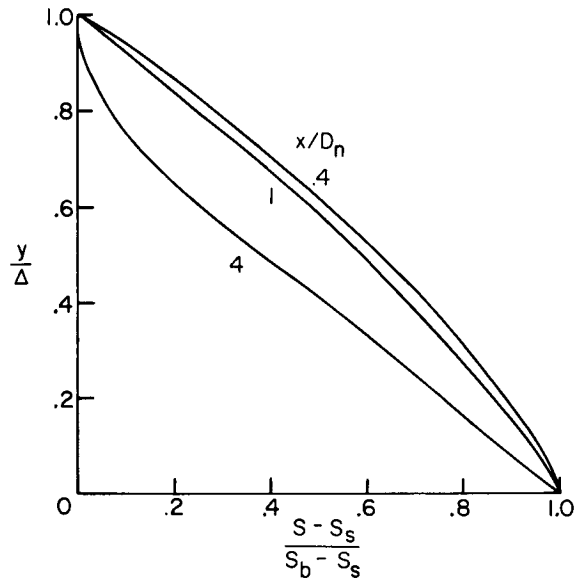


Figure 3

NORMALIZED FLOW-FIELD PARAMETERS
SHOCK-WAVE AND BODY-SURFACE PRESSURES; HEMISPHERE,
9° SEMIAPEX CONE

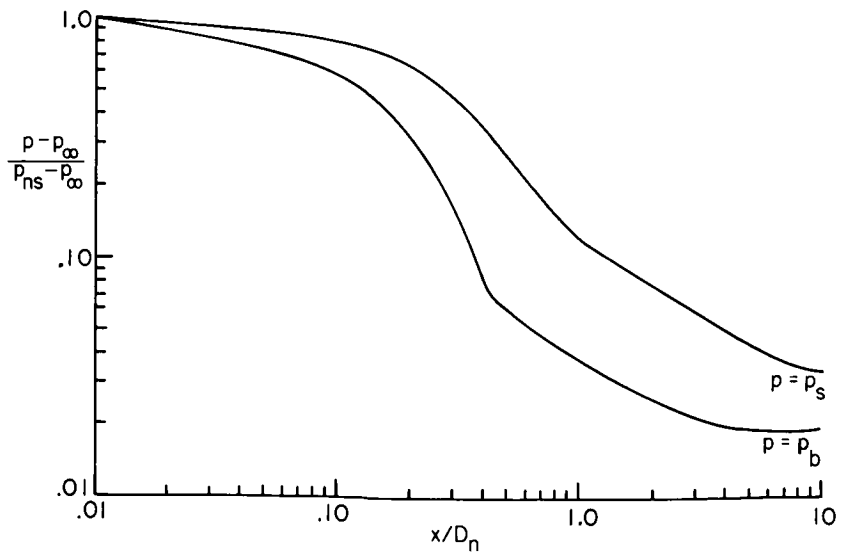
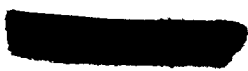


Figure 4



NORMALIZED FLOW-FIELD PARAMETERS
SHOCK-LAYER PRESSURE DISTRIBUTION; HEMISPHERE,
9° SEMIAPEX CONE

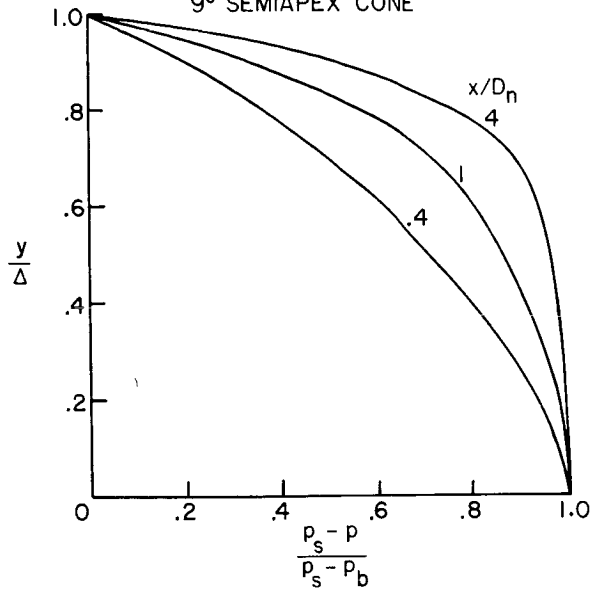


Figure 5

ELECTRON DISTRIBUTION ALONG A TYPICAL STREAMLINE

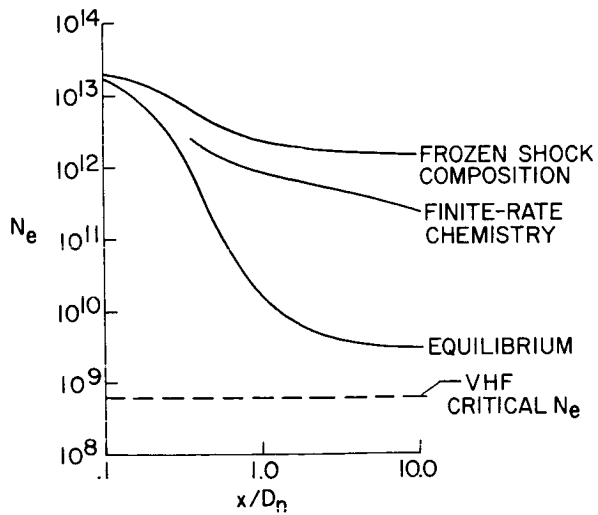


Figure 6

TYPICAL SHOCK-LAYER ELECTRON DISTRIBUTION

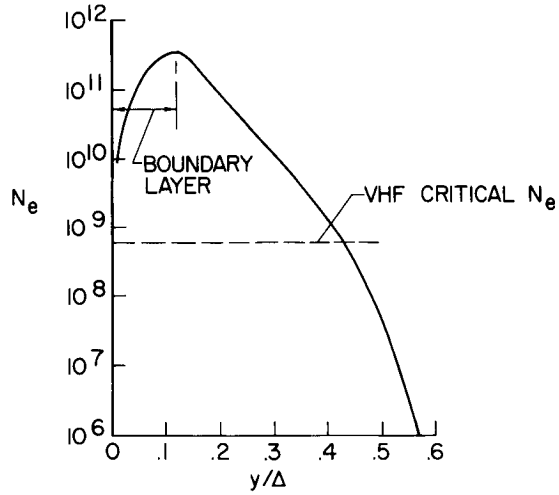


Figure 7

PREDICTED SIGNAL-BLACKOUT REGIONS FOR BLUNT-BODY EARTH REENTRY
BLACKOUT BELOW DESIGNATED LINE

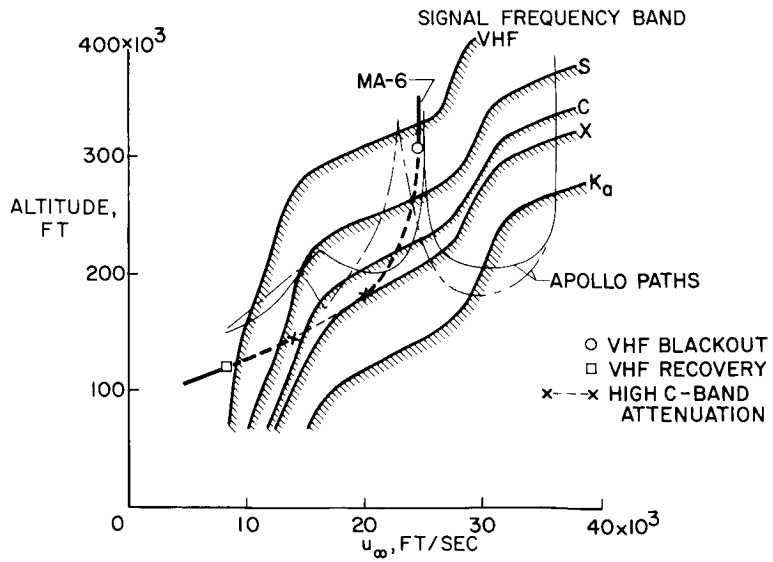


Figure 8



3. WAVE-PLASMA INTERACTION MODELS USEFUL FOR CALCULATION
OF SIGNAL LOSS DURING REENTRY

By John S. Evans and Calvin T. Swift
Langley Research Center

SUMMARY

The propagation of radio waves from an antenna on a reentering vehicle is treated as a boundary value problem in terms of two idealized plasma models. One of these models is an inhomogeneous slab model upon which plane waves are incident at arbitrary angles. The other is a radially varying cylindrical sheath on a slotted conducting cylinder. A comparison is given between attenuation computed by using these models and attenuation observed during the flights of the RAM A and RAM B vehicles. Remarks are made about the effects of diffraction on equatorial antenna patterns and about reduction of transmitted signal strength due to degraded performance of sharply tuned antennas when covered by a plasma.

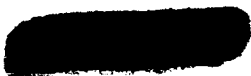


INTRODUCTION

This paper is concerned with propagation of radio signals in the presence of an ionized medium and not with the determination of the properties of the medium. More specifically, it is concerned with the theoretical calculation of antenna patterns for vehicle-mounted transmitting antennas during the high-heating phase of atmospheric reentry. Some of the characteristic features of the problem are: the plasma has strong gradients (adds previously negligible terms to wave equation), diffraction effects are present for wavelengths comparable to body dimensions (makes problem sensitive to geometry), and coupling exists between antenna and plasma (shifts resonant frequency of antenna and also alters its efficiency).

SYMBOLS

- \vec{E} electric field intensity, V/m
- E_y y-component of \vec{E} , V/m
- \vec{H} magnetic field intensity, amp-turns/m
- H_y, H_z y- and z-components of \vec{H} , amp-turns/m
- k_0 free-space wave number, m^{-1}
- n complex index of refraction





r cylindrical coordinate

$$V = 1 - \frac{1}{(\omega/\omega_p)^2 + (\nu/\omega_p)^2}$$

$$W = \frac{\nu/\omega_p}{\omega/\omega_p} \frac{1}{(\omega/\omega_p)^2 + (\nu/\omega_p)^2}$$

x Cartesian coordinate

y Cartesian coordinate

z Cartesian or cylindrical coordinate

ϵ permittivity, F/m

θ angle of incidence, deg

ν collision frequency, radians/sec

ϕ cylindrical coordinate

ω transmitting frequency, radians/sec

ω_p plasma resonant frequency, radians/sec

DISCUSSION

The study of radio wave propagation in inhomogeneous ionized media is not new, since the passage of such waves through the ionosphere has been of interest for many years. What is new is the necessity for working with inhomogeneous plasmas whose dimensions are comparable to the wavelength. For such plasmas certain useful devices, such as ray tracing and impedance ratios, lose their validity and one is forced to fall back on direct solution of the wave equations, subject to appropriate boundary conditions.

The following wave equations for \vec{E} and \vec{H} are for an inhomogeneous medium:

$$\nabla^2 \vec{E} + k_0^2 n^2 \vec{E} = -\nabla \left(\vec{E} \cdot \frac{\nabla n^2}{n^2} \right)$$

$$\nabla^2 \vec{H} + k_0^2 n^2 \vec{H} = \frac{-\nabla n^2}{n^2} \times (\nabla \times \vec{H})$$



where

$$n^2 = n^2(z) = V + jW$$

The properties of the medium enter through the dependence of the complex index of refraction n on the position coordinates of the field point. Closed-form solutions have been found for a few special cases (ref. 1), but for arbitrary variation of plasma properties, solutions must be found by integrating the equations through the plasma on electronic digital data processing machines. Even this has been done only for one-dimensional variation in plasma properties.

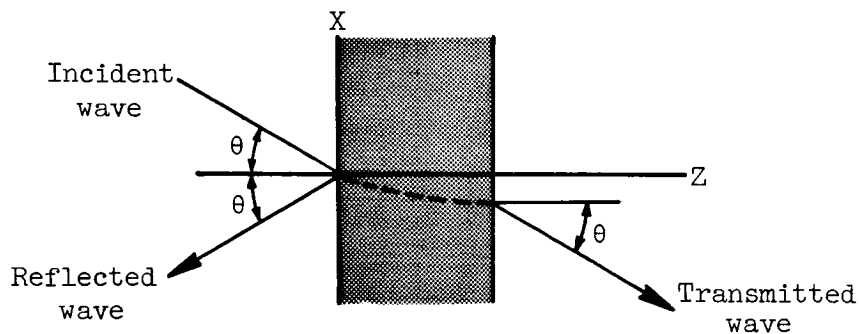
The equations and boundary conditions used in reference 2 to study transmission and reflection of plane waves incident at arbitrary angles on inhomogeneous plane parallel plasmas are as follows:

$$\frac{\partial^2 E_y}{\partial x^2} + \frac{\partial^2 E_y}{\partial z^2} + k_0^2 n^2 E_y = 0$$

$$\frac{\partial^2 H_y}{\partial x^2} + \frac{\partial^2 H_y}{\partial z^2} + k_0^2 n^2 H_y = \frac{1}{n^2} \frac{\partial n^2}{\partial z} \frac{\partial H_y}{\partial z}$$

Boundary conditions:

Tangential components of \vec{E} and \vec{H} are continuous across boundaries.



This model does not account for body geometry or plasma curvature, and the boundary conditions on the incidence side are appropriate for a plasma located far from the transmitting antenna rather than for one located very near to the antenna. In spite of these limitations there is some indication that the predictions may be valid for very short wavelength radiation from a highly directive antenna like an open-end X-band waveguide. Paper no. 18 discusses some ground facility tests in which good correlation between theory and experiment for such an antenna was found.

The equations and boundary conditions used in reference 3 to calculate radiation patterns for an axial slot on a conducting cylinder covered by a radially varying plasma are as follows:

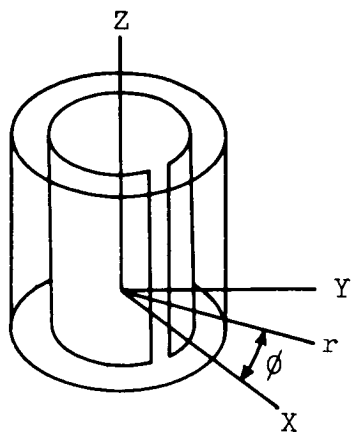


$$\frac{1}{r} \frac{\partial}{\partial r} \left(r \frac{\partial H_z}{\partial r} \right) + \frac{1}{r^2} \frac{\partial^2 H_z}{\partial \phi^2} + k_0^2 n^2 H_z = \frac{1}{n^2} \frac{\partial n^2}{\partial r} \frac{\partial H_z}{\partial r}$$

$$\vec{E} = \frac{1}{j\omega\epsilon} \nabla \times \vec{H}$$

Boundary conditions:

Tangential components of \vec{E} and \vec{H} are continuous across air-plasma interface. Tangential \vec{E} is specified under slot.



By solving these equations, far-field antenna radiation patterns are obtained in the equatorial plane.

This model has proved to be much better for predicting attenuation from axial slot antennas at VHF frequencies than the slab model. Two reasons can be given for this: One, it roughly approximates the size and shape of the vehicle and can, therefore, account for diffraction. Two, the boundary conditions on the incidence side are more realistic than those of the slab model.

Figure 1 shows the locations of antennas flown on RAM vehicles. The basic shape for both RAM A and RAM B is a 90 degree half-angle blunt cone with a cylindrical afterbody. Except for the afterbody diameter, the dimensions of RAM B are larger by a factor of four than those of RAM A.

Radiation patterns for the VHF slot antennas are best analyzed with the slotted cylinder model, since the slotted cone problem has not been solved. Attenuation for X-band is found with the use of the slab model. The ring antennas are fully open slots along the circumference of a circle. Analysis is available for this model (ref. 3), but it has not yet been programed for computation. In lieu of a better model, slab computations are used.

Table I shows calculated and measured values of attenuation for RAM antennas at a speed of 17,700 ft/sec and an altitude of 170,000 feet, which corresponds approximately to peak heating and attenuation during the flights.

RAM A1 was the first vehicle flown in this series. At that time only the slab theory was available, and the substantial agreement between theory and experiment for the VHF slot antenna was a source of satisfaction. In fact, the agreement appeared to be better than this table indicates since the discrepancy between 18 dB and 23 dB could be roughly accounted for by a theoretical correction for detuning based on VSWR (voltage-standing-wave-ratio) measurements included on the telemeter records. The agreement for the VHF ring antenna was not considered particularly good, but it could be excused on the basis that the flow-field analysis on that portion of the body was compromised by uncertainties connected with the flow-field calculations near the cone-cylinder junction.

After the flight of RAM A2, which carried the same antennas on the same flight trajectory, it was evident that something was wrong with either the A1 or A2 data. The VHF ring attenuation was the same as before, but the VHF slot attenuation was much lower than before and disagreed seriously with the theoretical prediction. A search for an explanation revealed that the RAM A1 vehicle carried a sharply tuned VHF slot antenna and that the same antenna on RAM A2 had a broad tuning characteristic, because of an electromagnet installed under it. A reasonable hypothesis for the difference in the two experimental measurements appeared to be that the narrowband antenna suffered a larger loss of efficiency due to detuning by the plasma. Laboratory experiments which were performed to test this hypothesis are described in paper no. 4, which shows that the signal received from the narrowband antenna is indeed more severely attenuated in the presence of plasma than that received from the broadband one.

When viewed in this light the 18 dB predicted by the slab model was not satisfactory. However, a computer program based on the axially slotted cylinder (ref. 3) became available about the time of the RAM A2 flight. It was pleasing to find that the results agreed with the measurement in which detuning was expected to have the smaller effect.

The RAM B2 vehicle which was flown later carried a narrowband VHF slot antenna in order to enhance the ability to observe signal recovery by addition of water to the flow, which was the principal purpose of the flight. Agreement between the slotted cylinder calculations and the observed attenuation while the water flow was cut off was neither expected nor obtained.

A definitive test of these ideas will be made on the next RAM flight. One of the secondary objectives will be to obtain simultaneous attenuation measurements on two VHF slot antennas, one of which is narrowband and the other of which is broadband. This experiment is discussed in paper no. 4.

Slab theory predicted very small attenuation for X-band, and that is what was observed. A more positive check with measurable attenuation is needed for this antenna.

Figure 2 shows antenna patterns computed for the VHF slots on RAM A and RAM B. These are polar plots in the plane perpendicular to the vehicle axis. The radial distance which represents 0 dB is marked on the line corresponding to propagation in the direction normal to the surface and is referenced to the signal strength of a distant receiver when no plasma is present over the antenna.



Negative gain (or attenuation) increases along any radius toward the center.

Figure 2 is presented because it illustrates the effect of diffraction when body dimensions are of the order of the radiation wavelength. The cylinder used to represent RAM B has a circumference slightly larger than one free-space wavelength, whereas the one used for RAM A is smaller by a factor of about 3. In general, as cylinder diameter increases the pattern changes from near circular for small diameters to lobes in the forward direction for large diameters. In the limit of infinite diameter the pattern becomes that of a slot in an infinite conducting plane.

Figure 3 illustrates a series of interesting patterns obtained by Calvin T. Swift (LRC) and Charles M. Knop (The Hallicrafters Company) for axial slots on cylinders in near-resonant plasmas ($\omega \approx \omega_p$, $\nu \approx 0$). For exact resonance ($\omega = \omega_p$, $\nu = 0$) the pattern is circular, and this result is independent of the cylinder radius and of the thickness of the plasma coating, except that the plasma thickness cannot be exactly zero. Zero thickness of the coating corresponds to no plasma, for which the pattern is noncircular. The discontinuous behavior indicates that pattern shape should be very sensitive to plasma parameters under near resonant conditions. This conclusion is borne out by noting that small departures from exact resonance cause marked changes in the computed patterns, as shown. Sensitivity of pattern shape at near resonance may prove to be a valuable diagnostic tool.

Mathematical analyses of antenna-plasma systems such as those discussed herein can be useful for design studies as well as for data analysis. For example, patterns for different types of antennas can be calculated for identical plasma coatings to determine which is best suited to the intended purpose. This is an important capability, since the simulation in a ground facility of a plasma-coated antenna in a free-space environment is so difficult to achieve that experimental patterns are not available.

On the other hand, there is much work to be done before mathematical analyses can adequately perform this function. Since the approaches used involve idealizations of real problems and since antenna radiation is notoriously sensitive to disturbing influences, experimental checks must be used to validate the results. Such checks necessarily include some carefully executed flight experiments because no combination of ground facilities has yet been devised which can adequately reproduce all of the pertinent factors.

Table II summarizes the Langley Research Center computing programs for inhomogeneous plasmas. Theoretical studies are also being carried out on detuning effects, antenna arrays, and scattering from inhomogeneous plasmas.

CONCLUDING REMARKS

The principal points to remember about antennas for use during reentry are as follows: Gradient terms in the wave equation cannot be neglected.

Antenna pattern shape is strongly dependent on body size and shape, as well as on antenna type. The plasma may shift antenna resonant frequency and reduce antenna efficiency. Antenna selection and design should be evaluated on the basis of operation under expected reentry conditions. Experimental capability for complete evaluation in ground facilities is lacking; therefore, theoretical capability must be developed. Theoretical treatments are inexact; therefore, experimental checks must be employed.

REFERENCES

1. Graf, K. A., and Bachynski, M. P.: Existing Solutions for Interaction of Electromagnetic Waves With Plasma of Simple Geometries. DAMP Tech. Monograph No. 62-07 (Contract DA 36-034-ORD-3144RD), Radio Corp. of America, June 1962.
2. Swift, Calvin T., and Evans, John S.: Generalized Treatment of Plane Electromagnetic Waves Passing Through an Isotropic Inhomogeneous Plasma Slab at Arbitrary Angles of Incidence. NASA TR R-172, 1963.
3. Swift, Calvin T.: Radiation From Slotted-Cylinder Antennas in a Reentry Plasma Environment. NASA TN D-2187, 1964.

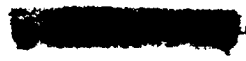


TABLE I.- ATTENUATION FOR RAM ANTENNAS

RAM	Antenna	Attenuation, dB			
		Calculated		Measured	
		Slotted cylinder	Slab	Narrowband	Broadband
A1	VHF slot	2	18	23	6
A1	VHF ring		10		
A2	VHF slot	2	18	>30	≈5
A2	VHF ring		10		6
B2	VHF slot	6.5	23	>30	17
B2	HF ring		30		
B2	X-band		0.0086		

TABLE II.- SUMMARY OF LANGLEY COMPUTER PROGRAMS
FOR INHOMOGENEOUS PLASMAS

Program	Description	Comments
Plane wave inhomogeneous slab	Computes reflection and transmission coefficients; also phase shifts For plane waves at arbitrary angle of incidence	Also available with uniform magnetic field (normal incidence only) Probably limited to far-field application
Axial slot on cylinder	Computes transmission patterns in equatorial plane	Detuning effects not included
Circumferential slot on cylinder	Computes transmission patterns in equatorial plane	Detuning effects not included Not yet in computational form



ANTENNAS ON RAM VEHICLES

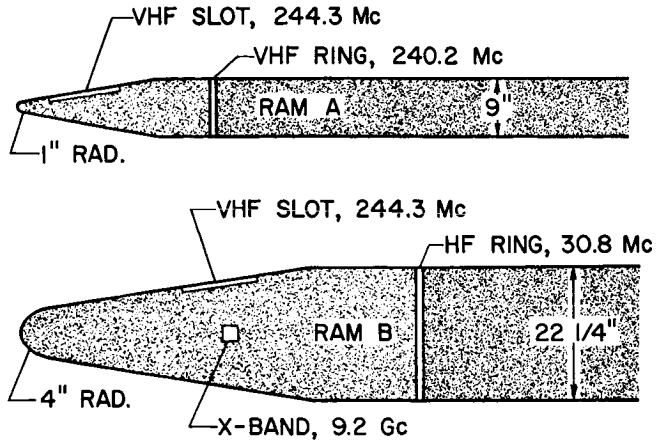


Figure 1

ANTENNA PATTERNS COMPUTED FROM SLOTTED-CYLINDER MODEL

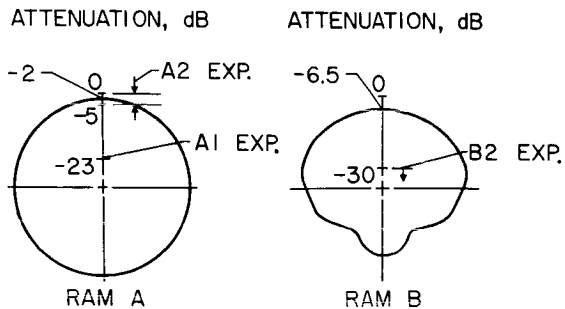


Figure 2

PATTERN SENSITIVITY FOR NEAR-RESONANT PLASMAS

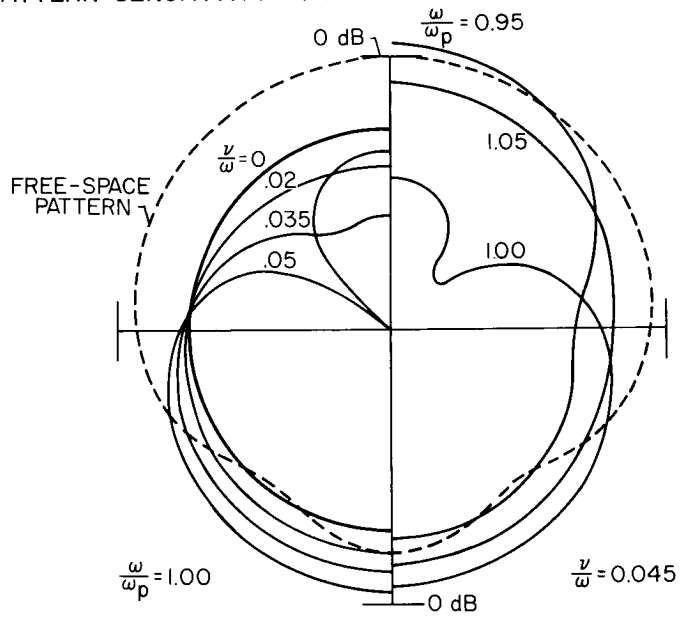


Figure 3



4. ANTENNA RESPONSE TO A PLASMA ENVIRONMENT

By Francis P. Russo and Thomas G. Campbell
Langley Research Center

SUMMARY

This paper presents some experimental results of the investigation made by the Langley Research Center to determine the effects of antenna detuning upon the radiated signal. The results of simulated detuning tests indicated that substantial changes in resonant frequency and bandwidth occurred. From the measured signal losses, it was concluded that antenna detuning is a first-order effect which can be minimized by broadbanding techniques.

INTRODUCTION

The interaction of antennas with the ionized flow field may produce substantial changes in the radiation characteristics which deteriorate antenna performance and contribute additional signal losses. Factors such as pattern distortion, antenna detuning, and the excitation of new propagation modes are near-field effects that are not adequately determined by far-field electromagnetic theory. As a result, the additional signal losses contributed by the near field are difficult to account for. It is the purpose of the investigation undertaken by the Langley Research Center to provide theoretical and experimental data on antenna performance and to determine the loss of radiated power resulting from changes in the electrical properties of the antenna. This program includes theoretical and experimental work at Langley which is supplemented by research study contracts.

The specific area discussed in this paper is the experimental investigation being made of antenna detuning. This investigation is an attempt to determine the changes in antenna characteristics caused by detuning and to relate these changes with the resulting signal losses. In order to simulate antenna detuning in the laboratory, use was made of dielectric shrouds, conductive fluids, and plasma facilities. Although the first two methods do not simulate the actual plasma medium, justification for their use lies in the fact that they provide a known environment in which to analyze and compare the antenna response.

FLIGHT DISCUSSION

Although the question of antenna behavior in a plasma environment had been considered early in the reentry program, its influence upon measured signal loss was demonstrated in the RAM A1 and RAM A2 flight experiments (refs. 1 and 2, respectively) which were discussed in paper no. 3 by John S. Evans and Calvin T. Swift. Figure 1 shows the RAM A conical-nose configuration and the



location of the VHF slot antenna. A broadband split-body dipole, which is referred to as a ring antenna, was located at the junction of the cone and cylindrical aft section. The 244.3-mc slot antenna was located on the forward section of the cone. A plot of voltage standing-wave ratio (VSWR) against frequency, which is indicative of the antenna bandwidth characteristics, is given in figure 2 for the RAM A1 and RAM A2 slot antennas. It is evident that the RAM A1 slot antenna is a sharply tuned high Q resonator compared with the RAM A2 antenna. For a VSWR of 2:1, the relative bandwidth ratio is approximately 10:1. Although the greater signal loss of 18 dB on RAM A1 was attributed to detuning of the sharply tuned antenna, flight measurements showed a maximum VSWR of 8:1, which corresponds to a mismatch loss of only 4 dB. The maximum VSWR on the RAM A2 slot antenna, however, was only 1.7:1 during the ionization period.

DETUNING TESTS WITH DISTILLED WATER AND SALINE SOLUTIONS

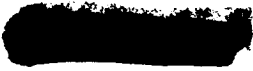
By using distilled water and saturated saline solutions as the detuning medium, a comparison was made of the radiation properties of the RAM A1 and RAM A2 slot antennas. Figure 3 shows the test model and the fiber-glass cone used to contain the solution. A thin plastic cover was placed over the test model to prevent direct contact with the solution. The transmitter and its power source were placed within the cone to prevent radiation from external cables. Measurements of VSWR and impedance were made with a diagraph which was connected to the antenna through a 0.5-wavelength section of transmission line. The signal level of each antenna was obtained by averaging the signal over 360° of rotation in the electric-field plane, which is shown in figure 1 as the XZ-plane. The results of these tests are summarized in the following table:

Medium	VSWR		Relative signal strength, dB	
	Narrowband	Broadband	Narrowband	Broadband
Distilled water	19	6.5	-24	-13
Saturated saline solution	15	5.5	-39	-27

As evident by the high VSWR and signal losses, the narrowband antenna shows greater detuning effects in both media and exhibits a signal loss of about 12 dB greater than that of the broadband antenna.

60-FOOT VACUUM SPHERE TESTS

Maintaining the same bandwidth characteristics, the two slot antennas were mounted to opposite sides of the RAM A nose cone. Signal-strength measurements were then made in the 60-foot-diameter vacuum sphere at the Langley Research



Center by using the free electrons in small solid-propellant rocket exhausts as a plasma simulator. The experimental test section within the sphere is shown in figure 4. The test model and receiving antennas were placed within an anechoic chamber to simulate free space. The receiving antennas were coaxially coupled to a receiving station outside the sphere where signal strength was recorded. In order to obtain a direct comparison of antenna performance under plasma conditions, the transmitter power was alternately switched to each antenna for 2 seconds. A portion of the signal-strength record is shown in figure 5. Because of the unstable flow conditions just after rocket-motor ignition, the first switch position should be ignored. As in the previous tests, the narrowband antenna exhibits greater signal loss than the broadband antenna under identical conditions. Although the results of these tests can only be compared qualitatively with the flight results, they do lend evidence to the fact that the sharply tuned antenna is susceptible to greater detuning losses than the broadband antenna.

RAM B2 DIELECTRIC SHROUD TESTS

By using dielectric shrouds as the detuning mechanism, tests were conducted with the RAM B2 antenna systems shown in figure 6. The antennas tested were a 244.3-mc slot antenna located on the forward section of the cone, a 30.8-mc ring antenna, and a 9210-mc four-horn array. A typical shroud covering the payload is shown in figure 7. The dielectric material was silicon rubber compound impregnated with graphite and had a dielectric constant of 10 and a loss tangent of 0.112. Figure 8 shows the free-space bandwidth characteristics of the 30.8-mc antenna and its response to a 0.5-inch shroud. Only a slight change is seen in the shape of the bandwidth curve, and the resonant frequency remains unchanged. Figure 9 shows the free-space bandwidth characteristics of the 244.3-mc slot antenna and its response to a 0.5-inch and a 1.5-inch shroud. In this case there is a substantial shift in resonant frequency to a lower frequency for increased shroud thickness. Although the antenna retains its resonant properties, there is a broadening of the bandwidth characteristics. Radiation patterns taken with the shrouds showed negligible change in shape for either vertical or horizontal polarization. Similar tests with the horn array showed only slight response to the shrouds and consequently are not shown. The results of these tests are summarized in the following table, and comparison is made with calculations based on far-field theory:

Shroud thickness, in.	Frequency, mc	Antenna	VSWR		Relative signal, dB	
			Predicted	Measured	Predicted	Measured
0.5	244.3	Narrowband slot	1.77	22.5	-0.66	-14.0
1.5	244.3	Narrowband slot	4.20	14.4	-2.85	-13.0
0.5	30	Broadband ring	1.08	1.65	-0.047	<-1.0
0.5	9210	Horns	3.48	2.9	-14.42	-15



As evident from the table, the broadband ring and horn antennas show close agreement with predictions based on far-field theory; whereas, the narrowband slot antenna, being more sensitive to its environment, exhibits greater signal losses because of detuning. By retuning the slot antenna to the shroud, however, almost complete signal recovery was obtainable.

RAM B3 DIELECTRIC SHROUD TESTS

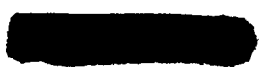
Similar detuning tests with the shrouds were conducted with the VHF slot antennas to be flown on RAM B3. An important experiment on this flight will be the comparison of narrowband and broadband antenna performance under plasma conditions. The operating frequencies and bandwidth characteristics of the two antennas are shown in figure 10. The free-space resonant frequency of the narrowband antenna is 244.3 mc and its gain relative to a reference dipole is -4 dB. The broadband antenna has a free-space resonant frequency of 231.4 mc and relative gain of -7 dB. The free-space radiation patterns of both antennas are essentially the same over the frequency range indicated. Figure 11 shows the narrowband antenna response to the 0.5-inch and 1.5-inch shrouds. A lower frequency shift of 4 mc and 8 mc results for increased shroud thickness. At the free-space resonant frequency, there is a maximum VSWR of 19:1 and total signal loss of 20 dB. Mismatch losses, however, account for only an 8-dB loss of radiated power. The response of the broadband antenna is shown in figure 12. A lower frequency shift of 2 mc and 4 mc results for the 0.5-inch and 1.5-inch shrouds, respectively. At the free-space resonant frequency, there is a maximum VSWR of 3.5:1 and total signal loss of 3 dB.

DISCUSSION OF DETUNING TESTS

The results of these tests show that antenna detuning contributes appreciable signal losses. Of significance is the fact that measured mismatch losses did not account for the total detuning effects. As is well known, however, it is extremely difficult to measure accurately the high standing-wave ratios which may be encountered. On the RAM A1 flight, for instance, if it were assumed that mismatch losses could account for the 18-dB difference in signal between the narrowband and broadband antennas, the RAM A1 flight instrumentation should have been capable of measuring voltage standing-wave ratios on the order of several hundred to one. Standing-wave measurements of this magnitude obviously transcend the capability of any instrument. It has not been determined, however, what effect the changes in resonant frequency and bandwidth characteristics have on the radiation efficiency of the antenna.

20-INCH HYPERSONIC ARC-HEATED TUNNEL

In order to provide a comparison of antenna response to the dielectric shrouds, a test was made under plasma conditions in the Langley 20-inch



hypersonic arc-heated tunnel. The antenna configuration used was an axial slot on a cylindrical body. In order to obtain the antenna bandwidth characteristics under plasma conditions, the slot antenna was swept ± 10 mc from its center frequency of 244.3 mc, at a sweep rate of 60 cps. A bidirectional coupler in the transmission line enabled forward and reflected power to be monitored. By applying the reflected power and sweep signals to the plates of an oscilloscope, the bandwidth characteristics could be photographed during the test. Although the ionized flow field over the antenna was not adequately defined, interferometer measurements of the free stream indicated an electron density on the order of 10^9 electrons per cm^3 and a collision frequency of 10^8 per second. Figure 13 shows a typical response curve at peak ionization. The broken curve indicates the free-space bandwidth characteristics. With the ionized flow over the antenna there is a substantial broadening of the bandwidth curve with no well-defined resonant point, and the VSWR at the free-space resonant frequency is 9:1. As the ionization trailed off at the end of the run, the response curve shown in figure 14 was obtained. Although a lower frequency shift still exists, the antenna appears to have regained its resonant properties at a new resonant frequency of 238 mc. A comparison of these results with those of the dielectric tests shows that both methods produce a similar effect on antenna response.

CONCLUDING REMARKS

From the results of the experimental data presented, it can be concluded that antenna detuning is a first-order effect on measured signal loss, which can be minimized by antenna broadbanding techniques. As yet, considerable effort must be directed toward a theoretical analysis relating antenna response to the plasma medium so that correlation can be made with experimental measurements.

REFERENCES

1. Sims, Theo E., and Jones, Robert F.: Flight Measurements of VHF Signal Attenuation and Antenna Impedance for the RAM Al Slender Probe at Velocities up to 17,800 Feet Per Second. NASA TM X-760, 1963.
2. Russo, F. P., and Hughes, J. K.: Measurements of the Effects of Static Magnetic Fields on VHF Transmission in Ionized Flow Fields. NASA TM X-907, 1964.

CONICAL NOSE SECTION OF RAM A

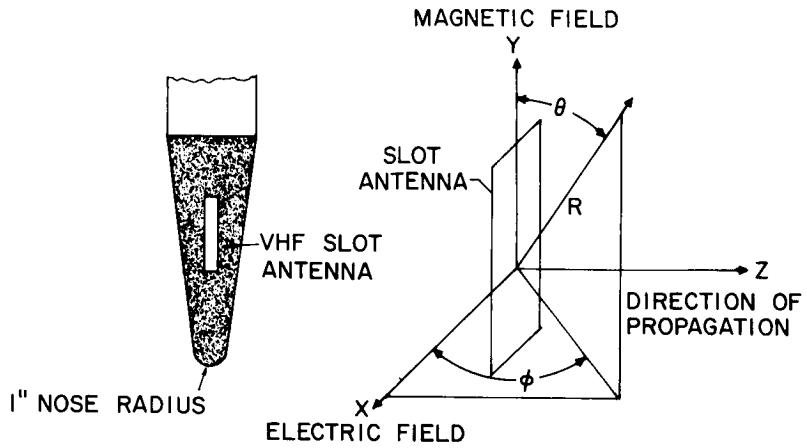


Figure 1

RAM A1 AND A2 ANTENNA BANDWIDTH CHARACTERISTICS

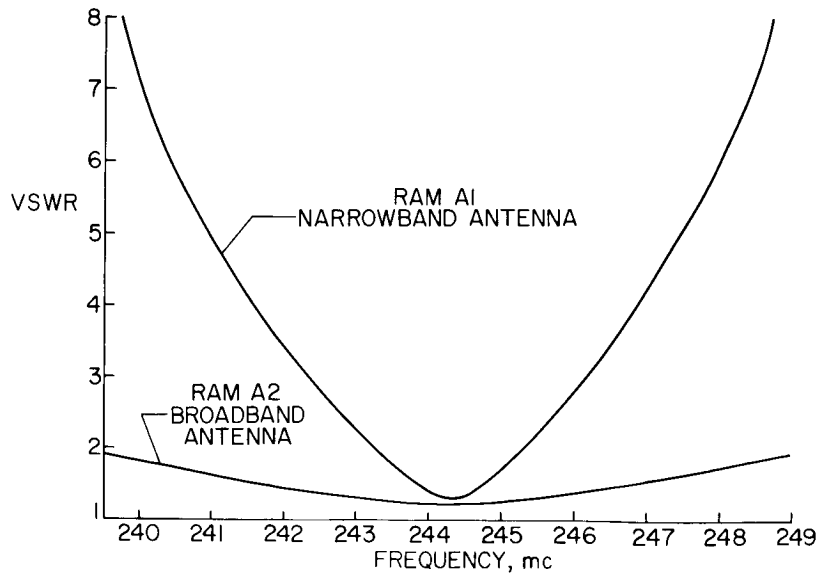


Figure 2

DETUNING TEST SETUP FOR SALT AND DISTILLED WATER

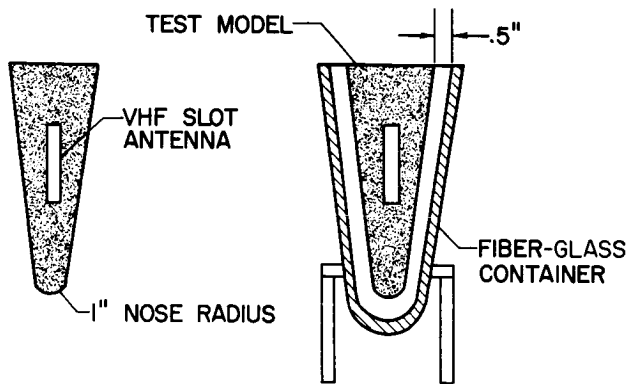


Figure 3

TEST MODEL IN ANECHOIC CHAMBER

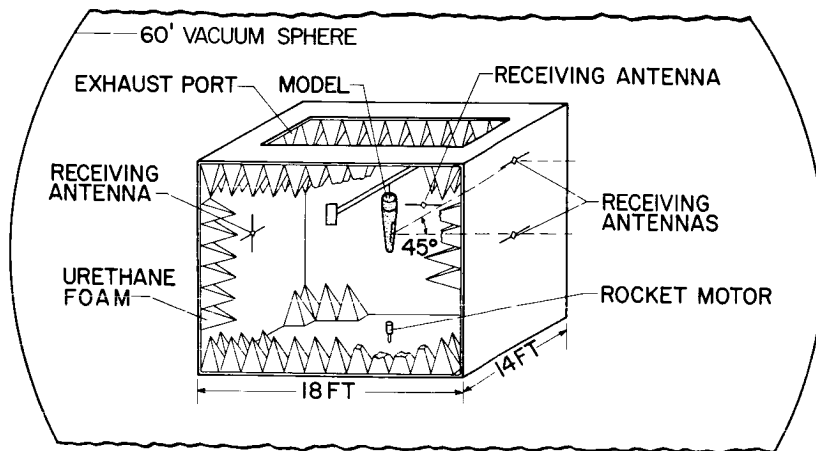


Figure 4

RADIATION FROM BROADBAND AND NARROWBAND SLOT ANTENNAS

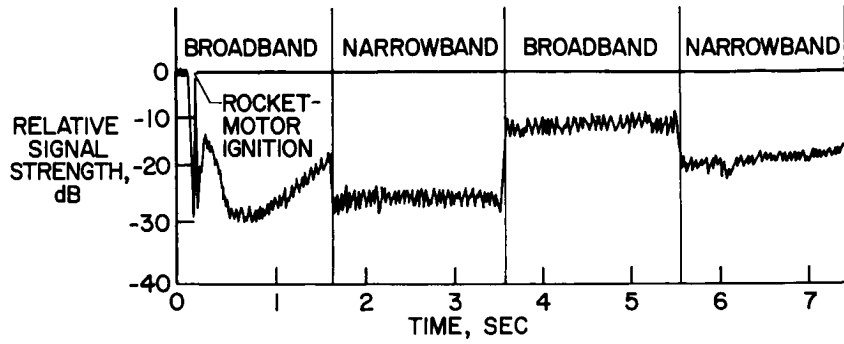


Figure 5

RAM B2 PAYLOAD

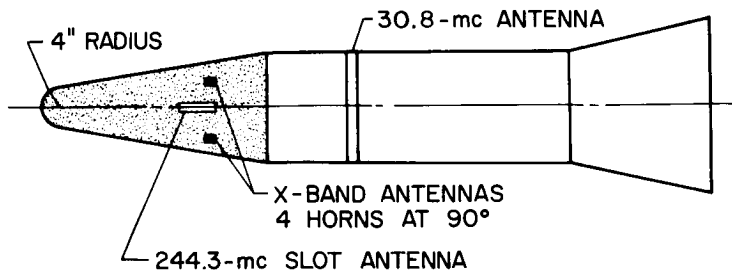
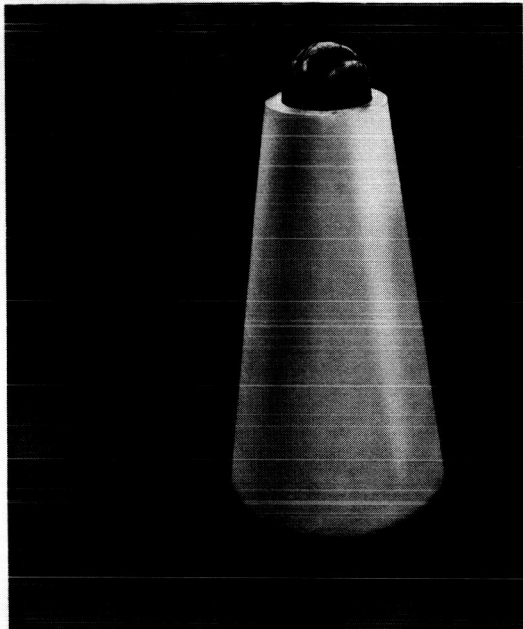


Figure 6

TYPICAL SHROUD COVERING THE RAM B2 PAYLOAD



L-2165-15

Figure 7

BANDWIDTH CHARACTERISTICS OF 308-mc RING ANTENNA

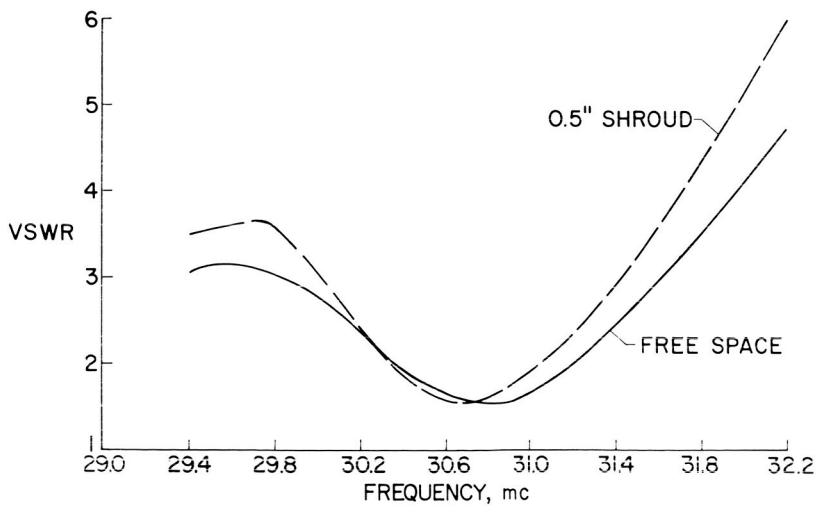


Figure 8



BANDWIDTH CHARACTERISTICS OF SLOT ANTENNA

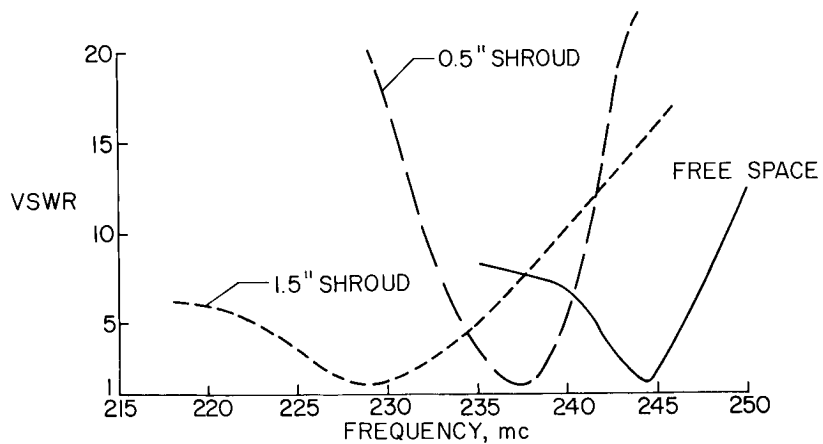


Figure 9

RAM B3 SLOT-ANTENNA CHARACTERISTICS FOR FREE SPACE
NARROWBAND ANTENNA: CENTER FREQ, 244.3 mc; GAIN, -4 dB
BELOW REFERENCE DIPOLE; BROADBAND ANTENNA: CENTER
FREQ, 231.4 mc; GAIN, -7 dB BELOW REFERENCE DIPOLE

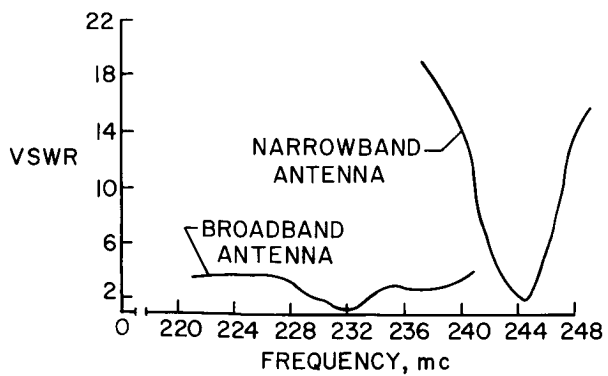


Figure 10

RAM B3 NARROWBAND ANTENNA
FREE-SPACE RESONANT FREQ., 244.3 mc;
NARROWBAND SIGNAL, -20 dB

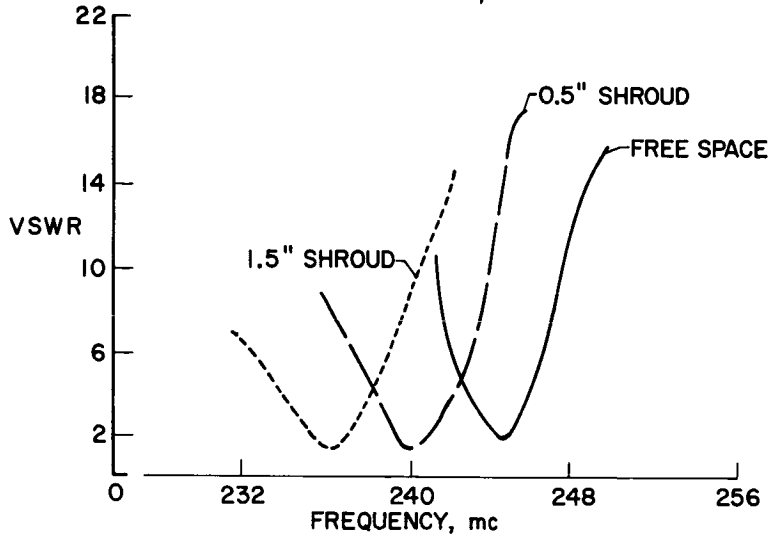


Figure 11

RAM B3 BROADBAND ANTENNA
FREE-SPACE RESONANT FREQ., 231.4 mc; BROADBAND SIGNAL, -3 dB

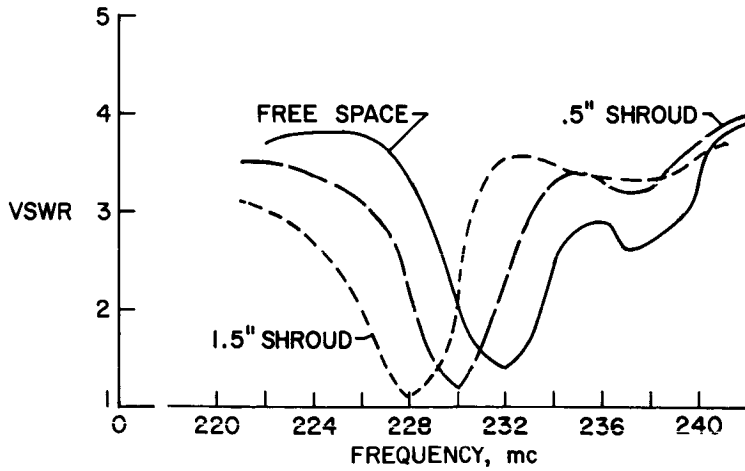


Figure 12



0374 [REDACTED]

**DETUNING TEST IN THE LANGLEY 20-INCH HYPERSONIC
ARC-HEATED TUNNEL**
SLOT-ANTENNA BANDWIDTH CHARACTERISTICS; 8 SEC

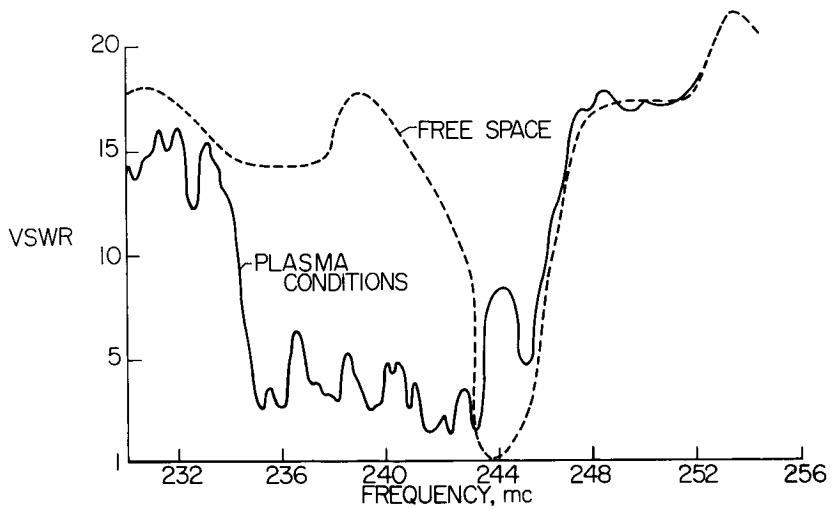


Figure 13

**DETUNING TEST IN THE LANGLEY 20-INCH HYPERSONIC
ARC-HEATED TUNNEL**
SLOT-ANTENNA BANDWIDTH CHARACTERISTICS; 14 SEC

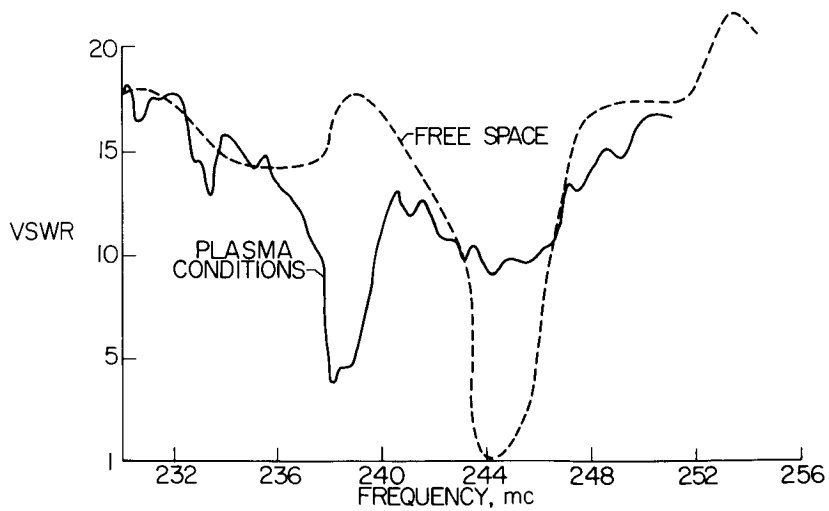


Figure 14



5. PRESENT PLANS FOR APOLLO COMMUNICATIONS
AND TRACKING DURING REENTRY

By George B. Gibson
Manned Spacecraft Center

SUMMARY

This paper presents some of the results of the Manned Spacecraft Center planning to date on Apollo communications during the reentry phase. Included are plots of reentry areas, reentry profiles, operating frequencies, and anticipated blackout times for the Apollo command module.

RESULTS

The NASA Manned Spacecraft Center has been engaged in extensive trajectory studies for use in determining tracking requirements for Project Apollo. The purpose of this paper is to present some of the significant results that are particularly related to tracking and communications during reentry.

Figure 1 is a plot of the ground track for a landing in the vicinity of the Samoan Islands. Such a track will generally result when the moon has a positive declination at the time of the departure of the Apollo spacecraft.

Figure 2 is a plot of the ground track for a landing in the vicinity of the Hawaiian Islands and results when the moon has a negative declination at the time of departure of the spacecraft.

Figures 3 and 4 are profiles of the short range and the skip trajectories, respectively. As can be seen in the foregoing figures, the permissible reentry range limits are a maximum of 5000 and a minimum of 1200 nautical miles.

The operational frequencies which will be used for the Apollo Command and Service Module are as follows:

Functions	Frequency, mc
Spacecraft to Earth	
VHF telemetry	237.8
VHF voice	296.8
S-band ranging, voice, telemetry, television, etc.	2287.5
C-band radar	5765.0
Earth to spacecraft	
VHF voice	296.8
UHF data	450.0
S-band ranging, voice, and data	2106.4
C-band radar	5690.0



The North American Aviation Company has calculated the command-module reentry flow field on a simplified one-dimensional nonequilibrium basis and has made the assumption that transmission through the resulting plasma sheath is completely attenuated when the operating frequency is less than the plasma frequency.

Figures 5 and 6 (from ref. 1) show the blackout times for the various operating frequencies which are expected for the short range and for the skip trajectories. Regarding the skip trajectory, it will be highly advantageous to know accurately the altitude and velocity at which the system will emerge from blackout and at which it will reenter the second phase of the blackout trajectory. High-altitude aircraft will be positioned near these points and since these aircraft will have good direction-finding capabilities, the knowledge of such points will be a great aid in determining the impact area of the spacecraft. As an example, postflight analyses of Project Mercury show that the impact area could be determined accurately from a knowledge of the time at which a blackout of VHF communications occurred.

Figure 7 is really a "do-it-yourself kit" for predicting blackout of the operating frequency from the knowledge of altitude and velocity. The expected blackout lines are calculated by applying certain scaling rules and representative electron densities. Lines are also shown for electron densities an order of a magnitude higher and lower than the calculated value.

No claim is made that the foregoing blackout transition charts are the most accurate calculations which can be made of Apollo blackout times; however, they are believed to be the most accurate available to date. Their accuracy will also be improved by incorporating blackout data resulting from a super-orbital reentry flight.

Projects which are underway and which tend to minimize the blackout time are followed with interest by engineers associated with the Apollo Program. However, it must be realized that Apollo is a "state-of-the art" project and requirements can therefore not be based on techniques which are not proved at this time. Any practical breakthroughs in solving the blackout problem will be an obviously welcome bonus.

REFERENCE

1. Daniels, R. L.: Final Report on Apollo Plasma Reentry Studies. Rep. No. SID 63-746, North American Aviation, Inc., July 5, 1963.

SAMOA ISLAND LANDING

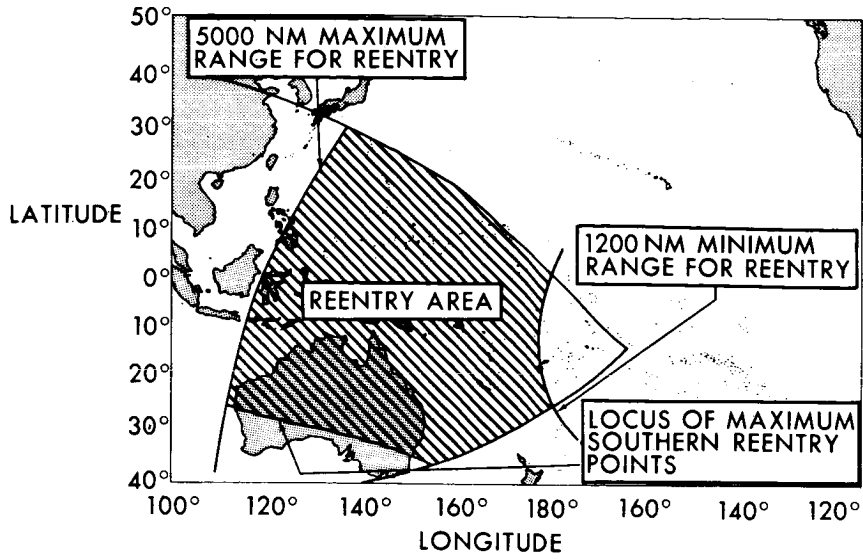


Figure 1

HAWAIIAN LANDING

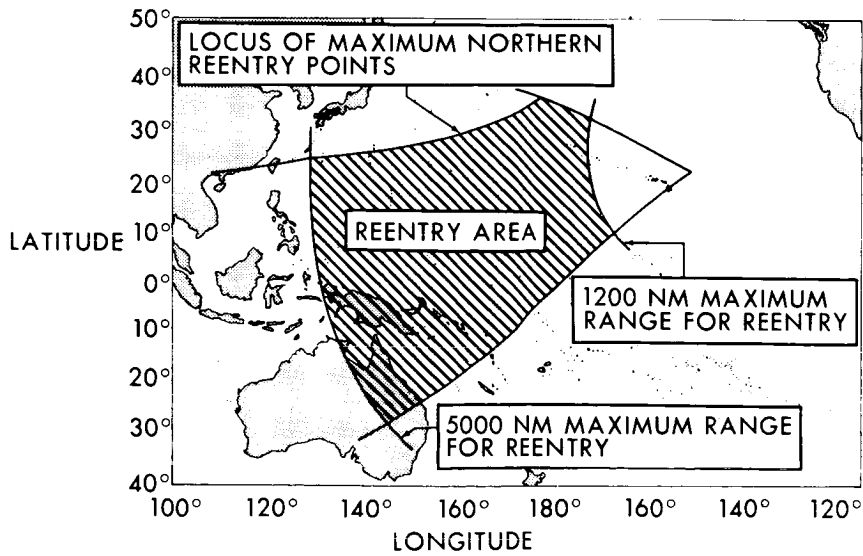


Figure 2





REENTRY TRAJECTORY PARAMETERS AS A FUNCTION OF RANGE FOR AN INITIAL FLIGHT-PATH ANGLE = -6.4° AND A REENTRY RANGE = 1000 NM

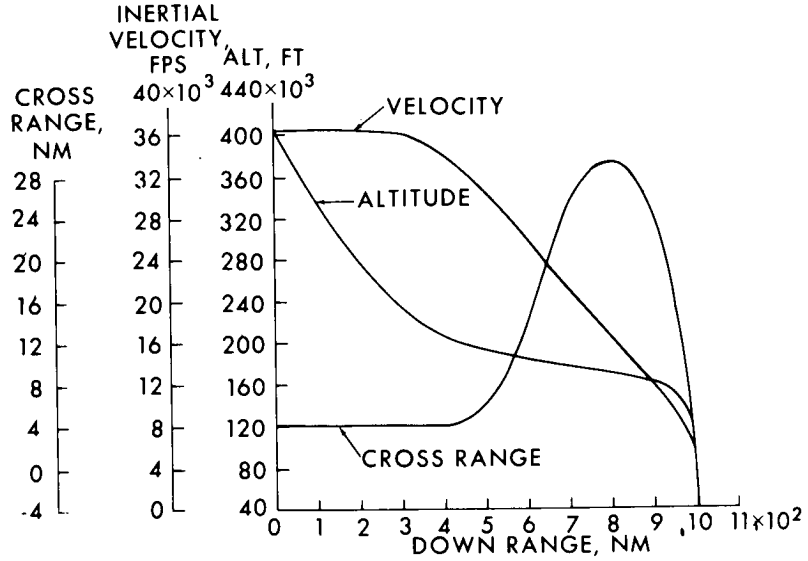


Figure 3

REENTRY TRAJECTORY PARAMETERS AS A FUNCTION OF RANGE FOR AN INITIAL FLIGHT-PATH ANGLE = -6.4° AND A REENTRY RANGE = 5000 NM

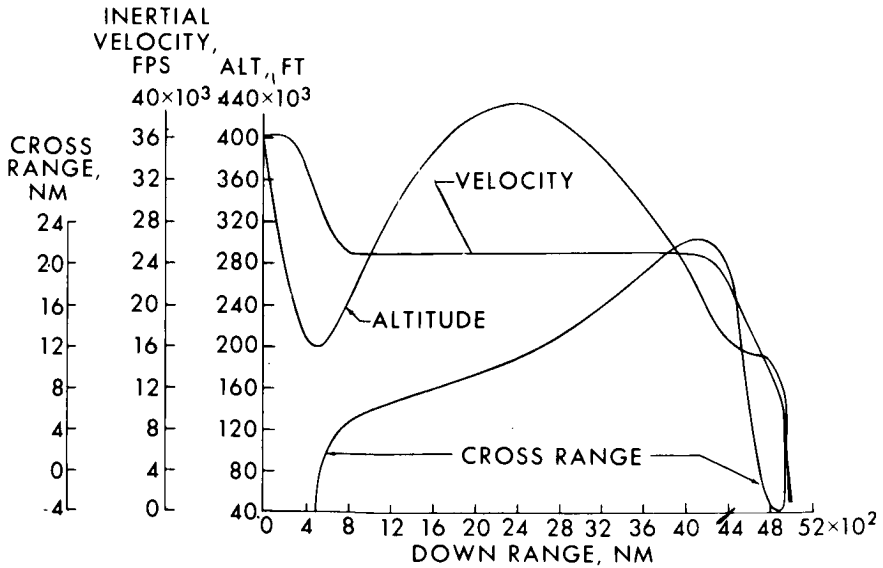


Figure 4



SHORT RANGE TRAJECTORY BLACKOUT RANGES

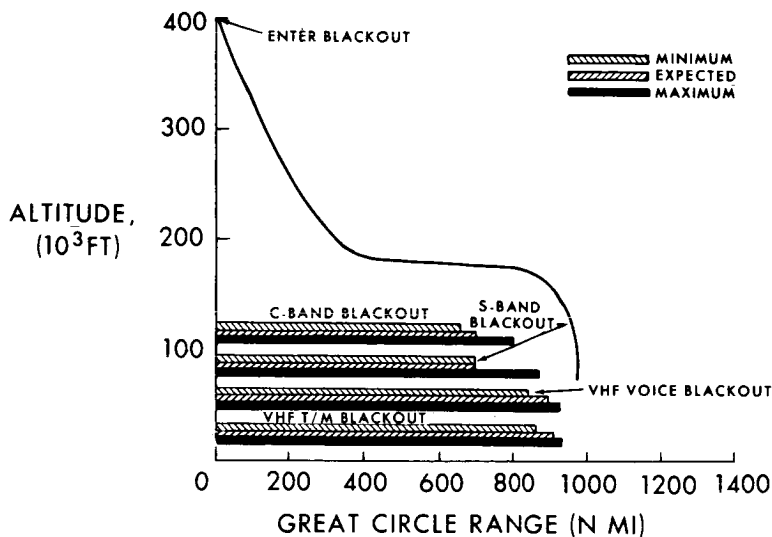


Figure 5

SKIP TRAJECTORY BLACKOUT RANGES

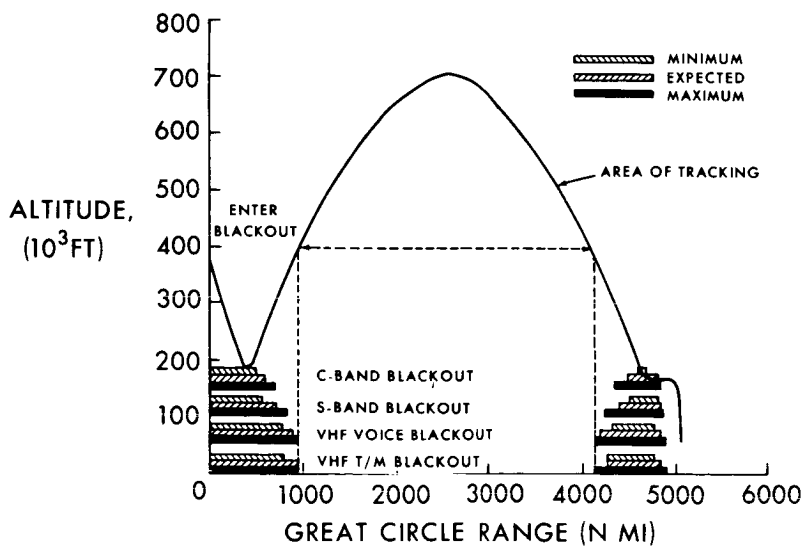


Figure 6

APOLLO COMMUNICATION SYSTEMS BLACKOUT TRANSITIONS

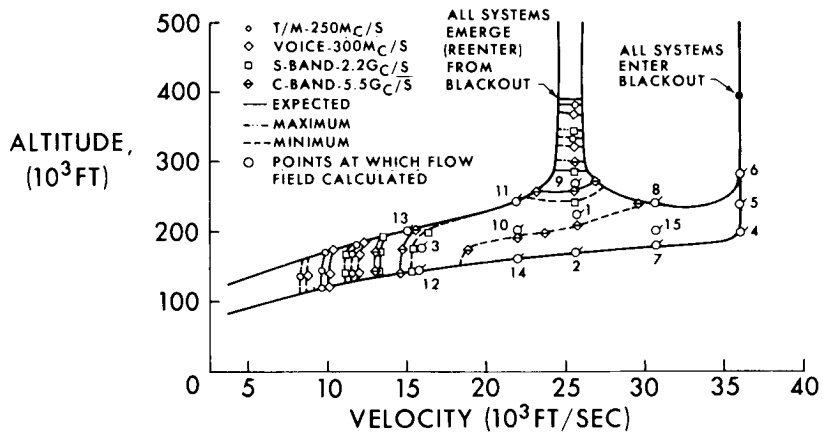


Figure 7



6. PLASMA EFFECTS ON APOLLO REENTRY COMMUNICATION

By Richard Lehnert and Bernard Rosenbaum
Goddard Space Flight Center

SUMMARY

Plasma effects on tracking and communication during Apollo reentry from a lunar mission have been reviewed. Several characteristic Apollo reentry trajectories are given as examples for the demonstration of rf-signal blackout areas expected to occur during skip-type and direct-descent reentry flights. The presently existing uncertainties in the determination of electrical properties in the Apollo plasma sheath and the plasma effects on antenna performance have led to widely differing estimates of blackout area predictions. The most desirable case of continuous tracking and communication throughout the entire reentry phase could be achieved only by developing ameliorative methods for preventing blackout. In order to accomplish this, the complex physicochemical phenomena of the asymmetric ionized flow field peculiar to Apollo and the three-dimensional wave propagation through the highly inhomogeneous plasma sheath must be more clearly understood. However, the development and implementation of preventive techniques will be confronted with the intricate matter of conforming to overall system requirements.

For the establishment of a most economical and effective Apollo reentry ground-support network, GSFC needs to know precise blackout bounds for all possible types of reentry trajectories. The accuracy or uncertainty of the prediction of blackout area bounds are determining factors in the assessment of the ground-support capabilities during Apollo reentry.

INTRODUCTION

Tracking and communication problems caused by radio-frequency-signal blackout during the reentry phase of Apollo spacecraft returning from a lunar mission are considered in this paper. Reentry into the earth's atmosphere is generally defined as commencing at an altitude of 400,000 feet. Upon deeper penetration into the regimes of exponentially increasing air density, the drag of the reentering spacecraft causes a considerable amount of its kinetic energy to be transferred into heat predominantly by compression in the stagnation region and partially by skin friction in the boundary layer, which is also referred to as the shear layer. Temperatures in the heat cap between bow shock and spacecraft surface rise to such magnitudes that dissociation and ionization of the environmental air takes place. Consequently, the flow field surrounding the spacecraft becomes highly conductive with respect to electromagnetic wave propagation and markedly enhances attenuation of rf-signals. In the most critical case, radio communication is completely blacked out. This signal blackout has already been experienced during the reentry of the Mercury spacecraft. A much more serious condition of tracking and communication blackout is expected during the reentry





flight of the Apollo spacecraft because of the higher Apollo reentry velocity (35,000 ft/sec) in comparison with Mercury velocity (24,000 ft/sec). Signal blackout will be particularly critical since its occurrence will coincide with the maneuver phase of the spacecraft and may eliminate the ground support during a vital portion of this phase or even during the entire regime of effective maneuverability (depending upon the type of reentry trajectory).

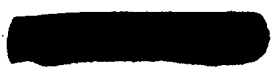
From the viewpoint of the generation of the most efficient and reliable reentry ground support, it is necessary to recognize all possible reentry trajectories within the constraints of presently existing ground rules and to establish the degree of assistance needed from the ground to assure a full success of any reentry mission. In this consideration, in turn, the capability of tracking and communication must be investigated in the light of adverse effects imposed by rf-signal blackout and a solution of the blackout problem be sought for trajectory regions where proper signal transmission may decide upon the successful continuation and completion of the reentry mission.

REENTRY

Reentry shall be defined as that phase of the Apollo Command Module flight which originates at the reentry point upon return from a lunar mission. The reentry point is the locus of first encounter with the atmosphere conventionally assumed to occur at an altitude of 400,000 feet. At an altitude of about 50,000 feet, the programed termination of the operation of the onboard automatic guidance system determines the end of the reentry phase.

The presently considered range variation of nominal Apollo reentry trajectories to be flown with the MIT automatic guidance and control extends from approximately 1,000 to 5,000 nautical miles. Information on the trajectories for use in determining tracking requirements for project Apollo has been assembled by the Flight Operations Division of NASA Manned Spacecraft Center (MSC). Control maneuvers during reentry can be performed only by rolling the Command module. By means of the roll maneuver the lift vector is being rotated into a desired direction. Lift is generated in the pitch plane of the Command Module at a trim angle ($\alpha = 33^\circ$) which is attained by a prescribed displacement of the center of gravity from the longitudinal axis of rotational symmetry. At this trim angle where a lift-to-drag ratio $L/D = 0.5$ is established, an equilibrium exists between overturning moment and aerodynamic restoring moment. Maneuvers are consequently dependent upon the existence of adequate aerodynamic forces and are therefore restricted to altitudes where the air density ρ and velocity v are sufficiently high to insure an effective dynamic pressure $\rho \frac{v^2}{2}$. The threshold value for the dynamic pressure can be determined by a minimum effective drag reference level (ref. 1). This drag reference level is attained at an altitude of about 300,000 feet, above which the automatic guidance system is inoperative with respect to vehicle control.

Typical Apollo reentry trajectories are presented in figure 1 for ranges of 5,000, 3,000, and 1,000 nautical miles at a nominal reentry flight-path



angle, $\gamma = -6.4^\circ$. (Information for trajectories presented in figures 1 to 4 is from MSC.) For a given landing site and depending upon the ground distance of the reentry point from the landing area, the trajectories can vary from a characteristic skip trajectory (1) to a typical direct-descent trajectory (3). Considering the skip trajectory first, the onboard automatic guidance and control mode calls for corrective maneuvers pertaining to range and cross range in two areas. The area of major control-maneuver effectiveness is located in the dip-in region of the trajectory commencing shortly after the reentry point and is fading out at an altitude above 300,000 feet upon skipout. Above this altitude the dynamic pressure becomes so small that a ballistic trajectory prevails until the Command Module again returns into a region of effective aerodynamic forces. This second area of maneuverability lends itself only to minimal corrections on account of the rapidly decreasing velocity and the remaining short range-to-go. The lower altitude bound of maneuverability (obtained from NASA Manned Spacecraft Center) is 50,000 feet where the automatic guidance system program terminates.

The direct-descent type of trajectory (3) does not have a skipout phase. It has only one upper and one lower altitude bound for maneuverability coinciding with the altitudes of original onset and ultimate termination of maneuver capability expected during the skip trajectory. Consequently, the major portion of the direct-descent reentry constitutes a controlled flight.

The variation of the altitude with range profile within a reentry flight-path-angle corridor from $\gamma = -5.4^\circ$ to $\gamma = -7.4^\circ$ for a nominal 5,000-nautical-mile Apollo reentry trajectory is shown in figure 2. Particularly noteworthy is not only the large change in maximum altitude as a function of extreme reentry angles but also the shift in range-to-go from the point of deepest initial penetration for different reentry angles amounting to a maximum of 500 nautical miles. This latter effect is a basic factor for ground-support coverage.

An example for the reentry flight-path-angle effect on shorter skip trajectories (3,000 nautical miles) is given in figure 3. Although the magnitude of maximum altitude variation with γ is greatly reduced in comparison with the 5,000-nautical-mile trajectory, the maximum downrange variation of the minimum altitude in the initial dip of the flight still amounts to 500 nautical miles.

Direct-descent trajectories shown in figure 4 are not expressly affected by the reentry flight-path angle.

In view of the strong requirements for the safe return of the astronauts, a manual emergency reentry mode suggested by North American Aviation is being considered as a backup control procedure in case of a failure of the onboard automatic guidance and control system. The manual emergency reentry mode is based on an independent semiautomatic onboard system consisting of an accelerometer and a real-time display of the accelerometer output in terms of gravity g against velocity v . The velocity is obtained by integration of the accelerometer output. Figure 5 is a schematic diagram of the gravity-velocity display which is an integral part of the Command Module pilot's control board. The pilot, in turn, takes over the roll control of the Command Module by using the gravity-velocity display as a guide for staying within prescribed g -limits and for reducing gradually his velocity to slightly below orbital



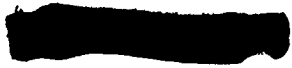
speed in order to avoid a fatal skipout. During the manual emergency mode, the astronauts do not have any onboard indication of the spacecraft position, and range and cross-range deviations from the prescribed flight path become incidental. For reasons of giving a characteristic example, three 5,000-nautical-mile trajectories generated with the MIT automatic guidance system have been plotted in the gravity-velocity display for reentry angles $\gamma = -5.4^\circ$, $\gamma = -6.4^\circ$, and $\gamma = -7.4^\circ$. They all demonstrate that the gravity and velocity constraints are properly taken into consideration.

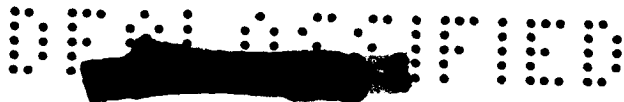
Present investigations at North American Aviation (NAA) indicate that the manual reentry emergency mode is capable of flying trajectories ranging up to 7,500 nautical miles within the prescribed gravity and velocity constraints. The tentative noncompatibility with the maximum range of presently considered nominal automatically guided reentry flights is subject to current studies at NAA.

BLACKOUT AREAS

With the predictions on hand for Apollo rf-signal blackout, one can make preliminary approximate estimates of blackout area during typical reentry trajectories. It should be pointed out, however, that these predictions, based on unpublished information from AVCO, Cornell Aeronautical Laboratory, and the previous work of F. J. Tischer at Goddard Space Flight Center (GSFC) are made under very simplifying assumptions. These assumptions suggest 'summa summarum' that all conditions of the rf-signal blackout for a given operational frequency during any Apollo reentry trajectory are prescribed by only two parameters, namely, velocity and ambient air density. If a standard atmosphere density profile is assumed, the second determining parameter becomes the altitude. Under these assumptions, blackout areas have been coordinated with some characteristic Apollo reentry trajectories. An example of an altitude-velocity presentation of the trajectories considered in figure 1 is given in figure 6. Plotted in this diagram are two sets of parameter family curves, (4) and (5), indicating predicted blackout bounds for operational frequencies of 250 mc, 2 Kmc, and 5 Kmc. The predictions for the parameter curves (4) by AVCO are based on equilibrium flow assumptions and an antenna location on the windward side (attached inviscid flow) of the conical Apollo afterbody. Parameter curves (5), in turn, were obtained at GSFC by adjusting the geometry factors of F. J. Tischer's flow-field model at an antenna location on the leeward side (separated flow) of the Apollo afterbody for nonequilibrium conditions in the stagnation region.

By using the scheme demonstrated in figure 6 as a tentative approach, S-band blackout areas have been determined for all trajectories given in figures 1 to 4. Figure 1 shows the estimated blackout regions for S-band of nominal 5,000- and 3,000-nautical-mile reentry trajectories with a nominal reentry flight-path angle, $\gamma = -6.4^\circ$. Considering the 5,000-nautical-mile skip trajectory, curve (1), there are two areas of blackout which are located within the two regimes of spacecraft maneuver capability described in the section entitled "Reentry." The first blackout commences upon initial Apollo penetration into the atmosphere at an altitude of about 310,000 feet and





prevails through the major portion of the maneuverable flight up to an altitude of approximately 250,000 feet during skipout.

The second blackout takes place in an altitude region from about 250,000 feet to 180,000 feet after the spacecraft returns from the skip. For comparison, predictions of S-band blackout by NAA (ref. 2) are plotted in figure 1. This work is based on equilibrium flow field and plane wave-propagation calculations made with an assumed antenna location on the windward side of the Apollo spacecraft more commensurate with the Mercury C-band antenna position. Electron density or plasma frequency, calculated along the wave-propagation path, has been supplied with an uncertainty factor of plus or minus an order of magnitude. This uncertainty factor may include the neglected effects of nonequilibrium flow, three-dimensional wave propagation, and ablation. Taking into account this order-of-magnitude variation of the electron density, NAA gives maximum and minimum extent of S-band blackout applicable to the two described areas of blackout for trajectory (1). It is interesting to note that with the exception of the location of the initial onset of blackout, the NAA minimum blackout area predictions are in fairly good agreement with the GSFC estimates (except that there is disagreement with the NAA assumption that blackout for all operational frequencies starts at the reentry point (400,000 feet)). (See also fig. 2.) This agreement, however, should not be overemphasized because the not yet accountable effects of ablation may further enhance attenuation.

General tendencies of S-band blackout area behavior for the skip-type Apollo reentry trajectories may be recognized by inspection of figures 1 to 3. The extent of the duration of the first blackout area is subject to variation while the second blackout region is not greatly affected by changes of trajectory profiles.

The contributing parameter for the changes in extent of the first blackout area is the reentry flight-path angle. Practically independent of the range of skip-type trajectories, the maximum variation of the length of the blackout area within the considered reentry angle corridor amounts to as much as 600 nautical miles.

The most serious blackout effect is imposed on short-range direct-descent type of reentry trajectories. (See fig. 4.) Practically the entire maneuverable portion of the reentry flight appears to be in the S-band blackout region. Comparison with NAA blackout data shows that the Goddard Space Flight Center prediction of the termination of blackout for a reentry angle of -6.4° lies about halfway between the NAA lower altitude bounds of maximum and minimum blackout area extent. Again there is disagreement with the NAA assumption of the onset of blackout at an altitude of 400,000 feet. It is interesting to note that almost the entire flight phase during the manual emergency reentry mode (see fig. 5) is immersed in S-band blackout.

EFFECT OF BLACKOUT ON GROUND SUPPORT

The tracking and communication network can participate in an important role in the reentry flight and assist the spacecraft crew in their task. A



critical matter in reentry will be the initial phase of deceleration to sub-orbital velocity. In this phase precise guidance and maneuvering are essential. It is a pressing consideration that the ground network should provide monitoring capability for the prime guidance system and function as an integral link between the spacecraft and control center should the vehicle be flying in a manual emergency mode. In case of improper functioning of the automatic guidance system and for the manual emergency reentry mode, the reentry network should also predict the locale of an emergency landing and thus aid in recovery.

The reentry environmental conditions, as mentioned, have a debilitating effect on communication and tracking. Consequently, the role and operation of the ground network must be reviewed in the light of the strong interaction between radio signal and the ionized flow field surrounding the reentering spacecraft and its radio antenna. This degrades the overall performance of the radio channel. The S-band transponder-signal level as well as the other radio channels can be severely attenuated. The proximity of the plasma to the antenna introduces a severe impedance mismatch which can drastically weaken the signal power and thereby reduce the channel capacity of the telemetry system and make voice communication impossible. Tracking errors also will arise from a degradation of Doppler range rate measurements. Even skin tracking can be unsatisfactory because of confusion introduced by the ionized vehicle trail and precursor ionization in front of the shock.

The ideal condition for reentry is that the blackout intervals be completely eliminated. This would permit continued tracking throughout the atmospheric flight and make communication possible. The development and implementation of methods of circumventing blackout is a prime need of the reentry phase. Ways of eliminating the blackout in the severe Apollo reentry flight conditions have not yet been developed within the Apollo mission requirements. Some methods suggested of modifying flow-field chemistry are seeding the flow field with electronegative materials and injecting a fluid into the boundary layer. The water injection has been successfully demonstrated in the RAM project (ref. 3) through an actual flight experiment. This result is most encouraging for Apollo. To evaluate the effect of water injection for Apollo, experiments need to be conducted by taking account of the stagnation condition attending superorbital reentry and the complex fluid mechanical problems stemming from the geometry of the Command Module.

In the event that techniques are not developed to overcome blackout, the operational plan for the Apollo ground support must be prepared to function within restrictive communication conditions imposed by blackout. A critical interval can develop during the reentry phase when the spacecraft descends to 200,000 feet and initiates the skipout of the atmosphere. Emergency conditions at this juncture make it necessary to execute corrective maneuvers quickly because the vehicle is soon in an ascending phase and aerodynamic conditions are not favorable for maneuvers. Time for decisions is at a premium. This is where the ground support may be able to help, but is at present handicapped by the blackout state. The precise limit of the communication rupture is important because it will have a critical bearing on the placement of a tracking ship and other communication problems. Assuming, for instance, a continental landing in the southern part of the United States, a tracking ship would be placed in a most effective strategic position in the Pacific Ocean as indicated by the

generalized term "ground station view" in figures 1 to 3. The range of a nominal reentry trajectory is approximately known well in advance depending upon the launch date. For each prescribed trajectory range, the ship has to seek its position so that the spacecraft can be acquired immediately after escaping from blackout. This event, however, occurs in an area whose location relative to the reentry point is a function of the reentry flight-path angle and the performance of the onboard automatic guidance system during the blackout. The reentry flight-path angle is fairly well determined by the Manned Space Flight Network after the last major midcourse correction which takes place about a day prior to the reentry phase. However, if according to recently obtained information from Manned Spacecraft Center, additional midcourse maneuvers can still be performed until 1 hour prior to landing, the reentry angle may be affected considerably. Consequently, a change in trajectory profile on short notice will be significant with respect to positioning the ship. The present uncertainty in blackout termination during skipout also poses a problem on the positioning of the ship and consequent acquisition and tracking capabilities. As yet, it is not possible to make accurate predictions where blackout is relieved in the ascent phase, but 250,000-foot altitude may be a reasonable estimate.

In order to optimize the Apollo tracking network and meet its requirements during reentry, the plasma effects on communication must be understood and degrading effects accurately evaluated. Analytical methods of investigating the signal degradation on reentry from lunar return are encumbered by two fundamental tasks that are, in fact, common to all reentry communication problems. One is the determination of the plasma properties of the hypersonic ionized flow field, the so-called plasma sheath. The other is the behavior of an antenna clad by the plasma sheath. The treatment of these problems is very difficult and stems in large part from the multiplicity and complexity of the phenomena involved, also from the lack of physical data, and in other instances from intractable mathematical problems. The plasma properties in particular are a very sensitive function of complex physicochemical processes in the shock layer and the calculation of these processes is subject to doubt arising from further uncertainty in basic physical parameters. Of the numerous chemical reactions requiring consideration, the reaction-rate constants of many are only very crudely known. Recombination-rate constants theoretically predicted by various authors differ by as much as three orders of magnitude. Therefore, most efforts at evaluating the blackout problem are primarily handicapped by the uncertainty in the crucial plasma properties. Furthermore, the behavior of an antenna immersed in a plasma can be very difficult to analyze. When observed signals have been attenuated 20 decibels or more, the changes wrought by the plasma sheath in signal-propagation characteristics are so drastic that the antenna radiation pattern will be quite unlike the pattern in the absence of a plasma and further complicate detailed analysis of signal attenuation by the plasma.

The major effect of the plasma is to attenuate the signal strength available for communication between ground and spacecraft. In the high-altitude

regimes of the Apollo flight, the critical parameter controlling the attenuation is the ratio of signal frequency to the maximum plasma frequency attained in the antenna region. The attenuation in general is relatively high or low according as the ratio is less or greater than unity. The positions in the vehicle trajectory where the ratio equals unity are those used in this paper for determining the blackout limits. The rule-of-thumb condition for blackout then predicts that for the planned skip trajectories of Apollo, blackout will occur in two intervals - one for each entry phase of the skip (see figs. 1 to 3).

To determine the effect of the plasma sheath on radio communication during reentry, the free-electron-density distribution must be known in the antenna region. This distribution is a function of the airflow and reaction kinetic intervening between the stagnation region and antenna region. During the reentry flight, the Apollo spacecraft will be surrounded by an asymmetric flow field because of its trim angle of 33° . Since the trim angle does not change during roll maneuvers, the flow field will remain unchanged. As a consequence there will only be one flow field for Apollo for a given altitude and vehicle velocity. The flow-field asymmetry can be examined by taking a cross section of the flow field in the plane containing the symmetry axis and lift vector (fig. 7). A stagnation point develops in this plane at a position not far from the vehicle shoulder. The expanded airflow around one shoulder will have, at altitudes above 170,000 feet, an inviscid attached flow with presumably laminar boundary layer; about the other shoulder, the airflow will be unable to follow the converging vehicle contour and in this case a separate flow regime follows. The free-electron-density distribution in the aftersection of the vehicle can differ appreciably for the two flow patterns described. The antennas placed on the vehicle wall bordering these flow regimes can have different radio characteristics and the blackout intervals will not be the same. The separated-flow regime has circulatory flow and is broad in extent, with a relatively large quantity of ablation products and hence high electron concentration. The thermochemical state of this region is difficult to describe. The flow field around the shoulder having an attached flow field is more amenable to analysis. To calculate the electron-density distribution in the antenna region, a stream-tube analysis can be used for the inviscid flow regions. The plasma-sheath properties for Apollo are a sensitive function of the nonequilibrium conditions prevailing in the stagnation region. The finite-rate reaction kinetic of species must therefore be considered in this region. A sudden expansion of the airflow about the Apollo shoulder will inhibit electron-ion recombination and maintain the electron concentration at a high level. An accurate evaluation of the downstream electron distribution will involve analyses of a multitude of coupled chemical reactions.

GODDARD SPACE FLIGHT CENTER EFFORTS

In connection with the preparation of the layout for the Apollo ground-support network in general and the Apollo reentry network in particular, GSFC became concerned with the plasma effects on reentry tracking and communication. The guiding idea for the attack of this problem was the establishment of a

quick-look program which in its first formulation would provide approximate predictions of blackout areas and for future work would lend itself for the incorporation of refinements. These refinements could be based for instance on more elaborate theoretical treatments of wave propagation as well as on more commensurate experimental data of chemical kinetics not presently predictable by accuracies better than several orders of magnitude.

With this program as a guide, simplified mathematical models of electrical flow-field properties and wave propagation with applications to the Mercury and Apollo reentry problems were developed by F. J. Tischer at GSFC. Results of these investigations are reviewed briefly in the following paragraphs.

The attenuation level of signals and the blackout conditions during reentry can be determined in an approximate manner in terms of plasma properties in the antenna region. The plasma sheath properties are described in an analytic form which facilitates a direct calculation of signal attenuation. According to this representation, the properties of the sheath at the antenna region are governed by two factors: (1) the plasma properties in the stagnation region and (2) a modulating factor which essentially lumps the controlling physical effects on the plasma intervening between the stagnation region and antenna location. A product representation for the plasma parameters is thus

$$N_e = N_s(h, V)F\left(\frac{x}{D}, \frac{y}{\Delta}, h, V, B, A, \dots\right) \quad (1)$$

$$\nu = \nu_s(h, V)G\left(\frac{x}{D}, \frac{y}{\Delta}, h, V, B, A, \dots\right) \quad (2)$$

where N_e and ν are the electron density and collision frequency in the shock layer; N_s and ν_s are these parameters in the stagnation region; F and G are the form factors; x and y are points in the shock-layer measuring distances, respectively, along a near-body streamline originating from the stagnation region and along a body normal; D and Δ are the vehicle nose radius and shock-layer thickness; h is the altitude; V is the vehicle velocity; B is the body configuration; and A is the spacecraft attitude. The advantage of this representation (eqs. (1) and (2)) is that it allows the incorporation into the calculation of the signal attenuation the known properties of the plasma sheath.

In the treatment of the wave-propagation problem, a method of successive approximation is invoked. The attenuation R^{db} is written in the form

$$R^{db} = R_0^{db} + \sum \nu \Delta R_\nu^{db}$$

where R_0^{db} is a first-order approximation based on a plane wave propagating in a stratified medium. The higher order terms which account for reflection,

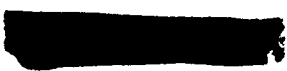


multiple scattering, and antenna configuration are calculated by a recursion method. Thus, approximate calculation of the decibel attenuation for the plasma-sheath characteristic of a blunt-nose vehicle becomes

$$R_0^{db} = 0.012N_s(h, v)F_1\left(\frac{x}{D}, \frac{y}{\Delta}, B\right)G_1\left(\frac{x}{D}, \frac{y}{\Delta}, B\right)\delta_{eq}/f^2$$

where F_1 and G_1 are slowly varying geometrical form factors describing the variation of electron density in the aft section of the vehicle and δ_{eq} is an equivalent thickness of the plasma sheath. This formula was tested in connection with the Mercury MA-6 flight attenuation data. Utilizing the in-flight observed C-band data which show a brief marginal blackout interval and treating the factors F_1 and G_1 as constant factors, a prediction for the limits of the VHF blackout altitude range is obtained. This was in reasonable agreement with the observed data. Figure 8 presents an altitude-velocity plot of the Mercury MA-6 reentry trajectory with blackout curves adjusted for observed blackout bounds of rf-signals at operational frequencies of 250 mc and 5 Kmc. The blackout curve for 2 Kmc was obtained by the use of the geometry factors of the flow-field model established for 5 Kmc. The plasma and collision frequencies on which the blackout predictions for the MA-6 were based are given in figure 9. In this figure f_{ps} is the plasma frequency at the stagnation point under assumed equilibrium conditions while f_{p1} , f_{p2} , and f_{p3} are the plasma frequencies at different antenna locations. The collision frequency at the stagnation point is ν_s , and ν_1 is the collision frequency which is assumed to be constant for all considered positions of antennas. Figure 10 is a plot of maximum plasma frequency during the MA-6 reentry; f_{ps} again is the stagnation-point plasma frequency (curve A) while $f_p^{(-2.5)}$ (curve B) is the plasma frequency for the C-band antenna location calculated with flow-field geometry factors adjusted for in-flight measured C-band signal attenuation. From C-band data modified by the longitudinal electron-density variation between the C-band and the telemetry antennas the plasma frequency $f_p^{(-2.7)}$ (curve C) was obtained. Points P_1 and P_2 , the intersects of curve C with the 260-mc line at altitudes of 306,000 feet and 125,000 feet, respectively, give the VHF blackout bounds in general agreement with in-flight observations.

There are numerous and crude approximations in the present application of the method discussed. However, the intuitive appeal of the method and its heuristic character have been the basis for further investigation along this path and the search for more refined calculations. One- and two-dimensional calculations based on analytical methods and numerical procedures are currently being made under contract to the University of Alabama Research Institute. In the current reformulation the impedance mismatch between antenna and plasma is assumed to be an impedance input of the antenna system. This method offers a more satisfying conception of the antenna problem and considerably simplifies the wave-propagation calculation and calculation of the radiation pattern.



Cornell Aeronautical Laboratory (CAL) working on reentry radiation and air-flow under contract NASr-119 for the NASA Office of Advanced Research and Technology has done some nonequilibrium flow-field calculations pertaining to the characteristic reentry conditions of the Mercury spacecraft. A stagnation-region solution under application of their finite rate normal shock program has been used to compute plasma frequencies over the Mercury reentry altitude range. Figure 11 shows the results in comparison with equilibrium conditions and an estimate of nonequilibrium viscous effects for high altitudes. A single ionization model (one dominant ionization reaction) with 8 species and 10 chemical reactions was used for the low-altitude conditions while the complex kinetic model consisting of 12 species and 28 chemical reactions (19 ionization reactions) was applied for the high-altitude case.

For superorbital velocities as many as 11 additional electron-forming reactions have been considered. These reactions are closely coupled to a multitude of other reactions involving numerous atomic and molecular chemical species. A computational program in this regard has been developed by Paul V. Marrone of CAL (ref. 4) for an equilibrium composition of air behind a normal shock for flow velocities up to 50,000 ft/sec. The program comprises 20 chemical species and 40 reactions. An application to Apollo would instead require a detailed calculation of the nonequilibrium state. The investigation of these problems is, however, handicapped by the previously mentioned uncertainty and lack of basic physical data on reaction-rate kinetics of ions and neutral chemical species. The CAL has formulated an experimental program whose purpose is to fill this need. The investigation will utilize a shock-tube tunnel capable of developing stagnation condition of high enthalpy at the nozzle throat corresponding to superorbital reentry velocities. This will make possible the study of non-equilibrium ionization in an aerothermochemical environment appropriate to stream tubes about the Apollo vehicle. The objective of this program is to obtain basic data on reaction-rate kinetics and develop methods for calculation of the plasma-sheath properties for the lunar reentry mission. A more accurate and meaningful prediction of the plasma effects will then be possible.

Techniques for eliminating blackout such as water injection often rely on modifying the nonequilibrium chemistry and ionization level. The basic studies of CAL will provide more effective procedures for developing and evaluating these remedial procedures.

CONCLUDING REMARKS

Plasma effects on tracking and communication during Apollo reentry from a lunar mission have been reviewed. Several characteristic Apollo reentry trajectories are given as examples for the demonstration of rf-signal blackout areas expected to occur during skip-type and direct-descent reentry flights. The presently existing uncertainties in the determination of electrical properties in the Apollo plasma sheath and the plasma effects on antenna performance have led to widely differing estimates of blackout area predictions. The most desirable case of continuous tracking and communication throughout the entire reentry phase could be achieved only by developing ameliorative methods for preventing blackout. In order to accomplish this, the complex physicochemical

CONFIDENTIAL

phenomena of the asymmetric ionized flow field peculiar to Apollo and the three-dimensional wave propagation through the highly inhomogeneous plasma sheath must be more clearly understood. However, the development and implementation of preventive techniques will be confronted with the intricate matter of conforming to overall system requirements.

For the establishment of a most economical and effective Apollo reentry ground-support network, GSFC needs to know precise blackout bounds for all possible types of reentry trajectories. The accuracy or uncertainty of the prediction of blackout area bounds are determining factors in the assessment of the ground-support capabilities during Apollo reentry. In order to aid in this effort a contract has been let to the University of Alabama Research Institute for the development of refined ionized flow-field and wave-propagation models pertaining to specific characteristics of the Apollo spacecraft. In support of this study Cornell Aeronautical Laboratory (CAL) will investigate basic reaction kinetics of chemical species in high-temperature air flow under conditions simulating Apollo reentry from lunar missions. The effect of ablation impurities in the plasma sheath will also be subject to studies by CAL in their high-enthalpy shock-tunnel facilities. In addition, ameliorative techniques such as water injection found to be very successful for RAM flights (ICBM reentry conditions) by Langley Research Center are considered for testing with respect to applicability to Apollo reentry in the CAL facilities.

For an ultimate confirmation of predictions based on theoretical treatments and experimental investigation in ground facilities, it is suggested to investigate the possibility of incorporating coordinated experiments in the Gemini and early Apollo flight programs. Although it is realized that environmental conditions pertaining to reentry velocities upon return from a lunar mission cannot be met in these programs, flight experiments of the suggested kind may give valuable reconfirmation of predicted blackout bounds within altitude and velocity regimes common to the near-earth and lunar missions.

REFERENCES

1. Lickly, D. J., Morth, H. R., and Crawford, B. S.: Apollo Reentry Guidance. Rep. R-145 (Contract NAS9-153), Instrumentation Laboratory, M.I.T., July 1963.
2. Daniels, R. L.: Final Report on Apollo Plasma Reentry Studies. Rep. No. SID 63-746, North American Aviation, Inc., July 5, 1963.
3. Cuddihy, William F., Beckwith, Ivan E., and Schroeder, Lyle C.: RAM B2 Flight Test of a Method for Reducing Radio Attenuation During Hypersonic Reentry. NASA TM X-902, 1963.
4. Marrone, Paul V.: Normal Shock Waves in Air: Equilibrium Composition and Flow Parameters for Velocities From 26,000 to 50,000 Ft/Sec. CAL Rep. No. A.B.-1729-A-2 (Contract NASr-119), Cornell Aero. Lab., Inc., Aug. 1962.

CONFIDENTIAL

SECRET

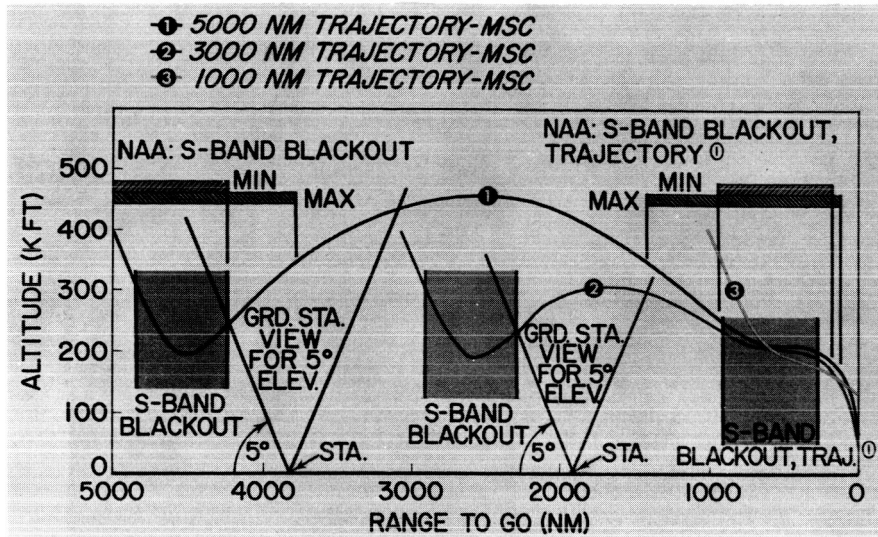


Figure 1.- Apollo reentry trajectories; $\gamma = -6.4^\circ$.

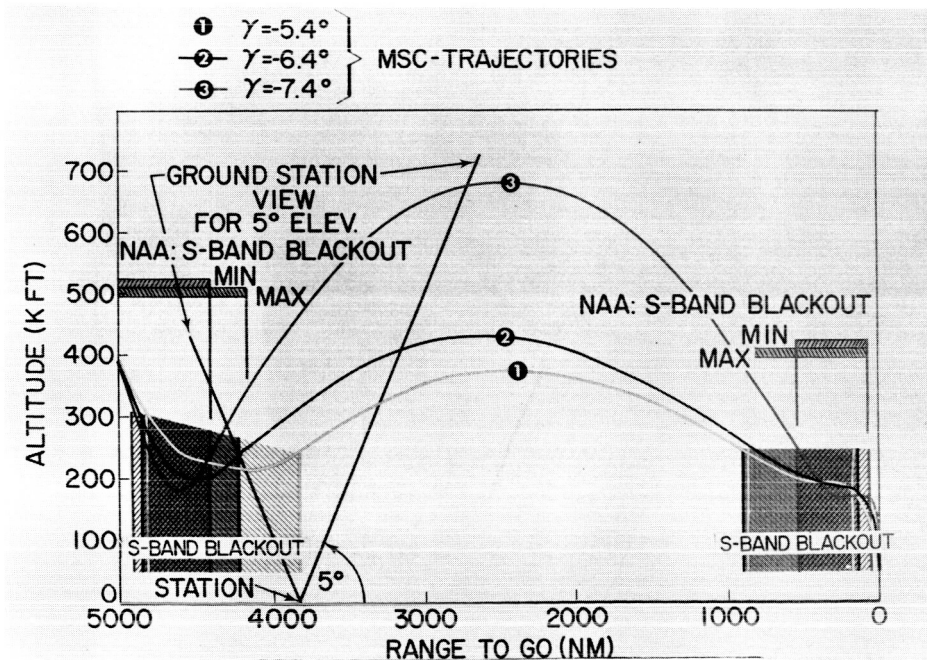


Figure 2.- 5,000-nautical-mile Apollo reentry trajectories.

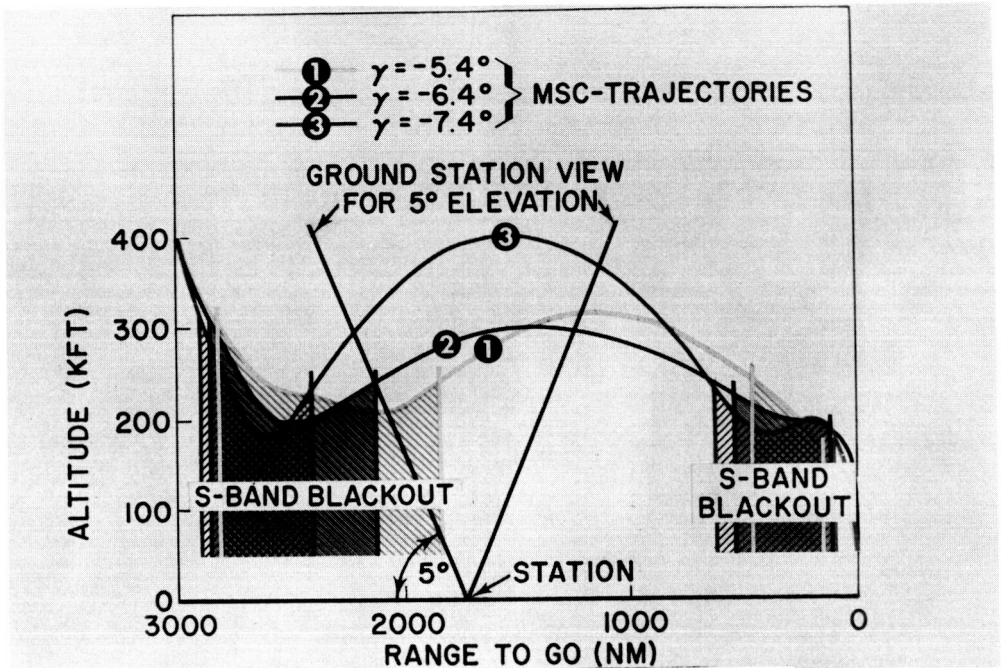


Figure 3.- 3,000-nautical-mile Apollo reentry trajectories.

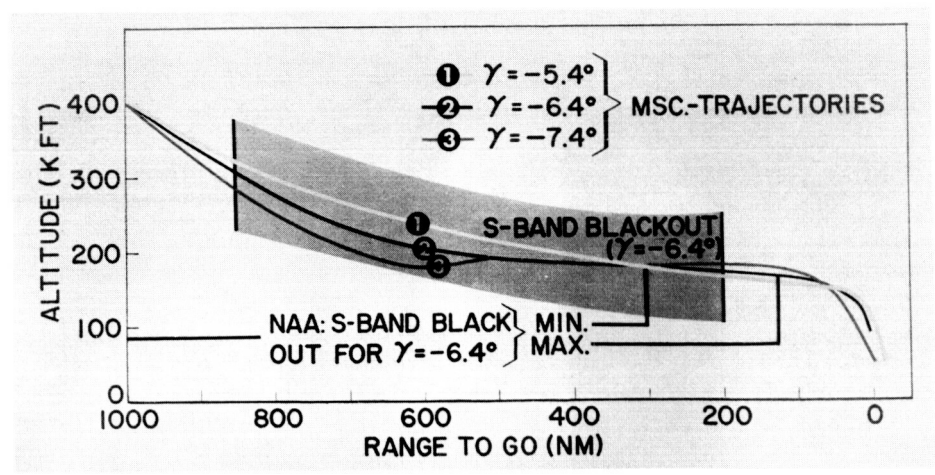


Figure 4.- 1,000-nautical-mile Apollo reentry trajectories

[REDACTED]

DECLASSIFIED

- ① $\gamma = -5.4$
 - ② $\gamma = -6.4$
 - ③ $\gamma = -7.4$
- Scheme by North American Aviation

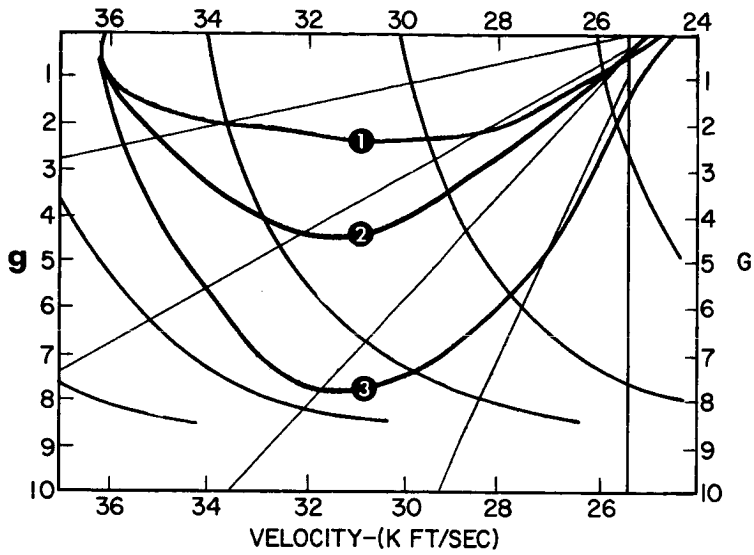


Figure 5.- Manual emergency reentry mode.

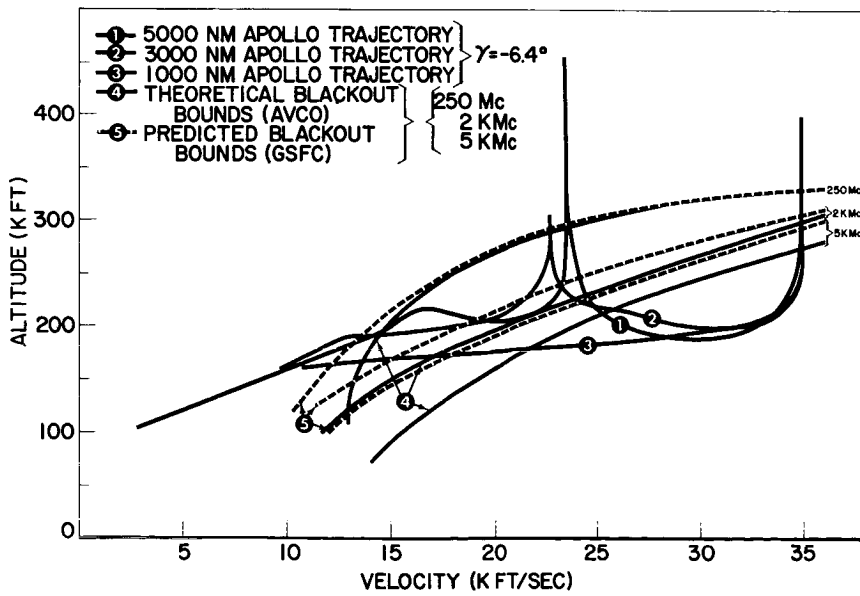


Figure 6.- Blackout bounds of typical Apollo reentry trajectories.

[REDACTED]

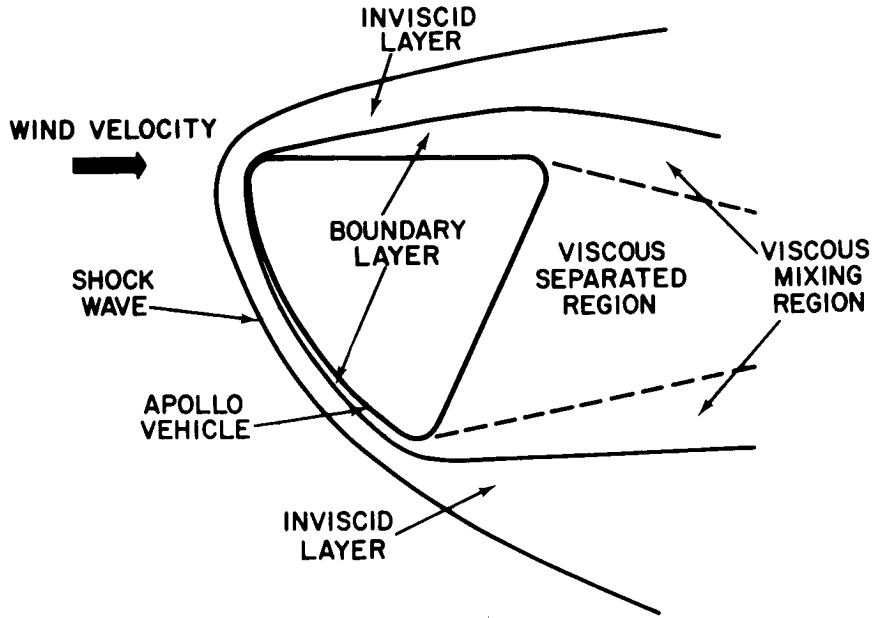


Figure 7.- Apollo hypersonic flow regions.

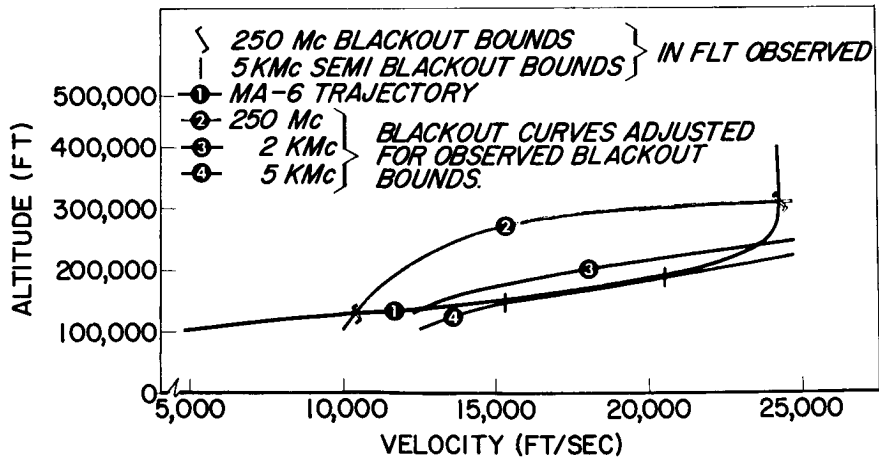


Figure 8.- Mercury MA-6 reentry trajectory.

[REDACTED]

DECLASSIFIED

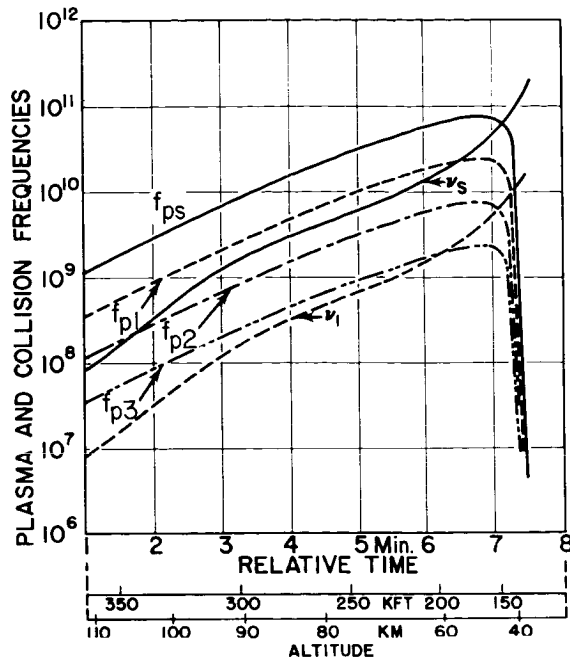


Figure 9.- Plasma and collision frequencies in flow field near the Mercury afterbody. (Data supplied by F. J. Tischer.)

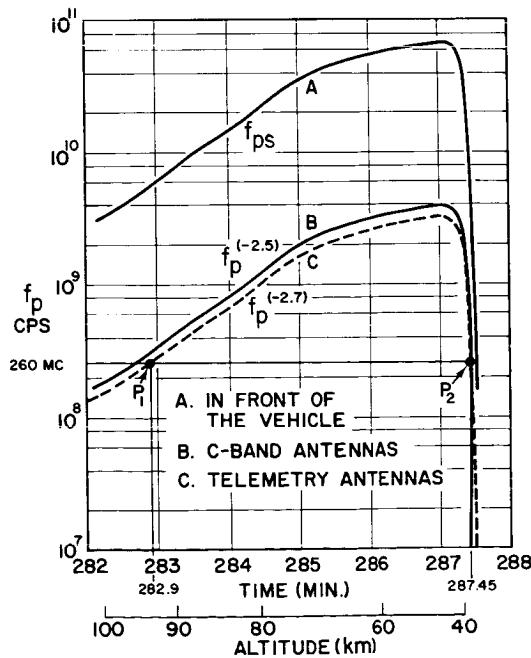


Figure 10.- Maximum plasma frequency during reentry of the Mercury MA-6 vehicle. (Data obtained from F. J. Tischer.)

[REDACTED]

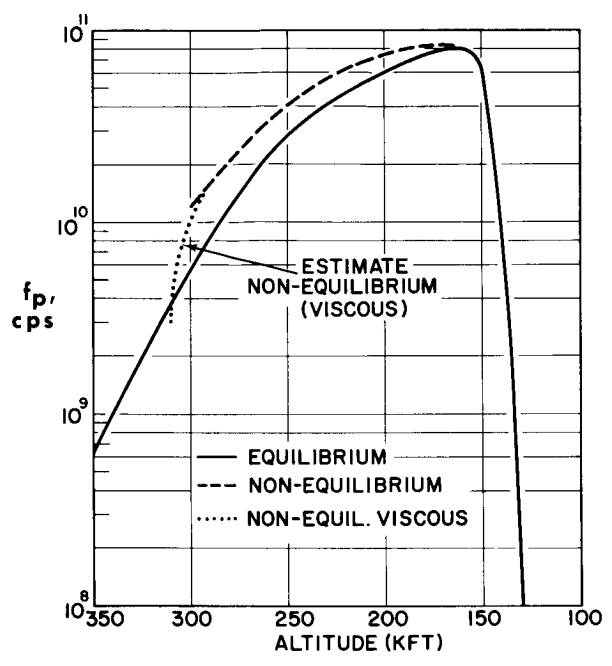
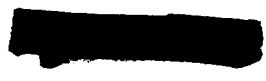


Figure 11.- Plasma frequency at Mercury MA-6 stagnation point. (Data obtained from Cornell Aeronautical Laboratory.)



[REDACTED]

7. MICROWAVE APPLICATIONS DEVELOPED AT LANGLEY RESEARCH CENTER

FOR THE REENTRY COMMUNICATIONS PROGRAM

By W. Linwood Jones and Bruce M. Kendall
Langley Research Center

SUMMARY

Microwave instrumentation systems have been developed at Langley Research Center for acquiring nonperturbing diagnostic measurements over a wide density range of plasmas under both flight and simulated-flight conditions. In this paper the theory, techniques, and capabilities of these systems and the facilities utilized are discussed. Also as an outgrowth of the plasma diagnostics work, a microwave telemetry system, which represents a practical solution to the radio-blackout problem for small bodies reentering at velocities up to 25,000 ft/sec, will be described. When combined with other techniques such as material addition, this system holds promise for real-time telemetry in regimes of even higher velocity.

INTRODUCTION

The need for communications during atmospheric reentry has been fully established in preceding papers. In support of Project RAM (Radio Attenuation Measurement), microwave systems have been developed at Langley Research Center (LRC) for two purposes, microwave plasma diagnostics and microwave telemetry.

Microwave diagnostic systems have been utilized to obtain nonperturbing measurements of certain plasma parameters under both flight and simulated-flight conditions. The plasma parameters of interest are the electron density, collision frequency, and temperature.

An X-band microwave telemetry system was developed as a technique for avoiding blackout by operating the radio frequency (RF) link at a frequency greater than the critical frequency of the reentry plasma.

SYMBOLS

A_{ω}	plasma power absorptivity
c	speed of light in free space, cm/sec
N_e	electron density, electrons/cm ³
P	power

- R_T tube wall reflection coefficient
- R_{ω} plasma power reflectivity
- T_A effective antenna noise temperature
- T_b body surface temperature
- $T_{EXTERNAL}$ sum of external noise temperatures
- T_e electron temperature
- T_p plasma noise temperature
- T_R reference temperature
- T_{ω} plasma power transmissivity
- α attenuation coefficient, dB/cm
- β phase coefficient, $\frac{2\pi}{\lambda}\eta$, radians/cm
- β_0 free-space phase coefficient
- γ complex propagation constant
- η index of refraction
- λ free-space wavelength, cm
- ν electron-neutral particle collision frequency, collision/sec
- ρ plasma power reflection coefficient
- ω radiated microwave frequency, radians/sec
- ω_p plasma frequency, radians/sec

Subscripts:

- 1,2 different frequencies

MEASUREMENT OF PLASMA ELECTRON DENSITY AND COLLISION FREQUENCY

A simplified theoretical investigation of the interaction of electromagnetic waves with a plasma shows that the RF attenuation and phase shift can be related to the plasma electron density and collision frequency.

For a given electron density there is an associated critical radio frequency called the plasma frequency which can be determined from the following expression:

$$\omega_p = 5.64 \times 10^4 \sqrt{N_e}$$

Assuming normal-incidence plane-wave interaction with a homogeneous, semi-infinite plasma slab and requiring that the inequality

$$\left(\frac{\omega_p}{\omega}\right)^4 \ll 1$$

hold, from reference 1 the complex propagation constant γ may be expressed in terms of the plasma properties in the following simplified form:

$$\gamma = \alpha + j\beta$$

where

$$\alpha \approx \frac{8.686\nu\omega_p^2}{2c(\omega^2 + \nu^2)}$$

and

$$\beta \approx \frac{2\pi}{\lambda} \left[1 - \frac{\omega_p^2}{2(\omega^2 + \nu^2)} \right]$$

In figure 1, α and β are plotted to arbitrary scales to show their dependence on the microwave frequency ω , the plasma frequency ω_p , and the collision frequency ν .

For diagnostic purposes, to determine both the electron density and the collision frequency, two measurements are necessary. The general procedure is to make attenuation measurements at two frequencies and solve the following equation for the collision frequency:

$$\nu \approx \sqrt{\frac{\alpha_2\omega_2^2 - \alpha_1\omega_1^2}{\alpha_1 - \alpha_2}}$$

An alternate approach is to measure both the attenuation and phase-shift coefficients at one frequency; this method results in the expression:

$$\nu \approx \frac{\beta_0 c \alpha}{8.686(\beta_0 - \beta)}$$

Once ν has been determined, the value of the electron density is determined from the expression:

$$N_e \approx \frac{1}{8.686} \frac{1}{3.178 \times 10^9} \left[2c\alpha \frac{(\omega^2 + \nu^2)}{\nu} \right]$$

For a low collision frequency, where $\nu \ll \omega$, the attenuation coefficient becomes small and cannot be measured. The electron density may then be calculated independently of ν from a single-frequency phase measurement with the following equation:

$$N_e \approx (1.242 \times 10^{-8}) \frac{\omega c}{2\pi^2} (\beta_0 - \beta)$$

Figure 2 is a plot of the plasma power reflection coefficient as a function of ω_p/ω . The equation for this coefficient is

$$\rho = \frac{(\beta - \beta_0)^2 + \alpha^2}{(\beta + \beta_0)^2 + \alpha^2}$$

This figure indicates that the plasma is nonreflecting until the critical frequency is reached. At that point, the plasma surface appears highly reflective. For low collision frequencies the reflections occur very sharply at $\omega = \omega_p$; however, as the collision frequency increases, the reflections occur less sharply and, thus, the critical frequency is not clearly defined. This subject is covered in detail in paper no. 18.

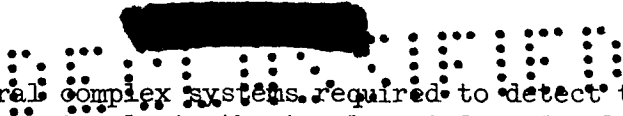
EXPERIMENTAL APPARATUS

Figure 3 is a block diagram of three diagnostic measurements; namely, attenuation coefficient α , reflection coefficient ρ , and phase coefficient β .

The attenuation measurement utilizes a precision variable attenuator to calibrate the output of the crystal diode detectors in decibels. The change in received signal strength when the plasma is inserted between the antennas is the plasma attenuation.

The reflectometer measures the onset or decay of the critical plasma density. In the measurement, the transmitted and reflected power are monitored. When the reflected power changes abruptly, it is known that the plasma has reached the critical density.

The phase measurement utilizes a bridge technique where the energy is coupled into a work leg and reference leg. The block labeled "phase detector"



is actually one of several complex systems required to detect the relative phase changes between the signals in the two legs independently of oscillator frequency or amplitude variations in either leg. The change in relative phase when the plasma is inserted into and removed from the work leg is the phase shift due to the plasma.

Figure 4 is a block diagram of a heterodyne phase system. To measure a phase shift accurately, the RF signals of the two klystrons are frequency locked by the use of synchronizers and then heterodyned in waveguide mixers to produce a 27-kc intermediate frequency. These video signals are then fed to the precision phasemeter and magnetic tape recorder. The analog output of the phasemeter is a direct-current voltage proportional to the microwave phase. The amplitude of the 27-kc signal is also employed to determine signal attenuation due to the plasma.

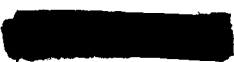
The capabilities of the diagnostic systems at LRC which operate over a frequency range of 2 Gc to 140 Gc are listed as follows:

Frequency, Gc	Capabilities
2.0 to 2.5	Attenuation and phase
4.0 to 6.0	Attenuation
8.2 to 12.4	Attenuation and phase
17.6 to 26.7	Attenuation and phase
26.4 to 40.1	Attenuation
60.5 to 92.0	Attenuation and phase
90.0 to 140.0	Attenuation

Because the measurable density range of the phase systems is a decade greater than that of the attenuation systems, not all frequency bands are required to have both capabilities to diagnose the desired plasmas. The measurable range of collision frequency is 10^8 to 10^{13} collisions/sec and the measurable range of electron density is 10^8 to 10^{15} electrons/cm³.

Most flight simulation for Project RAM has been accomplished by placing scale models of the RAM payload in the exhaust of small solid-propellant rocket motors fired in a large vacuum chamber; figure 5 shows this experimental setup. The microwave techniques discussed in the preceding paragraphs have been employed to measure the parameters of the exhaust-free jet in support of the experiment downstream. As the size of the hot plasma core is generally small (2 to 6 inches in diameter), antennas had to be developed to focus the microwaves to a small spot to insure that all the energy would pass through the plasma. In addition, these antennas had to be sufficiently removed from the rocket exhaust to prevent disturbing the gas flow.

One of the two types of focusing antennas shown in figure 6 is a conical-horn—hyperbolic-dielectric-lens combination. The lens is 12 inches in diameter



[REDACTED]

and is made of polystyrene. In the investigation the antennas are used as focused pairs and are separated by twice the focal length, or 60 inches. When operated at X-band, the antenna columnates the energy into approximately a 4-inch beam at the half-power points with a corresponding focal length of 30 inches.

The other antenna shown in figure 6 is an ellipsoidal dish. It is spun cast of aluminum, is 46 inches in diameter, and is illuminated by a buttonhook waveguide feed. When operated at X-band, the antenna focuses the energy into approximately a 1.5-inch column at the half-power points 24 inches from the lip of the dish.

The expression for spot size $d = \frac{K\lambda f}{D}$ is Rayleigh's resolution criterion where

- d spot diameter, in.
- K distribution constant, 1.5 for antenna-beam half-power points
- λ free-space wavelength
- f focal length
- D aperture diameter

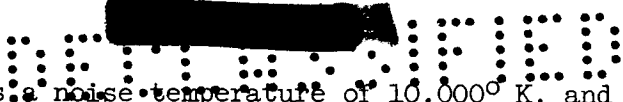
MEASUREMENT OF PLASMA NOISE TEMPERATURE

Purpose

The microwave noise emission from a reentry plasma which could be received by an antenna located on a reentry vehicle is significant to the performance of an onboard receiver. Such noise, in effect, will increase the overall receiver noise level and thus decrease receiver sensitivity. Since such emission would affect only onboard vehicle receivers, the frequency of 5 Gc was chosen for the RAM B3 radiometer experiment to provide data near the operating frequencies of the LRC C-band radar transponders. The intention of this experiment is to measure approximate levels of C-band noise emission from a reentry plasma, which will enable the degradation of onboard receiver sensitivity to be determined.

Radiometer

The radiometer, as shown in figure 7, is essentially a sensitive microwave receiver whose input is switched, at a 10-cps rate, between the antenna terminal and a matched resistive load at ambient temperature (290° K). The output of the radiometer appears as a voltage square wave whose amplitude represents the difference between the effective antenna noise temperature and reference noise temperature. The radiometer is calibrated by means of a standard noise



tube source, which emits a noise temperature of 10,000° K, and a precision attenuator.

Ground Tests

Radiometer measurements have been made on three ground plasma sources: the cyanogen flame, plasma discharge tube, and various rocket-motor exhausts. These measurements enabled the correlation of theory with obtained data. The results obtained from the plasma discharge tube were the most useful, since plasma parameters of the tube were obtainable for use in the calculation of expected noise levels. The plasma noise emission values, for various tube currents, were calculated by use of the following equation for effective antenna noise temperature:

$$T_A = A_{\omega} T_e (1 - R_T)$$

The value of absorptivity A_{ω} was obtained from the program developed by Calvin Swift and John Evans for an inhomogeneous plasma slab (ref. 2), utilizing the electron density profile and electron temperature T_e data obtained from probe measurements. The reflection coefficient R_T for the glass tube wall was approximated by that for a slab of the same thickness and dielectric coefficient. The noise emission levels, as calculated by use of the preceding equation, were in fair agreement with the actual measured levels.

Plasma Noise During Reentry

In the calculation of plasma noise emission levels for a reentry vehicle, several sources must be considered as shown in figure 8. First, there is the plasma noise temperature as "seen" by the onboard antenna; second, the portion of the vehicle surface temperature reflected off the plasma boundary into the antenna; and, third, all external noise temperatures, such as the sun and earth, which are transmitted through the plasma to the antenna. Therefore, the effective antenna noise temperature may be found from the following equation (ref. 3):

$$T_A = A_{\omega} T_p + R_{\omega} T_b + T_{\omega} T_{EXTERNAL}$$

The values of plasma noise temperature T_p , electron density, and collision frequency can be obtained from available aerodynamic data. The values of body surface temperature T_b can be obtained from data on previous vehicle flights, such as the RAM B2 flight. The values of external noise temperatures $T_{EXTERNAL}$ are obtainable from known references. The values of the plasma power absorptivity, reflectivity R_{ω} , and transmissivity T_{ω} are derived from the program of Swift and Evans, by utilizing the previously mentioned electron density and collision frequency profiles.



A graphic illustration of the ability of a system operating at a frequency of X-band to provide direct telemetry for a small payload reentering at a velocity of 25,000 ft/sec is shown in figure 9. This figure also compares the relative ability of conventional VHF telemetry frequencies to cope with the reentry blackout problem.

A number of means for avoiding or minimizing the effect of reentry radio blackout have been suggested (ref. 4), although as a practical matter only two are proved and in common use.

The oldest technique is that of employing an onboard magnetic tape recorder to store the data for transmission after the vehicle emerges from the blackout region. Unfortunately, the size, weight, and environmental characteristics of available tape recorders prevent their application to small solid-propellant reentry-vehicle payloads. While ferrite-core storage systems can overcome these disadvantages, they are of limited data capacity.

The other technique for avoiding blackout is the operation of the telemetry system at a frequency greater than the critical frequency of the plasma surrounding the reentry vehicle. An X-band system operating on that principle has been flown on the RAM B2 vehicle.

RAM B2 FLIGHT

The experimental apparatus for the RAM B2 flight consisted of an onboard, free-running, pulsed transmitter and three receiving stations located at Wallops Island, Virginia, at Coquina Beach, North Carolina, and at Bermuda. Photographs of the X-band transmitter and receiving stations are shown in figures 10 and 11, respectively. The object was to investigate X-band propagation characteristics and to verify preflight predictions of RF attenuation due to the plasma sheath. In particular, onboard VSWR (voltage standing wave ratio) measurements were made to determine plasma reflections and antenna detuning; received signal strength was recorded to indicate plasma attenuation; and the received pulse wave shape was analyzed for antenna breakdown. The results of this flight have led to the development of an improved and miniaturized telemetry system.

MIN-X TELEMETRY SYSTEM

In order to avoid the associated radio-blackout problem and to permit the use of small severe-environment, solid-propellant vehicles for reentry research the NASA has developed a 3-pound, 1,000-watt X-band telemetry system (ref. 5). This telemetry system (MIN-X) can operate under accelerations greater than 100g and will be able to transmit high-rate data directly during the reentry blackout period from vehicles traveling at 25,000 ft/sec. Its small size

[REDACTED]

and weight will permit use in vehicles whose payload capacity is 10 pounds or less.

This direct reentry X-band telemetry system is a time-division multiplex type having a peak power output of 1,000 watts, employing pulse-position modulation, and having a data capacity of 900 samples per second. The combined weight of the two units which comprise the system - encoder and transmitter - is 3 pounds. Both units have been especially developed to provide a small, lightweight, and environmentally rugged system and, in that regard, represent a substantial improvement over the X-band system previously employed on the RAM B2 vehicle. The system, including the low-level commutator, is completely solid state with the exception of the transmitter magnetron.

A good illustration of an application of this X-band telemetry system is a payload which will be flown on a Trailblazer II vehicle. Figure 12 shows a photograph of the transmitter and encoder and figure 13 shows the general overall configuration of the payload. This configuration has a conical shape, a relatively sharp nose, a maximum diameter of about 7 inches, and an overall length of about 30 inches. The manner in which the encoder and transmitter are installed is also shown; in addition, the antenna and battery-pack components are identified.

CONCLUDING REMARKS

Microwave diagnostic systems capable of measuring electron density, collision frequency, and temperature of both flight and simulated-flight plasmas have been developed at Langley Research Center in support of the reentry communications program. As a necessary extension of this development, existing microwave measurement techniques and simulation of reentry plasma are being improved and comprehensive flight experiments are being investigated.

An X-band telemetry system, which represents a practical solution to the reentry radio-blackout problem, has been developed and is now operational.

1. Calcote, H. F., and Silla, H.: Radar Attenuation in Solid Propellant Rocket Exhausts. Bull. 18th Meeting, JANAF-ARPA-NASA Solid Propellant Group, Vol. III, June 1962, pp. 3-50.
2. Swift, Calvin T., and Evans, John S.: Generalized Treatment of Plane Electromagnetic Waves Passing Through an Isotropic Inhomogeneous Plasma Slab at Arbitrary Angles of Incidence. NASA TR R-172, 1963.
3. French, I. P., and Bachynski, M. P.: The Radio Spectrum From 10 Gc to 300 Gc in Aerospace Communications. Volume V - Plasma Effects in Aerospace Communications. Res. Rep. No. 6-400-5(7-401-3) (ASD-TR-61-589, Vol. V), RCA Victor Co., Ltd. (Montreal), Mar. 1962.
4. Huber, Paul W., and Nelson, Clifford H.: Plasma Frequency and Radio Attenuation. Proceedings of the NASA-University Conference on the Science and Technology of Space Exploration, Vol. 2, NASA SP-11, 1962, pp. 347-360. (Also available as NASA SP-25.)
5. Harrington, R. F., Brummer, E. A., and Southall, W. A.: A 3-Pound, 1,000-Watt X-Band Reentry Telemetry System. New Links to New Worlds. PTGSET Record, Inst. Electrical and Electronics Eng., Oct. 1963, paper 1.1.

MICROWAVE PLASMA DIAGNOSTIC MEASUREMENTS

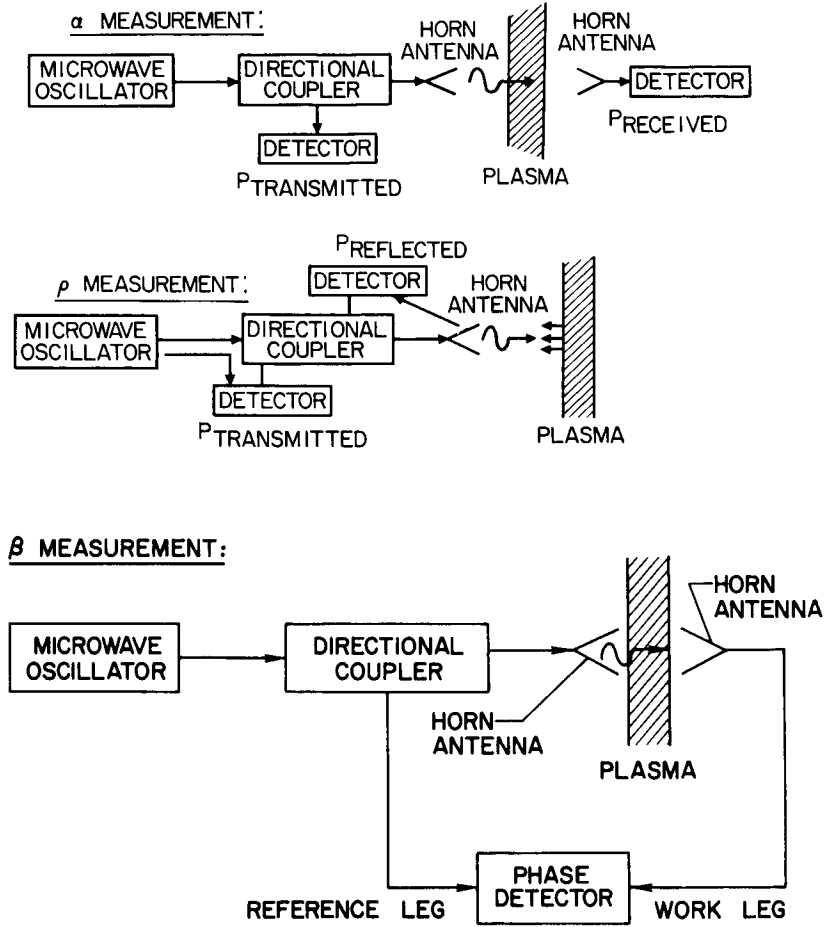


Figure 3

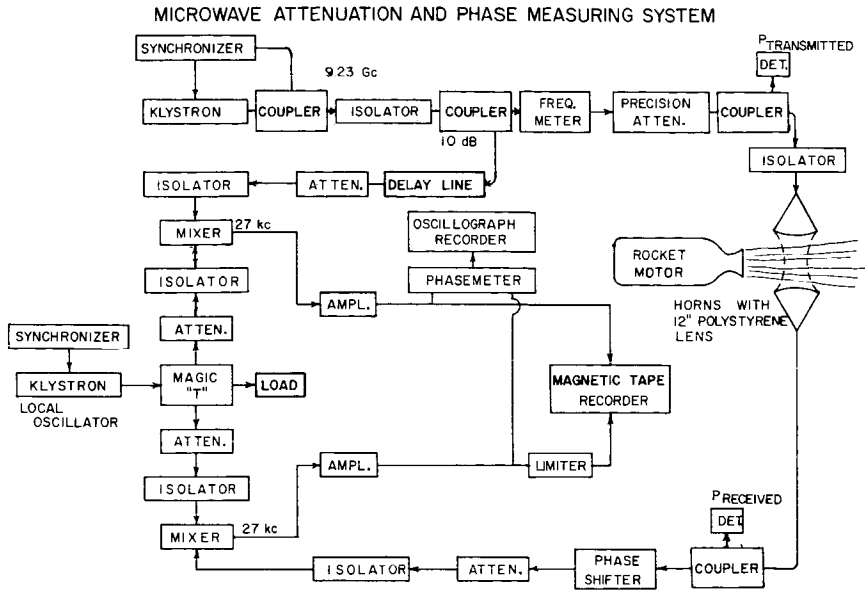


Figure 4

GROUND TEST OF TYPICAL RAM PAYLOAD

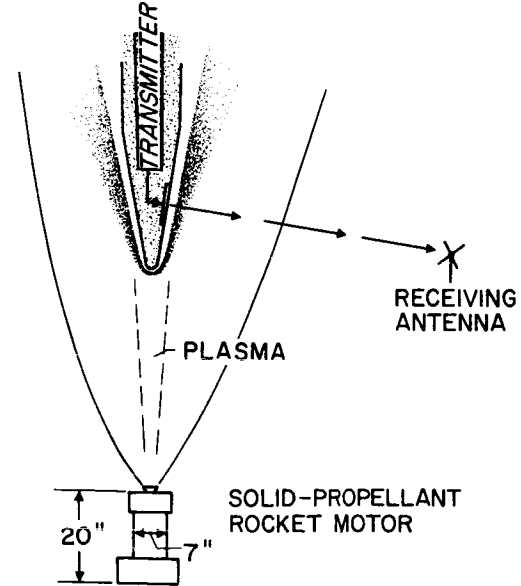


Figure 5

FOCUSING MICROWAVE ANTENNAS

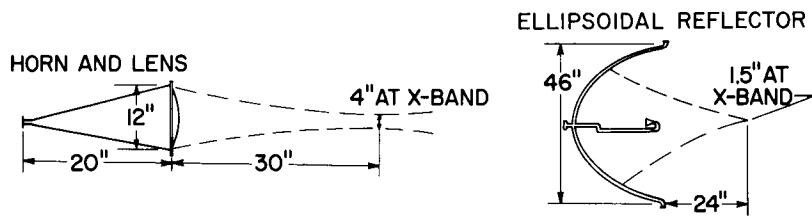


Figure 6

MICROWAVE RADIOMETER SYSTEM

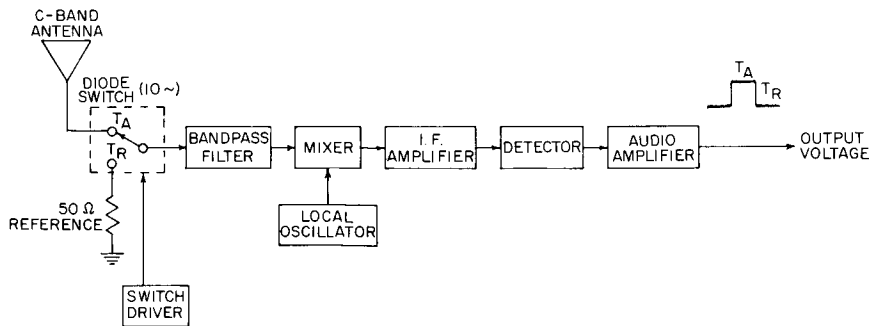


Figure 7

C-BAND RADIOMETER ON TYPICAL RAM VEHICLE

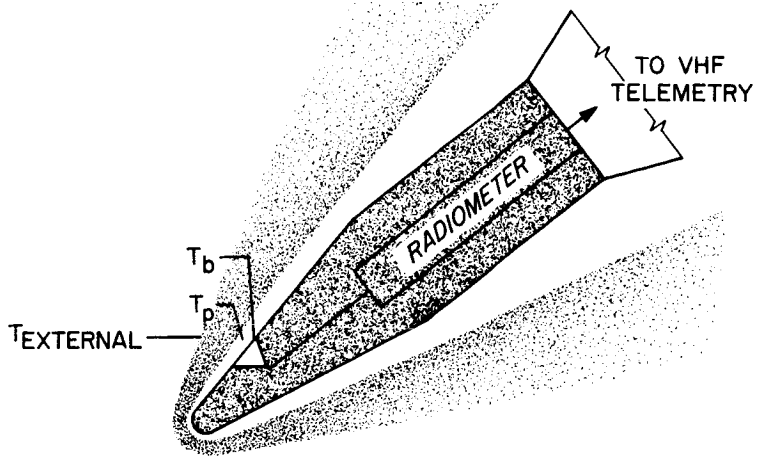


Figure 8

COMPARISON OF X-BAND AND VHF REENTRY ATTENUATION

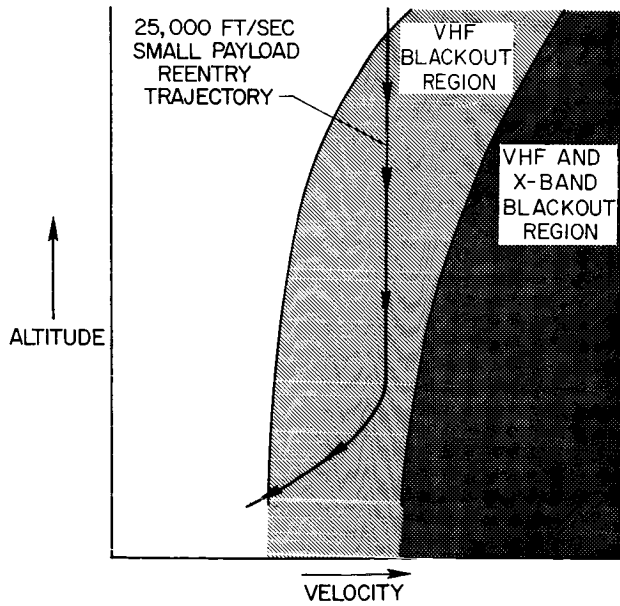


Figure 9

0371 [REDACTED] 30

X-BAND TELEMETRY TRANSMITTER



Figure 10 L-63-2161

X-BAND TELEMETRY RECEIVING STATION



Figure 11 L-2170-15

[REDACTED]

~~SECRET~~

TRANSMITTER AND ENCODER

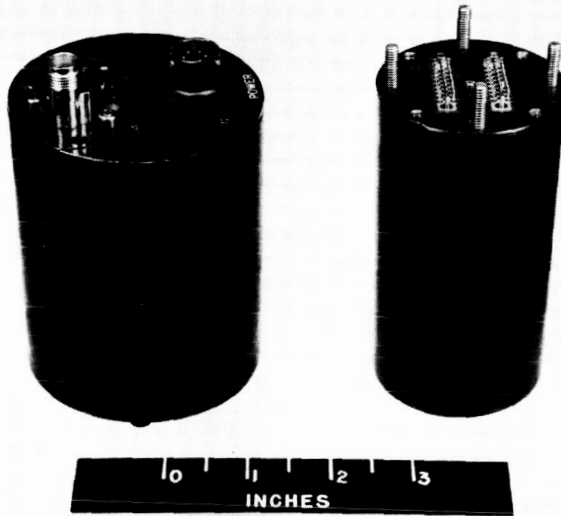


Figure 12

L-2170-16

TRAILBLAZER II PAYLOAD CONFIGURATION

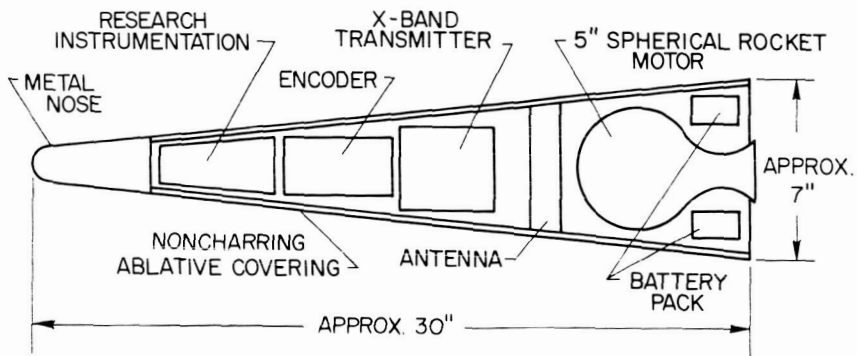


Figure 13

~~SECRET~~

8. QUALIFICATION TESTS OF A MICROWAVE REFLECTOMETER

USING A GAS DISCHARGE PLASMA

By Richard W. Morton
Langley Research Center

SUMMARY

In preparation for one of the radio-attenuation-measurement flights (RAM B3), qualification tests were made on a 3,000-megacycle reflectometer. Reflections from a cylindrical overdense plasma were compared with reflections from metal cylinders. It was found that when the reflected amplitudes were equal, the radius of the metal cylinder agreed with the plasma radius corresponding to the critical density. This finding qualified the reflectometer for plasma measurements in the limited case when the ratio of collision frequency to operational frequency is less than 0.1. The plasma utilized was a glow discharge and was calibrated by means of a Langmuir probe and a microwave interferometer.

INTRODUCTION

In the project RAM program there are investigative flights designed to explore the communications problem, curative flights designed to find a blackout remedy, and diagnostic flights designed to determine the nature of the vehicle flow field.

The RAM B3 flight is diagnostic, and the principal tools are microwave reflectometers operating at 10,000, 3,000, and 1,000 megacycles. In paper no. 18 by William L. Grantham, the details of this equipment are given.

Since reflectometers were to be used in flight, it was desired to apply them to a laboratory plasma. The purpose of the tests was to validate the reflectometer measurements on the project RAM B3 flight. A cylindrical glow discharge tube 34 inches long and 2.7 inches in diameter was built. The tube utilized argon gas at a pressure of 250 microns Hg and the collision frequency was approximately 10^8 cycles per second. After calibration with both a Langmuir probe and a microwave interferometer, it was found that electron densities were suitable to reflect 3,000-megacycle waves. Reflectometer measurements were thus made at 3,000 megacycles on the plasma and also, for purposes of comparison, on metallic cylinders.

f	frequency
N_e	electron concentration, electrons/cm ³
$N_{e,cr}$	critical electron concentration, electrons/cm ³
r	radius
ν	collision frequency
ρ	power reflection coefficient
$\omega = 2\pi f$	
$\omega_{p,max}$	maximum plasma frequency
Subscripts:	
1,2	particular values
mc	metallic cylinder

EQUIPMENT AND TESTS

Figure 1 shows the discharge tube operating at a current of 2 amperes. The cathode is at the far end of the tube, and the anode is on the right, just out of the picture. At the middle of the tube can be seen two brass entrance ports attached at right angles. These ports were used to admit Langmuir probes. Between the cathode and these ports is the portion of the tube used for microwave experiments.

Figure 2 is a photograph of the Langmuir probe. Tungsten wire of 1-mil diameter is exposed for a length of 50 mils. The wire is sealed into the tip of a fused-quartz tube whose diameter is about 10 mils. These dimensions were found necessary in order to satisfy the conditions of free-molecular flow on which Langmuir probe theory is founded.

Figure 3 presents electron-density data as determined by using the Langmuir probe for several tube currents. The points displayed were computed from voltage-current curves by using simple free-molecular flow theory.

Figure 4 illustrates a basic microwave interferometer. Energy from the oscillator is split, and part of the energy is sent through the plasma while part is sent through a reference leg. The energy is recombined in a phase comparator whose output is proportional to the phase shift suffered by the energy transmitted through the plasma.

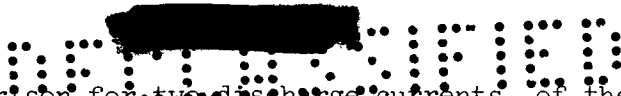


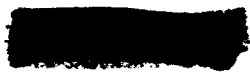
Figure 5 is a comparison for two discharge currents, of the average electron densities along a diameter, as computed from the probe data of figure 3 and as determined from the phase shift experienced by the 10,000-megacycle interferometer. The probe data were taken along a diameter, and the average amplitude of the distributions in figure 3 is used in plotting figure 5. The interferometer beam was principally confined to a diameter. When the path length and measured phase shift are known, the transmission equations can be used to determine the average electron density. (See paper no. 7 by W. Linwood Jones.)

In order that the interferometer data be checked, the electron-density distributions of figure 3 were fed into the program described in paper no. 3 by John S. Evans and Calvin T. Swift, and the phase shifts were computed. Also, the data of figure 3 were cut into a finite series of sections and phase shifts were computed for each section and the sum of the sections. In both cases, the computed phase shifts agreed with the measured phase shift. It should be realized that the plasma was highly transmissive; the maximum plasma frequency was 5,300 megacycles or one-half the interferometer frequency, and $\nu/\omega < 0.01$.

Figure 6 shows a basic reflectometer. Microwave energy from the oscillator is radiated from the horn antenna and strikes the reflector. Some of this energy is reaccepted by the horn antenna and is picked off by the directional coupler. A detector reads this output from the directional coupler and displays this signal on an indicator whose deflection can be calibrated according to the characteristics of the reflector being examined.

Figure 7 presents the two kinds of reflectometer tests and their results. The first experiment was to place a 3,000-megacycle reflectometer 0.25 inch from the plasma and read the amplitude reflection coefficients for several tube currents. For the second experiment, the plasma was replaced with highly reflective metal cylinders whose diameters were varied. The second experiment therefore allowed the reflection coefficients to be known as a function of the cylinder radius. Now if the plasma is highly reflective at the plasma frequency when $\nu/\omega < 0.1$, then, when the reflected waves have equal amplitudes for plasma or metal cylinders, the effective plasma radius should equal the metal-cylinder radius.

Figure 8 shows a test of this proposition. Here, the electron-density distributions for 1 and 2 amperes, as determined by the probe, are replotted. The apparent radii of reflection for the 1- and 2-ampere plasmas are also presented. If the proposition is true, then the intersection of the radii and the electron-density distributions should in both cases occur at the critical electron density corresponding to the plasma frequency. For 1 ampere the data are scattered about the critical density, and for 2 amperes the data are slightly above the critical density. It is thought that the disagreement at 2 amperes is due to experimental error.



0370 [REDACTED] 0000
CONCLUDING REMARK

Tests of a microwave reflectometer using a gas discharge plasma have shown that the reflectometer is qualified for plasma measurements in the limited case when the ratio of collision frequency to operating frequency is less than 0.1.

VARIATION OF ELECTRON-CONCENTRATION DISTRIBUTION
WITH TUBE CURRENT
LANGMUIR PROBE DATA; ARGON GAS, 250 MICRONS Hg

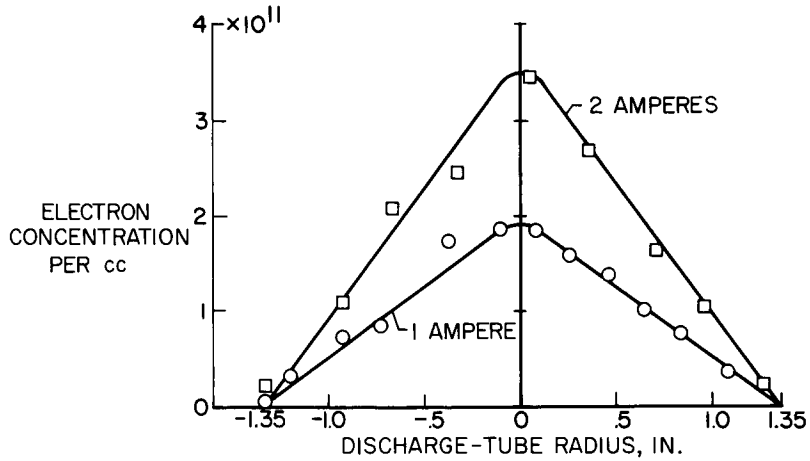


Figure 3

BASIC MICROWAVE INTERFEROMETER

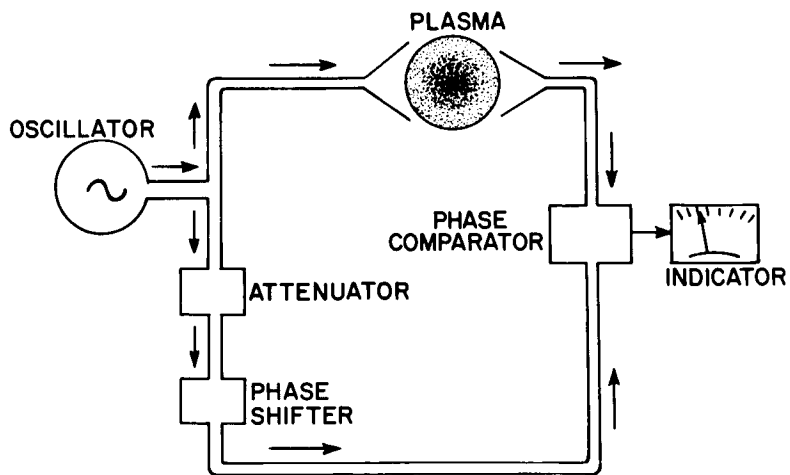


Figure 4

COMPARISON OF AVERAGE PATH DENSITIES
 ALONG A DIAMETER
 MEASURED BY LANGMUIR PROBE AND MICROWAVE INTERFEROMETER

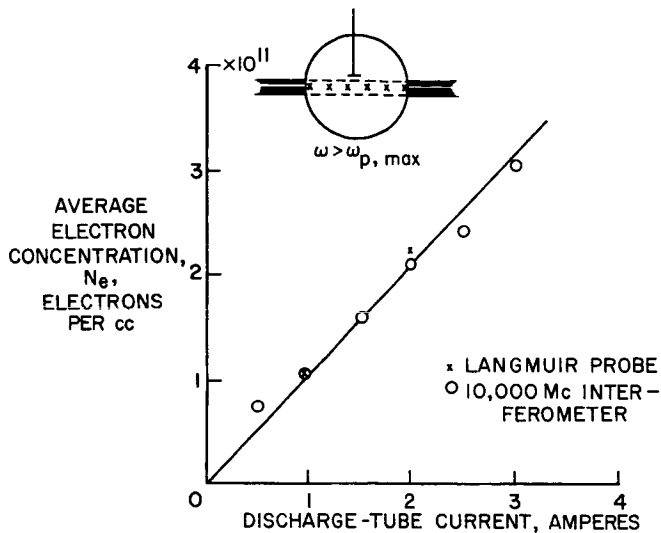


Figure 5

BASIC REFLECTOMETER

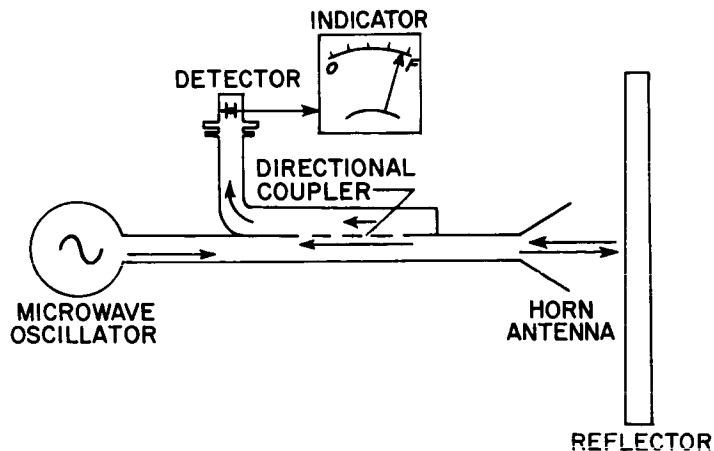


Figure 6

REFLECTOMETER TESTS PLASMA AND METALLIC CYLINDERS

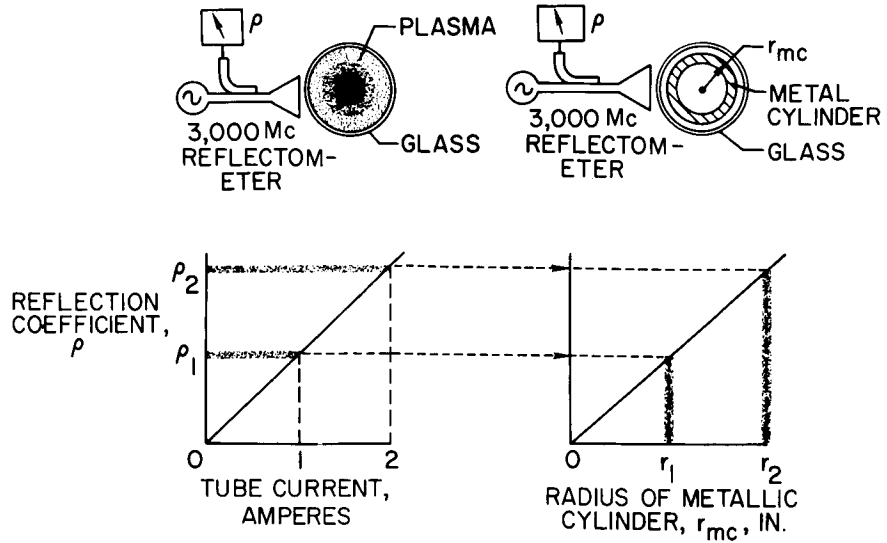


Figure 7

COMPARISON OF ELECTRON DENSITIES AS MEASURED BY LANGMUIR PROBE AND REFLECTOMETER

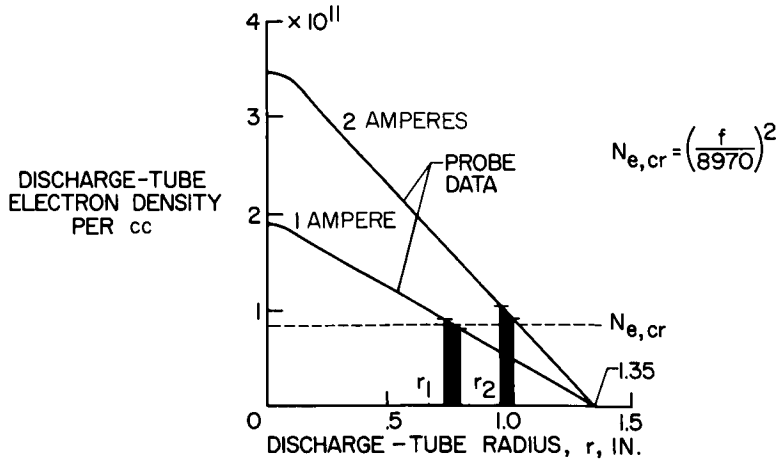


Figure 8

[REDACTED]

9. PENETRATION OF DROPS INTO HIGH-VELOCITY AIRSTREAMS

By Robert D. Ingebo
Lewis Research Center

SUMMARY

The purpose of this investigation was to determine the drop-size distribution for sprays produced by the crosscurrent injection of a liquid jet into a high-velocity airstream and to determine the distance of penetration of the measured drops into the airstream. The penetration distance may be calculated, with empirical expressions obtained in this investigation, from both the volume-number mean diameter and the maximum observed drop size in the spray.

INTRODUCTION

Methods of injecting a fuel into an oxidizing gas stream, such as that produced in a jet engine or a rocket combustor, generally fall into one of three categories, namely, gaseous, liquid, or slurry fuel injection systems. The most generally used type, of course, is liquid injection, since it is relatively easy to break up liquids and the droplets thus formed penetrate farther into the gas stream than gaseous jets. The slurry fuels (solid-liquid combinations) are also more advantageous than gaseous jets from a penetration standpoint.

The method used to inject liquid fuels into airstreams is important to the performance of jet engines (refs. 1 and 2). There is still, however, a lack of knowledge of the effect of many of the factors important to the breakup process and the subsequent trajectory, acceleration, and vaporization of the drops.

The purpose of this investigation was to determine the drop-size distribution for sprays produced by the crosscurrent injection of a liquid jet into a high-velocity airstream and to determine the distance of penetration of the measured drops into the airstream. For these purposes, a high-speed camera, capable of photographing microscopic droplets traveling at high velocities in airstreams (ref. 3), was used in combination with a sampling probe (ref. 4). From the data obtained with the high-speed camera and the sampling probe, it was possible to obtain empirical expressions for the penetration distance of drops produced by crosscurrent injection of liquid-fuel jets into airstreams.

EXPERIMENTAL PROCEDURE

The equipment used in this study is shown in figure 1. Details of the injector are shown in figure 2. Isooctane (2,2,4-trimethylpentane) was injected through a simple orifice in a flat plate, with the liquid jet oriented normal to the airstream at the center of the test section.

████████████████████

The spray was photographed with a high-speed camera developed at the Lewis Research Center to track droplets accelerating and vaporizing in airstreams. Construction details of the camera have been previously reported (ref. 3). To obtain drop-size-distribution data, photomicrographs of the sprays were obtained (fig. 3). The photomicrographs were taken along a vertical traverse of the spray center line, normal to the airstream, at a distance of $1 \pm \frac{1}{4}$ inch downstream from the injector. Vertical traverses made at distances of 1 inch on either side of the spray center line showed no measurable effect of horizontal displacement on drop-size distribution.

The sampling probe, shown in figure 1 and described in reference 4, was used for continuous sampling of the spray, at airstream velocity, along the same vertical traverse used for the camera. The iso-octane and air mixtures captured by the probe were passed through the NASA fuel-air mixture analyzer. Results from this sampling technique gave the spray-concentration data shown in figure 4.

ANALYSIS

Photomicrographs obtained at a magnification of 21, shown in figure 3, indicate that partial fractionation occurs in the atomization process inasmuch as the high-momentum large drops penetrate farther into the airstream than the low-momentum small drops. Thus, in the momentum exchange process between the high-velocity airstream and the liquid drops formed by atomization, there is apparently a relation between the penetration distance of droplet spray x and the airstream velocity V_g and the volume-number mean drop size D_{30} . This relation may be expressed as

$$x = f(V_g, D_{30}) \quad (1)$$

The volume-number mean drop size D_{30} is defined as follows:

$$D_{30} = \left(\frac{\sum_{D=0}^{D=D_m} nD^3}{\sum_{D=0}^{D=D_m} n} \right)^{1/3} \quad (2)$$

and may be obtained directly from the drop-size-distribution data. In equation (2), D is the average drop diameter for a given size increment, D_m the maximum drop size for each spray, and n the number of drops in each size increment.

Drop-size-distribution data were tested for agreement with the Nukiyama-Tanasawa expression for size distribution,

$$\frac{dR}{dD} = \frac{b^6}{120} D^5 e^{-bD} \quad (3)$$

or

$$\log \frac{\Delta R}{(\Delta D)D^5} = \frac{-b}{2.3} D + \log (b^6/120) \quad (4)$$

where ΔR is the volume fraction of drops having diameters less than D and b is a constant. The plots in figure 5, for three airstream velocities, show that the data points tend to follow equation (4) fairly well.

Attempts to relate the penetration distance x to D_{30} and V_g showed that the best results could be obtained by rewriting equation (1) as

$$x = f \left[\log \left(\frac{D_{30}^3}{V_g} \right) \right] \quad (5)$$

A plot of all the data given in table I is shown in figure 6, where $\log \left(\frac{D_{30}^3}{V_g} \right)$ is plotted against penetration distance x . The equation for the line in figure 6 is

$$\log \left(\frac{D_{30}^3}{V_g} \right) = 0.71x + 1.93 \quad (6)$$

or

$$\left(\frac{D_{30}^3}{V_g} \right)^{0.6} = e^{x+2.7} \quad (7)$$

where D_{30} , V_g , and x are expressed in units of microns, feet per second, and inches, respectively. Thus, equation (7) relates the mean drop size D_{30} obtained from the photomicrographs (fig. 3) to the penetration distance x determined from the point of maximum fuel concentration in the spray-profile data obtained from the sampling probe (fig. 4).

The penetration distance x of the volume-number mean drop diameter D_{30} into an airstream of velocity V_g is thus given by equation (7) for cross-stream injection of isooctane jets into airstreams. In order for equation (7) to be useful in calculating penetration distances, the airstream velocity and values of D_{30} must be known.

In reference 5, considerable data were obtained for cross-stream injection of liquid jets into airstreams, and the following expression was obtained:

$$\frac{D_{30}}{D_o} = 3.9 / (N_{We} N_{Re})^{0.25} \quad (8)$$

where D_o is the orifice diameter, $N_{We} = \rho_s D_o V_s^2 / \sigma$, and $N_{Re} = D_o V_s / \nu$, in which ρ_s is the airstream density, and σ and ν are the liquid surface tension and kinematic viscosity, respectively. An expression was also obtained for the maximum observed drop size D_m :

$$D_m / D_o = 22.3 / (N_{We} N_{Re})^{0.29} \quad (9)$$

When equations (7) and (8) are combined, the penetration distance x of the mean drop size D_{30} may be determined directly from the orifice diameter D_o and the air velocity V_g , if values for N_{We} and N_{Re} are known. Thus,

$$\left[D_o^3 / V_g (N_{We} N_{Re})^{0.75} \right]^{0.6} = e^{x+0.25}$$

where x is the penetration distance of the mean drop size D_{30} .

A plot of $\log \left(\frac{D_m^3}{V_g} \right)$ against the penetration distance x_m of the maximum observed drop size in the spray is shown in figure 7. The equation for the line in figure 7 is

$$\log \left(\frac{D_m^3}{V_g} \right) = 0.49 x_m + 3.3 \quad (10)$$

or

$$\left(\frac{D_m^3}{V_g} \right)^{0.9} = e^{x_m + 6.7} \quad (11)$$

When equations (9) and (11) are combined, the following expression is obtained:

$$\left[D_o^3 / V_g (N_{We} N_{Re})^{0.87} \right]^{0.9} = e^{x_m - 1.7} \quad (12)$$

where x_m is the maximum penetration distance of the maximum observed drop size D_m .

[REDACTED]

CONCLUDING REMARKS

The cross-stream injection of isooctane jets into an airstream produces a spray of drops that penetrate a given distance into the airstream; the distance is determined primarily by the size of the drops and the velocity of the airstream. The distance may be calculated, with empirical expressions obtained in this investigation, from both the volume-number mean diameter and the maximum observed drop size in the spray.

The data show that the orifice diameter is a very important parameter in the design of liquid-fuel injection systems from the standpoint of the drop size thus produced and the drop penetration distances.

REFERENCES

1. Sharp, J. G.: Effects of Fuel Type on the Performance of Aero Gas Turbine Combustion Chambers, and the Influence of Design Features. Jour. R.A.S., vol. 58, no. 528, Dec. 1954, pp. 813-825.
2. Staff of the National Gas Turbine Establishment: The Correlation of Combustion Efficiency and Injector Characteristics Under Simulated Altitude Conditions. AGARDograph 9, North Atlantic Treaty Organization (Paris), 1955, pp. 53-57.
3. Ingebo, Robert D.: Vaporization Rates and Drag Coefficients for Isooctane Sprays in Turbulent Air Streams. NACA TN 3265, 1954.
4. Foster, Hampton H., and Ingebo, Robert D.: Evaporation of JP-5 Fuel Sprays in Air Streams. NACA RM E55K02, 1956.
5. Ingebo, Robert D., and Foster, Hampton H.: Drop-Size Distribution for Cross-current Breakup of Liquid Jets in Airstreams. NACA TN 4087, 1957.

TABLE I.- PENETRATION DISTANCE AND
CHARACTERISTIC DROP SIZES

Mean drop size, D_{30} , microns	Penetration distance of D_{30} , x, in. (a)	Airstream velocity, V_g , ft/sec	Maximum observed drop size, D_m , microns	Maximum observed penetration distance of D_m , x_m , in.
55	1.8	100	175	3.0
68	2.2	100	225	3.7
69	2.3	100	190	3.0
81	2.5	100	225	3.6
65	2.2	100	175	3.2
62	1.8	180	190	2.6
47	1.0	180	150	1.9
47	1.2	180	140	1.8
49	1.2	180	150	1.8
47	1.0	180	140	2.0
52	1.4	180	150	2.0
40	.6	300	115	.9

^aBased on point of maximum fuel concentration in spray-profile data.

DECLASSIFIED

DIAGRAM OF TEST SECTION EQUIPMENT AND CAMERA UNIT

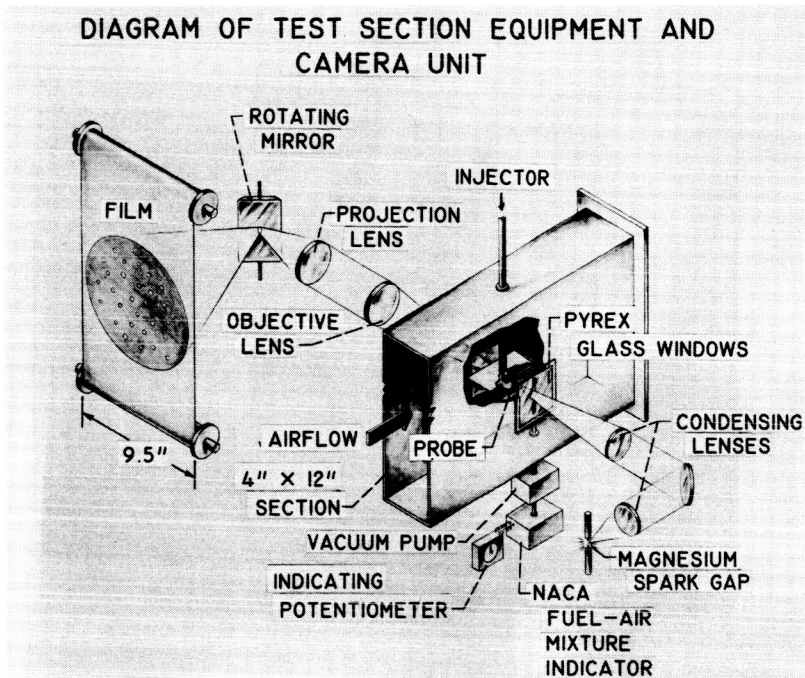


Figure 1

SKETCH OF INJECTOR

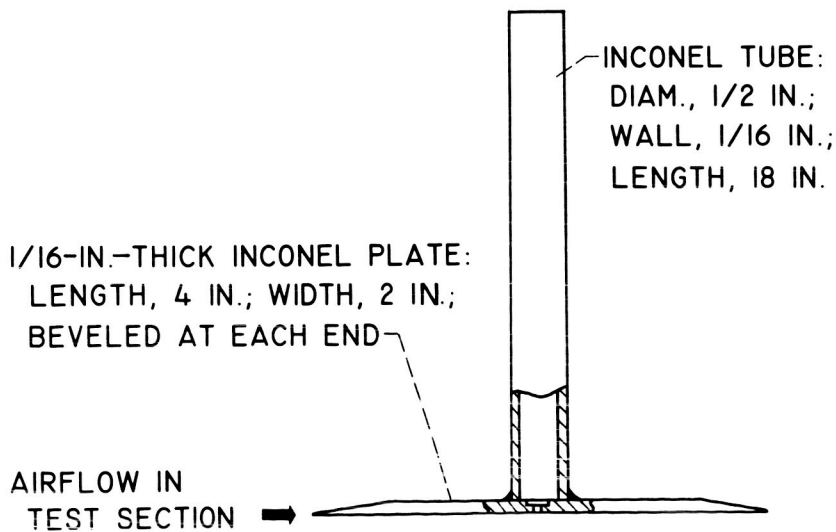


Figure 2

PHOTOMICROGRAPHS OF ISOCTANE SPRAY IN 100 FT/SEC VELOCITY AIRSTREAM

CONFIDENTIAL

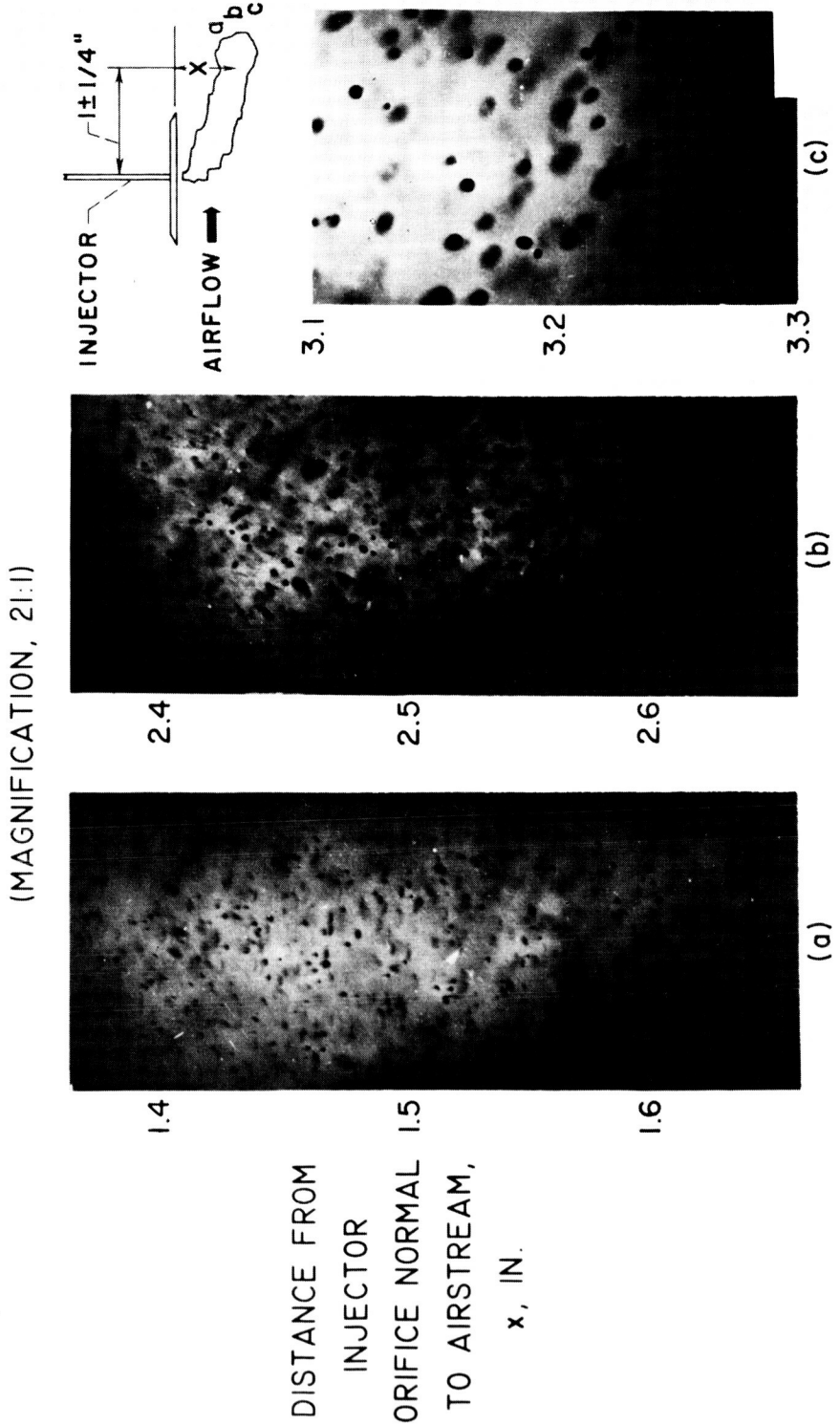


Figure 3

XXXXXXXXXX
 DISTRIBUTION OF ISOCTANE SPRAYS NORMAL TO
 THE AIRFLOW AND 1" DOWNSTREAM FROM THE INJECTOR

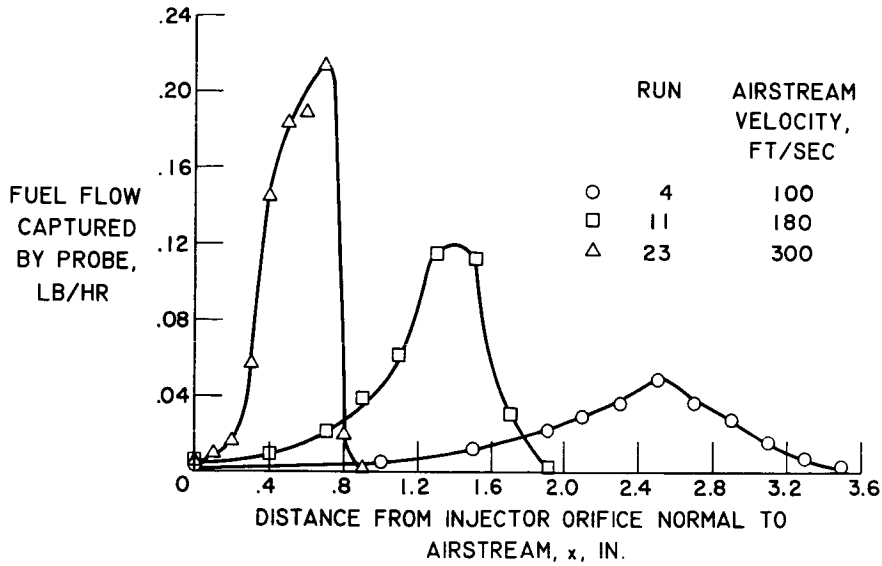


Figure 4

EFFECT OF AIRSTREAM VELOCITY ON ATOMIZATION OF
CROSSCURRENT ISOCTANE JETS

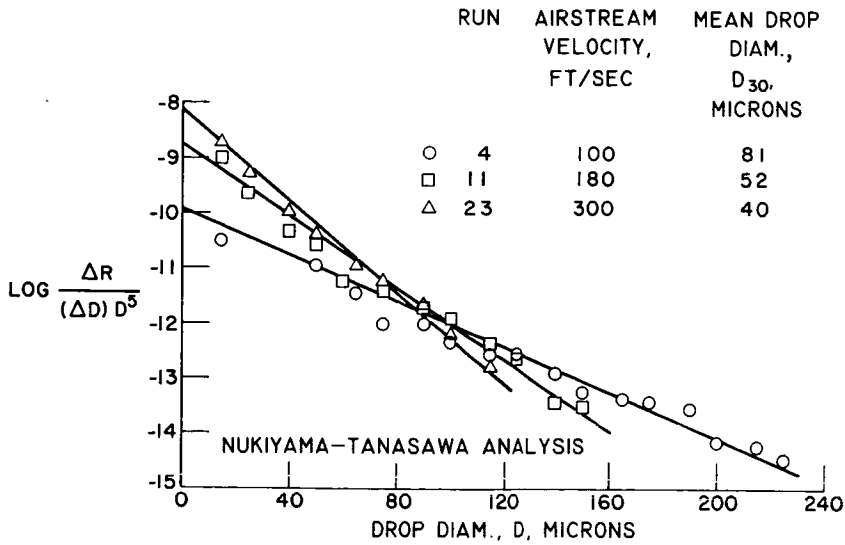


Figure 5



RELATION BETWEEN PENETRATION DISTANCE x AND D_{30}^3/V_g

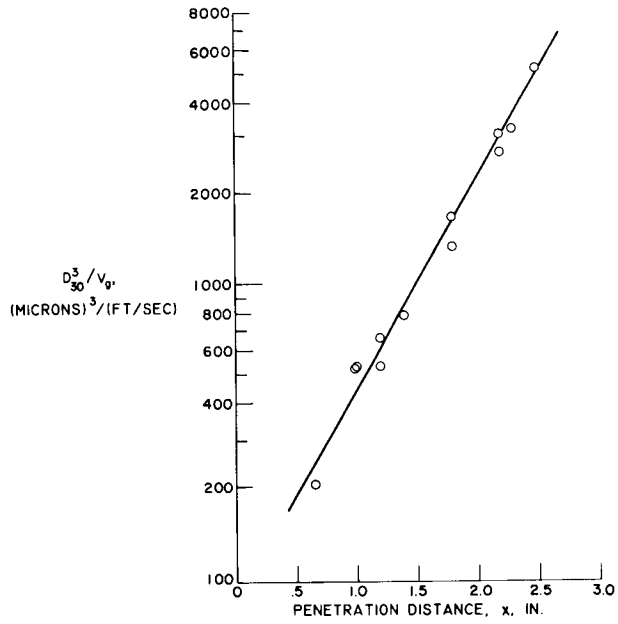


Figure 6

RELATION BETWEEN MAXIMUM PENETRATION DISTANCE x_m AND D_m^3/V_g

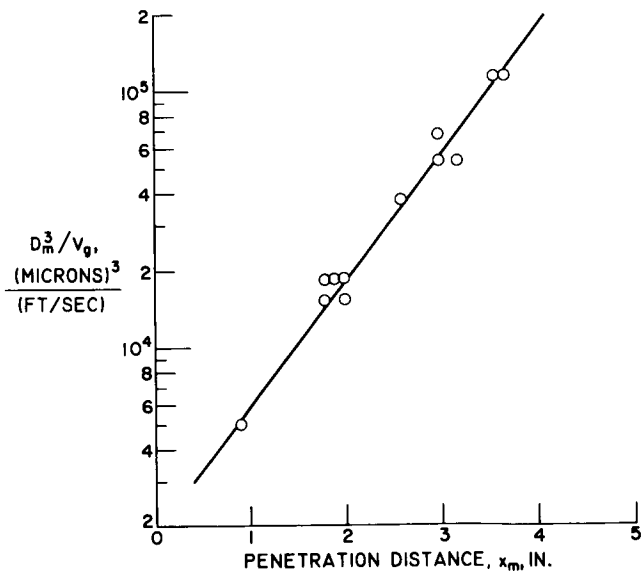
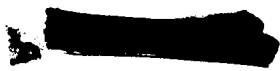


Figure 7



measured. Data for the coefficients were taken on the first pulse of an S-band repetitive pulse discharge. Data were also taken on successive pulses. These data gave coefficients that were nearly independent of water concentration above a small percentage and agreed with the values found by the authors of reference 7 (3×10^{-6} to 2×10^{-5} cc/ion-sec). On the first pulse, the gas is thus ionized, and the water aids in recombination, whereas on succeeding pulses the water enters into the ionization process. For both the reentry model and the electron-ion recombination experiments, the water was added prior to ionization, so that there was still some question as to the applicability of the results to the reentry communication problem. For this reason, another model was constructed in which the water could be added after ionization (ref. 11).

SYMBOLS

l	distance through plasma layer
\bar{n}	mean electron density
\bar{n}_c	mean electron density at cut-off
T_e	electron temperature, $^{\circ}\text{K}$
ϵ_v	collision correction factor
$\Delta\theta$	phase shift
$\Delta\theta_c$	phase shift at cut-off
ω	frequency
ω_p	plasma frequency
$\bar{\omega}_p$	mean plasma frequency

APPARATUS

Figure 2 is a photograph of the new experimental model. Experiments were conducted in a 4-foot-diameter vacuum chamber that was attached to a continuously pumped low-density facility. The chamber was lined with microwave-absorbing material. The gas used (nitrogen, air, or argon) was first dried by a dry-ice trap before entering the system. The gas was fed into a flat supersonic nozzle (exit, 0.75 by 4.5 in.) with the exit flow over the flat-plate model. The stream static pressure varied from 0.02 to 0.07 torr.

The gas was ionized by pulsed microwaves as the gas passed the ceramic window. This method produced slugs of ionized gas at a repetition rate of

[REDACTED]

REFERENCES

1. Belcher, H., and Sugden, T. M.: Studies on the Ionization Produced by Metallic Salts in Flames - I. The Determination of the Collision Frequency of Electrons in Coal-Gas/Air Flames. Proc. Roy. Soc. (London), ser. A, vol. 201, May 23, 1950, pp. 480-488.
2. Belcher, H., and Sugden, T. M.: Studies on the Ionization Produced by Metallic Salts in Flames - II. Reactions Governed by Ionic Equilibrium in Coal-Gas/Air Flames Containing Alkali Metal Salts. Proc. Roy. Soc. (London), ser. A, vol. 202, June 22, 1950, pp. 17-39.
3. Page, F. M.: The Determination of the Electron Affinity of the Hydroxyl Radical by Microwave Measurements on Flames. Discussions Faraday Soc., no. 19, 1955, pp. 87-96.
4. Bass, Arnold M., and Broida, H. P., eds.: Formation and Trapping of Free Radicals. Academic Press, 1960, pp. 61-62.
5. Loeb, Leonard B.: Basic Processes of Gaseous Electronics. Univ. of California Press, 1955, pp. 129-141.
6. Munson, R. J., and Tyndall, A. M.: Mobility of Alkali Ions in Gases. I. The Attachment of Water Molecules to Alkali Ions in Gases. Proc. Roy. Soc. (London), ser. A, vol. 172, July 19, 1939, pp. 28-42.
7. Takeda, Susumu, and Dougal, Arwin A.: Microwave Study of Afterglow Discharge in Water Vapor. Jour. Appl. Phys., vol. 31, no. 2, Feb. 1960, pp. 412-416.
8. Kuhns, Perry: Microwave Interferometer Measurements of Electron-Ion Recombination in Nitrogen, Air, and Argon. NASA TN D-1191, 1962.
9. Kuhns, Perry W.: Microwave Measurements of Steady-State and Decaying Plasmas. IRE Trans. on Space Electronics and Telemetry, vol. SET-8, no. 2, June 1962, pp. 173-178.
10. Kuhns, Perry W.: Effect of Addition of Impurities on Electron-Ion Recombination Times and on Transmission Through Ionized Layers. NASA paper presented at Second Symposium on the Plasma Sheath (Boston, Mass.), Apr. 10-12, 1962.
11. Kuhns, Perry W., and Cooper, Dale W.: Effect of Water Addition on Microwave Transmission Through a Cold Plasma Layer. NASA TM X-874, 1963.
12. Huber, Paul W., and Gooderum, Paul B. (With appendix A by Theo E. Sims and Duncan E. McIver, Jr., and appendix B by Joseph Burlock and William L. Grantham): Experiments With Plasmas Produced by Potassium-Seeded Cyanogen Oxygen Flames for Study of Radio Transmission at Simulated Reentry Vehicle Plasma Conditions. NASA TN D-627, 1961.

- [REDACTED]
13. Balwanz, W. W., and Stine, P. T.: The Plasmas of Missile Flight - Analysis of Polaris A2X Signal Absorption. NRL Rep. No. 5636, U.S. Naval Res. Lab., July 24, 1961.
 14. Balwanz, W. W.: Weeding in Rocket Exhausts, Appendix B. NRL Memo. Rep. 1310, U.S. Naval Res. Lab., Apr. 1962.
 15. Sims, Theo E., and Jones, Robert F.: Rocket Exhaust Effects on Radio Frequency Propagation From a Scout Vehicle and Signal Recovery During the Injection of Decomposed Hydrogen Peroxide. NASA TM X-529, 1961.
 16. Lin, Shao-Chi, and Theofilos, George P.: Hydrodynamic Effects Produced by Pulse Microwave Discharges. The Physics of Fluids, vol. 6, no. 10, Oct. 1963, pp. 1369-1379.
 17. Stratton, Julius Adams: Electromagnetic Theory. McGraw-Hill Book Co., Inc., 1941.

[REDACTED]

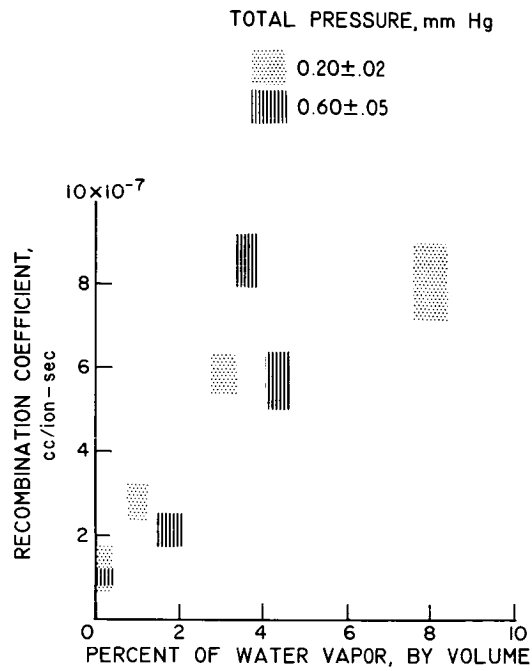


Figure 1.- Effect of addition of water vapor on electron-ion recombination coefficient of air.

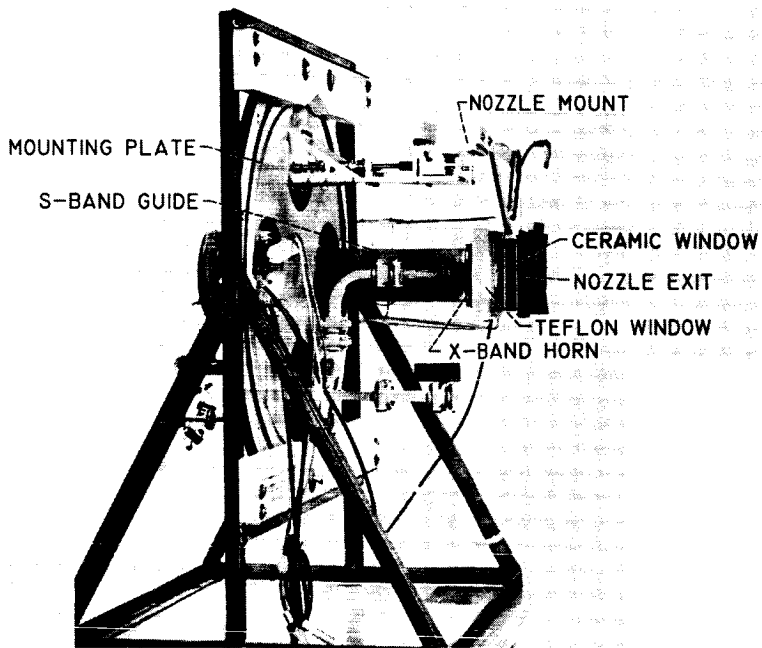


Figure 2.- Model, nozzle, and transmitting section.

[REDACTED]

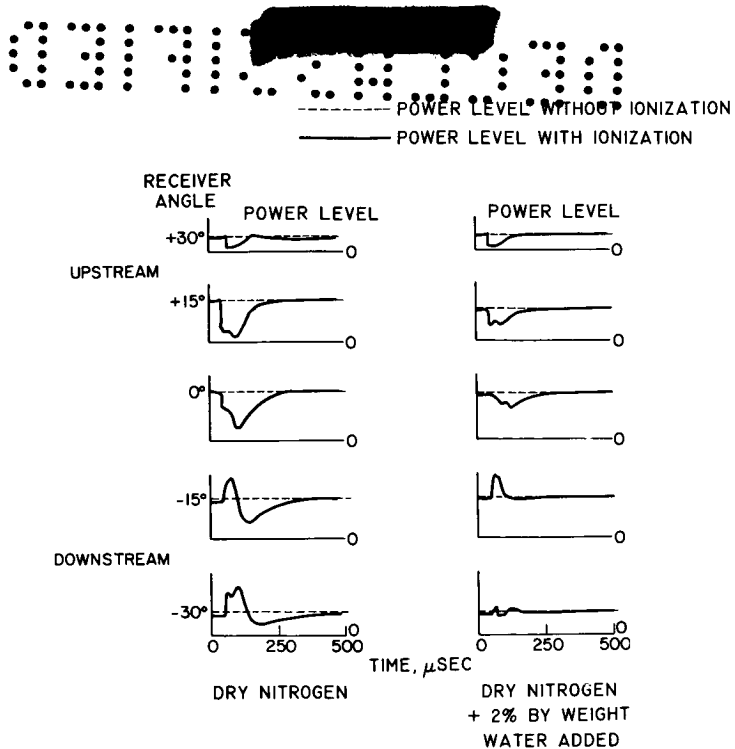


Figure 3.- Copies of oscilloscope traces of relative X-band power received as function of angle and time after pulse. Dry nitrogen and nitrogen with water added.

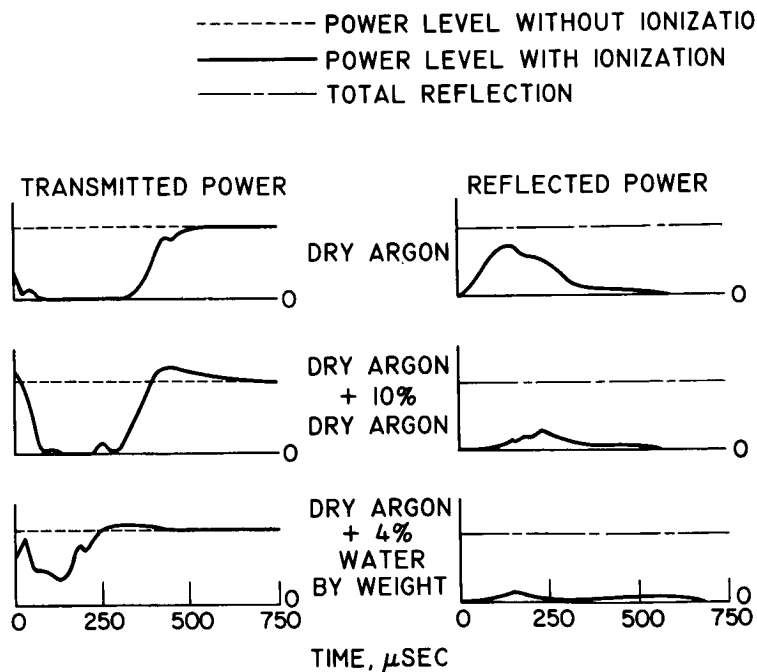


Figure 4.- Copies of oscilloscope traces of normal X-band transmission and reflection as function of time after ionizing pulse. Dry argon and dry argon with argon or air added to stream; pressure, 0.037 torr.

SECRET

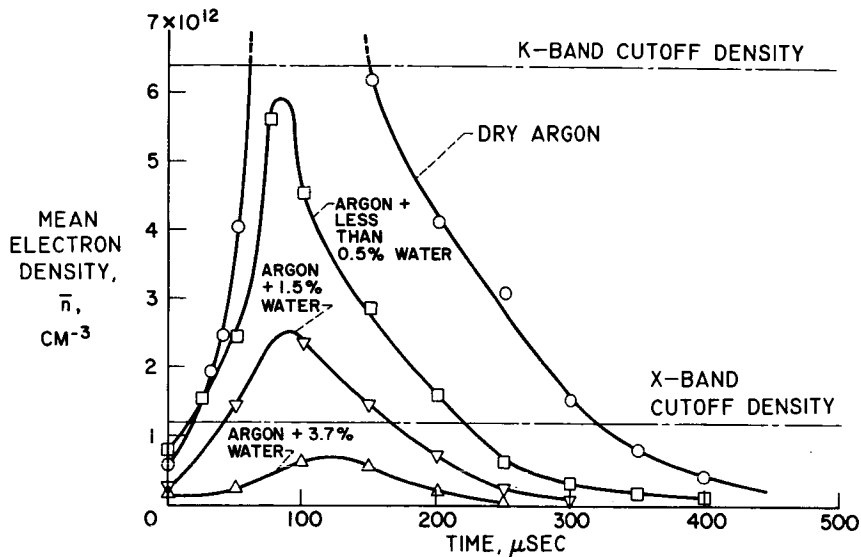


Figure 5.- Mean electron density of plasma as function of time after pulse for various amounts of water added. Pressure, 0.037 torr; K-band microwaves; plasma thickness, 0.7 inch.

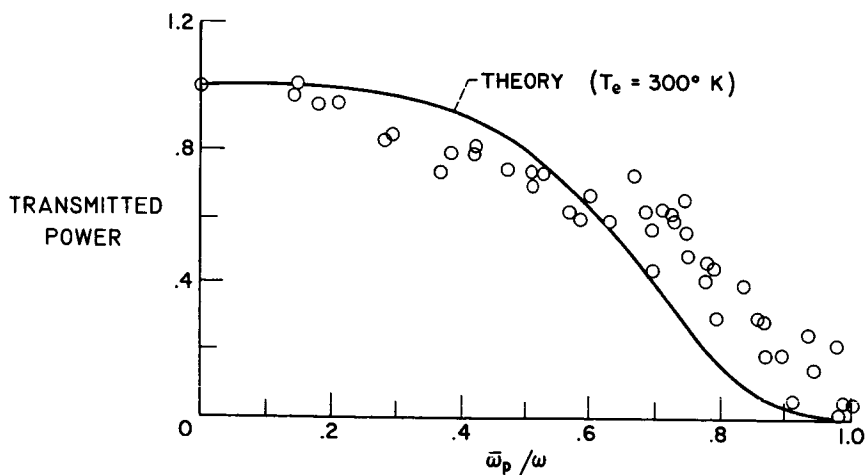
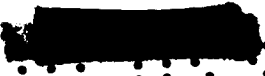


Figure 6.- Experimental values of transmitted power as function of $\bar{\omega}_p / \omega$. K-band; argon gas; plasma thickness, 0.7 inch.

SECRET


11. A STUDY OF DIELECTRIC-COVERED SHUNT SLOTS IN A WAVEGUIDE

By William F. Crosswell and Robert B. Higgins
Langley Research Center

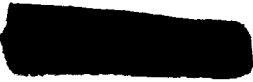
SUMMARY

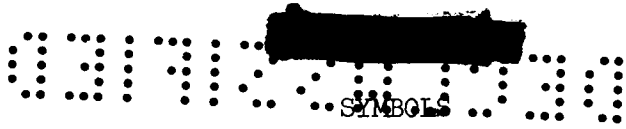
The purpose of this study was to determine experimentally the effects of placing dielectric covers of various thicknesses over a shunt slot in a waveguide. Slot lengths and displacements were chosen so that the data cover the waveguide bandwidth for dielectric constants from 1 to 4. By utilizing the measured data, formulas are developed for the mean values of slot conductance and resonant frequency for cover thicknesses greater than one-fourth of the wavelength in the dielectric material. In addition, it is shown that plane wave theory gives a bound on the conductance variation for covers thicker than one-fourth of the wavelength in the dielectric material. Pattern and voltage standing wave ratio (VSWR) measurements of arrays of dielectric-covered slots designed with single-slot data give predictable results.

INTRODUCTION

A space vehicle reentering the earth's atmosphere at hypersonic velocities will be subject to severe environmental conditions in the form of extreme structural loads, heat-transfer rates, and temperatures. Available weights for such vehicles are usually restricted, and the restriction results in the common use of dielectric-type ablative materials covering the entire structure. Trajectories of space-vehicle flight frequently contain long time periods before and after reentry. Antennas used for such applications must operate satisfactorily throughout the trajectory. Since the ablation process results in a change in material thickness, antennas proposed for such an application must be relatively insensitive to these changes in addition to fulfilling the usual requirements of minimum weight and volume. An antenna which meets many of these requirements at microwave frequencies is the shunt slot in a waveguide.

Typical array designs are shown in figure 1. The linear arrays are models used for study purposes because of their ease of fabrication and analysis. If a directive antenna were required for a stabilized vehicle, the array would be linear as shown. The circular array yields an omnidirectional radiation pattern as required on a spinning vehicle. However, use of a slot array in this application requires an extensive knowledge of slot characteristics as a function of thickness and dielectric constant of the covering material.



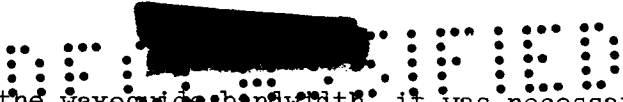


- f_r average resonant frequency, Gc
- l slot length, in.
- P_d power coupled out of slot resonant with an external medium μ_0, ϵ
- P_{MAX} maximum power
- P_{MIN} minimum power
- P_0 power coupled out of slot resonant with an external medium μ_0, ϵ_0
- r voltage reflection coefficient for single interface
- t thickness of dielectric material, in.
- w slot width, in.
- x slot displacement, measured from center line of waveguide to center line of slot, in.
- ϵ dielectric constant of covering material
- ϵ_{EQUIV} equivalent dielectric constant
- ϵ_0 dielectric constant of free space
- θ angle between radius vector and normal array plane, deg
- λ_0 free-space wavelength
- λ_ϵ wavelength in dielectric material
- μ_0 permeability of free space
- ρ voltage reflection coefficient for a plane dielectric sheet
- ϕ angle between reference axis and radius vector, measured in plane of array, deg

EXPERIMENT

The slots were fabricated by a process which uses electrode burning as a means of removing the metal. The size and shape of the slots are determined by the size and shape of the electrode. This method provides a means of fabricating very long arrays and sustaining required dimensional precision. Rectangular-shaped slots, 0.062 inch wide, in an RG52U waveguide constitute the samples used in this experiment. A typical test sample is shown in figure 2.





In order to cover the waveguide bandwidth, it was necessary to use at least eight slot displacements for each of the four dielectric materials. These materials are designated by the value of the dielectric constant as shown in table I with other pertinent data. Measurements were taken at several discrete thicknesses. Standard measurement methods were employed for determining normalized conductance values. The insertion technique, using precision calibrated attenuators, was used for measurement of high VSWR (ref. 1).

PRESENTATION OF EXPERIMENTAL RESULTS

Table I is an index to the measured data. Typical results for a slot at $x = 0.136$ inch with $l = 0.475$ inch are given in figure 3 where cover thickness t and dielectric constant ϵ are the major differentiating parameters.

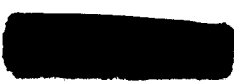
ANALYSIS OF DATA

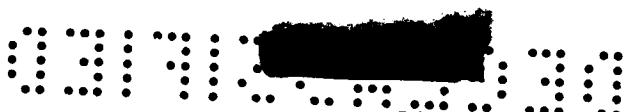
General

The changes in slot characteristics can be summarized in the following three observations:

1. The frequency at which resonance occurs (defined as the frequency at peak conductance) changes radically as a function of cover thickness up to $t = 0.15\lambda_{\epsilon}$. For $t > 0.15\lambda_{\epsilon}$, the resonant frequency changes sinusoidally as a function of thickness with a period of $0.5\lambda_{\epsilon}$.
2. Normalized conductance is significantly changed with the addition of dielectric covers up to $t = 0.15\lambda_{\epsilon}$. For $t > 0.15\lambda_{\epsilon}$, the normalized conductance varies sinusoidally as a function of thickness, with a period of approximately $0.5\lambda_{\epsilon}$.
3. The resonant conductance is much lower than that predicted for the case of no dielectric cover.

Analyses are given in succeeding paragraphs which give first-order predictions for all three of these major effects. It was necessary, for these analyses, to define an average resonant frequency f_r which is a function of the dielectric constant ϵ , is not a function of the slot displacement x or dielectric thickness t , and is dependent on slot length l . In order to accomplish this, for a particular dielectric constant, plots of resonant frequency as a function of thickness were made from the measured data for each of eight samples. By inspecting these curves in the region where the resonant frequency was periodic as a function of thickness, the average frequency for each sample was determined. Then, using the slot length l and average frequency for each sample, a value of l/λ_0 was calculated. All eight values of l/λ_0 were averaged to obtain a value related to the particular dielectric constant. This





last averaging process was necessary to eliminate the second-order effects of guide wavelength from the data. By utilizing this method, the experimental curve in figure 4 was obtained. With a knowledge of the dielectric constant ϵ and the slot length l an average resonant frequency pertaining to ϵ is defined. The vertical dashed line in the measured data (fig. 3) represents the defined average resonant frequency f_r .

Slot Conductance as a Function of Cover Thickness

By utilizing the definition of f_r , curves were obtained from the measured data in the form of the slot conductance plotted as a function of t/λ_ϵ . Figure 4 is such a plot for one waveguide slot, where $x = 0.136$ inch, $l = 0.475$ inch, and one dielectric is considered. From inspection of this curve and other similar curves, it was noted that the curves become periodic for $t > 0.15\lambda_\epsilon$. This fact suggested the application of plane wave theory to this problem. With normal incidence and lossless dielectrics assumed, the voltage reflection coefficient for a plane dielectric sheet with a plane wave incident is given in reference 2 (pp. 32-4 - 32-23) and may be expressed as

$$\rho = \frac{r \left(1 - e^{-\frac{j4\pi t\sqrt{\epsilon}}{\lambda_0}} \right)}{1 - r^2 e^{-\frac{j4\pi t\sqrt{\epsilon}}{\lambda_0}}} \quad (1)$$

where r is voltage reflection coefficient for a single interface $\left(r = \frac{1 - \sqrt{\epsilon}}{1 + \sqrt{\epsilon}} \right)$, t is dielectric-window thickness, ϵ is relative dielectric constant, and λ_0 is free-space wavelength.

When the extreme cases of thickness are considered, ρ may be expressed

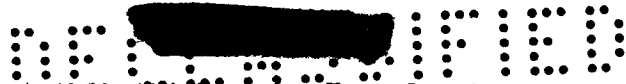
$$|\rho|_{t=\frac{n}{2}\lambda_\epsilon} = 0 \quad (2)$$

and

$$|\rho|_{t=\frac{(2n+1)}{4}\lambda_\epsilon} = \left| \frac{2r}{1 + r^2} \right| \quad (3)$$

where $n = 1, 2, 3, \dots$. It is assumed that the place where the maximum value of conductance occurs corresponds to the case of no reflections as given by equation (2). The first case corresponding to equation (2) occurs at $t \approx 0.65\lambda_\epsilon$ for all dielectric constants. It is assumed that maximum power is





coupled out of the slot at this thickness. In order to compute the effect of maximum reflection as predicted by equation (3), the amount of power coupled

out of the slot at $t \approx 0.65\lambda_\epsilon$ is reduced by $|\rho|^2 = \left| \frac{2r}{1+r^2} \right|^2$ and converted

into conductance. The dashed lines shown in figure 4 are the bounds on the conductance as a function of dielectric thickness, with the upper line corresponding to no reflections and the lower line to maximum reflections. In general, for a cover thickness greater than $0.15\lambda_\epsilon$ these bounds appear to give at least first-order prediction.

Change in Slot Conductance From Free-Space Values

From the preceding analysis and an inspection of the measured data, it is obvious that plane-wave—plane-sheet theory is not satisfactory to predict the change in slot conductance that occurs with a change from the uncovered slot to the covered slot. The purpose of this discussion is to obtain a first-order prediction of slot conductance that is strictly a function of the dielectric constant.

From reference 3 the radiation resistance R_r of a resonant half-wave slot in an infinite ground plane is given by

$$R_r = \frac{1}{4 \times 73} \eta^2 \quad (4)$$

where η is intrinsic impedance.

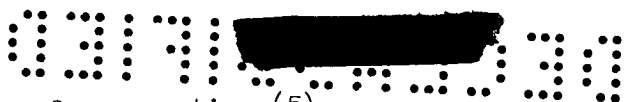
For the case of the slot located in a waveguide, the radiation resistance R_r is double the value given by equation (4) since the slot can radiate only in one direction (p. 295 of ref. 4). Placing a dielectric cover over the slot does not appear to produce any significant changes in the internal fields of the waveguide and the internal wall currents which excite the slot, if

$t \approx 0.65\lambda_\epsilon + \frac{n\lambda_\epsilon}{2}$ so that reflections are small. Restricting interest to this case, and assuming the waveguide and slot to be equivalent to a constant current source I , the power coupled out of the slot P_r is given by

$$P_r = \frac{I^2}{2 \times 73} \frac{\mu_0}{\epsilon_0 \epsilon} \quad (5)$$

where μ_0 is the permeability of free space and ϵ_0 is the dielectric constant of free space. In equation (5) the entire half space outside the waveguide is considered to be completely filled with the material of dielectric constant ϵ . If P_0 is the power coupled out of the slot resonant with an external medium μ_0, ϵ_0 and P_d is the power coupled out of the slot resonant with an external





medium μ_0, ϵ , then from equation (5)

$$P_d = \frac{P_0}{\epsilon} \tag{6}$$

A calculated value of conductance for shunt slots with a dielectric cover can be obtained by using standard conductance equations (pp. 9-3 - 9-5 of ref. 5) and equation (6). However, it must be remembered that a slot of given length will resonate at a lower frequency with the addition of a cover and the slot conductance is a function λ_g/λ_0 . (λ_g is waveguide wavelength.) Therefore, either f_r must be used to calculate λ_0 or, if a particular operating frequency is desired, the physical length l must be adjusted according to the experimental curve in figure 5. Table II shows the comparison between the calculated and the measured values of slot conductance. The measured values correspond to the value of conductance for $t = 0.65\lambda_\epsilon$.

Calculation of Resonant Length

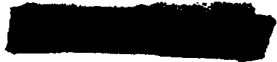
Placing a dielectric cover over a shunt slot causes a significant change in the resonant length. Figure 5 shows a measured curve of the resonant length as a function of dielectric constant. One simple method of calculating the resonant length is to assume that the slot is completely filled with the dielectric. Then

$$\left(\frac{l}{\lambda_0}\right)_\epsilon = \frac{l/\lambda_0}{\sqrt{\epsilon}} \tag{7}$$

where $\left(l/\lambda_0\right)_\epsilon$ is resonant length with a dielectric cover and l/λ_0 is resonant length with no cover.

Figure 5 shows curves for the original measured values and for those calculated from equation (7). Equation (7) predicts too short a resonant length. This means that the slot can be considered as equivalently filled with material having a dielectric constant less than ϵ . Pursuing the approach of obtaining an equivalent dielectric constant ϵ_{EQUIV} , the following approximate analysis was made.

Only the reactive fields are involved in the determination of resonant length. An inspection of the previous analyses indicates that far-field theory gives good approximations to conductance problems with covers $0.15\lambda_\epsilon$ thick. Therefore, the reactive fields most probably extend only into very thin layers near the slot. The source field may be considered as consisting of time-harmonic charge pairs which result from the excitation voltage across the slot. The displacement current across the slot must terminate in these charge pairs to satisfy continuity conditions. These source charge pairs can then be considered interchangeably as small current elements or Hertz dipoles having a current equal to the displacement current I . This concept is useful since the



exact fields of such a source are known. Near the Hertz dipole or, equivalently, the charge pairs, the field is predominantly electric and is of the so-called quasi-static form. Since only very thin layers appear to be of importance, quasi-static theory can be used to convert the problem to a simple capacitor equivalent as shown in figures 6(a) and 6(b). For electric fields parallel to the interface a reduction of the capacitor can be made as shown in figures 6(b) and 6(c). (See pp. 55-56 of ref. 6.) The slot then can be considered to be equivalently filled with a material having a dielectric constant ϵ_{EQUIV} given by

$$\epsilon_{\text{EQUIV}} = \frac{\epsilon_1 d_1 + \epsilon_2 d_2}{d_1 + d_2} \quad (8)$$

Unfortunately, the distances d_1 and d_2 are unknown. However, by using the Hertz dipole equivalent, a relationship between d_1 and d_2 can be obtained. From reference 7 the net radially propagating reactive energy W_R from a Hertz dipole can be given as

$$W_R = \frac{c}{\epsilon d^3} \quad (9)$$

where c is a constant. By assuming an equal distribution of energy on both sides of the slot, the following relationship can be obtained:

$$\frac{c}{\epsilon_1 d_1^3} = \frac{c}{\epsilon_2 d_2^3} \quad (10)$$

Combining equation (8) and equation (10) gives the resulting equation:

$$\epsilon_{\text{EQUIV}} = \frac{1 + \epsilon^{2/3}}{1 + \epsilon^{-1/3}} \quad (11)$$

when $\epsilon_1 = 1$ and $\epsilon_2 = \epsilon$.

A curve of resonant length plotted as a function of dielectric constant can be obtained from

$$\left(\frac{l}{\lambda_0}\right)_\epsilon = \frac{l/\lambda_0}{\sqrt{\epsilon_{\text{EQUIV}}}} \quad (12)$$

where ϵ_{EQUIV} is given in equation (11). Calculated results obtained by using equation (12) are shown in figure 5.

VSWR

The midband VSWR measured less than 1.1 on both designs. The VSWR characteristics of the 25-slot array plotted as a function of frequency, with cover thickness as a parameter, is shown in figure 7. The frequency band over which the array can be operated without major degradation of the main lobe shape or amplitude is indicated by the vertical dashed lines. Calculations based on single-slot measurements indicate midband variation of VSWR from 1.03 to 1.13 over the range of cover thickness indicated. Similar results were obtained on the 56-slot array, except that the operating band was approximately 0.05 Gc.

Radiation Patterns

Based on the usual assumptions of negligible source coupling and infinite ground plane, array patterns were calculated. (See ref. 8.)

The upper plot in figure 8 is a comparison of calculated and measured patterns for the 25-slot linear array pictured in figure 1. The 56-slot linear array is similar. Agreement between calculated and measured patterns indicates that for an array of dielectric-covered shunt slots mutual coupling is negligible. It should be noted that no unusual care was exercised in fitting the dielectric covers to the surface of the waveguide. It is therefore believed that for large arrays of shunt slots the tolerance on cover fit is not unduly critical. Within the operating band previously indicated in figure 7, the patterns were similar to those given at midband except for changes in the level and position of lower order sidelobes.

The lower plot in figure 8 represents a radiation pattern as a function of angle measured in the plane of the 50-slot circular array shown in figure 1. Array calculations indicate that this pattern should be very nearly a straight line, that is, omnidirectional in this plane. However, it has been found that the circular shape has caused large variations to occur in the orthogonal plane pattern. These variations appear here in the array plane pattern. Efforts are being made to correct this problem by recessing the slots.

CONCLUDING REMARKS

The primary purpose of this study was to determine the design parameters for dielectric-covered shunt-slot arrays, where the thickness of the cover was changing as a result of a reentry environment. It has been shown that array designs that are relatively insensitive to dielectric-cover properties are available for dielectric constants less than 4 over the normal waveguide bandwidth. By using the first-order formulas developed in this investigation to extend the data for dielectric constants greater than 4, it can be concluded that the VSWR of shunt-slot arrays will exceed acceptable bounds as a function of changes in cover thickness.



1. Ginzton, Edward L.: Microwave Measurements. McGraw-Hill Book Co., Inc., 1957, pp. 262-275.
2. Kay, Alan F.: Radomes and Absorbers. Antenna Engineering Handbook, Henry Jasik, ed., McGraw-Hill Book Co., Inc., 1961, pp. 32-1 - 32-40.
3. Harrington, Roger F.: Time-Harmonic Electromagnetic Fields. McGraw-Hill Book Co., Inc., 1961, p. 138.
4. Eaton, J. E., Eycles, L. J., and Macfarlane, G. G.: Linear-Array Antennas and Feeds. Microwave Antenna Theory and Design, Samuel Silver, ed., McGraw-Hill Book Co., Inc., 1949, pp. 257-333.
5. Ehrlich, M. J.: Slot-Antenna Arrays. Antenna Engineering Handbook, Henry Jasik, ed., McGraw-Hill Book Co., Inc., 1961, pp. 9-1 - 9-18.
6. Richmond, Jack H.: Electromagnetic Field and Optic Theory. Techniques for Airborne Radome Design, Thomas E. Tice, ed. WADC Tech. Rep. 57-67, ASTIA Doc. No. AD 142001, U.S. Air Force, Sept. 1957, pp. 23-70.
7. Schelkunoff, Sergei A., and Friis, Harald T.: Antennas - Theory and Practice. John Wiley & Sons, Inc., 1952, p. 122.
8. Kraus, John D.: Antennas. McGraw-Hill Book Co., Inc., 1950, pp. 57-126 and 356-361.

EXPERIMENTAL DIELECTRIC-COVERED SHUNT-SLOT DATA

Dielectric constant of covering, ϵ	Slot displacement, x, in.	Slot length, l, in.	Cover thickness, t, in.	Frequency range, Gc
2.10	0.066	0.475	0.095 to 0.935	9.4 to 10.7
	.096	.449	.095 to .935	10 to 11.4
	.093	.475	.095 to .935	9.2 to 11.0
	.094	.506	.095 to .935	9.0 to 10.5
	.133	.449	.095 to .935	10 to 11.6
	.136	.475	.095 to .935	9.0 to 10.8
	.132	.506	.095 to .935	9.0 to 10.4
	.185	.449	.095 to .935	10.1 to 11.4
	2.78	0.066	0.475	0.090 to 0.710
.096		.449	.090 to .710	9.2 to 11.0
.093		.475	.090 to .710	8.6 to 10.4
.094		.506	.090 to .710	8.2 to 9.8
.133		.449	.120 to .860	8.7 to 11.0
.136		.475	.090 to .710	8.7 to 10.2
.132		.506	.120 to .800	8.2 to 10.0
.185		.449	.120 to .860	8.9 to 11.0
3.31		0.066	0.475	0.100 to 0.900
	.096	.449	.100 to .900	8.7 to 10.1
	.093	.475	.100 to .900	8.6 to 9.8
	.094	.506	.100 to .900	8.0 to 9.2
	.133	.449	.100 to .900	8.0 to 10.1
	.136	.475	.100 to .900	8.2 to 9.6
	.132	.506	.100 to .900	7.7 to 9.2
	.185	.449	.100 to .900	8.9 to 10.2
	3.78	0.066	0.475	0.125 to 0.875
.096		.449	.125 to .875	8.4 to 9.6
.093		.475	.125 to .875	8.0 to 9.2
.094		.506	.125 to .875	7.6 to 8.7
.133		.449	.125 to .875	8.4 to 9.6
.136		.475	.125 to .875	8.0 to 9.2
.132		.506	.125 to .875	7.7 to 8.6
.185		.449	.125 to .875	8.4 to 9.6

TABLE II

COMPARISON OF MEASURED AND CALCULATED VALUES OF NORMALIZED CONDUCTANCE
FOR VARIOUS DIELECTRIC COVERS

Slot displacement, x, in.	Normalized conductance for cover having -							
	$\epsilon = 2.10$		$\epsilon = 2.78$		$\epsilon = 3.31$		$\epsilon = 3.78$	
	Calculated	Measured	Calculated	Measured	Calculated	Measured	Calculated	Measured
0.066	0.019	0.021	0.019	0.019	0.019	0.020	0.024	0.021
.096	.028	.028	.028	.028	.026	.025	.031	.029
.093	.037	.036	.036	.036	.030	.034	.042	.038
.094	.049	.046	.048	.045	.045	.047	.053	.050
.133	.050	.044	.048	.042	.042	.042	.053	.048
.136	.071	.066	.062	.056	.056	.057	.063	.069
.132	.080	.081	.075	.077	.077	.078	.071	.090
.185	.079	.077	.072	.075	.075	.066	.068	.083

0317: [REDACTED] 030

TYPICAL SHUNT-SLOT ARRAYS

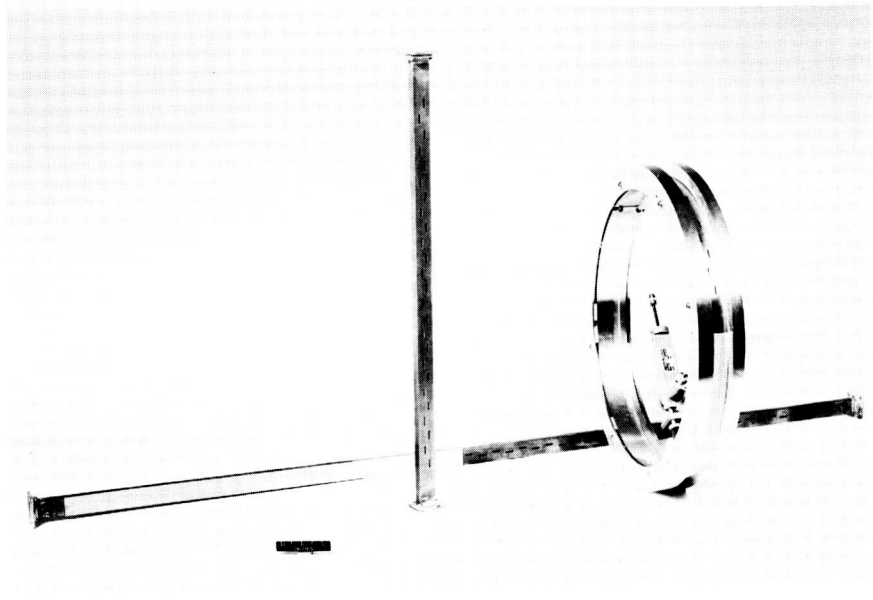


Figure 1

L-2167-7

TYPICAL TEST SAMPLE

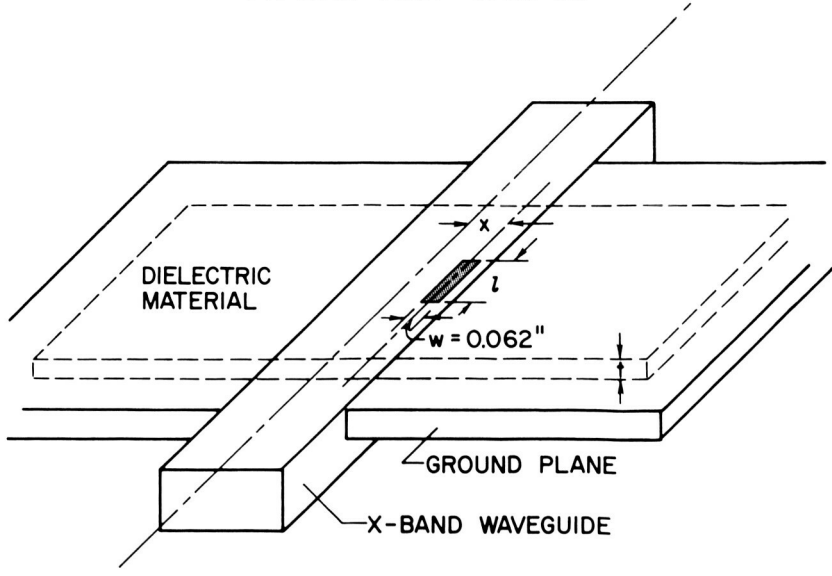


Figure 2

[REDACTED]

VARIATION OF NORMALIZED CONDUCTANCE
WITH FREQUENCY

$\epsilon = 2.78$; $x = 0.136$ "; $l = 0.475$ "

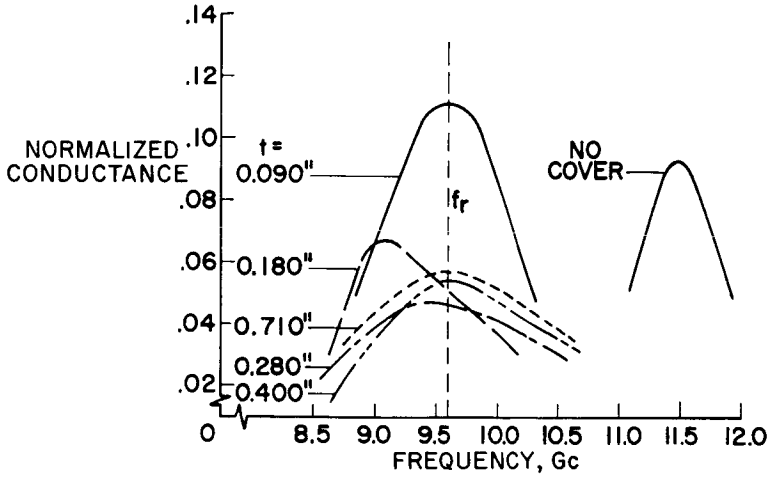


Figure 3

VARIATION OF NORMALIZED CONDUCTANCE
WITH COVER THICKNESS

$\epsilon = 2.78$; $f_r = 9.6$ Gc; $x = 0.136$ "; $l = 0.475$ ";

P_0 , POWER COUPLED OUT IN FREE SPACE AT f_r ; $r = \frac{1-\sqrt{\epsilon}}{1+\sqrt{\epsilon}}$

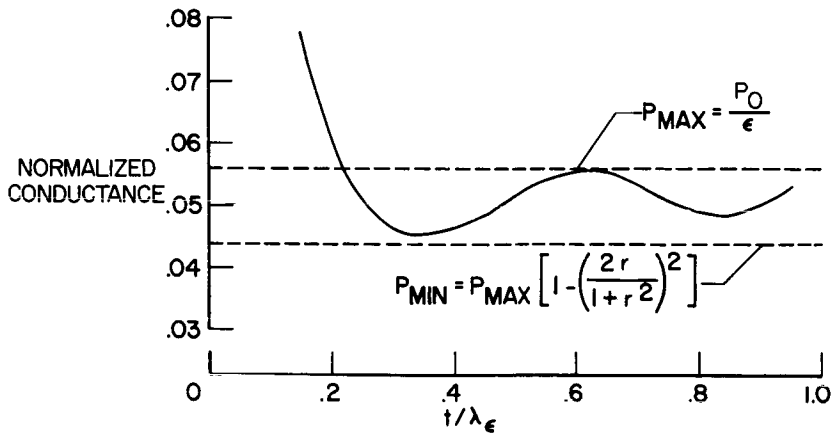


Figure 4

COMPARISON OF EXPERIMENTAL AND THEORETICAL
RESONANT LENGTH RATIOS

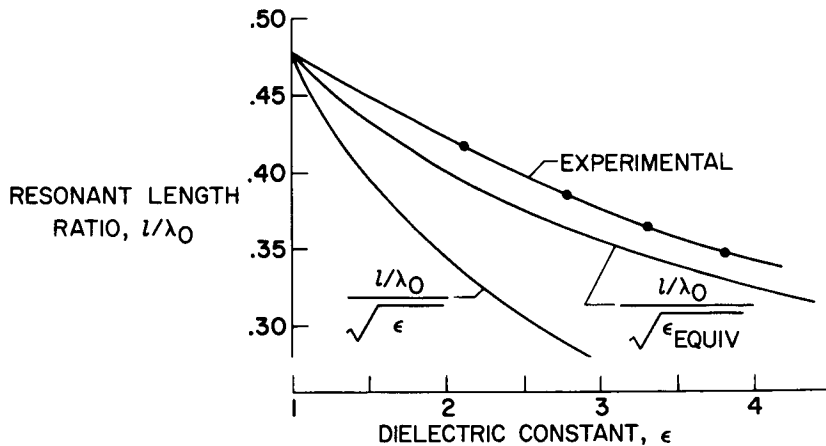


Figure 5

REDUCTION OF SLOT IN GROUND PLANE TO
A QUASI-STATIC EQUIVALENT

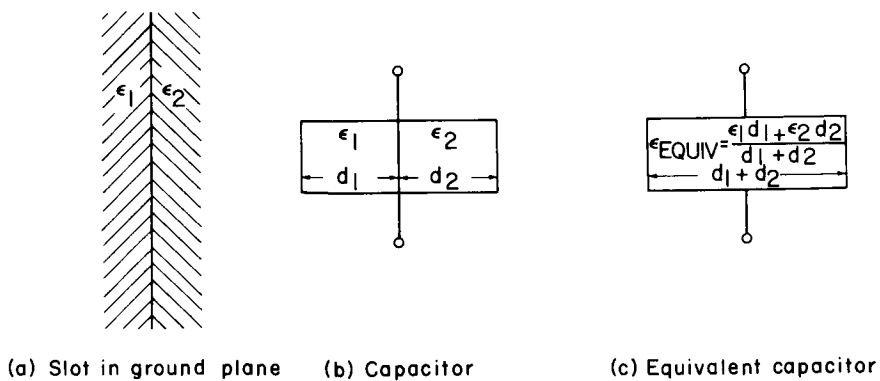


Figure 6

[REDACTED]

DECLASSIFIED

VARIATION OF VSWR WITH FREQUENCY
25-SLOT LINEAR ARRAY

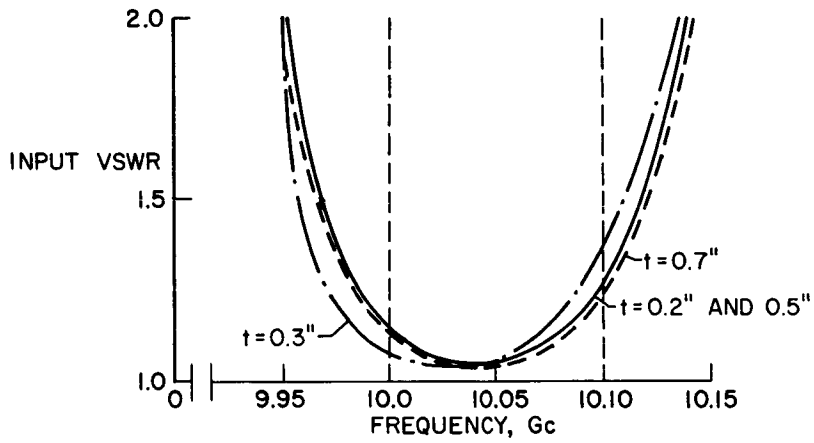


Figure 7

RADIATION PATTERNS

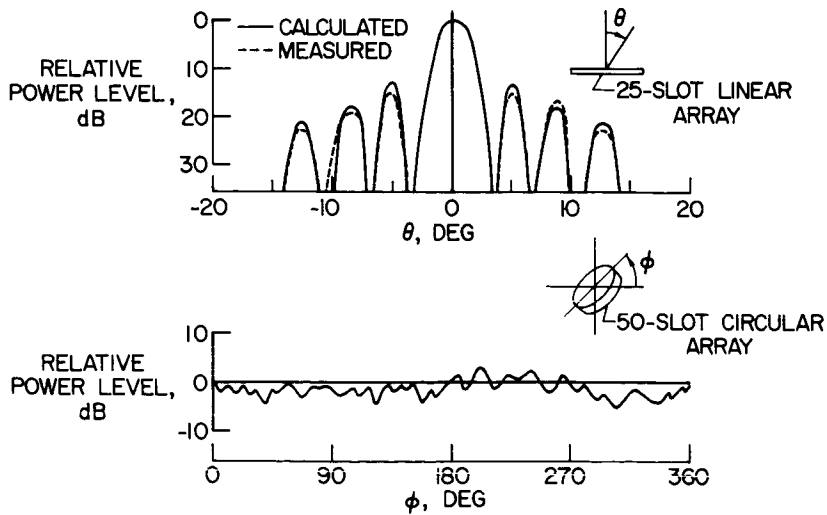


Figure 8

[REDACTED]

12. INVESTIGATION OF THE RADIO BLACKOUT PROBLEM
IN A PLASMA-SHEATH SIMULATION FACILITY

By J. Kenrick Hughes
Langley Research Center

12

SUMMARY

A technique is described wherein ionized exhausts from solid-propellant rocket motors are used to simulate reentry plasmas. The paper outlines the test facility and experimental procedures, and presents data obtained in tests performed to evaluate possible solutions to the radio blackout problem such as the use of the static magnetic field, material addition to the flow field, and a dielectric-filled slot in the plasma.

INTRODUCTION

In a program with the objectives of investigating the effects of reentry plasmas on electromagnetic propagation and evaluating possible solutions to the radio blackout problem, there is no ideal substitute for carefully planned and successfully executed flight experiments.

Unfortunately, flight testing requires the expenditure of considerable time, effort, and money. For this reason, it is highly desirable to have a technique by means of which each proposed flight experiment can first be proved in a laboratory facility under simulated reentry conditions.

The usual sources of plasmas, all of which have been utilized at the Langley Research Center, are glow discharge tubes, direct-current and radio-frequency arcs, alkali-seeded flames, shock tubes, and hypervelocity tunnels. Invaluable as they are, these techniques do not lend themselves to full-scale model testing.

There is another source of plasma - the high-temperature exhaust gases produced during rocket-propellant burning. It is well known (ref. 1) that rocket exhausts interfere with electromagnetic propagation, a fact which in itself is of great concern to some investigators. On the other hand, such a plasma has merit as a research tool, even though its characteristics may never be known precisely. In the experiments to be described, the technique consists simply of immersing a test model in the exhaust of a solid-propellant rocket motor.

Since it is desirable to have some knowledge of conditions in the exhaust for comparison of theoretical computations and experimental results, a concurrent program was undertaken in which microwave diagnostics were employed in an attempt to obtain representative numbers for electron concentration and collision frequency. This is the program discussed in paper no. 7 by W. L. Jones.

[REDACTED]

The results of this work indicate an electron density of $3 \times 10^{10}/\text{cm}^3$ and a collision frequency of $4.4 \times 10^8/\text{sec}$ in the region of interest, that is, the slot antenna of the model.

TEST SETUP

To perform the tests at simulated altitude, a vacuum sphere, 60 feet in diameter, is used. Although this facility has a minimum pressure capability of 10^{-4} mm Hg, most tests are carried out at 10^{-1} mm Hg, corresponding to an altitude of 200,000 feet. Of particular interest is the precaution that is taken to ensure that reflections do not interfere with signal-strength measurements. This precaution is made by enclosing the whole experiment in an anechoic chamber. Figure 1 shows the relative sizes of the test chamber and the sphere. Because of the enormous volume of the sphere and the low propellant mass flow, the sphere pressure is not seriously affected.

Figure 2 illustrates the chamber in more detail. It is constructed of carbon-loaded urethane foam, a radio-frequency absorber. At 244 mc, this material gives an attenuation of 28 decibels at normal incidence. The model is suspended nose down from an insulated frame, and the rocket is aligned to fire upward. Crossed dipoles are used to detect horizontal and vertical components of the electric field, and these signals are fed to separate telemetry receivers. The automatic gain control (AGC) voltages of the receivers are recorded on magnetic tape. In general, the signal strengths as recorded for the different antennas are found to be almost identical. For this reason, only the record from the antenna labeled "A," being representative, is shown in following figures.

ROCKET MOTORS

The rocket motors contain 2 pounds of double-base propellant with an aluminum content of 20 percent. Nozzle throat diameter is 0.232 inch and the exit diameter is 0.70 inch. The chamber pressure is 500 psi, and the temperature $6,000^\circ$ F. The rockets produce a thrust of 100 pounds for 10 to 15 seconds, with an exit Mach number of 5. Because of the low sphere pressure, exhaust gas expansion is very rapid, and the Mach number in the vicinity of the model is about 10.

TEST MODEL

The completely self-contained test model shown in figure 3 is constructed of inconel with a copper nose. It is a 9° half-angle cone, with a 2-inch-diameter hemisphere nose and a 9-inch-diameter cylindrical afterbody. The transistorized FM/AM telemetry transmitter delivers 7 milliwatts at 244 mc. Radiation is from a longitudinal slot on the conical section. The model can be rotated, if desired, to check antenna-radiation patterns. This basic model is modified to suit a particular experiment.

[REDACTED]

PRELIMINARY INVESTIGATIONS

Before running ground checks on flight experiments, it was logical to gain some assurance that the simulated reentry plasma would provide significant signal loss. Other than the plasma parameters, the answers to two main questions were desired - how much attenuation could be expected and what region of the exhaust made the greatest contribution to the attenuation. The answer to the first question was obtained readily. A series of motors was fired and the signal loss was measured at 244 mc. The results were very encouraging. While individual motors gave considerable variation, the average signal loss was about 35 decibels.

With respect to the second question, photographs generally show an ill-defined plume, with a central cone of high luminosity, as shown in figure 4. Intuitively, it was suspected that the attenuation was caused by this part of the exhaust. To verify this, a test, popularly called the "rocking rocket" was tried. In this test, a motor was mounted so that it could be swung, once per second, through an arc of $\pm 30^\circ$. The test model was used; the transmission frequency was 244 mc. A typical sweep is shown in figure 5, where the attenuation is shown plotted against motor-tilt angle.

The first point to note is the sharpness of the curve, which shows that most of the signal loss takes place over a small angular displacement. The second interesting fact is that maximum attenuation does not occur when the model and motor axes are aligned, but takes place when the motor is tilted between 2° and 3° toward the antenna side. The question arises - is this a consequence of accumulated errors in motor alignment, angle calibration, and nozzle machining. It is believed that the measurements were accurately carried out. A suggested explanation is that the effect is one of simply varying the thickness of the ionized layer over the antenna.

PRIME EXPERIMENTS

Experiment I - The Use of the Static Magnetic Field

The purpose of this experiment was to evaluate the concept of electron immobilization by means of a static magnetic field oriented in the direction of wave propagation. While the idea is not radically new, in recent years Hodara (ref. 2) and others have given it extensive theoretical treatment prior to suggesting its use on reentry vehicles.

For the test, the model was adapted as shown in figure 6. A magnetic-field assembly was constructed and installed behind the slot antenna. The winding consisted of eight 50-turn coils connected in a series-parallel arrangement. The current through each coil was 75 amperes. The total current of 300 amperes was supplied by silver cell batteries. The resulting 30,000 ampere-turns produced a flux density of 750 gauss at the surface of the slot. To delineate its effects, the field was pulsed on and off one and one half times

CONFIDENTIAL

per second, and operation was monitored by telemetering the switching relay current.

The signal-strength record is shown in figure 7. Obviously, the motor used in this test was unusually hot, giving a signal drop of 60 decibels, and a noisy trace as evidenced by the noise spikes. Signal recovery is definite and amounts to about 20 decibels.

Experiment II - The Use of Material Addition

These tests were conceived to evaluate the effect of material addition to an ionized flow field. The nose cone was modified as shown in figure 8. There were two nozzles located 180° apart just aft of the stagnation point, each of which could be replaced with a plug. Each nozzle contained seven, 0.015-inch-diameter orifices. The accumulator, with a volume of 55 cubic inches (910 cc) was pressurized by nitrogen gas at 300 psi. Pulsed flow could be obtained by opening and closing the solenoid valve. Originally, the valve was located back in the canister, but the 24 inches of line between it and the nozzles resulted in a dribble effect due to line bleed. Moving the valve to the nose reduced this problem, but did not eliminate it as is apparent in the figures. A variable flow could be achieved by means of the motor-driven needle valve. As the valve opening was made increasingly larger, each successive pulse contained a larger amount of additive. For fixed flow the needle valve was set in one position. A turbine flow meter monitored flow rate.

A discussion of all the variations tried, such as fixing the model, rotating the model, fixing the flow, and varying the flow are not included herein. Only two tests, considered representative, are given.

Experiment II-A.- In figure 9, signal-strength records are shown for the test in which the additive was water. Water was chosen because its high thermal capacity makes it an excellent coolant. Evaporation requires 1,000 Btu/lb, and hydrogen-oxygen dissociation requires 17,000 Btu/lb.

The model was not rotated in this experiment. Water-on time was 0.40 second, off time was 1.5 seconds. Injection was from both sides of the model. The burning time was 14 seconds, giving a total propellant mass flow for 2 pounds of propellant of 0.143 lb/sec. A close look at the pulses discloses that signal recovery begins immediately with the onset of the water and that full recovery of 20 decibels is obtained when the water-flow rate is 0.01 lb/sec. Compared with the propellant flow, the water flow is about 7 percent. It can be seen from figure 9 that the water flow does not cut off immediately with the closing of the valve. One other fact to note from these curves is that once a critical amount of water is reached, larger amounts have no appreciable effect.

Experiment II-B.- For this experiment all test conditions were the same as for the previous one, with the exception that freon was used in place of water. Freon was tried because two of its constituents, chlorine and fluorine, are in the halogen family and are electrophilic.

[REDACTED]

As shown in figure 10, the signal-strength records are almost identical to those for water. For the particular conditions under which the experiment was performed, there is no significant difference to indicate the superiority of one material over the other. For another set of conditions, of course, this may not necessarily be true.

Experiment III - The Use of a Dielectric Fin

The previous tests had one similarity. Whether the method was by magnetic field or material addition, the effect appeared to be one of creating a window in the plasma. As the next step, it was logical to consider creating a window by placing a dielectric fin over the antenna. This was a faired slab 12 inches long, 4 inches high, and thick enough to cover the antenna, and was installed as shown in figure 11. Naturally, it would have been preferable to wait until full signal loss was established, and then install the fin. This procedure, of course, was impossible; the fin had to be in place before firing. However, on the basis of experience, maximum signal loss always occurred at maximum motor-chamber pressure. Therefore, it was only necessary to monitor chamber pressure, and an instant after maximum was reached, eject the fin by means of the solenoid-operated release mechanism. Signal-strength records are shown in figure 12. Note that there is no attenuation, even at the maximum pressure point, until the instant of fin ejection. The experiment was repeated with the fin on the side of the model opposite to the antenna and the results were substantially the same. The interpretation of this phenomenon is not clear and further investigation is suggested along this line.

CONCLUDING REMARKS

Utilization of a rocket exhaust as a plasma simulator has certain disadvantages. One is never quite sure of its characteristics. No two motors can be expected to give identical results. The exhaust can be called a "dirty" plasma, consisting as it does of a complex mixture of gases and solid particles. On the other hand, its use has proved profitable as an indication of flight results. This is borne out by a recent flight test of the material-addition concept where substantially the same results were obtained. The flight results are the subject of paper no. 17 by William F. Cuddihy.

REFERENCES

1. Calcote, H. F., and Silla, H.: Radar Attenuation in Solid Propellant Rocket Exhausts. Bull. 18th Meeting, JANAF-ARPA-NASA Solid Propellant Group, Vol. III, June 1962, pp. 3-50.
2. Hodara, H.: The Use of Magnetic Fields in the Elimination of Re-Entry Blackout. Proc. IRE, vol. 49, no. 12, Dec., 1961, pp. 1825-1830.

RELATIVE SIZE OF SPHERE AND ANECHOIC CHAMBER

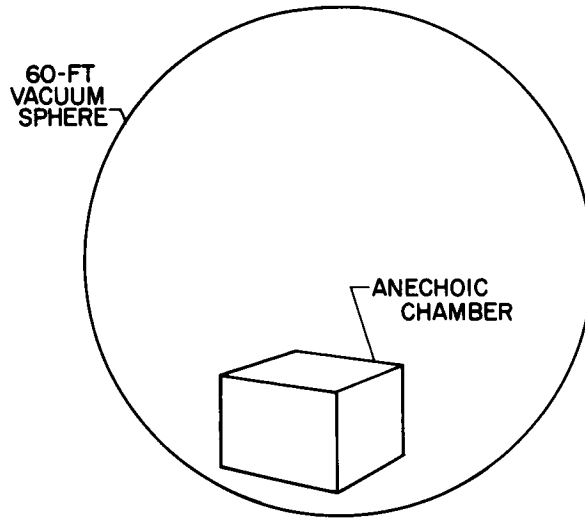


Figure 1

TEST MODEL IN THE ANECHOIC CHAMBER

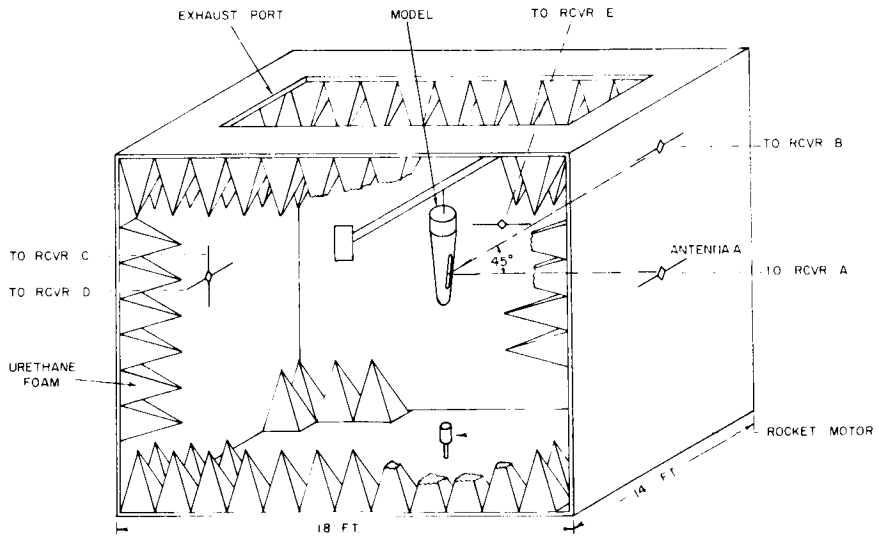


Figure 2

[REDACTED]

DECLASSIFIED

BASIC MODEL USED IN EXPERIMENTS

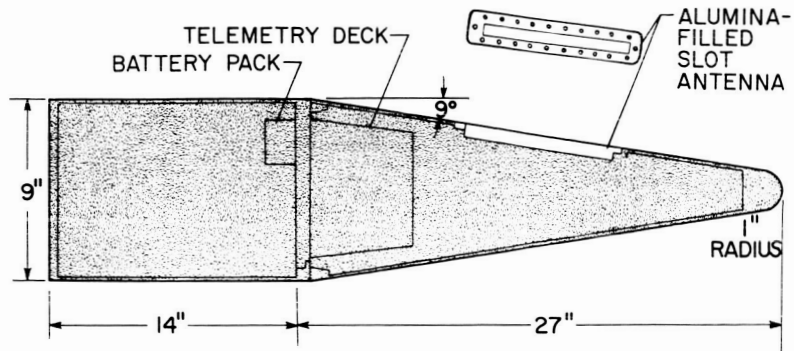


Figure 3

ROCKET EXHAUST FLOWING OVER MODEL

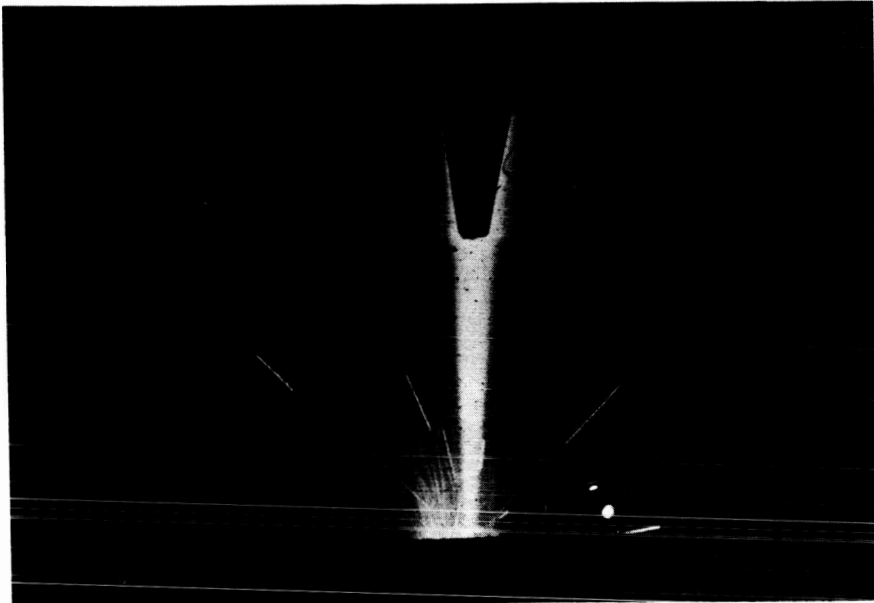


Figure 4

L-2176-4

[REDACTED]

03 17 20 10 30

VARIATION OF SIGNAL WITH ROCKET-MOTOR TILT ANGLE

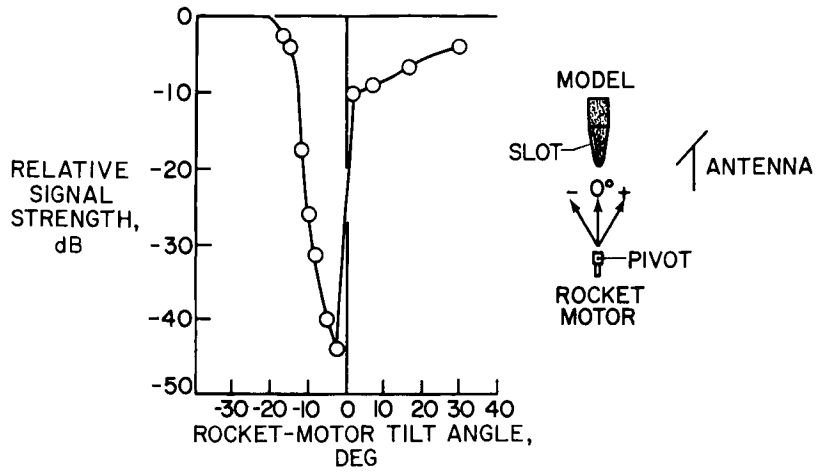


Figure 5

MODEL MODIFIED FOR STATIC MAGNETIC-FIELD TEST

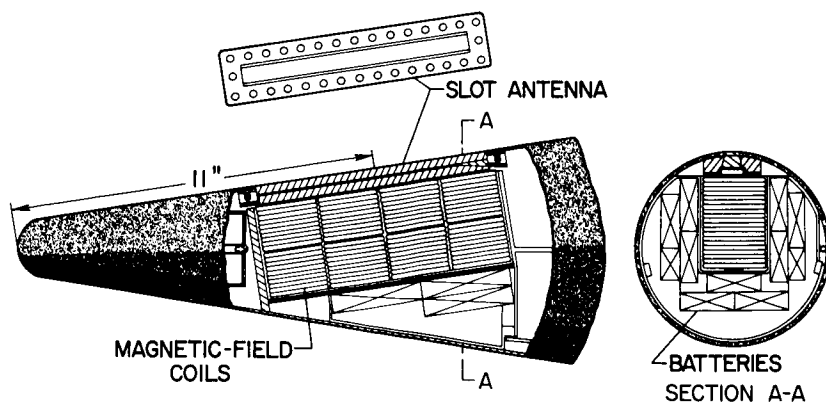


Figure 6

[REDACTED]

DECLASSIFIED

SIGNAL-STRENGTH RECORDS FOR STATIC MAGNETIC-FIELD TEST

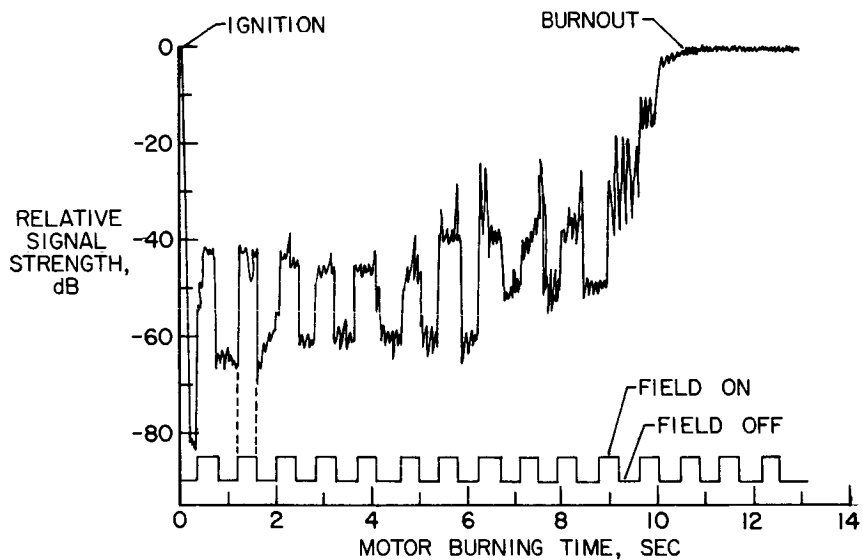


Figure 7

MODEL MODIFIED FOR MATERIAL-ADDITION TEST

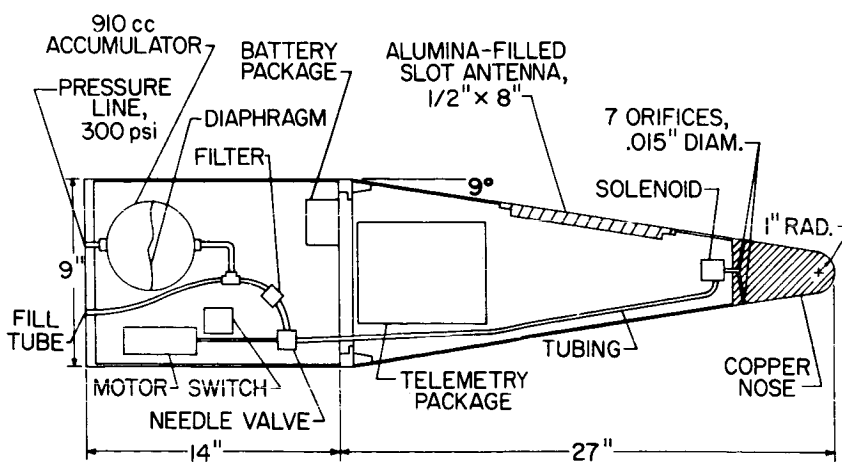


Figure 8

[REDACTED]

0 1 2 3 4 5 6 7 8 9 0

SIGNAL-STRENGTH RECORDS FOR WATER-INJECTION TEST

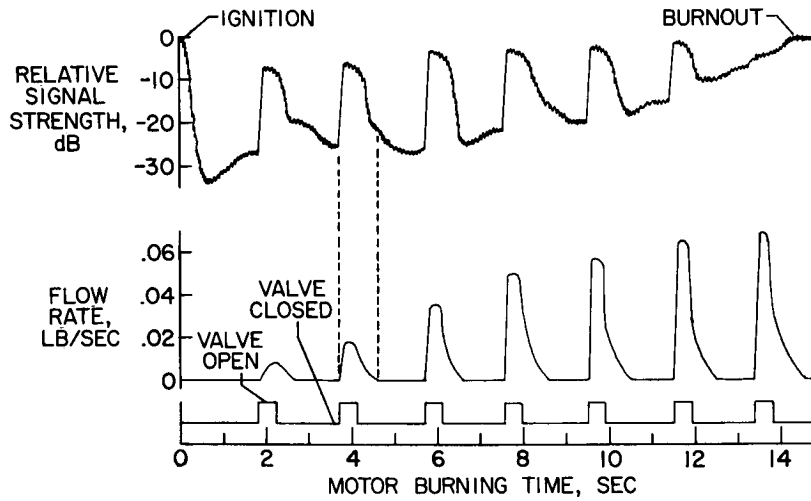


Figure 9

SIGNAL-STRENGTH RECORDS FOR FREON TEST

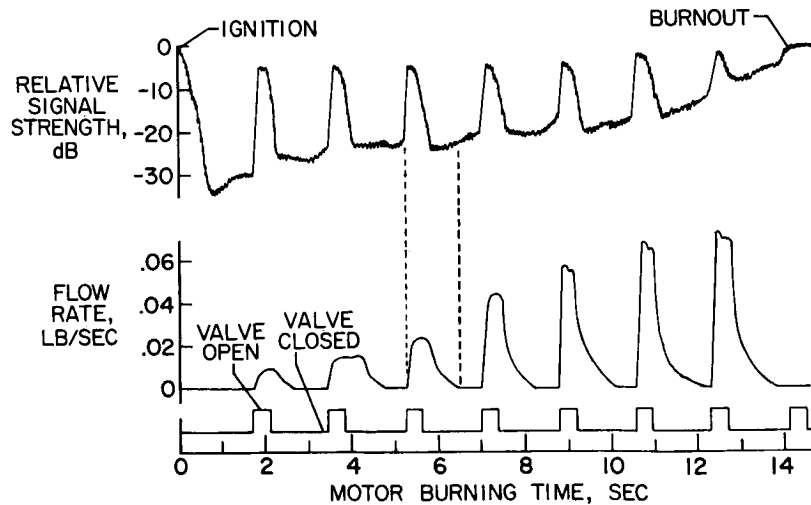


Figure 10

[REDACTED]

DECLASSIFIED

MODEL MODIFIED FOR DIELECTRIC-FIN TEST

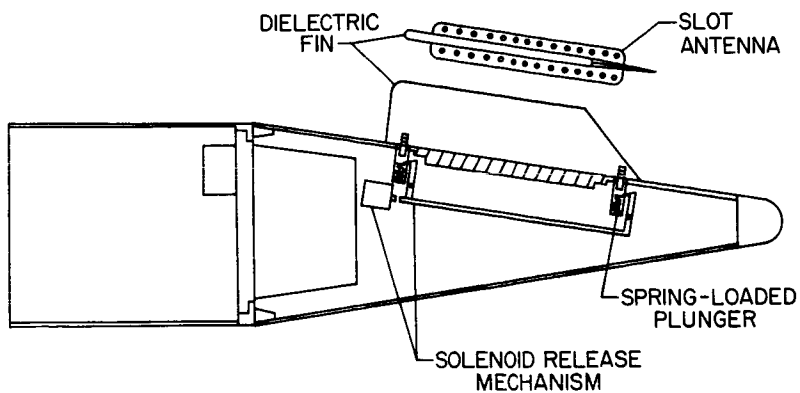


Figure 11

SIGNAL-STRENGTH RECORDS FOR DIELECTRIC-FIN TEST

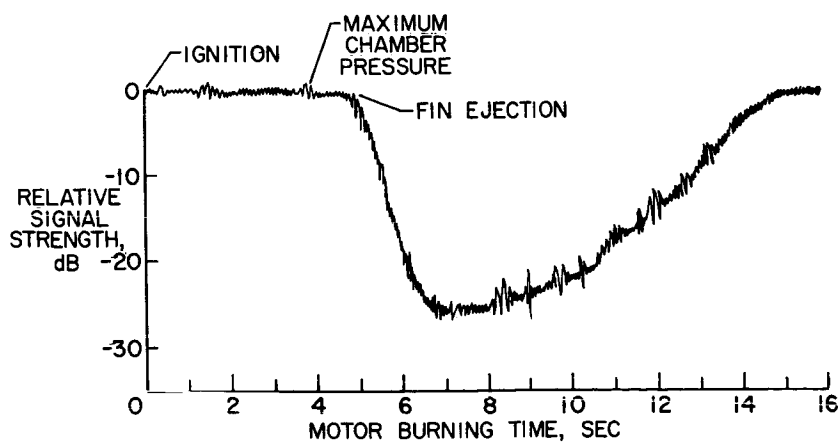


Figure 12

[REDACTED]

13. SUMMARY OF RADIO-FREQUENCY FLAME EFFECTS ON
MARSHALL SPACE FLIGHT CENTER VEHICLES

By J. W. Harper and Olen P. Ely
George C. Marshall Space Flight Center

SUMMARY

The effects of ionized exhaust gases on radio transmission have been studied for several years by rocket development personnel who are now located at the George C. Marshall Space Flight Center (MSFC). It has been observed that the magnitude of the flame effects is highly dependent on various flight conditions, widely varied values of attenuation being experienced for different flights and ground stations. Although much theoretical work has been done, no method has been developed for accurately predicting these effects. Most of the results available are based solely on experimental results. This paper describes the flame effects which have been observed during the firings of several rocket vehicles developed at the Marshall Center, with particular emphasis on the Saturn launch vehicles.

Signal-strength data during flight have been derived from automatic-gain-control recordings at the ground receivers at various locations. Flame effects have been extracted from these records, and comparisons have been made to determine the effects of look angles, altitude, frequency, fuel type, and thrust on the signal strength.

INTRODUCTION

Tail-flame attenuation, retro-rocket effects, and pyrotechnic-flare effects have been observed throughout the development programs of the Redstone, Jupiter, Jupiter C, Juno II, and Saturn I. In some cases, these ionized gas effects on radio transmission have been rather severe, resulting in some loss or degradation of the data. In other cases, the effects have been negligible. It has long been evident that several factors are involved in the phenomenon, and wide variations in flame effects may be experienced with various combinations of flight parameters. Unfortunately, it is not normally possible to control these parameters for the purpose of studying radio transmission effects, and it becomes difficult to analyze the part which each parameter plays in the overall effect. An analysis of aspect-angle dependence was hampered in early programs by the small number of ground receiving sites available. Throughout the rocket development programs, the accuracy of attenuation measurements has been degraded by receiver automatic-gain-control (AGC) characteristics, by inaccurate calibration, and by a lack of polarization information. Within these limitations, attenuation data have been extracted from ground station AGC recordings and related to vehicle altitude, aspect angles, flame shape, and other factors.

[REDACTED]

As early as 1950, effects of rocket exhausts on radio propagation was observed in the V-2 firings at White Sands Proving Grounds. At that time a water-alcohol fuel mixture was used, and sodium compounds in the water were suspected of causing the attenuation. Distilled water was then used, with some apparent improvement in reception. However, no firm conclusions were drawn as a result of the experiment.

JUPITER AND JUNO II RESULTS

Attenuation measurements from firings of the Jupiter and Juno II rockets were taken from two ground receiving sites: Hangar D at Cape Kennedy and the telemetry receiving station at Grand Bahama Island (GBI). Attenuation values are shown in table I for the Jupiter and Juno II rockets. Juno II was a satellite launcher that used a Jupiter first stage; therefore the flame effects of the two vehicles are comparable. The attenuation measurements shown are measured at the instant of engine cutoff and are not necessarily the maximum values encountered; however, in nearly all cases attenuation was maximum at cutoff.

Aspect-angle dependence is illustrated in figure 1, in which attenuation at engine cutoff is plotted against aspect angle for 20 firings of the Jupiter and Juno II rockets. Factors other than aspect angle are different for the various firings. This fact illustrates the difficulty of isolating a particular variable. Although a scarcity of points exists for intermediate angles, the following facts are evident:

- (1) Highest attenuation occurs at small values of aspect angle.
- (2) A wide dispersion of values exists for given values of aspect angles, apparently caused by variations in altitude and other parameters.
- (3) Attenuation values decrease with increasing angle but extend in some cases beyond 100° of aspect angle.

Engine cutoff occurred at altitudes varying from 56 to 186 km, but for most of the firings cutoff occurred at approximately 110 km. When attenuation values for this altitude and an approximately constant aspect angle are compared for several firings, a considerable dispersion exists; thus, it appears that some other factor is strongly affecting the transmission. Antenna pattern difference is suspected as a significant factor, but insufficient data exist to support any definite conclusion.

Juno II vehicles carried four retro-rockets on the first stage. These rockets were fired at separation to prevent contact between the first stage and the upper stages. Although they were comparatively small and were located about 9 meters from the antennas, the rockets, when fired, produced an attenuation at the Cape stations from 20 to 40 dB in the very high-frequency (VHF) telemetry signal strength.

Retro-rocket attenuation was also severe at GBI, although, in one firing (AM-19C), the rocket flame produced an 8-dB increase in signal strength; this

[REDACTED]

increase indicated strong reflections from the flame. This result suggests that much of the attenuation experienced is produced by reflection (or perhaps refraction) rather than by absorption.

HISTORY OF FLAME EFFECTS ON SATURN

At this writing, four Saturn boosters have been launched successfully from Cape Kennedy. All onboard radio-frequency (RF) systems, except a C-band radar beacon on the third launch, have operated satisfactorily on each of the missions. All the RF equipment has experienced problems caused by flame attenuation and modulation of the signal as it passed through the flame. However, the signal level was always sufficient to construct an accurate trajectory and to give uninterrupted telemetry data.

Flame interference may be divided into two classes - interference caused by liquid-fuel engine exhaust flame and interference caused by the solid-fuel retro-rockets - and each one is discussed in detail. As a rule, the solid fuel usually caused the greatest problems.

The Cape Telemetry 2 station has been able to receive uninterrupted telemetry data on all flights. This fact can probably be attributed to the use of a high-gain 60-foot TLM-18 antenna. Some tracking systems have experienced periods of interruption.

SATURN ONBOARD EQUIPMENT

The onboard RF equipment flown on Saturn may be divided into four categories: telemetry, tracking, command, and antennas. A description of these systems is given in table II. Typical antenna patterns may be seen in figure 2.

Figures 3(a) and 3(b) show the locations of this equipment on the vehicles. Beginning with the block II series of vehicles (SA-5 to SA-10), the telemetry equipment is to be located in the S-I stage, the S-IV stage, and the Instrument Unit. All tracking equipment is in the Instrument Unit. Each live stage will carry its own command-destruct system, and beginning with SA-6 the Instrument Unit will carry a digital command system. Each stage will carry its own antennas. Figures 4 and 5 are typical of the block II configuration.

The equipment carried on the block I vehicles covered a very wide frequency band. The VHF telemetry system operated in the frequency band between 240 and 260 MHz. The command system operated in the range from 400 to 410 MHz. The UDOP signal was transmitted at 450 MHz and received at 900 MHz. The radar altimeter operated at 1610 MHz, the ultra-high-frequency (UHF) telemetry link at 2287 MHz, the S-band radar at 2900 MHz, the Azusa tracking system at 5000 MHz, the C-band radar at 5580 MHz, and the Mistram tracking system at 8216 MHz. The Azusa system, the Mistram system, and some of the UDOP stations used phase-locked ground receivers.

[REDACTED]

LOCATIONS OF GROUND STATIONS

Locations of the ground stations are shown in figures 6 and 7. Figure 6 represents the launch pad and the main tracking stations at Cape Kennedy, and figure 7 represents the stations on the coast of Florida and on GBI. Several of these stations were used for studying the flame characteristics only. The data gathered to date indicate that flame attenuation caused by the S-I stage is limited to a region within 30 and 35 km of the launch site.

Figure 7 also shows the ground projection of the trajectory flown by a typical vehicle. Each vehicle was flown at an azimuth of 100° east of north. The altitude at inboard-engine cutoff varied from 45.2 km on SA-4 to 60 km on SA-3.

VEHICLE CHARACTERISTICS

Each of the four vehicles created a thrust of approximately 5.78 million newtons (1.3 million pounds). Fuel for the main engine consisted of liquid oxygen and RP-1 (kerosene). All eight engines operated as planned on each of the four vehicles. The normal operating sequence is to cut off the four inboard engines and, approximately 8 seconds later, to cut off the four outboard engines. This sequence was used in all cases except for SA-4 when the number five inboard engine was cut off at 100 seconds to check the guidance system in the event of an engine malfunction on a future flight.

No separation occurred between the S-I stage and the inert S-IV stage on any of the flights. However, retro-rockets were fired on the third and fourth flights. The block I series used four solid-fuel retro-rockets equally spaced around the vehicle. Each retro-rocket burned for approximately 2 seconds.

FLAME EFFECTS ON TELEMETRY SYSTEMS

VHF Telemetry

More information is available on VHF telemetry than on any other system because more telemetry stations than tracking stations are available, and because the AGC response of the telemetry receivers is better than that for most tracking systems.

Flame attenuation caused by ionized gases from the liquid-fuel engines is discussed first. Figure 8 represents a typical AGC record made at the Cape Telemetry 2 station during the time the signal was experiencing flame attenuation.

Figure 9 shows a similar AGC recording before and after the noise caused by the flame has been removed. Since the AGC response of a receiver is a non-linear function of the input, the AGC voltage as a function of signal strength

[REDACTED]

must be linearized before it can be filtered. This process was accomplished by means of a special analog-computer technique. Most of the data presented in this report were derived by using this technique.

A sufficient amount of data has been analyzed to show that the attenuation is dependent on the aspect angle. The VHF telemetry signal is affected by the flame when this angle is approximately 16° or less from the roll axis of the vehicle. Figure 10 is a curve of attenuation plotted against aspect angle; the data were obtained from telemetry information gathered at the Cape Telemetry 2 and Cape Telemetry 3 stations during the four Saturn firings. The curve was obtained from a least-squares fit of measured values.

Figure 11 is a curve of attenuation plotted against altitude for the first four vehicles measured at the Cape Telemetry 2 and the Cape Telemetry 3 stations. The dependence of the aspect angle is borne out again by the fact that SA-4 experienced attenuation at lower altitude than the other vehicles. Figure 12 shows that the aspect angle for SA-4 was less than for the other three vehicles. This angle dependence is also evident from the data received at the Cape Telemetry 3 station on SA-2. Figure 11 shows that the signal was attenuated later in flight and that the attenuation was less than for the Cape Telemetry 2 station.

The magnitude of the attenuation of the VHF telemetry signal varies from no attenuation to approximately 30 dB, depending on aspect angle and altitude. Superimposed on the average signal level is a random fluctuation which modulates the signal as much as 20 to 25 dB, peak to peak. However, the signal margin is usually 20 dB for the worst case.

The relationship between attenuation and altitude is not clearly defined in figure 11 because of the different aspect angles involved. However, it is interesting to note that in some cases the attenuation had already begun to decrease before the first engine cutoff. On SA-3 the attenuation and noise modulation had completely ceased 2 seconds prior to the first engine cutoff. Figure 13 shows the linearized AGC from Cape Telemetry 2 station for this flight. The signal level began to increase very rapidly when the vehicle reached an altitude of approximately 55 km (180,000 ft) and was entirely normal prior to engine cutoff. This phenomenon was recorded at both the Cape Telemetry 2 and the Cape Telemetry 3 stations.

The stations up and down the coast of Florida (New Smyrna Beach, Patrick Air Force Base, Melbourne Beach, Vero Beach, and Jupiter Inlet) were chosen as locations in the study of flame effects at various aspect angles. The AGC records at the New Smyrna Beach station and the Vero Beach station showed some modulation on the SA-4 flight, but it has not been definitely decided if this was caused by flame since it appeared on only a few of the links and was at a lower frequency than flame modulation. The aspect angles were approximately 35° at New Smyrna Beach and 75° at Vero Beach at the time of the modulation.

The GBI station has always experienced aspect angles greater than 90° during powered flight and has never experienced flame attenuation from the main engine of a Saturn vehicle.

[REDACTED]

[REDACTED]

The experiment on SA-4 in which one of the inboard engines was cut off produced some interesting results. The cutoff was accompanied by a momentary increase in signal level of approximately 7 dB. This increase can be seen in figure 14, which is an AGC record made at the Cape Telemetry 2 station. Motion pictures show that the flame size decreased momentarily and then blossomed again. The decrease in attenuation was coincident with the decrease in the plume size.

The effects of ionized gases from the solid-fuel retro-rockets are in general more severe than the effects from the main engines. Figure 15 shows two typical AGC records made during the time of retro-rocket ignition, and figure 16 shows the same records after they have been linearized and filtered. Figures 17 and 18 show some typical curves of attenuation plotted against altitude for the retro-rockets. The attenuation from these retro-rockets varied from approximately 25 to 30 dB at the Cape stations to approximately 50 dB at some of the stations on the Florida coast, such as Vero Beach.

The data indicate that the attenuation from the retro-rockets is also somewhat dependent on aspect angles, but no definite relationship has been determined. Attenuation at the stations along the coast appeared greater than at the Cape stations.

Even though the attenuation has been very severe, the stations using the TLM-18 ground antenna system have not experienced any loss of data.

Another important fact is that location of the vehicle antenna does not necessarily solve the problem. On the SA-3 flight, all the VHF telemetry antennas except one were located forward of the retro-rockets. The antenna for link 10 was located aft of the retro-rockets, and the difference in attenuation was insignificant. On SA-4, all the VHF telemetry antennas were located aft of the retro-rockets, and the attenuation was more severe than on SA-3. However, there are data available on the UHF telemetry system that can be explained best by antenna location.

On both the SA-3 and the SA-4 flights, the retro-rockets used the same fuel and the burn time was approximately the same - just over 2 seconds in both cases. Figure 15 represents the AGC record at the Cape Telemetry 2 station for both flights. It can be seen that the flame effects lasted longer on the SA-4 flight than on the SA-3 flight. The effects on SA-3 lasted approximately 2 seconds and the effects on SA-4 lasted 5 seconds. The only difference in the two flights is that the SA-3 retro-rockets were fired at approximately 76 km (250,000 ft) and the SA-4 retro-rockets were fired at approximately 60 km (195,000 ft). It is doubtful that this longer duration was the result of antenna breakdown because it happened to all systems on the vehicle at frequencies ranging from 240 MHz to 8.2 GHz. In addition to the frequency difference, the onboard antennas were located at several different positions on the vehicle.

[REDACTED]

UHF Telemetry

The effects of the flame on the UHF telemetry system (2287 MHz) are not as well defined as the effects on the VHF telemetry system because of the low frequency response of the AGC system at the ground station. The AGC records from the SA-3 flight indicated that UHF telemetry might solve the problem of flame attenuation because hardly any flame attenuation from the main engines was seen in the records and the retro-rocket attenuation was less than that for the VHF links. However, noise in the data prompted an investigation of the amplitude-modulation (AM) input to the limiter stage of the ground receiver to investigate the receiver dynamic characteristics.

The results of this experiment showed that the input to the limiter was noisy at a time when the AGC indicated a condition 27 dB above the receiver threshold. An investigation of the frequency response of the AGC at this time indicated that the 3-dB frequency response of the system was 2 Hz. It was concluded that the data were being lost, not necessarily because of flame attenuation, but because the loop response of the AGC was too slow to follow the changes in the signal level during the period of flame attenuation.

The curves of attenuation plotted against altitude are shown in figure 19. The accuracy of these data is open to question. According to this record, the main-engine flame attenuation began later than it did at the Cape Telemetry 2 station, which is as it should be because of the difference in aspect angle. This station was located at the Mandy facility, which is several kilometers south of the Cape Telemetry 2 station.

The flame attenuation from the main engine was recorded as being 20 dB, whereas the retro-rocket attenuation was 37 dB. The large difference in the retro-rocket attenuation at this station and at some of the VHF telemetry stations may be partially accounted for by the difference in location of the antennas. The UHF antenna was located on the dummy spacecraft approximately 21 meters (69 ft) in front of the retro-rockets. Additional tests with an improved ground receiver would be required to make any definite conclusions about flame effects on this system.

FLAME EFFECTS ON TRACKING SYSTEMS

Descriptions of the tracking systems are given in table II. Each of these systems has experienced problems caused by the transmission of the signal through the flame. However, in most cases the main problem does not appear to be attenuation, but modulation of the signal. This problem is particularly troublesome to the Azusa and UDOP systems which are phase-locked systems. The Mistram system is also a phase-locked system; however, its first flight on SA-4 did not give much useful flame information because the aspect angle was too great for any main-engine flame to be observed.

Data from each of the four Saturn flights have been received at the Azusa MK II station located at the south end of the Cape. An analysis of the filtered AGC from the central receiving site has indicated that the signal in all cases was above the tracking threshold from lift-off to beyond powered flight. However, an analysis of the data failed to confirm this. The data from the first two flights were practically unusable until 60 seconds after launch. The data from SA-3 were unusable until 80 seconds. The data from the fourth flight improved so that they were usable at 25 to 30 seconds or sooner.

The reasons for this discrepancy in the data were studied, and some very interesting conclusions were drawn. A fast-response AGC record was made at this site and it showed that the signal level was actually fluctuating as much as 25 to 30 dB at a rate from 70 to 100 Hz. (A quantitative analysis of this record could not be made because it was only a strip chart. If the data had been on magnetic tape, they would have been more useful.)

These high-amplitude fluctuations were coincident with the times when the data were poor. The 2,000-Hz beat-frequency output, which is used to determine cosine data, was also erratic at this time. Both of these measurements were normal during the times of good data. When the aspect angle reached a point where flame attenuation would normally be expected, the high-speed AGC measurement and the beat-frequency output became noisy again and the quality of the data decreased. After main-engine cutoff and retro-rocket ignition, both of these measurements were smooth and the quality of the data was excellent again.

An investigation of the vehicle antenna pattern showed that the main lobe of the antenna was only 12° from the roll axis of the vehicle, and a major part of the main lobe actually passed through the flame. It was concluded that the effects were caused by multipath propagation off the flame. This conclusion was not reached until after the SA-4 flight. The SA-4 flew with the same type of vehicle antenna as did the three previous vehicles, yet the data were much better, even though the AGC records appeared no different from those of previous missions. A modification was made in the ground equipment between the SA-3 and SA-4 flights. The modification was a phase-locked filter servo that was added at the output of the 5-MHz coherent-carrier data channel. The servo effectively reduced the amount of frequency-modulation (FM) noise appearing at the output. Another result was the improvement of the threshold of the system by 20 dB. It can not be stated on the basis of this one test that this modification was the reason the data were better from the SA-4 flight than from previous missions, but this modification seems to provide the most logical explanation. Future Saturn flights probably will not verify this hypothesis because the antenna has been redesigned and relocated on the vehicle.

C-Band Radar

The C-band radar systems at the Cape and the Patrick Air Force Base (PAFB) stations have experienced signal attenuation during times of main-engine burn and retro-rocket ignition. The amount of attenuation cannot be defined precisely

[REDACTED]

because the AGC records available are limited to approximately 30 Hz and because the system seems consistently to experience excessively large pointing errors so that the measurement of the attenuation is indistinguishable from the effects of antenna searching. In many cases, the system used skin tracking during the periods of main-engine attenuation and retro-rocket ignition. The reason for switching to skin tracking was the undesirable tracking conditions in the beacon mode. However, these undesirable signals do not always reflect conditions caused by flame. Studies have proved that, during the times when flame attenuation would exist at the Cape station and the PAFB station, the signal is largely cross polarized with respect to the ground antenna.

One of the best comparisons available was on SA-1. The C-band radar system experienced approximately 7 dB of flame attenuation at the same time that a nearby VHF telemetry station was experiencing 20 dB of attenuation. The greatest problem with the signal strength at retro-rocket ignition seems to be noise in the AGC and not attenuation. On SA-4 the signal was not attenuated, but approximately 16 dB of noise was present in the signal at the Cape radar station. The PAFB station was skin tracking at this time. The results of retro-rocket ignition on the SA-3 flight probably would not be valid because the beacon was not operating properly at that time.

UDOP

The flame-attenuation data from the UDOP system have been of limited value because of the low frequency response of the ground receiver AGC at all stations except the Cape Mandy facility.

The Doppler data from many of the stations were unusable during certain periods of flight; yet, according to the AGC records the signal strength was 50 to 70 dB above the threshold of the receiver, and no noise was present in these records. This effect occurred during the times of expected flame interference at the Cape stations. However, the data from the downrange stations were also poor, although it was known that they were not receiving a signal through the flame. Reference to the telemetered AGC of the onboard transponder showed that the flame was attenuating and modulating the signal that was being transmitted to the vehicle from the Cape transmitter. Since the output of this system was dependent on the input, it was concluded that this was the problem affecting the downrange stations and that the Cape stations were actually experiencing two-way attenuation.

The Mandy station recorded AGC voltage and quadrature voltage on the SA-4 flight. Figure 20 shows that the quadrature voltage was several decibels below the AGC voltage during the times of both liquid-engine flame attenuation and solid-fuel retro-rocket attenuation. One possible reason for this difference could be that the flame phase modulated the signal and dispersed most of its energy into sidebands, and these sidebands were beyond the bandwidth of the quadrature detector. The fact that the signal is phase modulated by the flame could explain the unusable data during the times of flame interference. Additional tests will be made on future flights to reach a firm conclusion.

Only one Mistram transponder has been flown on a Saturn vehicle at the time of this writing. No evidence of flame interference from the main engines was present. However, this result was expected because the aspect angle was approximately 30° at outboard-engine cutoff. However, retro-rocket ignition caused the system to reach threshold; it took 15 seconds to recover completely. The reasons for this extended period of attenuation are unknown. The only conclusion about flame effects on this system is that 8216 MHz is not high enough in frequency to avoid the problem of flame attenuation.

COMMAND SYSTEMS

No extended studies have been made on flame interference to the command system. The only signal-strength record available is the telemetered AGC from the vehicle command receiver. Studies have shown that the signal transmitted to the vehicle is attenuated and noisy when the aspect angle reaches a low value during powered flight. Also, it is noisy and attenuated during retro-rocket firing. A fast response AGC would be required for a detailed analysis.

CONCLUDING REMARKS

Flame attenuation on the Saturn booster is a function of several variables. The most evident ones are fuel type, altitude, aspect angle, frequency, and antenna patterns. A sufficient amount of data have not been gathered to determine the degree of dependence on each variable.

Obtaining more complete signal-strength data is one of the first steps toward solving this problem. Necessary improvements include high-frequency-response measurements of signal strength, polarization component measurements, flame-modulation spectrum measurements, an ionization density profile of the flame, the relationship between antenna pattern and flame effects, additional information on fuel additives, and consistent calibration procedures at different stations. Much of the data available at present are questionable because of the lack of all or part of the information listed above. As an example, information could have been derived on signal strength as a function of the radio-frequency carrier if all systems had been capable of high-frequency signal-strength measurements.

Marshall Space Flight Center has taken steps to solve this problem in part. Special portable measuring facilities have been designed and will be operational for the next Saturn firing. These facilities will be capable of accurate high-frequency measurements of signal strength, and of measuring components of vertical, horizontal, right-circular, and left-circular polarization. Steps are also being taken to improve and obtain additional information from existing facilities.

[REDACTED]

DECLASSIFIED

TABLE I

ASPECT ANGLE AND ATTENUATION VALUES FOR JUPITER AND JUNO II FIRINGS

Vehicle	Cape Kennedy		Grand Bahama Island	
	Aspect angle, deg	Attenuation, dB	Aspect angle, deg	Attenuation, dB
Jupiter:				
AM-12	8.5	0	128	
AM-15	4.0	1	104	3
AM-17	3.3	14	77	0
AM-18	4.2	1 to 4	104	0 to 4
CM-21	4.4	8	104	0
CM-22	4.1	8	104	1
AM-24	4.2	5	95	0
AM-25	6.9	5	116	0
AM-26	9.3	3	121	0
AM-28	5.2	0	103	
AM-30	5.3	0	103	
CM-31	3.6	1	99	
AM-32	5.1	3	103	0
CM-33	5.3	3	103	0
Juno II:				
14	7.0	8	88	6
19	9.6	8	124	0
19A	9.6	20	57	
19C	25	10 to 40	83	0
19D	12	0	58	19
19F	10	15	63	9

[REDACTED]

03 15 20 25 30 35 40 45 50 55 60 65 70 75 80 85 90 95

TABLE II

RADIO-FREQUENCY EQUIPMENT ON SATURN I, BLOCK I VEHICLES

System	Ground receiver frequency	Antenna type
VHF telemetry	240 to 260 MHz	T-fed cavity slot (flush) Two-element array
UHF telemetry	2287 MHz	Waveguide aperture
Tracking: Azusa	5000 MHz	Surface wave
C-band radar	5580 MHz	Surface wave Waveguide aperture
Mistram	8216 MHz	Waveguide aperture
UDOP	900 MHz	Two-frequency cavity slot Folded monopole-phased pair
S-band radar	2900 MHz	Surface wave
Altimeter		Planar 16 slot Printed-circuit array
Command	400 to 410 MHz	Cavity slot Rectangular half-loop

[REDACTED]

SECRET

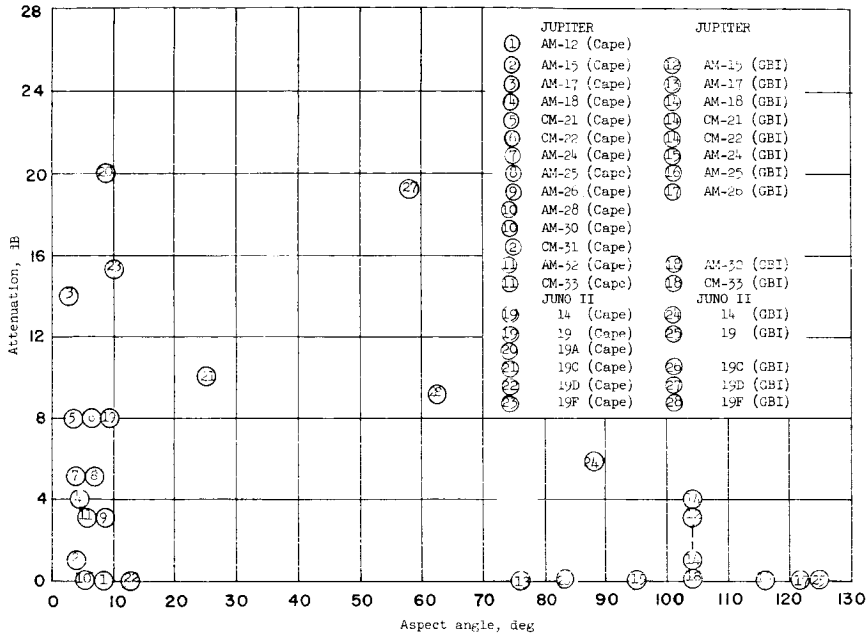


Figure 1.- Attenuation plotted against aspect angle at engine cutoff for 20 firings of Jupiter and Juno II rockets.

CONFIDENTIAL

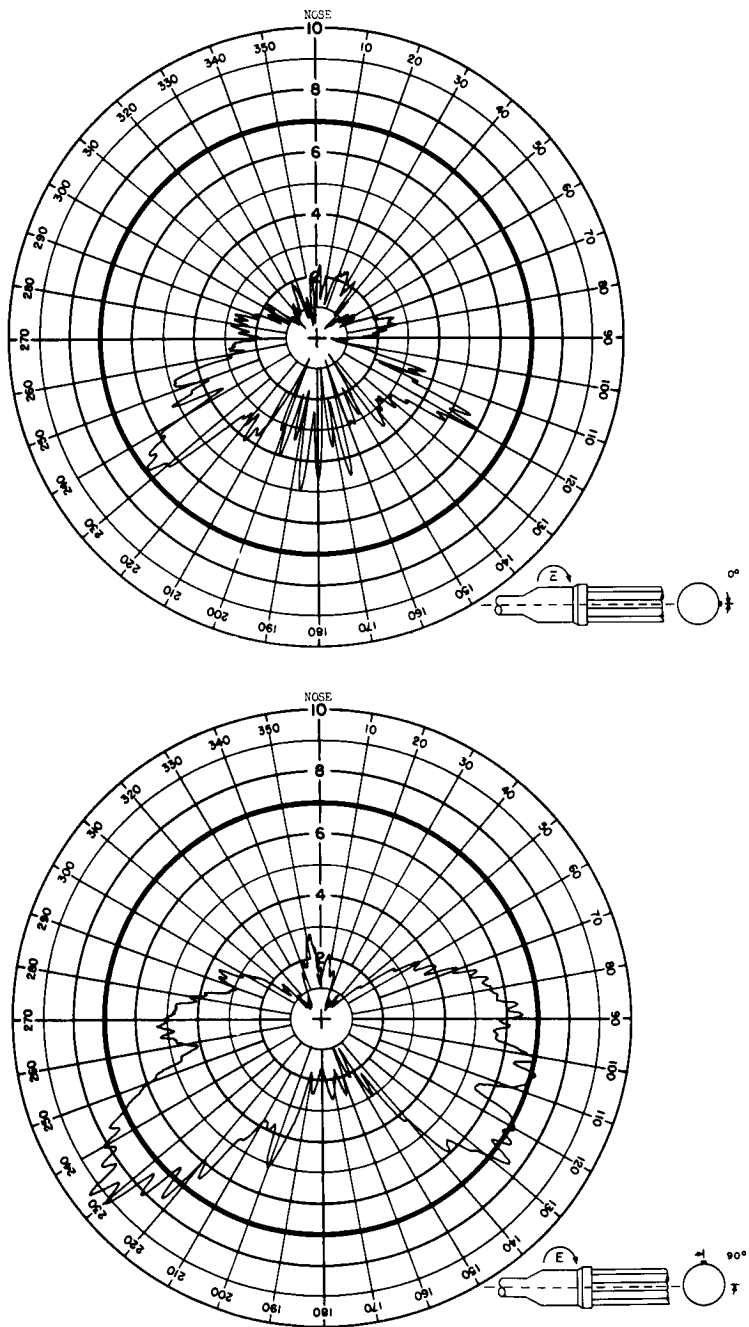
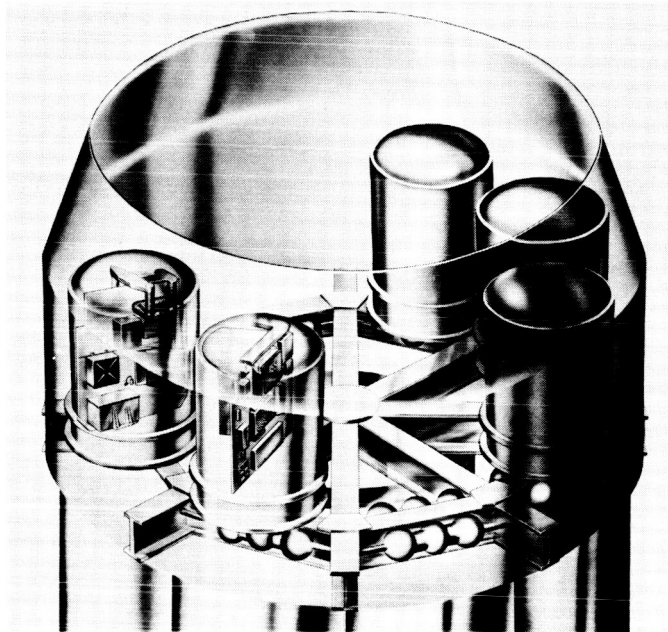


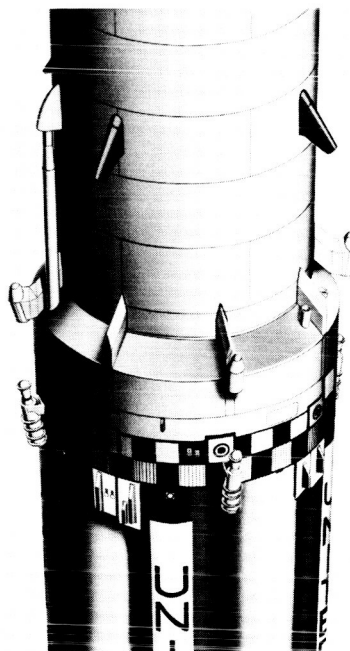
Figure 2.- Typical Saturn antenna patterns.

CONFIDENTIAL

DECLASSIFIED



(a) Equipment canisters.



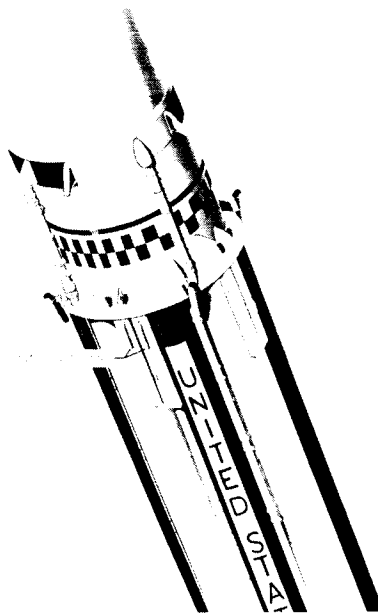
(b) Vehicle antennas and retro-rockets.

Figure 3.- Location of equipment on Saturn block I vehicle.

[REDACTED]
03 11 52 13 00



(a) Complete vehicle.



(b) Antenna configuration of S-I stage.

Figure 4.- Saturn block II vehicle.

[REDACTED]
DECLASSIFIED

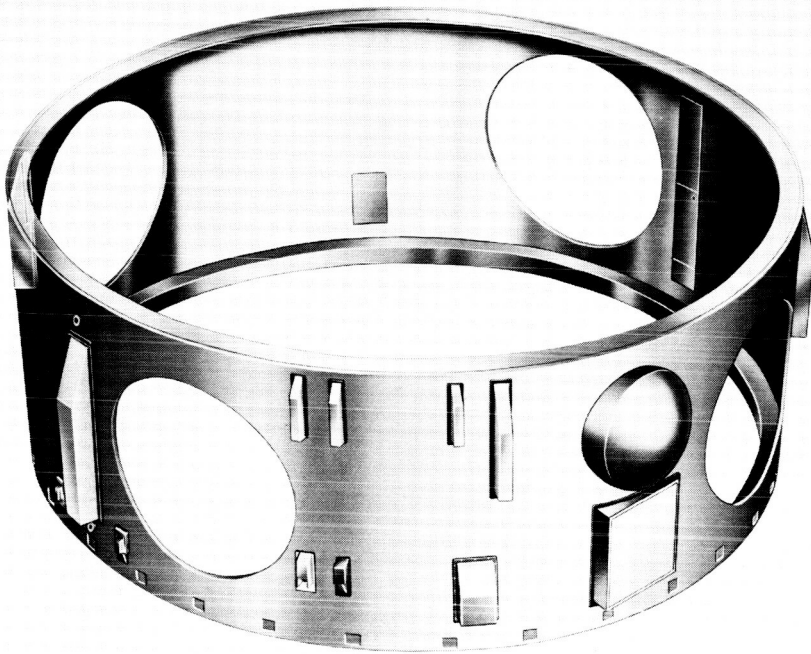


Figure 5.- Instrument-Unit antenna configuration of Saturn block II vehicle.

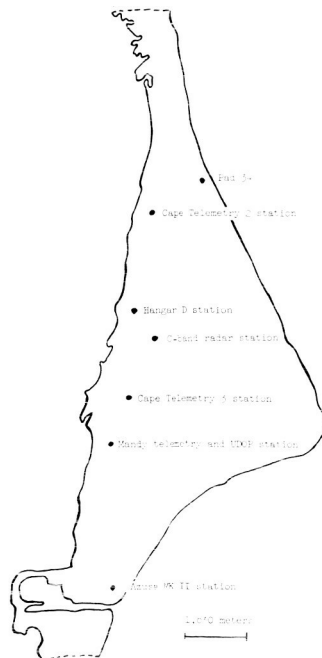


Figure 6.- Locations of Saturn ground receiving stations - Cape Kennedy area.

[REDACTED]

03750000

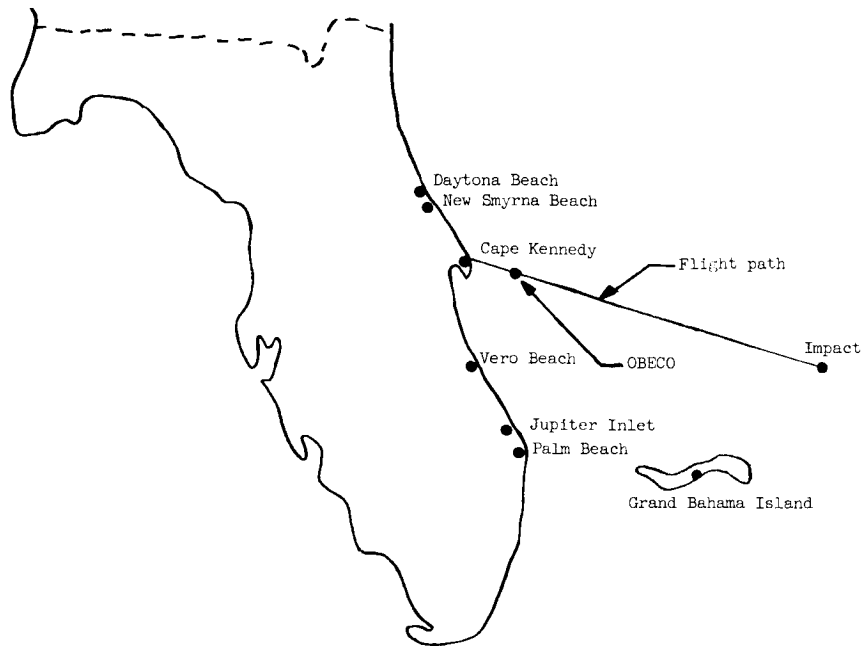


Figure 7.- Locations of Saturn ground receiving stations - Florida coast and Grand Bahama Island. (OBECO - outboard-engine cutoff.)

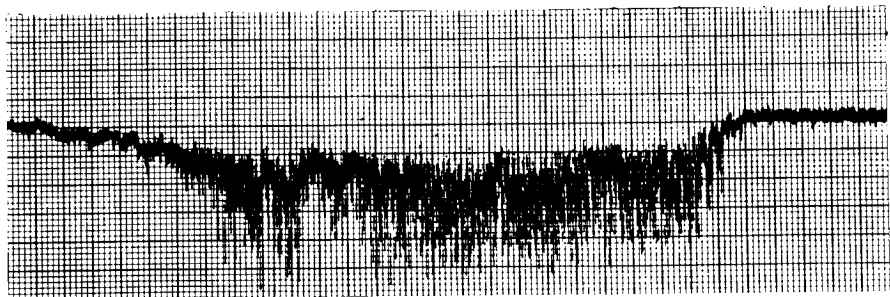


Figure 8.- Telemetry signal-strength (AGC) recording during flame attenuation period and retro-rocket ignition.

[REDACTED]

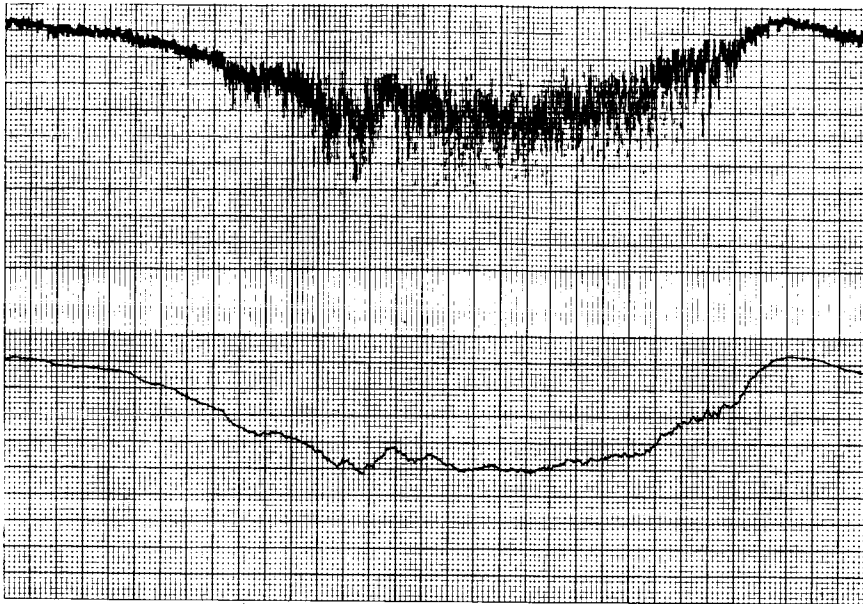


Figure 9.- Telemetry signal-strength (AGC) recording before and after linearizing and filtering.

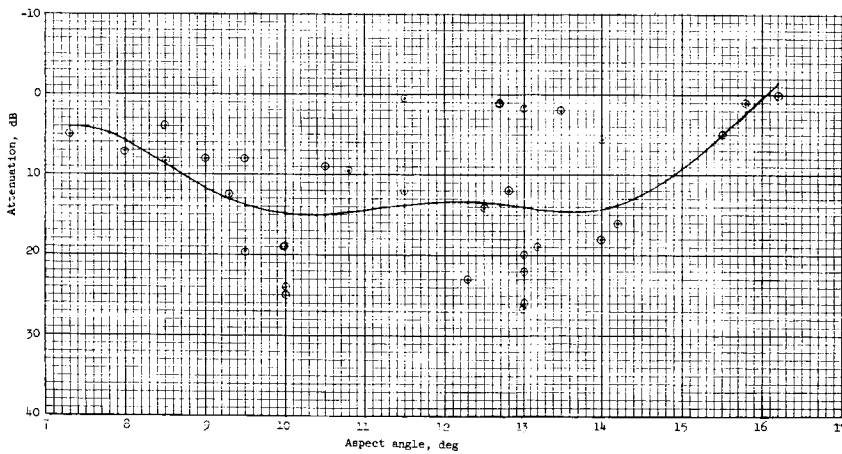


Figure 10.- Telemetry signal-strength attenuation plotted against aspect angle.

[REDACTED]

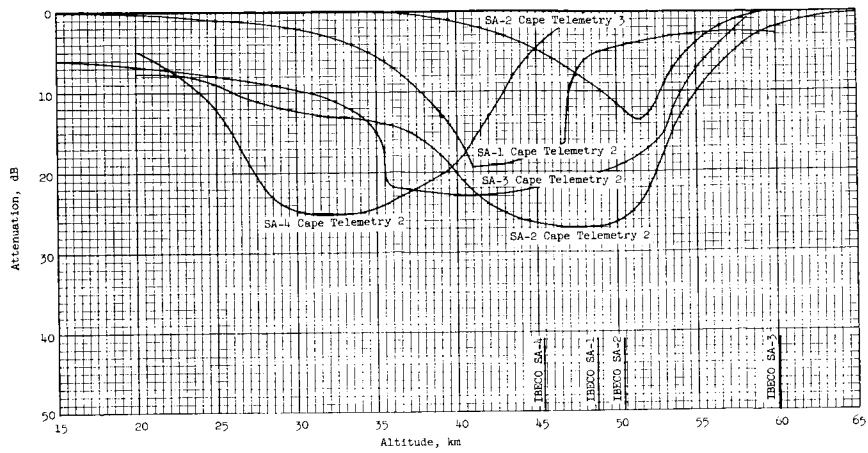


Figure 11.- Telemetry signal-strength attenuation plotted against altitude.
(IBECO - inboard-engine cutoff.)

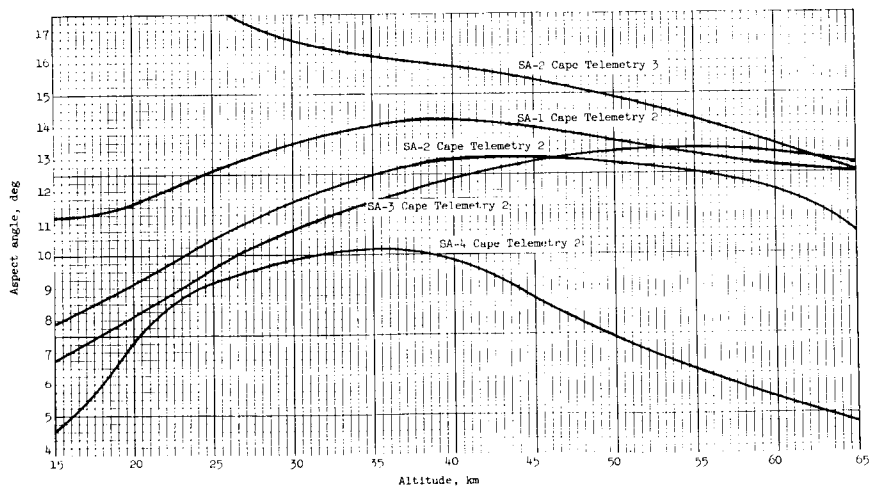


Figure 12.- Aspect angle as function of altitude.

[REDACTED]
DECLASSIFIED

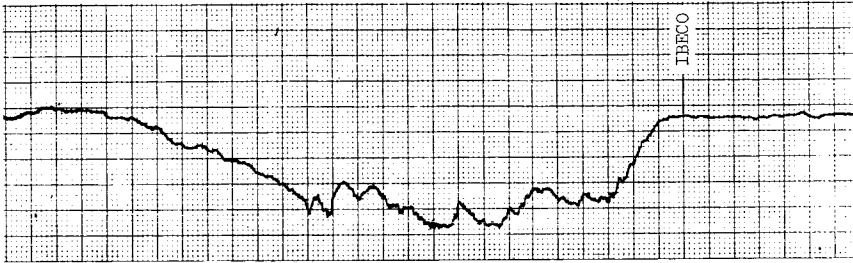


Figure 13.- SA-3 telemetry signal-strength (AGC) recording, linearized and filtered.

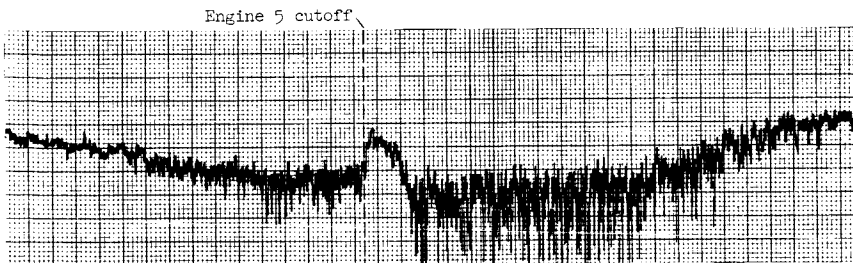


Figure 14.- SA-4 telemetry signal-strength (AGC) recording.

03702000

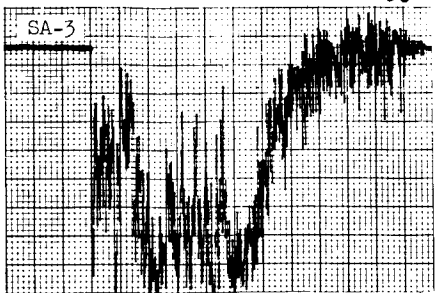


Figure 15.- Telemetry signal-strength (AGC) recordings showing comparison between SA-3 and SA-4 retro-rocket flame effects.

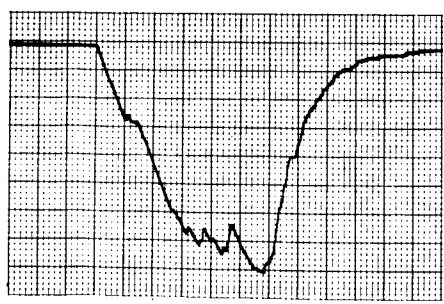
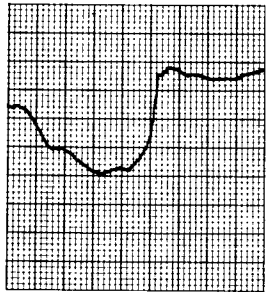


Figure 16.- Telemetry signal-strength (AGC) recording during retro-rocket ignition, linearized and filtered.

[Redacted]

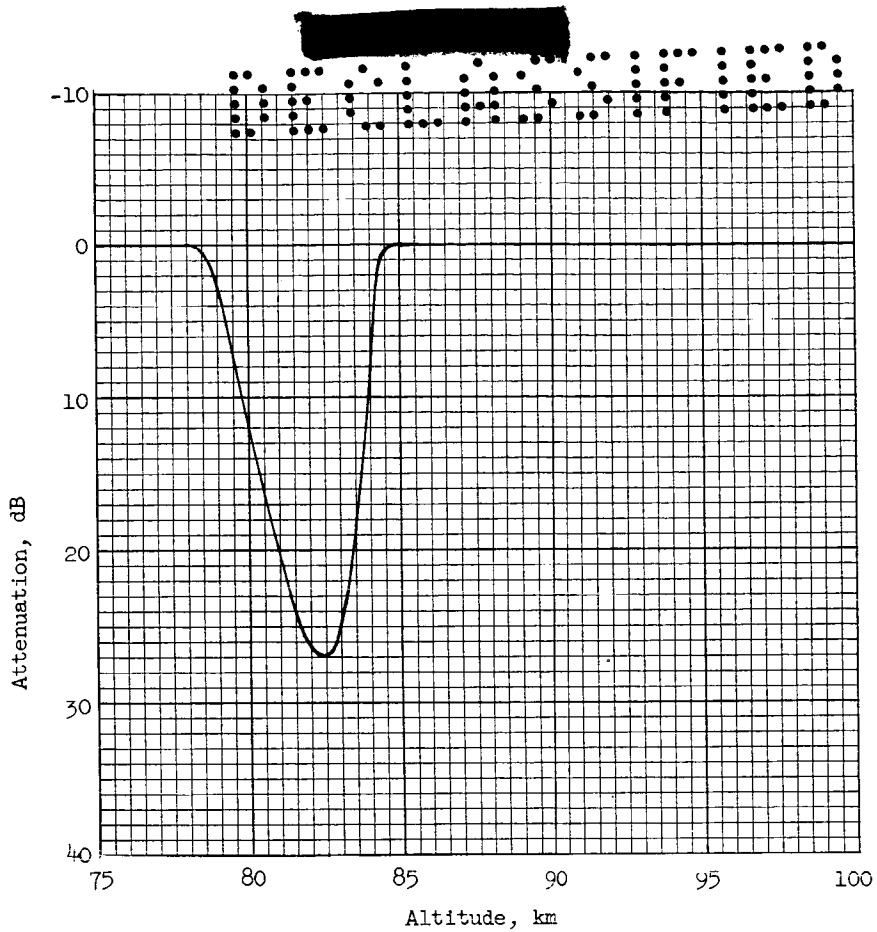


Figure 17.- SA-3 telemetry signal-strength attenuation plotted against altitude.

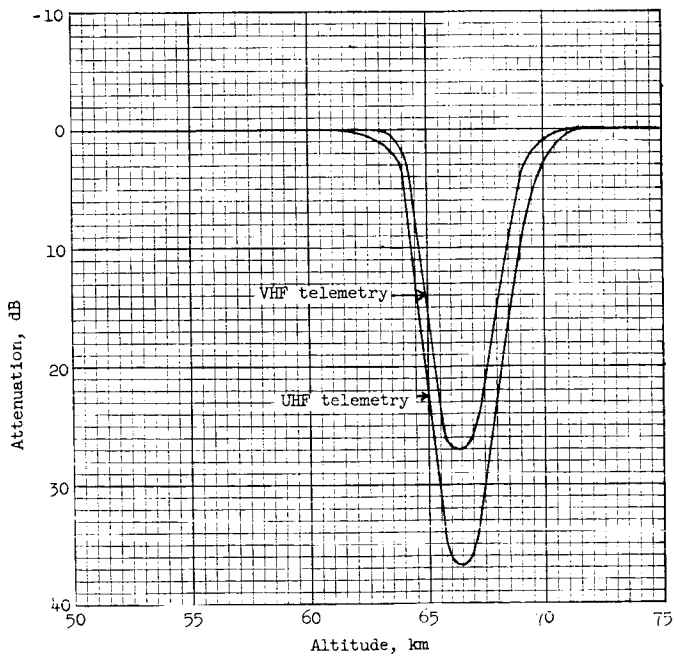


Figure 18.- SA-4 telemetry signal-strength attenuation plotted against altitude.

14. THE RADIO-FREQUENCY SIGNAL ATTENUATION PROBLEM

OF ROCKET EXHAUSTS

By Duncan E. McIver, Jr.
Langley Research Center

SUMMARY

The radio-frequency (RF) signal attenuation problem associated with rocket exhausts is similar to that associated with a spacecraft during reentry. Although both are caused by plasmas, the generation of the plasma and details of the electromagnetic signal interaction are somewhat different. Some of the factors which affect the degree of RF signal interference are: propellant composition, vehicle altitude, frequency of the radio signal, and aspect angle between vehicle and tracking station. Investigations at the Langley Research Center and elsewhere indicate four possible solutions to the problem: relocation of ground tracking stations, change in radio signal frequency, external injection of materials to quench the exhaust plasma, or change to low-attenuating propellant formulations. Closer cooperation between systems, propulsion, and communications personnel is recommended prior to final design of missile systems in order to avoid the attenuation problem.

14

INTRODUCTION

Severe radio-frequency (RF) signal attenuation associated with rocket exhausts has been observed for both liquid- and solid-propellant rocket motors during the boost phase of a space mission. (See refs. 1 and 2 and paper no. 13 of this compilation.) The attenuation is attributed to the exhaust plasma and differs from the reentry attenuation only in the generation of the plasma and details of the electromagnetic signal interaction. Considerable theoretical and experimental effort has been exerted toward understanding the problem and obtaining solutions (refs. 1, 3, and 4), and the Langley Research Center has conducted an extensive program in this area (see refs. 2, 5, and 6). With the use of information from the various studies, the basic elements of the exhaust attenuation problem are described, and four possible solutions to the problem are discussed: the relocation of ground tracking stations, the change in radio signal frequency, external injection of materials to quench the exhaust plasma, and modification of the exhaust propellant to reduce ionization.

SYMBOLS

w_I injection flow rate, lb/sec

w_E exhaust flow rate, lb/sec

ω_p

plasma frequency, radians/sec

ω

radio frequency, radians/sec

BASIC ELEMENTS

Aspect Angle

The aspect-angle dependence illustrated in figure 1 suggests the first of the possible solutions, the relocation of ground tracking stations. As the boosting vehicle rises in altitude, the exhaust plume increases in size because of the decreasing ambient pressure. If the communications path between a tracking station and the vehicle encompasses the exhaust plume, attenuation or other interference of the electromagnetic energy may occur. Stations which do not "look through" the exhaust suffer no attenuation. This fact is illustrated by the signal-strength records for stations A and B. Station A suffers severe attenuation, whereas station B at a larger aspect angle experiences no interference. At motor cut-off the signal at station A is restored. Employment of down-range stations to avoid the exhaust attenuation problem is a solution that is being used in many operational situations today, and one example is described subsequently in this paper.

Exhaust-Plasma Sources

Sources of the exhaust plasma are illustrated in figure 2 (from ref. 3). Thermal ionization of the propellant constituents is possible in the high temperature and high pressure of the combustion chamber especially when trace amounts of alkali metals contaminate the propellant, which is often the case. Analysis of solid propellants, for example, indicates alkali metal contamination sufficient to account for the plasma in terms of thermal ionization alone. Other constituents have been reported as possible electron contributors: aluminum, aluminum oxide, and carbon. Chemi-ionization, or ionization directly from a chemical reaction, may also occur. Electrons created in the combustion chamber will be ejected with the exhaust gases. Ion recombination downstream will reduce the electron population, unless the expansion is so rapid that the ionization is frozen.

Electrons may also be created outside the combustion chamber if after-burning occurs. This complex process, which involves the mixing of unburned gases from the combustion chamber with the atmosphere, may involve thermal and chemical ionization processes. Electrons may also be created from ablating rocket nozzles, ablating airframes, and shocks in the exhaust.

Exhaust Structure and Missile Flow Field

The plasma distribution is determined by the fluid dynamics of the exhaust and its interaction with the surrounding atmosphere. Three possible situations are illustrated in figure 3. At low altitudes the plume is compressed by atmospheric pressure and the vehicle flow field. There is a mixing region on

[REDACTED]

the surface where afterburning may occur and shocks are present in the exhaust. The small width of the exhaust suggests that only "beamrider" type missions would be jeopardized. At intermediate altitudes, the exhaust plume is larger and may cause separation of flow along the vehicle surface. The mixing or afterburning region is still present on the surface of the exhaust. At very high altitudes, where the mean free path is greater than the dimensions of the vehicle, there is no flow interaction with the exhaust and no afterburning, and because of the low ambient pressure, the exhaust becomes extremely large. For the latter situation attenuation is attributed solely to electrons created in the combustion chamber. Because of the rapid expansion of gases at the very high altitudes, the exhaust ionization is frozen and a theoretical model can be constructed (ref. 7). In this model the electron density is assumed to be proportional to the gas density. In the presence of flow interaction and afterburning, construction of such a model is extremely difficult.

Electromagnetic Signal Interaction

A second solution to the RF signal attenuation problem of rocket exhausts is suggested when the interaction of electromagnetic energy with the exhaust plasma is examined theoretically (refs. 7 and 8); this solution is to employ a radio frequency higher than the exhaust-plasma frequency ($\omega > \omega_p$). Flight data discussed subsequently illustrate the success of this second technique.

The change in radiated antenna pattern is a unique effect resulting from an overdense plasma on the surface of the exhaust ($\omega_p > \omega$), as illustrated in figure 4. Stations at low aspect angles will experience attenuation, whereas those at some greater aspect angle will experience an enhancement of the signal. This effect has been observed in flight (ref. 2) and in ground experiments in which the exhaust was simulated with a metal cone.

Summary of Factors Affecting Attenuation

From the preceding discussion it is obvious that several complex factors affect the degree of RF signal interference from a rocket exhaust; thus, the problem of predicting or analyzing a typical flight situation is extremely difficult. Some of these factors are:

- (1) Propellant composition
 - (2) Motor size and thrust (Size and thrust will affect the dimensions of the exhaust.)
 - (3) Combustion-chamber temperature and pressure
 - (4) Altitude of operation
 - (5) Occurrence of afterburning
 - (6) RF signal frequency
- [REDACTED]

[REDACTED]

(7) Antenna type, power, and location (The type and power will determine if antenna breakdown is a problem, and the location will affect the antenna pattern.)

(8) Aspect angle

(9) Vehicle flow field

FLIGHT RESULTS

Exhaust-induced RF signal attenuation has been observed during the boost phases of the NASA Scout vehicle, and these observations are considered representative. Flight results are presented to illustrate the two previously discussed solutions and to suggest a third.

Scout Third-Stage Motor

The following table shows range observations during the operation of the Scout third-stage motor:

	Wallops	Langley	Bermuda
Telemetry	No data (≈ 50 dB loss)	Partial data (40 to 50 dB loss)	Complete data
Radar	Track- marginal (40 to 50 dB loss)		Tracked
Command destruct	Loss of capability		
Aspect angle	6°	20° to 35°	100°

This motor operates in the altitude range from 300,000 to 700,000 feet; therefore its exhaust structure is probably that of the high-altitude case in figure 3. At the launch site, telemetry capability and command-destruct capability were completely lost and radar (5000 mc) track was marginal. These functions were recovered, however, by the Bermuda station which was at an aspect angle of 100° . For all subsequent firings of the Scout the down-range station is employed. For this motor the relocation of the ground station was a working solution; however, since the 5000-mc radar was severely attenuated the higher frequency solution was not entirely satisfactory. The propellant for the motor is a highly aluminized solid propellant similar to that used on Polaris and Minuteman.

A third possible solution to the exhaust attenuation problem is indicated by the results of the Scout second-stage motor shown in figure 5. Attenuation on the VHF telemetry link (244.3 mc) was eliminated each time small hydrogen peroxide control jets located near the second-stage motor nozzle were operated. Since the motor was operating in the intermediate altitude region (fig. 3), the cause of attenuation was assumed to be primarily afterburning. It was also assumed that the decomposition products of the control jets, principally water vapor, quenched the ionization and eliminated interference. The external addition of materials to quench the exhaust plasma is the third suggested solution.

A 5000-mc radar system was unaffected by the exhaust plasma probably because the propellant formulation for the second stage had less aluminum and a lower combustion temperature than that of the third stage. Also during the flight, a tracking station at an aspect angle of about 50° observed a 5-dB enhancement of the VHF signal, whereas the launch site observed attenuation.

In order to investigate the second-stage phenomena further, a recoverable camera was flown on a Scout to photograph the exhaust during the attenuation period (ref. 5). Figure 6 shows three consecutive frames from the flight film. The unusual picture results from the optical system employed and only one quadrant of the exhaust is visible. The luminous region on the periphery appeared at the onset of attenuation and is identified as the afterburning region on the surface. The center picture shows the effect of one of the control jets and corresponds to a period of signal recovery.

GROUND EXPERIMENTS

Ground experiments are desirable in order to investigate in detail some of the factors that affect the exhaust attenuation problem and to determine possible solutions. There are basically two types of ground experiments: full-scale motors fired at atmospheric pressure in a static test facility and small motors fired at simulated altitudes in a vacuum facility. The major problem with these tests is the difficulty in extrapolating specific results to flight situations; however, they have been extremely useful in establishing trends and in investigating propellant compositions.

Material Injection Tests

A series of experiments using material injection to quench ionization were conducted during the static firing of a fourth-stage motor of the Scout vehicle. These tests were based on the flight results of the Scout second stage. The propellant for the fourth-stage motor, however, is the same as that for the third stage of Scout. Figure 7 shows the experimental setup for these tests. The injection site was 3 inches downstream of the nozzle and both water and freon were used in a pulse mode of operation. A transverse attenuation measurement was obtained further downstream (101 inches) with an X-band microwave

[REDACTED]

system. Additional measurements included radiant intensity in the 0.6- to 1-micron region, C-band plasma noise, and acoustic noise.

Figure 8 is a sample of some of the data obtained in the experiments. The top trace shows the water flow rate plotted against time. The second trace is the attenuation plotted against time, and the bottom trace is the relative radiant intensity. Both attenuation and radiant intensity closely follow the injection of water. Plasma noise at C-band was eliminated by the injection and a reduction in acoustic noise of about 5 decibels was observed.

Figure 9 is the attenuation data plotted as a function of the ratio of the injectant mass flow rate to the exhaust mass flow rate. There is a significant amount of signal recovery when the ratio is about 10 percent and complete recovery when the ratio is between 40 and 50 percent. In most applications flow ratios less than 10 percent may be practical, especially during altitude operation. For example, the ratio for the Scout second stage was about 1.5 percent. Additional study is needed to determine the optimum injectant and the injectant scheme. (Freon used for these tests appeared to have the same effect as water.)

Following the full-scale tests, the injection idea was pursued in the 41-foot-diameter vacuum sphere at the Langley Research Center described in paper no. 7 of this compilation. Preliminary analysis indicates that comparable recovery numbers have been obtained for the small motors during atmospheric firings; however, the effect of altitude has not been determined. In addition to water and freon, urine and water with sodium chloride have been employed with comparable results.

Low-Attenuating Propellants

The final solution to be discussed is probably the most fundamental and that is to use a propellant composition or formulation that causes little or no attenuation.

A joint program has been conducted at Langley with the U.S. Army and some of its contractors to evaluate the attenuation characteristics of a new propellant candidate. One requirement for this propellant is that it have minimum RF signal attenuation. Ten motors, each containing the propellant, were fired in the 41-foot sphere facility and attenuation and phase measurements were obtained. Analysis of the data indicates that the propellant is a low attenuator compared with others (such as the Scout propellants).

The principal techniques employed in formulating the low-attenuating propellant are to overoxidize, to develop a low exit temperature (high expansion ratio), and to increase chamber pressure. All three techniques are intended to reduce afterburning. The following table is a summary of some tests run both at Langley and at the Allegany Ballistics Laboratory (refs. 9 and 10):

Propellant	Aluminum, percent	Attenuation, dB/cm	Oxidation index (a)
I	19.8	0.664	0.917
II	7	.482	.500
III	7	.314	.472
IV	7.3	.003 to .03	.267

a

$$\text{Oxidation index} = \frac{\text{H} + \text{H}_2 + \text{CO}}{\text{H} + \text{H}_2 + \text{CO} + \text{H}_2\text{O} + \text{CO}_2}$$

Propellant I is used in the Scout third stage and shows a high aluminum content and attenuation coefficient. The final column in the table is the oxidation index and is the ratio of burnable gas to total gas in the exhaust. For propellant I this value is quite high, 0.917. Propellants II and III show a reduction in the aluminum content but still a relatively high attenuation coefficient. The oxidation indices for II and III are also high. Propellant IV, the low-attenuating propellant mentioned previously, has a very low attenuation coefficient and a corresponding low oxidation index, although the aluminum content is the same as that for II and III.

Unfortunately, propellant IV cannot be a universal solution since it was developed for a specific vehicle; however, some of the philosophies behind its development may be useful. In addition, the propellant results suggest that closer cooperation should be exercised between systems, communications, and propulsion personnel during the planning stages of a missile system in order to avoid the exhaust problem if at all possible.

CONCLUDING REMARKS

Some of the basic elements of the radio-frequency signal attenuation problem of rocket-motor exhausts and four possible solutions to the problem have been presented. The solutions are:

- (a) Relocation of ground tracking stations
- (b) Change in radio signal frequency
- (c) External injection of materials to quench exhaust plasma
- (d) Low-attenuating propellant

The possibility of solution, especially in the area of propellant formulation, indicates that there should be closer cooperation between systems, communications, and propulsion personnel during the design stages of a missile so that the attenuation problem can be avoided. Additional basic research is needed in order that experimental ground and flight data and theoretical data can be correlated and used in preflight prediction and postflight analysis of exhaust attenuation.

REFERENCES

1. Balwanz, W. W., and Stine, P. T.: The Plasmas of Missile Flight - Analysis of Polaris A2X Signal Absorption. NRL Rep. No. 5636, U.S. Naval Res. Lab., July 24, 1961.
2. Sims, Theo E., and Jones, Robert F.: Rocket Exhaust Effects on Radio Frequency Propagation From a Scout Vehicle and Signal Recovery During the Injection of Decomposed Hydrogen Peroxide. NASA TM X-529, 1961.
3. Calcote, H. F., and Silla, H.: Radar Attenuation in Solid Propellant Rocket Exhausts. Bull. 18th Meeting JANAF-ARPA-NASA Solid Propellant Group, Vol. III, June 1962, pp. 3-50.
4. Smith, Felix T., and Gatz, Carole R.: The Chemistry of Ionization in Rocket Exhausts. [Preprint] 2581-62, American Rocket Soc., Oct. 1962.
5. McIver, Duncan E., Jr.: Study of the Effects of a Rocket Exhaust on Radio Frequency Signal Attenuation by the Use of a Recoverable Camera on the NASA Scout Vehicle. NASA TM X-888, 1963.
6. McIver, Duncan E., Jr.: Radio-Frequency Signal Attenuation by Plasmas of Rocket Exhaust Gases. A Compilation of Recent Research Related to the Apollo Mission. NASA TM X-890, 1963, pp. 135-144.
7. Altshuler, S., Moe, M. M., and Molmud, P.: The Electromagnetics of the Rocket Exhaust. GM-TR-0165-00397, Space Technology Labs., Inc., June 15, 1958.
8. Swift, Calvin T., and Evans, John S.: Generalized Treatment of Plane Electromagnetic Waves Passing Through an Isotropic Inhomogeneous Plasma Slab at Arbitrary Angles of Incidence. NASA TR R-172, 1963.
9. Vreeland, R. W.: Radar Attenuation Studies. Progress Rep. C-1-d, Allegany Ballistics Lab., Hercules Powder Co. (Cumberland, Md.), July 2, 1963.
10. Vreeland, R. W.: Sprint - Radar Attenuation Studies. Progress Rep. C-1-d-7, Allegany Ballistics Lab., Hercules Powder Co. (Cumberland, Md.), Oct. 31, 1963.

[REDACTED]

DECLASSIFIED

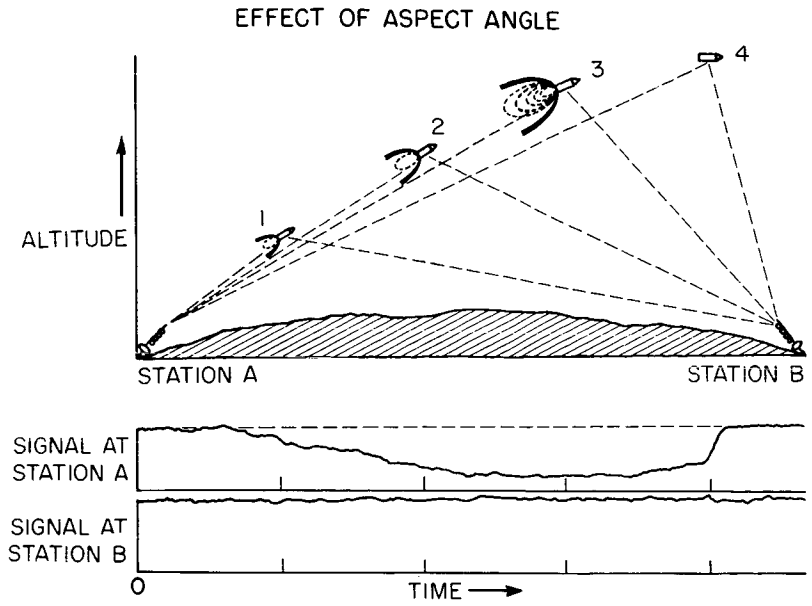


Figure 1

ELECTRON SOURCES IN SOLID-PROPELLANT ROCKETS

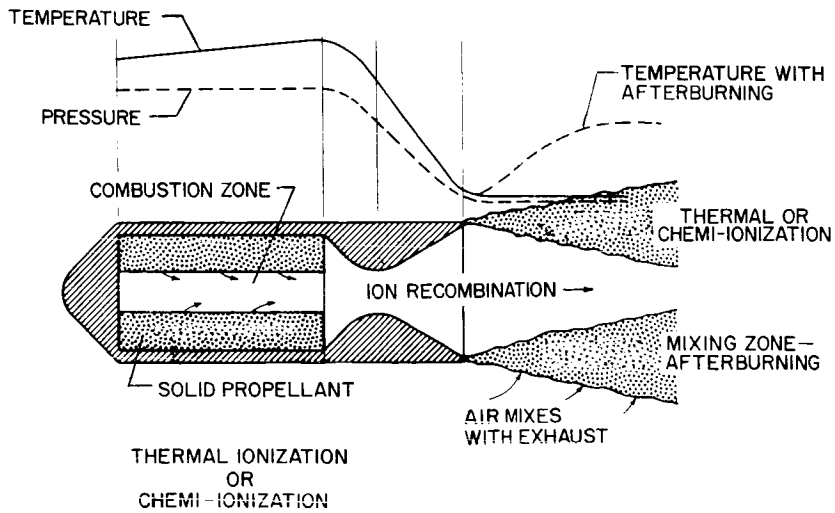


Figure 2

[REDACTED]

031201030

ROCKET EXHAUSTS AND FLOW FIELDS
AT VARIOUS ALTITUDES

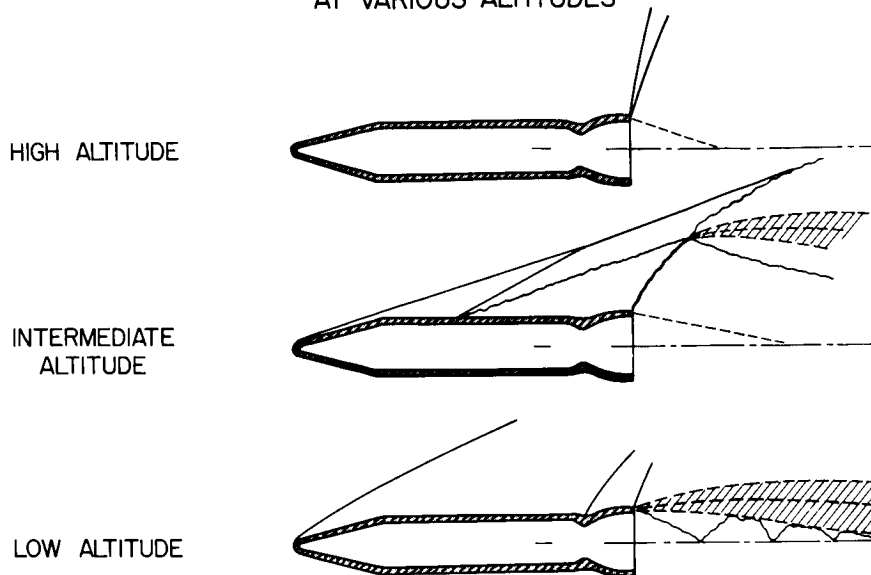


Figure 3

ANTENNA PATTERN CHANGE

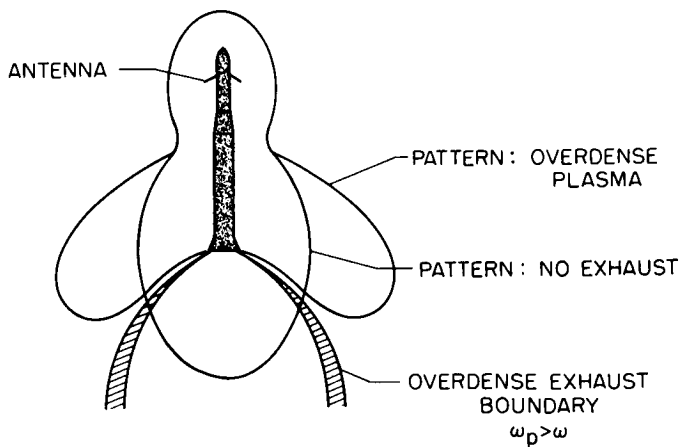


Figure 4

~~CONFIDENTIAL~~
DECLASSIFIED

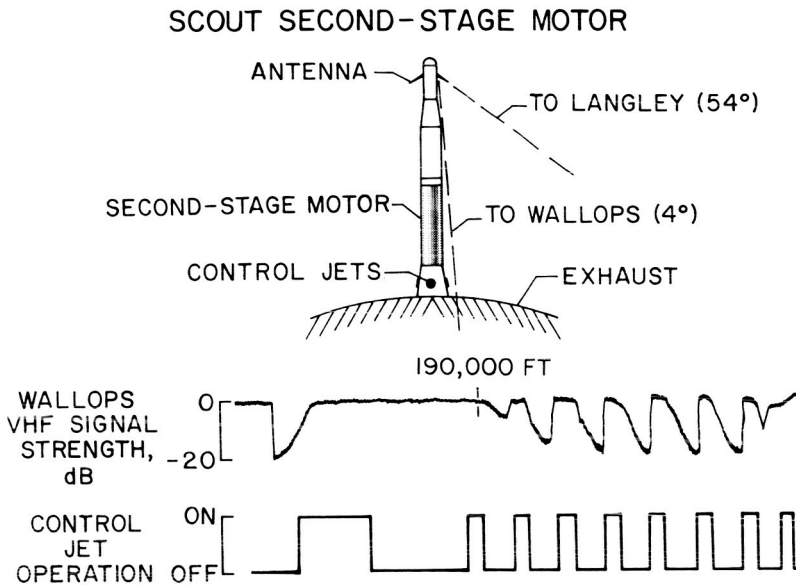
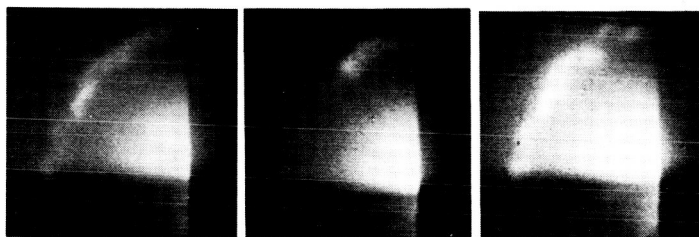


Figure 5

**CONSECUTIVE FRAMES FROM FLIGHT CAMERA FILM
OF SCOUT EXHAUST**

ALTITUDE, 215,000 FT; VELOCITY, 7,760 FT/SEC



HYDROGEN PEROXIDE CONTROL JET QUENCHES PORTION
OF IONIZED SHEATH AND ATTENUATION EFFECTS
DISAPPEAR

Figure 6

L-2166-12

~~CONFIDENTIAL~~

09 10 20 30 40 50

MATERIAL INJECTION TESTS TEST SETUP

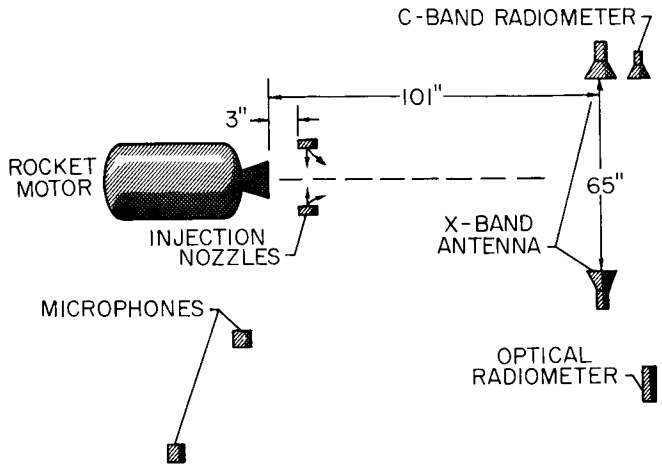


Figure 7

MATERIAL INJECTION TESTS SAMPLE DATA

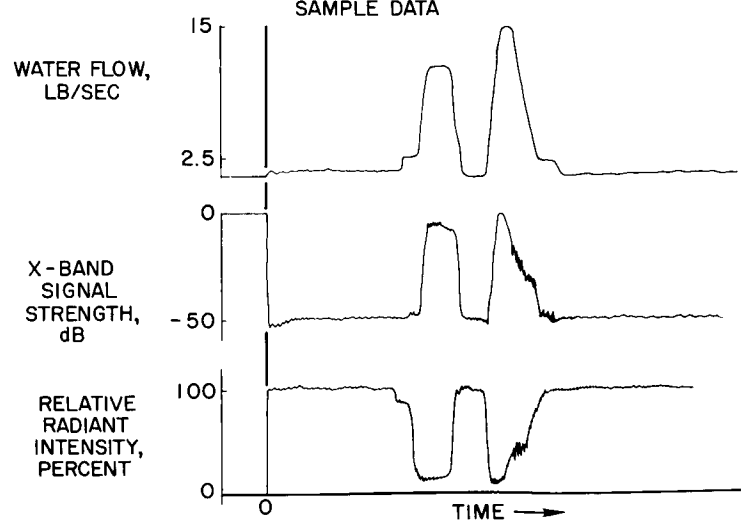
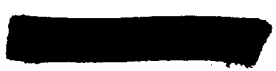


Figure 8



[REDACTED]

DECLASSIFIED

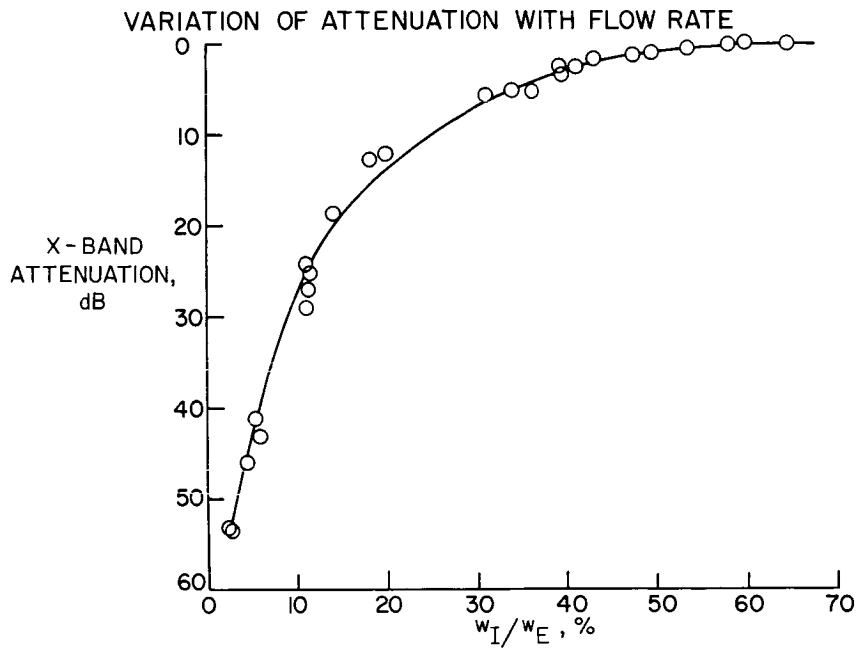


Figure 9

15. PROJECT RAM FLIGHT-TEST ROCKET VEHICLES

By James L. Raper
Langley Research Center

SUMMARY

This paper presents a summary of problems associated with the development of two Project RAM flight-test rocket vehicles. Solutions for these problems, the flight performance, and a brief description of each vehicle are given.

INTRODUCTION

The primary requirement for the Project RAM flight-test rocket vehicles was to boost instrumented payloads into an attenuation-producing environment of desired magnitude in order to verify theories and results of ground-based studies. Since for a given payload the magnitude of plasma attenuation due to flow-field ionization is primarily dependent upon the altitude and velocity, the prime vehicle requirement resulted in specific altitude and velocity conditions at payload-stage burnout. Figure 1 shows the required area of investigation in relation to the reentry corridors for vehicles such as Dyna-Soar, Mercury, and Apollo. Two additional requirements were specified for the flight tests: a data gathering period close to NASA Wallops Station and an ascending trajectory in order to exit the "radio blackout region" and to play back data stored on an onboard recorder. Figure 2 shows the flow field or environment that is typical of payload stages probing into and through the radio blackout region. Because of the nature of the radio blackout region, such areas as aerodynamic heating, jet pluming, aerodynamics, and body angle of attack are greater problems than usual.

PROBLEM AREAS

Numerous vehicle problems had to be solved in order to attain satisfactorily the payload mission requirements. The significant vehicle problem areas of concern and those areas where special investigations were required because of problems unique to the attainment of the RAM mission are as follows:

Aerodynamics
Aeroelasticity
Dynamic coupling
Jet-pluming instability
Heating
Motor-performance predictability
In-flight command ignition
Dispersion and range safety
Reliability and quality control

[REDACTED]

Aerodynamics, jet-pluming instability, heating, and in-flight command ignition required special investigations for the RAM vehicles.

Aerodynamics

Aerodynamics is an area of concern for every vehicle and is usually adequately handled by conventional techniques. However, for the RAM vehicles it was one of the most critical areas because of its influence on all other areas of concern. In general, theoretical calculations were not considered accurate enough and, therefore, wind-tunnel facilities were utilized to define the static aerodynamic characteristics over the Mach number range. The primary aerodynamic areas of concern were (1) accurate drag characteristics so that velocity increments could be predicted and (2) vehicle stability characteristics so that accurate wind compensation could be made and small angle of incidence could be assured during the data period.

Aeroelasticity

Aeroelastic effects did not present a special problem for the RAM vehicles. Conventional theoretical techniques were used in analyzing the flexible vehicles, and adequate stabilizing fins were provided so that a minimum static margin of one-half body diameter was maintained at all times.

Dynamic Coupling

Dynamic coupling occurs when the vehicle roll frequency inadvertently becomes resonant with either the body pitch or structural frequencies. Problems were not encountered in this area because a precise spin program was utilized to average the effects of thrust and body misalignments and because a detailed effort was made to define vehicle aerodynamics and body structural characteristics.

Jet-Pluming Instability

Jet pluming is caused by the expansion of the jet exhaust from under-expanded rocket motor nozzles. Pluming becomes a problem during flights where aerodynamic forces generated by stabilizing surfaces are required. For the RAM vehicles, the aerodynamic stabilizing forces were required in order to maintain low angles of attack during the data period. The effect of jet pluming was to reduce the effectiveness of the stabilizing surfaces through the phenomenon of induced flow separation over such surfaces. Figure 2 shows the flow separation that is characteristic of jet-pluming effects. The effect of jet-plume size, determined by motor chamber pressure and altitude, is to cause the extent of flow separation to move forward along the body for larger plumes. Jet-plume simulation in an appropriate hypersonic wind-tunnel facility was required to define accurately the effects of jet pluming on vehicle static aerodynamics.

[REDACTED]

The results of these tests showed that adequately low angles of attack for a given flight path could be maintained by proper flare size. Often trades had to be made between small-angle-of-incidence requirements and flare size because of drag penalties.

Heating

In order to produce the plasma environment required by the RAM payloads on an ascending trajectory, the vehicles must necessarily survive rather rigid heating environments. For the RAM vehicles, the heating is produced by both aerodynamic and jet-pluming effects. In comparing various vehicles for the RAM mission, it was determined that short-burning instead of long-burning rocket motors would reduce the overall heat problem. However, tests in arc-jet facilities were required to determine material efficiencies, and computer techniques were used to determine the amount of thermal protection required.

Motor-Performance Predictability

Motor-performance predictability affected the mission success by causing a higher or lower altitude to be attained because of a larger or a smaller velocity increment than expected. It was beyond the scope of the RAM project to improve the motors. In general, it has been observed that slow-burning highly efficient motors have larger percentage deviations in performance than the less efficient fast-burning motors.

In-Flight Command Ignition

For fast-burning rocket motors, it has been determined that specific burnout altitudes can be achieved, with little error, by using onboard ignition timers. However, the slow-burning stages require in-flight command ignition so that it is possible to compensate for flight-path and velocity deviations from nominal and achieve the desired burnout altitude, provided subsequent stages have predictable performance. A typical command ignition system consists basically of an onboard command receiver and a ground-based real-time analog computer tied to the output of the most accurate tracking radar available at NASA Wallops Station. Real-time data plots are used to decide the proper instant to ignite the stage so that a desired burnout altitude can be achieved. For the development of this system, an analog computer was utilized and it was determined from this device that errors expected in the first-stage performance would result in the payload-stage burnout altitude being missed by as much as 50,000 feet if an in-flight compensation technique was not utilized.

Dispersion and Range Safety

Conventional error-analysis techniques were found adequate for dispersion and range-safety considerations. It was necessary to position the launch azimuth angle accurately so that payload-stage impact would not occur on down-

range land masses, but would come close enough to permit tracking and data recovery.

Reliability and Quality Control

The balance of reliability and quality control between desired scheduling and practical economy is always a problem for programs where the success depends upon the few shots which are involved. Basically, for Project RAM, a component testing, inspection, and qualification program was set up and followed to give the greatest possible insurance of success for each mission. This program included (1) testing of hardware to destruction, (2) qualification of each set of flight hardware, (3) radiographic inspection of rocket motors, and (4) qualification testing of the payloads to the expected environmental levels.

RAM A AND RAM B VEHICLES

The combined solutions to the problems pointed out previously in the "Problem Areas" section have produced two entirely different rocket vehicles (fig. 3) suitable for boosting two different size payloads: a 1-inch-radius and a 4-inch-radius hemispherical-tipped 9° cone-cylinder. The first vehicle, RAM A, was long and slender and consisted of four stages of fast-burning solid-propellant rocket motors. When it was conceived, the RAM A represented a state-of-the-art booster for the payload size involved and consisted of a dual-Recruit-boosted-Castor first stage, Skat second and third stages, and a Recruit fourth stage. Nominal payload weight was 75 pounds. A second series of experiments was conceived to provide more comprehensive investigations and, consequently, a more efficient and powerful vehicle, RAM B, was required in order to boost nominal payloads of 200 pounds to speeds equal to or greater than those of RAM A. The RAM B launch vehicle consisted of three short, thick, slow-burning stages: Castor first stage, Antares second stage, and Alcor third stage. Both vehicles were unguided. A comparison of figures 4 and 5 shows the relative size as well as some of the more important details of the RAM A and RAM B payload stages.

Figure 6 shows the radio-blackout-region probe capability intended for the RAM A and RAM B vehicles. As indicated by the arrows, the trajectory is ascending. For RAM B, the apogee is relatively low and therefore will permit data gathering during reentry. It should be noted that the time required for RAM A and RAM B to reach payload-stage burnout differs by more than a factor of two.

Figure 7 shows a comparison of the RAM B2 nominal and flight trajectories. Postflight analysis confirmed that the in-flight command ignition properly compensated for a low-altitude and low-velocity first stage and that nominal third-stage burnout altitude would have been achieved if second- and third-stage motor performance was nominal. However, as indicated by the figure, the

[REDACTED]

velocity increment was lower than predicted by approximately 1,000 feet per second, with the result that burnout altitude and apogee were lower than desired. From flight instrumentation, it has been determined that the motors underperformed by 500 feet per second and that drag was underestimated by 500 feet per second. It should be noted, however, that the lower altitude compensated for the lower velocity and produced approximately the desired attenuation environment.

CONCLUDING REMARKS

As has been shown in the discussion of several problem areas, a detailed knowledge of the vehicle characteristics and its capability is required to probe a specific part of the "radio blackout spectrum." The RAM flight-test rocket vehicles fulfilled the stated mission requirements. Specifically, the RAM A and RAM B launch vehicles have been successful in placing the payloads in the desired attenuation region and have made it possible to obtain basic data measurements required for analysis and solution of some of the salient problems of radio signal blackout.

[REDACTED]

0310200000

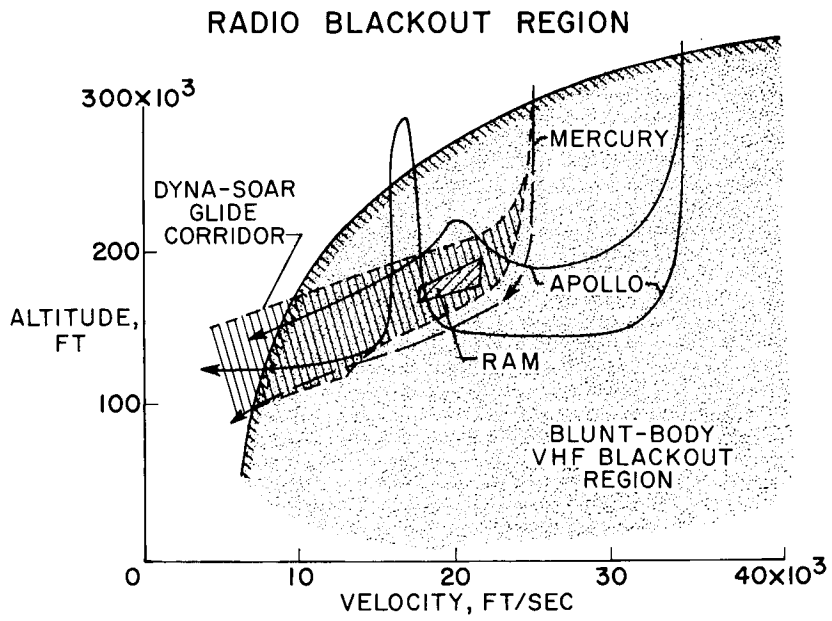


Figure 1

DECLASSIFIED

RAM PAYLOAD ENVIRONMENT

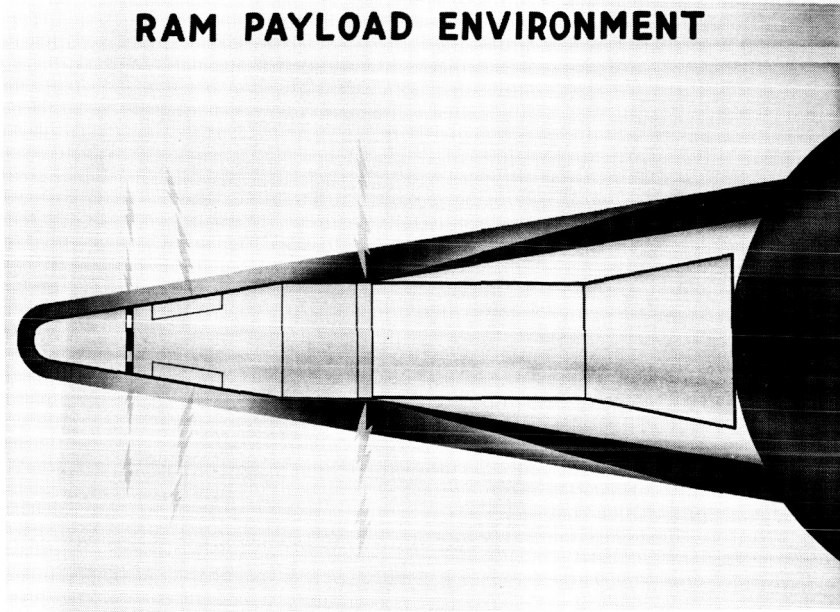
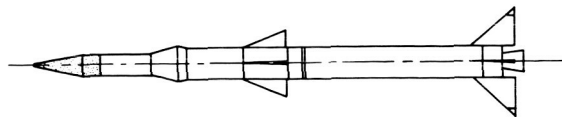


Figure 2

L-1440

RAM FLIGHT-TEST VEHICLES



RAM B



RAM A

Figure 3

0317020000

RAM A

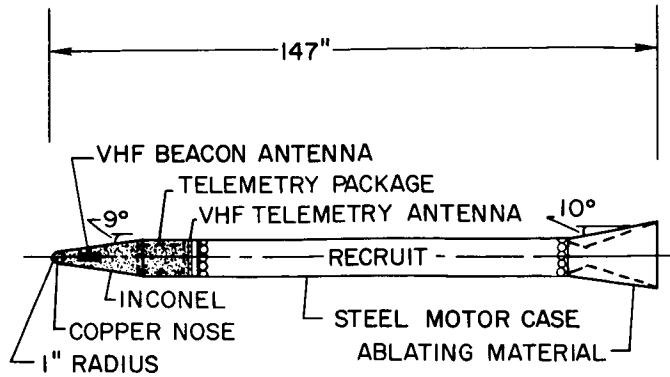


Figure 4

RAM B

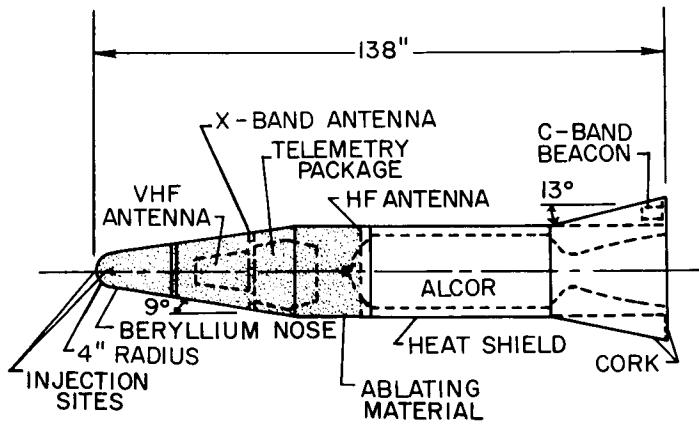


Figure 5

RAM VEHICLE BLACKOUT - PROBE PERFORMANCE

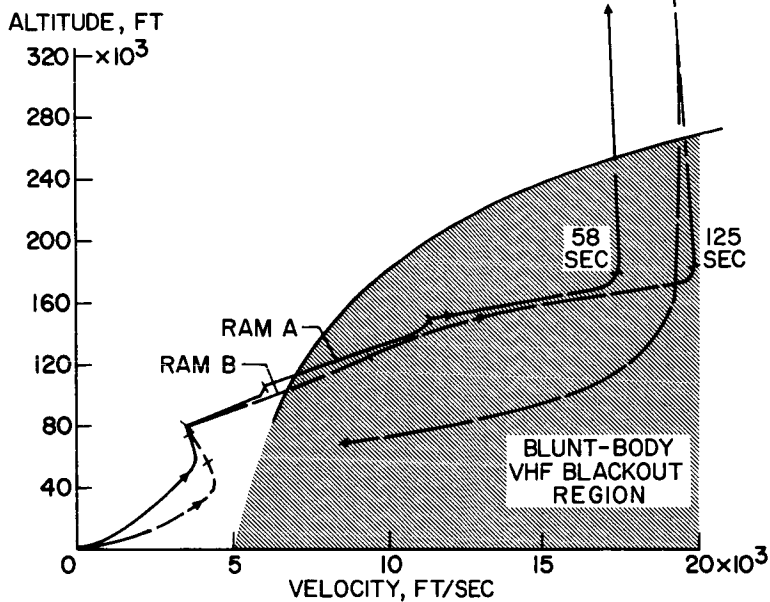


Figure 6

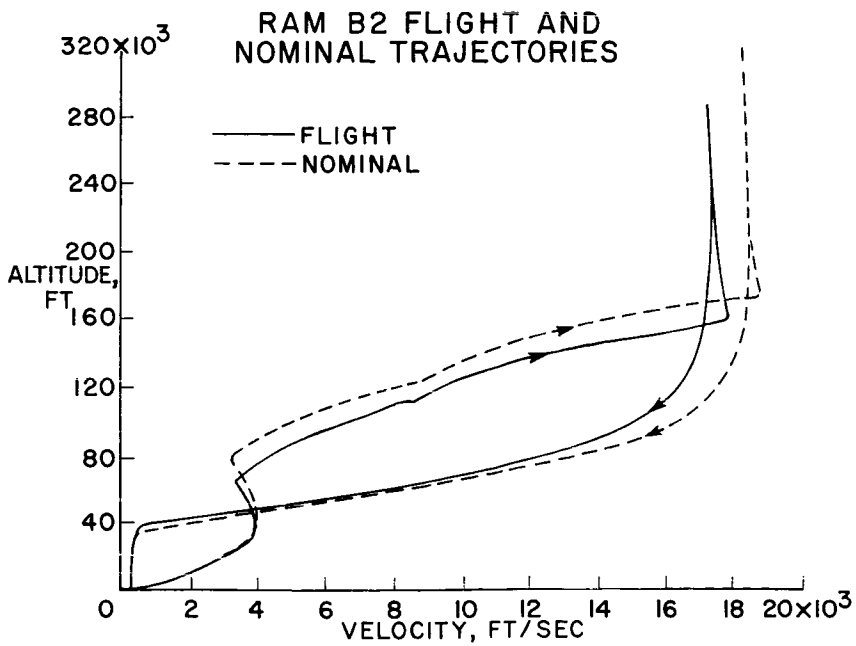


Figure 7

16. INJECTION, DISTRIBUTION, AND EVAPORATION OF LIQUIDS

IN THE FLOW FIELDS OF HYPERSONIC VEHICLES

By Ivan E. Beckwith
Langley Research Center

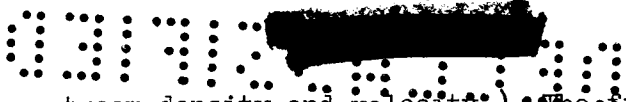
SUMMARY

Typical results of an experimental and theoretical investigation of the fluid mechanics aspects of liquid injection and evaporation processes are presented and discussed. The data were obtained in the Langley Mach 8 variable-density tunnel for both liquid nitrogen and water injection to provide a large range in latent heat of vaporization and other liquid parameters. For the case of side injection it is shown that the liquid can be injected without causing large secondary disturbances, that the distribution of the spray is uniform, and that evaporation is sufficiently rapid. For injection at the stagnation point, the bow shock is modified to a pointed configuration when the liquid jet momentum is large. Qualitative comparison of theoretical calculations for mean droplet trajectory and evaporation distances with the experimental data indicates reasonable agreement.

INTRODUCTION

Ground tests (ref. 1) and a flight test (ref. 2) conducted at the Langley Research Center have shown that material injection into the flow field of hypersonic vehicles alleviates radio attenuation. In fact, one of the obvious conclusions from the preceding papers in this conference is that whenever materials (including water, freon, and hydrogen peroxide) were injected into any hot or cold plasma, at least some signal recovery was observed. The present paper contains a brief discussion of some of the results of an experimental and theoretical investigation (refs. 3 and 4) of the fluid mechanics aspects of liquid injection and evaporation processes. The investigation was carried out in support of the RAM B2 flight which will be discussed in paper no. 17 by William F. Cuddihy.

The ultimate objective of material injection is to modify or quench the hot plasma so as to reduce the free electron concentration in the vicinity of the antennas. It became apparent early in the investigation that injection of a liquid rather than a gas would offer certain advantages. Some of these advantages are illustrated in figure 1. Figure 1 is an artist's conception comparing the general appearance of gas injection with liquid injection. The bow shock configuration is scaled from actual wind-tunnel tests with gas injection and liquid injection (made at different times) from a single orifice just aft of a hemispherical nose, as indicated. The ratio of injected mass flow to reference air mass flow w_c/w_{REF} was about 1.5 in both cases. (The reference air mass flow is defined as that quantity contained in a stream tube of model nose



diameter at free-stream density and velocity.) The first thing to be noted is the larger initial disturbance with gas injection with the possible additional ionization caused by the secondary shock. The hot ionized gases generated by the secondary shock, as well as by the bow shock at the nose, are forced away from the vehicle surface and cooled in the subsequent mixing region which may extend far downstream. In contrast, the liquid injection produces a smaller initial disturbance because of the smaller added volume. The liquid jet is rapidly atomized by the high-velocity airstream into a spray of fine droplets which are more or less uniformly distributed across the shock layer. The effective "mixing length" is then determined by the evaporation length of the droplets. Other advantages associated with liquid injection are the latent heat (which in the case of water is appreciable), better control of initial penetration and distribution in the flow field, and ease in handling and storage. Thus, if the liquid spray can be properly located and if evaporation occurs fast enough, the desired effects should be possible.

In order to determine the feasibility of liquid injection and to provide an answer to some of these questions, the present investigation of liquid injection into the flow fields of various shapes has been carried out.

A motion-picture film supplement (Film No. L-822) showing typical results for penetration and distribution of the liquid spray and its effect on the flow field is available on loan. A request card is included at the back of this document.

SYMBOLS

- D_n diameter of nose
- d_o diameter of injection orifice
- M_∞ Mach number ahead of shock
- N_e electron density
- r_n radius of nose
- T_{aw} adiabatic wall temperature
- T_o stagnation temperature
- V_l velocity of liquid
- V_∞ velocity ahead of shock
- w_a air mass flow
- w_c coolant mass flow
- w_{REF} reference mass flow, $\pi r_n^2 \rho_\infty V_\infty$



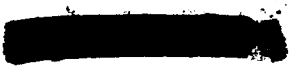


- x distance from injection orifice
- y coordinate
- y_{MAX} maximum penetration of liquid spray
- ρ_l density of liquid
- ρ_∞ density ahead of shock

APPARATUS AND PROCEDURE

The experimental data were obtained in the Langley Mach 8 variable-density tunnel with injection of both water and liquid nitrogen. The liquid nitrogen was used in the wind-tunnel tests because its small latent heat of vaporization and low temperature provided partial simulation of the evaporation rate for water injection at hypersonic flight conditions (ref. 3). The technique used for visual observation of the liquid spray in this investigation is illustrated in figure 2. This figure is a top view of the wind tunnel and model showing the arrangement of camera and light beam which was used to illuminate the liquid spray. The light was focused at the test section into a narrow beam about 1 inch wide by 8 inches high; the top edge view of the beam is shown in the figure. The beam could be moved fore and aft along the model during the tests to provide an indication of the cross-sectional shape and distribution of the spray at different axial stations as recorded by the camera.

The reflection of light from the spray was also visible in the schlieren photograph which was recorded by another camera not shown in figure 2. In figure 3 a typical schlieren photograph of the RAM B model is shown on the left with liquid nitrogen injection from a single orifice located on the bottom of the model 1.3 nose radii downstream of the stagnation point. The light reflected from the liquid spray can be seen just below the model at about 2 nose diameters downstream of the stagnation point; the other light bands are reflections from the near and far side windows. An idea of the magnitude of the flow-field disturbance can be obtained by comparing the bow shock configuration on the injection side (bottom) of the model with the shock on the undisturbed side (top) as shown in the figure. The other photograph (on the right) is for the same conditions but was taken by the side camera (shown in fig. 2) which sees, in effect, an oblique cross-sectional view of the spray. The illuminated section of the spray can be seen at about $2\frac{1}{2}$ nose diameters downstream of the stagnation point just below the model. Note that in this photograph the flow is from right to left and the model is near the top of the frame.



Values are given in the motion picture of the parameter w_c/w_{REF} (designated as m_c/m_{REF} in the motion picture), which is the ratio of coolant mass flow to free-stream air mass flow contained in a stream tube of model nose diameter. The quantitative influence of this parameter on the penetration and cooling effect will be discussed.

The first two runs in the motion picture show the liquid spray and schlieren superimposed on the RAM shape (spherically blunted, 9° cone) for side injection at two different values of the mass flow ratio w_c/w_{REF} . The third run is for the same conditions as the previous one but was taken with the camera shown in figure 2 and thus corresponds to the view shown on the right in figure 3. Note the lateral distribution and uniformity of the spray as illustrated in the third run. The fourth run shows the spray penetration and uniform distribution for injection from the shoulder of the Mercury shape for a small value of w_c/w_{REF} .

Details of the experimental and theoretical results are given in reference 3. One of the more significant experimental results is illustrated in figure 4. The maximum penetration of the liquid nitrogen spray as obtained from the wind-tunnel data is plotted in the form of y_{MAX}/d_0 against the correlating parameter. The coordinate axes used are defined in the figure. The parameter $\frac{\rho_l V_l}{\rho_\infty V_\infty}$ is the ratio of the liquid density and velocity to the free-stream density and velocity. All lengths are divided by the orifice diameter d_0 . This correlation was used directly to determine the orifice diameter and liquid velocity (or pressure) that would result in the desired spray penetration for the RAM B2 flight. As indicated in paper no. 17 by William F. Cuddihy these parameters were chosen in order to give the correct penetration during the early portion of the data period at the forward antenna.

So far not much has been said about stagnation-point injection. Emphasis has been on side injection since this appears more promising for application to large, blunt vehicles where a local hole or window in the plasma can be established. For smaller research vehicles such as the RAM B2, stagnation-point injection is practical. Figure 5 shows some typical schlieren photographs (using spark exposure) of stagnation-point injection. All three photographs are for the same run for which the momentum flux ratio was 0.19. This ratio is defined as the ratio of the liquid jet momentum to the momentum of the free stream in a stream tube of diameter equal to the nose diameter. The top photograph shows the peculiar pointed shock configuration which was sometimes observed. The liquid spray is illuminated about 2 diameters downstream of the nose. The lower left photograph shows a somewhat different shock configuration. The liquid spray is illuminated here at about 1 diameter ahead of the model and bow shock. This pointed configuration was very unsteady and appeared to collapse and re-form at a frequency of something like 50 to 100 cps. This unsteadiness is illustrated by the lower right photograph where the shock is seen to be collapsing.

SECRET

The maximum shock standoff distance, such as seen in the top photograph for stagnation-point injection, was correlated by the ratio of the liquid jet momentum to the momentum of the free stream (ref. 3). The values of this parameter for stagnation-point injection during the RAM B2 flight indicate that a similar modification of the bow shock during the flight could be expected. If such a pointed shock were established in flight, the production of free electrons would be essentially eliminated during stagnation-point injection.

A simplified quasi-one-dimensional theory has been derived and used to estimate the mean droplet trajectories and evaporation rates for crosscurrent injection (refs. 3 and 4). Semiempirical expressions have been developed for the droplet drag coefficient and Nusselt number (for heat transfer to the droplets) that are applicable over the entire range of conditions from free-molecule high-velocity flow prevailing near the injection site down to continuum, low relative velocity that occurs nearer the end of the droplet lifetime. The results of the theory applied to wind-tunnel conditions are illustrated in figure 6. Figure 6 is a schlieren photograph of liquid nitrogen injection on a hemisphere-cylinder model. The densest portion of the liquid spray is again illuminated by a light beam on the bottom side of the model about 3 diameters downstream of the nose. The inner line is the mean droplet trajectory as computed from the theory. The outer line is the maximum outer limit of the spray penetration as obtained by the side camera in figure 2. Comparison of the theoretical result with the denser portion of the spray as well as with the maximum penetration indicates that reasonable estimates of mean droplet trajectories can be obtained.

In figure 7 a qualitative comparison of predicted evaporation rates is made with wind-tunnel data by using the adiabatic wall temperature of the model. The ratio of the local adiabatic wall temperature to the free-stream stagnation temperature T_{aw}/T_0 is plotted against the axial distance from the injection orifice. The data points are experimentally determined values on the hemisphere-cylinder model with liquid nitrogen injection for the values of w_c/w_{REF} shown. The line is from the theory for a value of the ratio of coolant mass flow to air mass flow of 0.7. In this case the quantity w_a is the mass flow of air assumed to be entrained in the mixing region. Agreement between the data and theory at $x = 20$ inches, where the theory predicts about 80 percent of the injected coolant would be evaporated, was obtained with w_a slightly less than $1/4 w_{REF}$. The agreement indicates that reasonable estimates of evaporation distances are possible. A very important parameter involved in the evaporation rates and distances is the initial drop diameter which was obtained from reference 5.

Application of the theory to conditions typical of the early portion of the RAM B2 data period are illustrated in figure 8. The fraction of water evaporated is plotted against distance downstream of the injection site in inches. Also plotted is the temperature of the air vapor mixture. The ratio of injected coolant mass to air mass in the mixing region was taken as 0.5 for this calculation and thermodynamic equilibrium is assumed. (The thermodynamic properties of the mixture were obtained with the computer program of Zeleznik and Gordon (ref. 6).) At only 0.3 inch from the injection point, 20 percent of the injected mass would be evaporated and the temperature would

037: [REDACTED]

be reduced by more than $1,000^{\circ}$ K. The equilibrium electron concentration is reduced accordingly from almost 10^{12} to 4×10^9 . The rapid reduction in temperature is caused partly by the large latent heat of water and specific heat of steam but the greatest effect is the dissociation of the water molecules as indicated by the sudden increase in hydrogen atoms as shown in figure 9. Also shown in this figure are the variations in mole fraction of some of the other constituents of the mixture. The main source of electrons is the nitric oxide (NO) which is seen to increase. Whereas the nitric oxide is increasing, the temperature is decreasing, and the net effect is to reduce the N_e . The constituent that has the next largest effect on N_e would be the hydroxyl neutral (OH) due to the formation of negative hydroxyl ions. Although the mole fraction of the hydroxyl neutral becomes appreciable, it is still insufficient to give any significant reduction in N_e at these conditions.

CONCLUDING REMARKS

It has been shown that liquid injection into the flow field of hypersonic vehicles results in a uniform distribution of the materials across the shock layer. Also, in the case of side injection, the penetration of the spray can be controlled and does not cause a large secondary disturbance. For injection at the stagnation point the bow shock is modified considerably. The data and theory indicate that evaporation of the liquid spray is sufficiently rapid to obtain significant cooling of the plasma in reasonable distances. Based on the present equilibrium calculations for the RAM B2 flight conditions, the principal mechanism for the reduction of free electrons for side (or crosscurrent) injection would be the cooling of the plasma. For nose injection the principal mechanism may be the modification of the bow shock.

1. Cuddihy, W. F., and Hughes, J. Kenrick: Simulated Reentry Tests of a Method for Reducing Radio Blackout by Material Addition to Ionized Flow Field. NASA TM X-988, 1964.
2. Cuddihy, William F., Beckwith, Ivan E., and Schroeder, Lyle C.: RAM B2 Flight Test of a Method for Reducing Radio Attenuation During Hypersonic Reentry. NASA TM X-902, 1963.
3. Beckwith, Ivan E., and Huffman, Jarrett K.: Injection and Distribution of Liquids in the Flow Fields of Blunt Shapes at Hypersonic Speeds. NASA TM X-989, 1964.
4. Cuddihy, W. F., Beckwith, I. E., and Schroeder, L. C.: A Solution to the Problem of Communications Blackout of Hypersonic Reentry Vehicles. NASA paper presented at Anti-Missile Research Advisory Council Meeting (Annapolis, Md.), Oct. 22-24, 1963.
5. Ingebo, Robert D., and Foster, Hampton H.: Drop-Size Distribution for Cross-current Breakup of Liquid Jets in Airstreams. NACA TN 4087, 1957.
6. Zeleznik, Frank J., and Gordon, Sanford: A General IBM 704 or 7090 Computer Program for Computation of Chemical Equilibrium Compositions, Rocket Performance, and Chapman-Jouguet Detonations. NASA TN D-1454, 1962.

ADVANTAGES OF LIQUID INJECTION OVER GAS INJECTION

$$w_c / w_{REF} = 1.5; M_\infty = 8$$

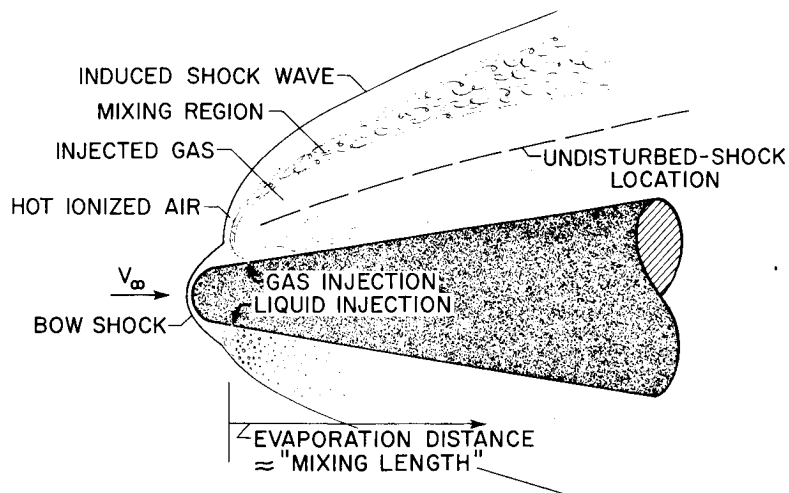


Figure 1

TECHNIQUE FOR VISUAL OBSERVATION OF LIQUID SPRAY TOP VIEW OF WIND TUNNEL AND APPARATUS

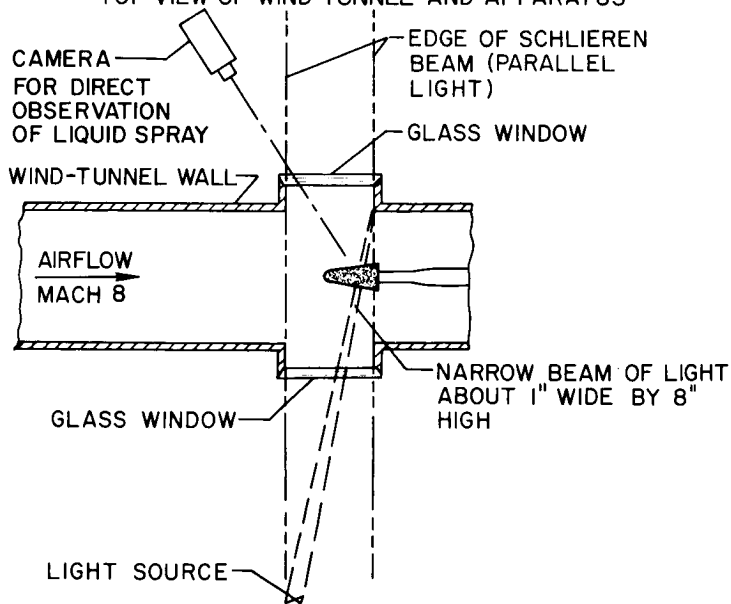
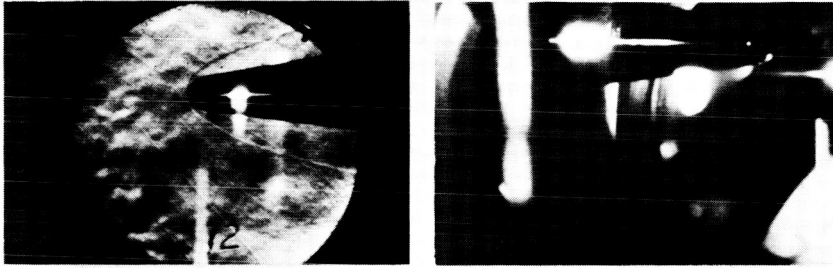


Figure 2

ILLUMINATION OF LIQUID SPRAY



SCHLIEREN; FLOW-FIELD DISTURBANCE SIDE CAMERA; SPRAY CROSS SECTION

Figure 3

L-2173-10

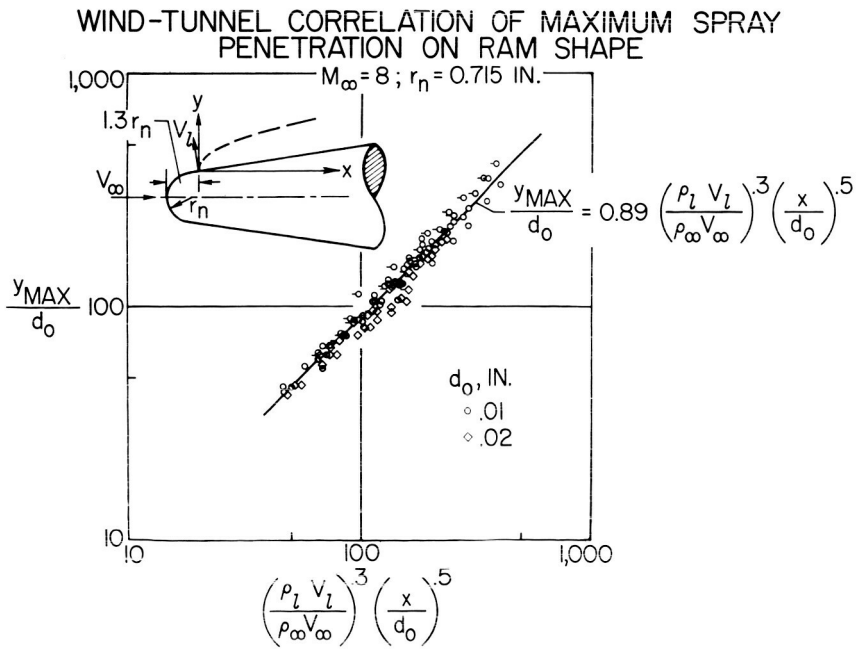


Figure 4

LIQUID NITROGEN INJECTION AT STAGNATION POINT
MOMENTUM FLUX RATIO = 0.19

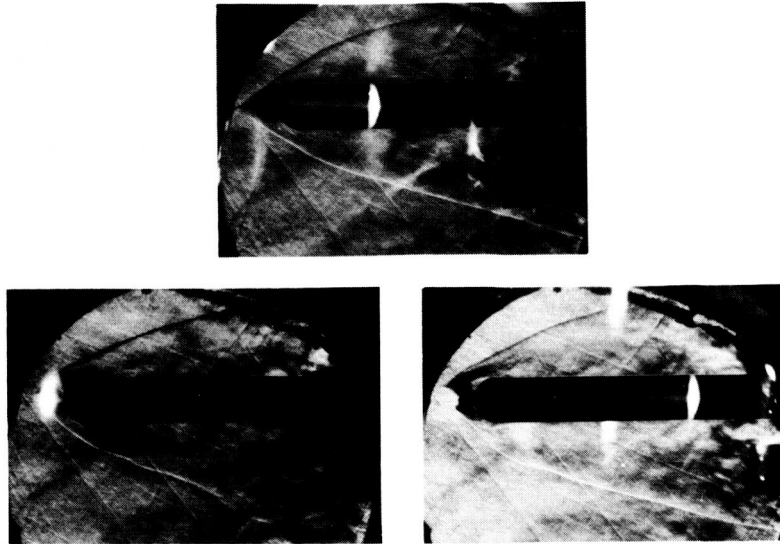
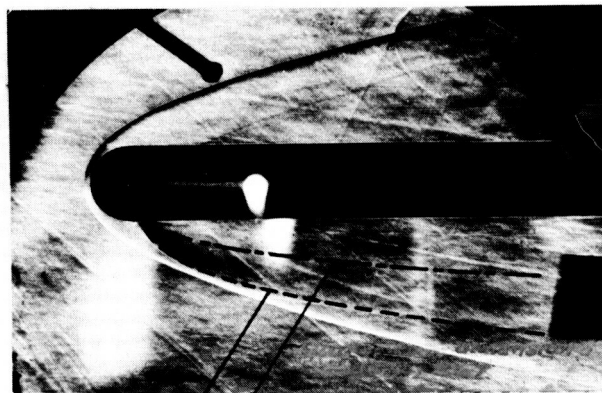


Figure 5

L-2173-9

COMPARISON OF THEORETICAL TRAJECTORY
OF MEAN MASS DROPLET WITH DATA

$M_\infty = 8, w_c / 1/4 w_{REF} = 0.58$



QUASI-ONE-DIMENSIONAL
THEORY, $w_c/w_a = 0.7$

EXPERIMENTAL MAXIMUM PENETRATION

Figure 6

L-2173-8



EFFECT OF LIQUID NITROGEN INJECTION ON ADIABATIC SURFACE TEMPERATURES

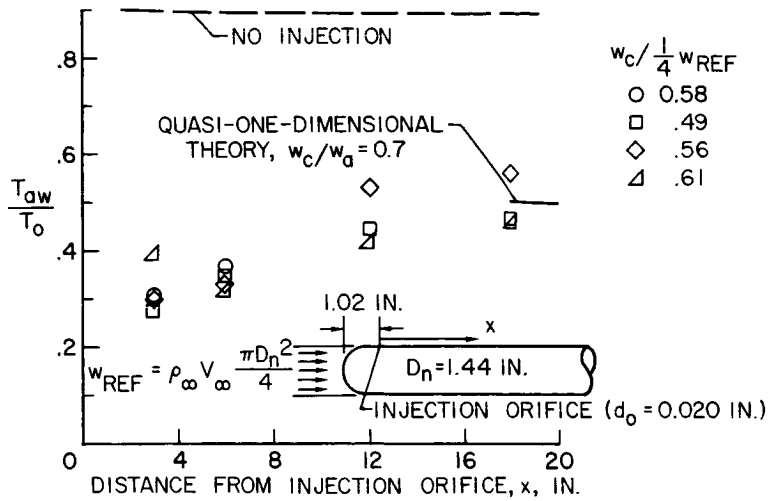


Figure 7

TYPICAL THEORETICAL RESULTS FOR WATER INJECTION ON RAM B2

ALTITUDE $\approx 170,000$ FT; VELOCITY $\approx 18,000$ FT/SEC
 LOCAL CONDITIONS: PRESSURE, 0.012 ATM; VELOCITY, 11,000 FT/SEC;
 SIDE INJECTION FROM 0.015-INCH-DIAM. ORIFICES

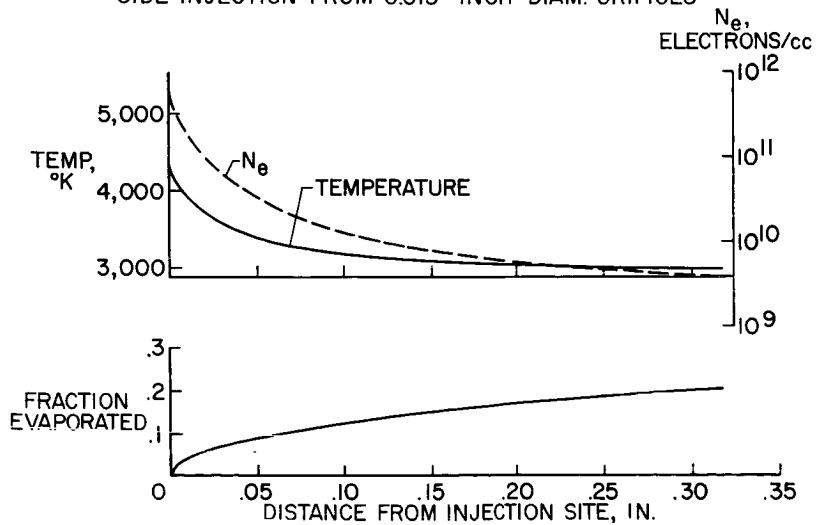


Figure 8



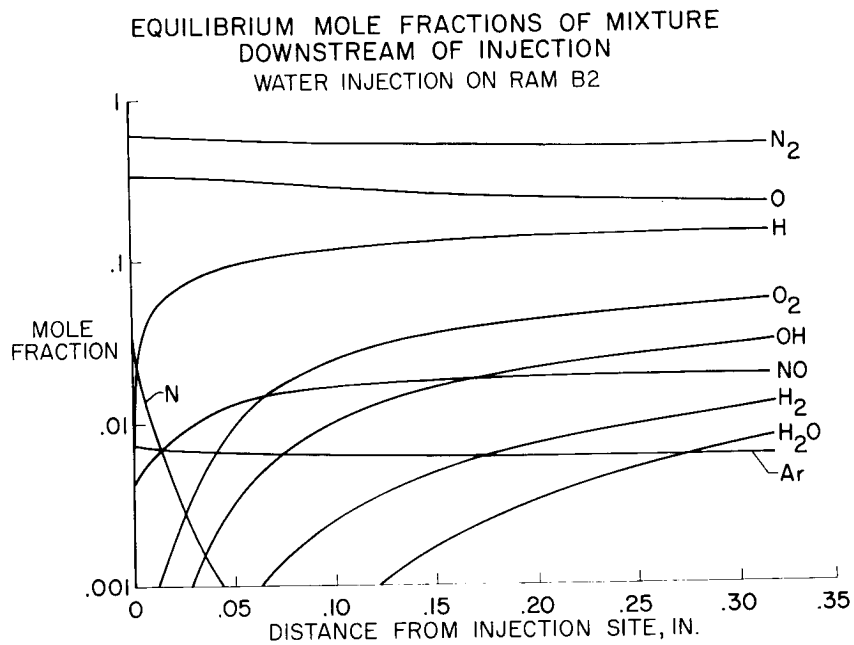
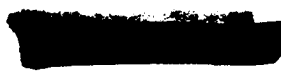


Figure 9



[REDACTED]

17. RESULTS OF THE RAM B2 MATERIALS-ADDITION FLIGHT EXPERIMENT

By William F. Cuddihy
Langley Research Center

SUMMARY

The materials-addition method has been flight tested and found to be effective for a vehicle the size of RAM B2 at velocities up to nearly 18,000 ft/sec over a range of altitudes. The results for both side and stagnation injection are presented and the effectiveness of each method is briefly discussed.

INTRODUCTION

In paper no. 16, it was shown that injection of a liquid into a hypersonic flow field is feasible for plasma suppression from the standpoint of penetration, flow-field disturbance, and evaporation distances. That is, it is possible to distribute water droplets throughout a reentry plasma without creating a large disturbance and the liquid can then evaporate before being swept away in the wake. (See ref. 1.) It has also been reported in paper no. 12 that ground tests indicate that small amounts of water are effective in reducing radio attenuation due to plasma.

The present paper discusses the results of a recent test which demonstrated that material addition was effective in establishing reentry communications in actual flight.

DISCUSSION

Figure 1 shows the three-stage solid-propellant RAM B2 vehicle. The third stage was flown into the blackout region on an ascending trajectory as described in paper no. 15. The antenna locations and injection sites on the third stage are given in figure 2. Details of nozzle design, of the injection system of figure 3, of the flow rates of water shown in figure 4, and of the range layout of figure 5 are given in reference 2. The only points necessary to make here are: (1) frequencies at HF, VHF, C-band, and X-band were transmitted from various antenna locations on the third stage, (2) the flow rate was varied through a range of flows for injection from the stagnation region and from side orifices, and (3) periods of zero water flow were provided during the data period to measure the plasma radio attenuation for the no-additive condition.

Typical signal strengths recorded at ground receiving stations during the data period are shown in figures 6, 7, and 8. These records have been smoothed to remove signal variation due to vehicle spin. C-band and X-band transmissions

CONFIDENTIAL

were not noticeably attenuated and are not shown. Complete recovery of all attenuated signals was obtained for the stagnation injection case for all antenna locations and for all flow rates used. From the flow-rate graph (fig. 4) it can be seen that less than 0.1 lb/sec of water was effective for these flight conditions. The side-injection method was found to give nearly complete recovery for the most forward antenna (244.3 Mc) and to become progressively less effective for antenna stations toward the rear.

Several possibilities for the effectiveness of stagnation injection are: (1) The material tends to stay mainly in the boundary layer and for this flight the electron concentration high enough to cause radio attenuation was near the outer edge of this boundary as shown in paper no. 2. (2) Aerodynamic shaping to produce a smaller effective nose radius would reduce attenuation. In figure 5 of paper no. 16 stagnation injection in the Langley Mach 8 variable-density tunnel was shown producing a pointed shock wave. (3) The presence of water and water vapor in the bow-shock region could inhibit the original formation of ionization.

The side-injection method is important and the nearly complete recovery for the most forward antenna is significant because it shows that, without modifying the stagnation region, radio attenuation relief can be obtained. The importance of side injection is realized when one attempts to scale the stagnation injectant flow rate for the area of a large body. On the other hand if side injection can be used to open a narrow window, the injectant rate need only increase to correspond to the plasma thickness increase.

For the RAM B2 experiment the calculated penetration was chosen to fit the requirements for the most forward antenna as shown in figure 9. This choice caused a penetration of droplets well beyond the undisturbed shock at the rearward antennas as is also shown in figure 9 and indicates an inefficient use of material at these aft antenna stations. Based on these data, an experiment with side injection penetration on the order of that obtained for the stagnation injection penetration would be of interest. Percent of the circumference from which injection occurred could be varied to determine the most efficient window width.

Some temperatures that were recorded for the beryllium heat-sink nose are mentioned. These temperature measurements do not bear directly on the radio attenuation measurements but are included here as flight results. Figure 10 shows the predicted temperatures for no water addition at a thermocouple located 13.5 inches from the stagnation point. The measured temperatures are also plotted in this figure and the material addition is seen to cause considerably lower temperatures as would be expected. Figure 11 shows temperatures for the water injection sequences and a comparison of measured temperatures for the water couple stations - one in line with a side injection site and one 90° away.

CONFIDENTIAL

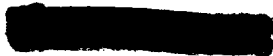


CONCLUDING REMARKS

The materials-addition method has been flight tested and found to be effective for a vehicle the size of RAM B2 at velocities up to nearly 18,000 ft/sec over a range of altitudes. The results for both side and stagnation injection have been presented and the effectiveness of each method has been briefly discussed. Further work is indicated to find the most efficient use of material and to define minimum flow requirements. Materials other than water are being investigated, and the scaling of the experimental results to larger vehicles is under investigation.

REFERENCES

1. Beckwith, Ivan E., and Huffman, Jarrett K.: Injection and Distribution of Liquids in the Flow Fields of Blunt Shapes at Hypersonic Speeds. NASA TM X-989, 1964.
2. Cuddihy, William F., Beckwith, Ivan E., and Schroeder, Lyle C.: RAM B2 Flight Test of a Method for Reducing Radio Attenuation During Hypersonic Reentry. NASA TM X-902, 1963.



RAM B2 VEHICLE

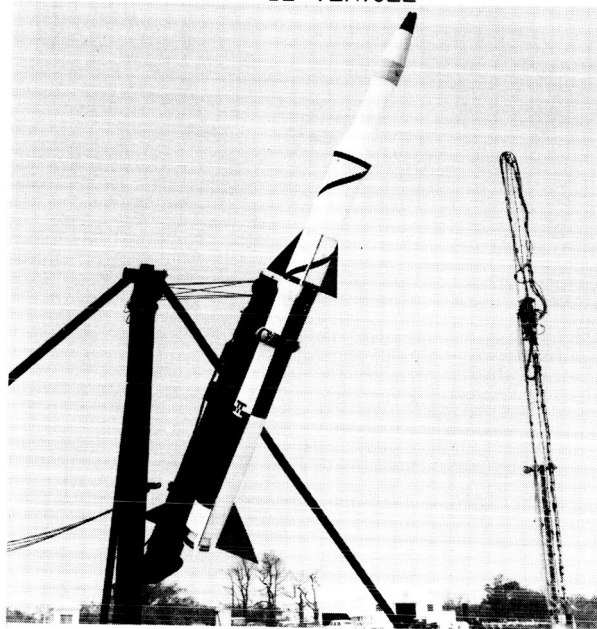
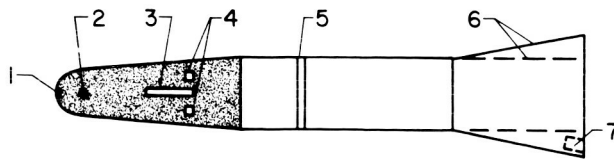


Figure 1 L-2175-1

RAM B2 PAYLOAD



ITEM	DISTANCE AFT OF STAGNATION POINT, IN.
1 STAGNATION INJECTION LOCATION	0
2 SIDE INJECTION LOCATION	5
3 244.3 Mc VHF ANTENNA	30
4 9210 Mc X-BAND ANTENNA	34
5 30.8 Mc HF ANTENNA	65
6 225.7 Mc VHF ANTENNA	125
7 5600 Mc C-BAND ANTENNA	138

Figure 2

RAM B2 WATER-INJECTION SYSTEM

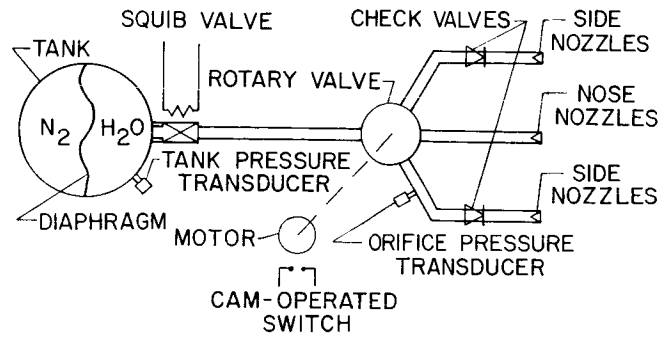


Figure 3

VARIATION OF FLOW RATE WITH TIME

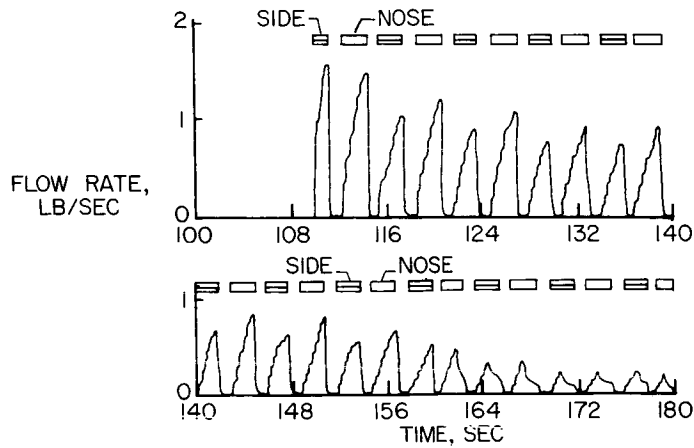


Figure 4

RAM B2 GROUND RANGE

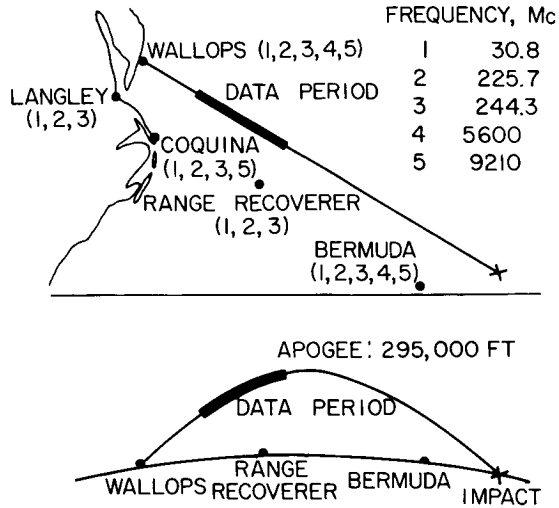


Figure 5

SIGNAL STRENGTH DURING RAM B2 DATA PERIOD
244.3Mc; NASA WALLOPS STATION

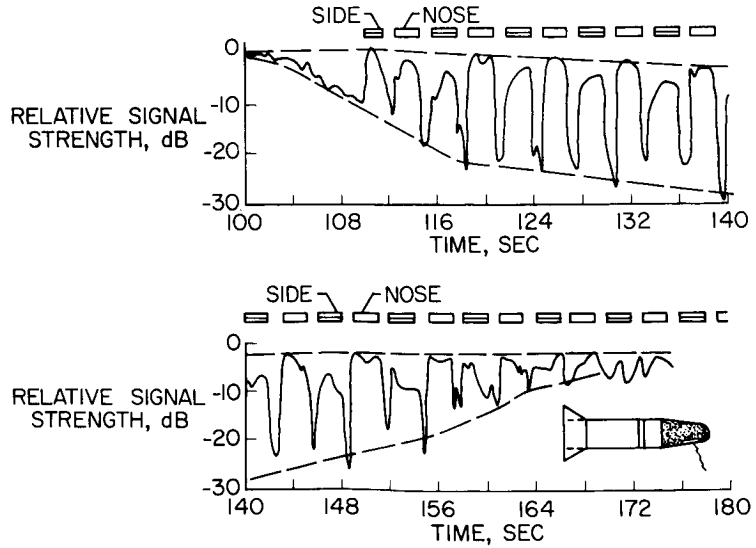


Figure 6

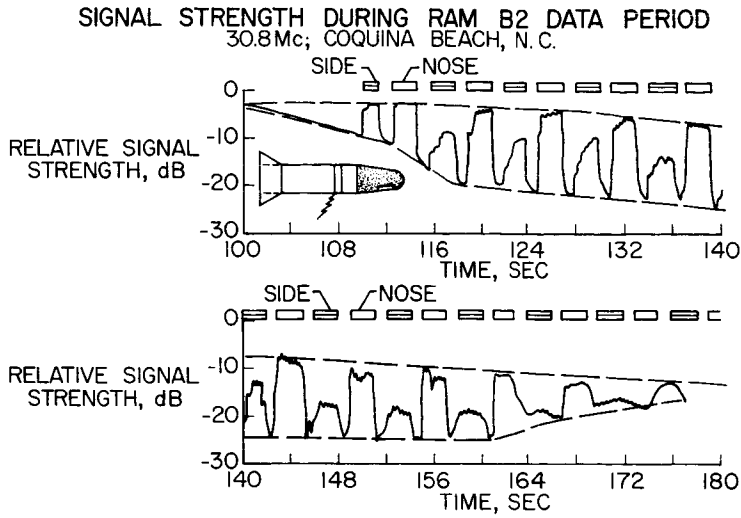


Figure 7

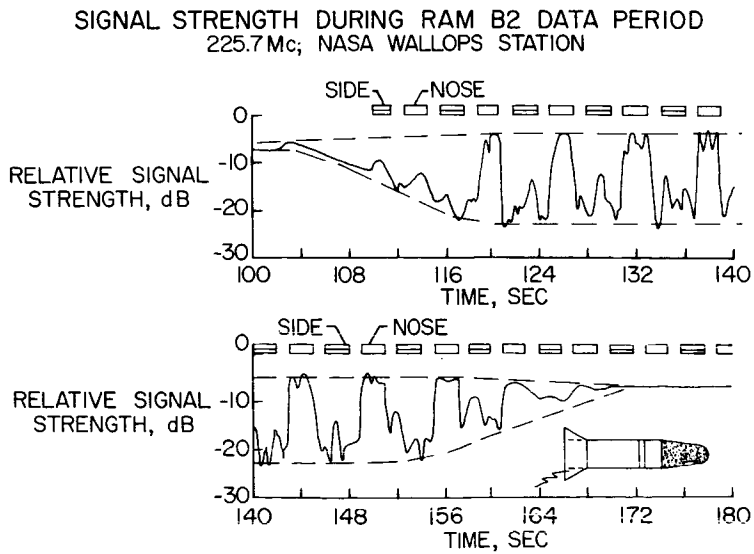


Figure 8

PREDICTED SPRAY PENETRATION FOR SIDE INJECTION ON RAM B2 FLIGHT

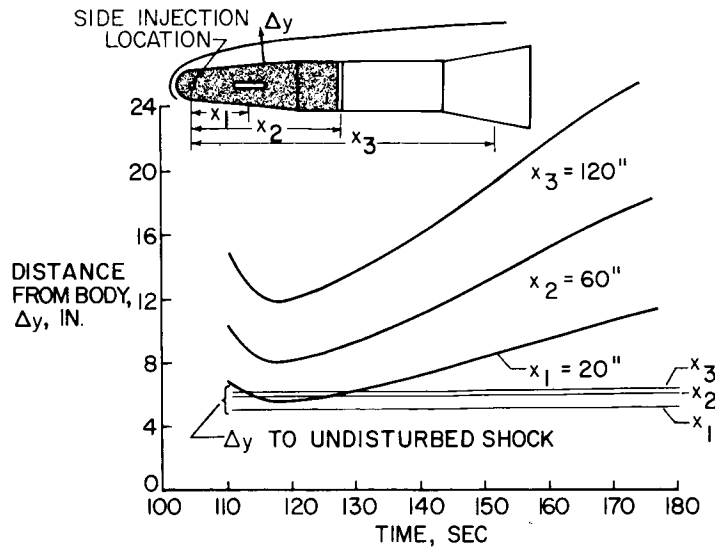


Figure 9

RAM B2 FLIGHT
THERMOCOUPLE 4

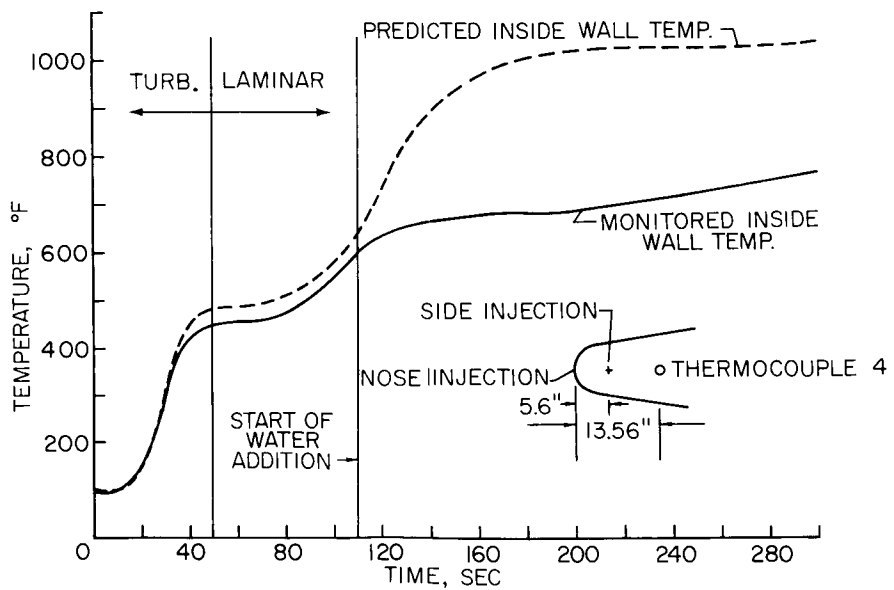
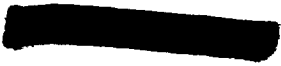
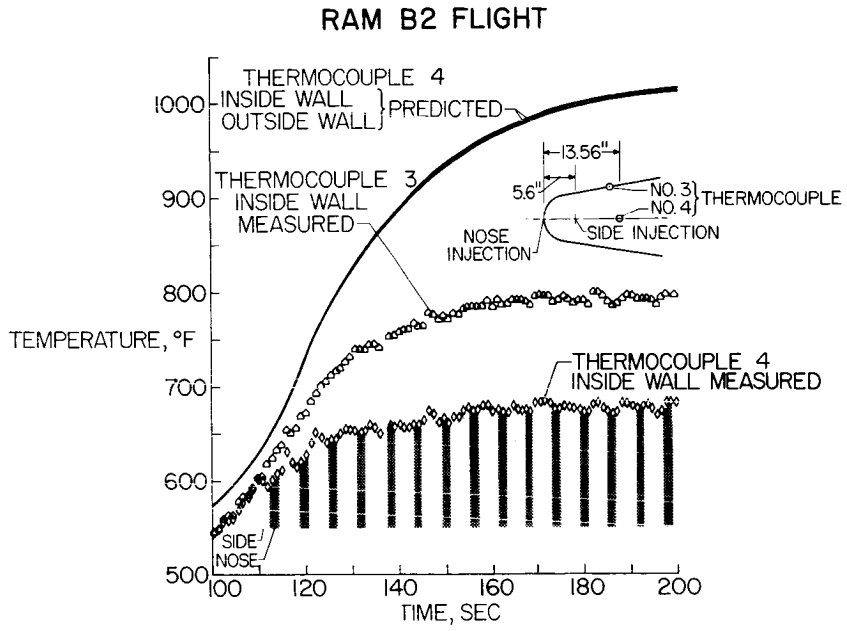


Figure 10





18. THE RAM B3 REFLECTOMETER EXPERIMENT

By William L. Grantham
Langley Research Center

SUMMARY

The RAM B3 experimental payload to be launched from the NASA Wallops Station this year will achieve a maximum velocity of about 19,000 ft/sec during the ascending portion of the flight. The payload will contain a three-frequency microwave system for measuring the electron density and the plasma standoff distance at discrete locations along the RAM body. An effort has been made to keep the plasma free of ablation products during the measurement by using a heat-sink type of nose cone. The nose cone of the RAM B3 has a hemispherical 4-inch radius and a 9° half-angle afterbody. A number of tests have been made for qualification of the reflectometer technique, and these tests show the method to be suitable for the in-flight measurement. The measured electron densities and plasma standoff distances will be compared with theoretical predictions to test the validity of the theory in the velocity region between 10,000 and 20,000 ft/sec. It is hoped that this comparison will be favorable and will give new confidence to radio-attenuation calculations which are highly dependent on the accuracy of aerodynamic theory. If the measured and calculated electron densities do not agree, the reflectometer measurements are thorough enough to suggest new directions for aerodynamic analysis.

INTRODUCTION

In this paper, a microwave plasma measurement technique is described which will be used on the RAM B3 flight experiment.

At the present state of the art, plasma-sheath calculations are of unknown accuracy and are particularly difficult to make on the aft portion of the spacecraft. The comparison of in-flight electron-density measurements with those calculated from aerodynamic theory should be of considerable value in understanding reentry physics and in developing blackout-alleviation techniques. Since the microwave measurement technique is based on well-known electromagnetic-plasma interaction equations, it is sufficient to discuss the application of this interaction for measuring electron density.

SYMBOLS

f	frequency, cps
N_e	electron density per cubic centimeter
x/D_n	body station normalized to nose diameter, measured from nose tip



θ electrical length, deg
 ρ power reflection coefficient

Subscripts:

cr critical

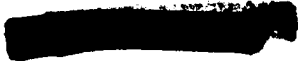
1,2,3 frequencies for L-, S-, and X-bands, respectively

EXPERIMENTAL METHODS

During the ascending portion of the flight, the flow-field electron density will increase to a maximum value and then decrease to zero as the vehicle exits from the earth's atmosphere. A microwave reflectometer system will be used to monitor the occurrence and decay of the critical electron density for the L-, S-, and X-band microwave frequencies used. The principle of the reflectometer measurement technique can be seen in figure 1. The reflectometer shown sends electromagnetic waves into the nonhomogeneous plasma, which has the electron-density gradient shown in the center of the figure. The wave will propagate into the plasma to its critical density $\left(N_{e,cr} \approx \frac{f^2}{108} \frac{\text{electrons}}{\text{cm}^3}\right)$ where the wave will be totally reflected due to the sharp impedance change at that point. This type of interaction is typical of plasmas when the collision frequency is low and the electron-density gradient is sharp with respect to wavelength. A higher frequency electromagnetic wave will penetrate deeper into the plasma to its respective critical-density boundary. The wave transmitted to the plasma is totally reflected only if its critical density exists in the plasma.

The use of the reflectometer principle for measuring in-flight plasma electron densities can be seen in figure 2. At the top of the figure is shown a typical electron-density time history for a given body station. The plasma reflection coefficient is measured as a function of time. When reflection occurs, the maximum electron density in the flow field at that body station equals the critical density of the electromagnetic frequency used. At the time reflection goes to zero, critical density has decayed at that body station. The time at which reflection occurs also depends on the plasma thickness (fig. 3), the electron-molecule collision frequency (fig. 4), and the electron-density distribution. The experiment is designed so that parameters other than electron density do not seriously affect the accuracy of the measurement. The measured time of onset and decay of critical density will be compared with the calculated time based on aerodynamic theory. It is intended that this comparison will shed some light on the validity of the aerodynamic theory used for the RAM flight velocity region.

The phase of the reflected wave is monitored, using nondirectional probes, to determine the critical-density standoff distance during flight. The phase of the reflected wave is, in part, determined by the distance between the vehicle surface and the critical-density boundary. The principle of this measurement



[REDACTED]

is shown in figure 5. If the reflecting boundary (critical-density boundary) moves a distance $\Delta\theta$ with respect to the transmitting antenna, the standing wave shifts the same amount. With proper calibration, the voltage change at either of the sampling probes would indicate the standoff distance of the reflecting boundary. The position of the probes with respect to the standing-wave-envelope null determines their rate of voltage change with respect to the reflector distance and thus determines the accuracy of the measurement. Two probes are employed one-quarter wavelength apart so that, at any time, one of the two probes will be in an accurate measurement region. Phase measurements will be made during flight with the L- and S-band systems. The critical-density standoff distance determined from the phase measurement will be compared with values computed from aerodynamic theory.

FLIGHT SYSTEM

A block diagram is shown in figure 6 of the L-, S-, and X-band flight systems. The L- and S-band systems are schematically identical. The basic measurements are forward power, reflected power, and probe voltages in the main transmission line. Flight antenna locations are shown in figure 7. Two antennas are used for each microwave frequency. A coaxial switch alternately transfers the microwave power from one antenna to the other in order to increase the number of data points available from each frequency used.

The two antennas near the stagnation region will monitor electron density where close agreement is expected between the measured and calculated values. With agreement at stagnation, added confidence will be given to the measured electron densities on the aft position of the body where the accuracy of aerodynamic theory is highly dependent upon deionization relaxation times.

The S- and X-band antennas located on the forward portion of the vehicle are open-ended circular waveguides with half-wavelength quartz windows. (See fig. 8.) The forward antennas will be exposed to a rather harsh environment during flight and the quartz windows will reach a temperature of about 2,500° F. Qualification tests have shown these antennas to be suitable for the expected flight environment. The L-band antennas are T-fed slots and are covered with a protective dielectric.

The reflectometer antennas are designed so that they "see" a reflecting plasma only if the reflecting plasma is located directly over the antenna aperture. This means that electron-density measurements can be made at discrete locations on the RAM body with a minimum of ambiguity caused by the electron-density gradient along the body (fig. 9).

The reflectometer principle discussed earlier assumes the plasma to be in the far field of the transmitting antenna. During flight, however, the plasma will be in the near field of the reflectometer antennas. It was therefore necessary to test the flight antennas to determine whether near-field plasma measurements would agree with far-field theoretical values. Two tests were made to qualify the antennas. First, a series of rocket-exhaust plasma measurements, using a flight type of reflectometer system, were made in the 41-foot-diameter

[REDACTED]

0371 [REDACTED]

vacuum sphere at the Langley Research Center. The system was packaged into a nose cone with a 1-inch-radius nose and a 9° half-angle afterbody (fig. 10). A trolley was used to move the rocket motor so that its ionized exhaust plume would periodically engulf the reflectometer model. The rocket-exhaust test simulates the near-field measurement conditions of flight. The results of three rocket-exhaust tests show good repeatability of the plasma and agreement between the calculated and measured electron density within a factor of two. Transmission signal-loss measurements were also made during the reflectometer tests and the results agree with the reflectometer measurements.

The second near-field qualification test was made by placing thin dielectric slabs over the antennas and comparing the near-field reflection coefficient with the calculated far-field coefficient. The calculated and measured reflection coefficients agreed very well, and the results of the test at X-band are shown in figure 11. The close agreement of far-field calculation and near-field measurements strongly suggests that the far-field theory can be used to interpret the near-field flight measurements.

Another ground test was made to exercise the reflectometer technique and to compare reflectometer plasma measurements with Langmuir probe measurements. The gas-discharge tube used as a plasma source and the details of the measurements are discussed in paper no. 8 by Richard W. Morton. The electron densities measured with the Langmuir probe and the reflectometer agreed within 25 percent.

IN-FLIGHT ELECTRON-DENSITY CALCULATIONS

An extensive effort has been made to calculate the electron-density profile at different stations along the RAM vehicle. These calculations are needed for comparison with the flight measurements. The details of the theoretical effort are discussed in paper no. 2 by Paul W. Huber and John S. Evans. Some preliminary calculations are discussed herein to tie the experimental and theoretical work together. The RAM B3 trajectory used for the study is shown in figure 12. A time history of the peak electron density at a given body station is shown in figure 13 for two gas conditions: one for frozen flow and the other for equilibrium flow. Of course, the flight electron-density time history will fall somewhere between these two boundaries. The two curves in figure 13 show that the time at which S-band critical density (approximately $10^{11} \frac{\text{electrons}}{\text{cm}^3}$) occurs is strongly dependent on the type of flow. Reflectometer measurement can thus readily distinguish between frozen and equilibrium gas conditions in the plasma. The accuracy of aerodynamic theory seems to be determined primarily by the accuracy of the deionization relaxation time. Fortunately, the reflectometer measurements are thorough enough to suggest new relaxation times if the initial calculations do not agree with the measurements.

The reflectometer technique for measuring electron density has been shown to be suitable for in-flight plasma measurements. The measured critical-density standoff distance and the plasma electron density will be compared with values calculated from aerodynamic theory. If the measured and calculated values agree, new confidence will be given to radio-attenuation calculations which are strongly dependent upon the accuracy of aerodynamic theory. If the measured and calculated electron densities do not agree, the reflectometer measurements are thorough enough to suggest new directions for aerodynamic analysis.

REFLECTOMETER PRINCIPLE

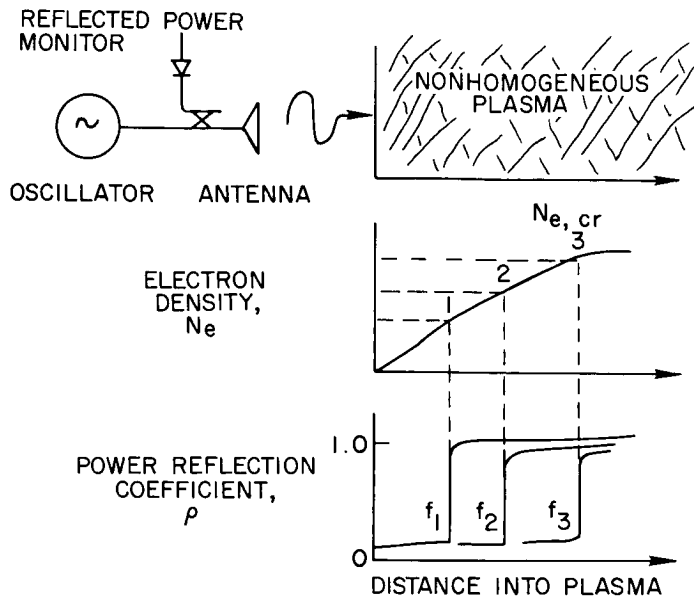


Figure 1

TYPICAL FLIGHT DATA

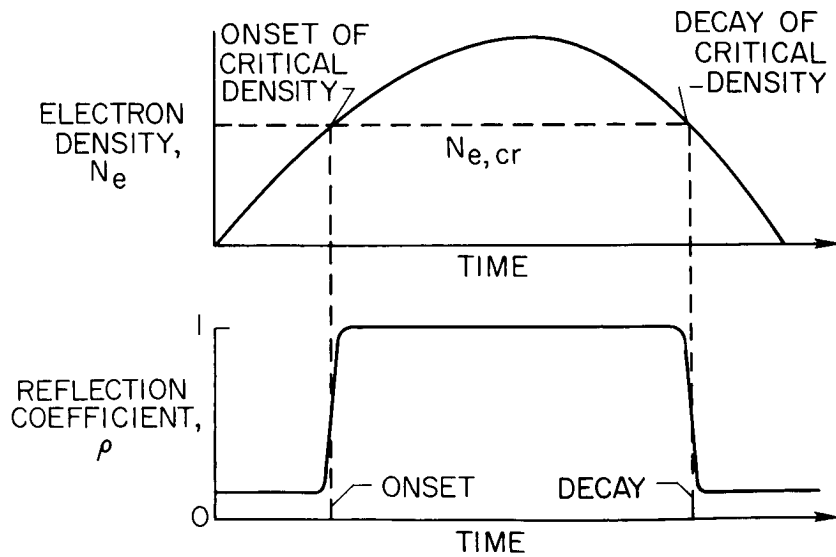
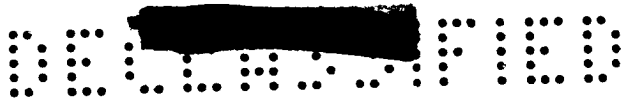


Figure 2



VARIATION OF POWER REFLECTION COEFFICIENT
WITH ELECTRON DENSITY FOR PLASMA SLAB
S-BAND; COLLISION FREQUENCY, 10^8 SEC^{-1}

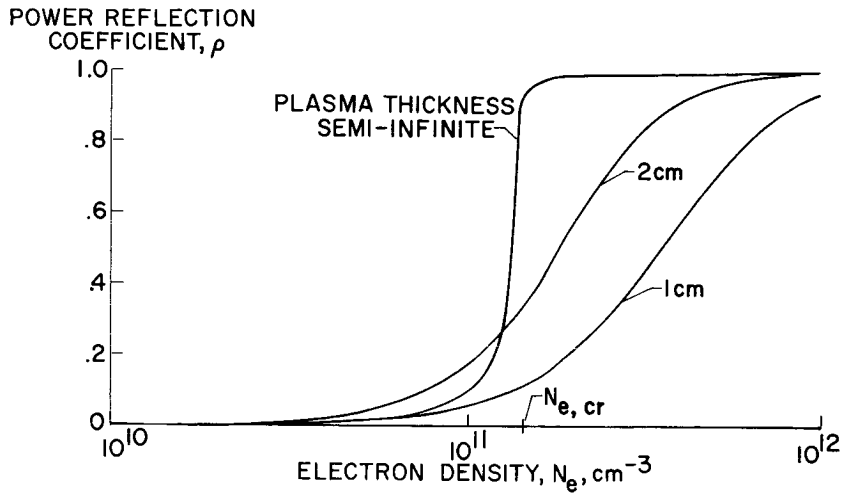


Figure 3

VARIATION OF SEMI-INFINITE POWER REFLECTION
COEFFICIENT WITH ELECTRON DENSITY
S-BAND

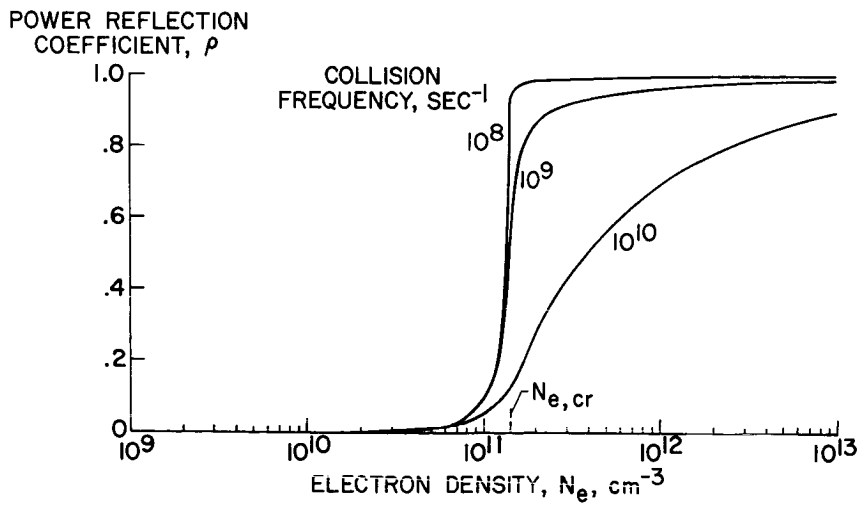


Figure 4



MEASUREMENT OF REFLECTING-BOUNDARY STANDOFF DISTANCE

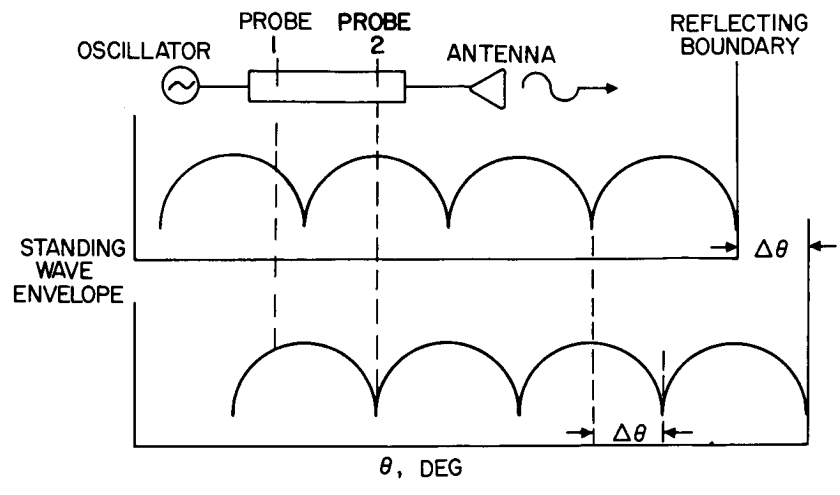


Figure 5

REFLECTOMETER FLIGHT SYSTEM

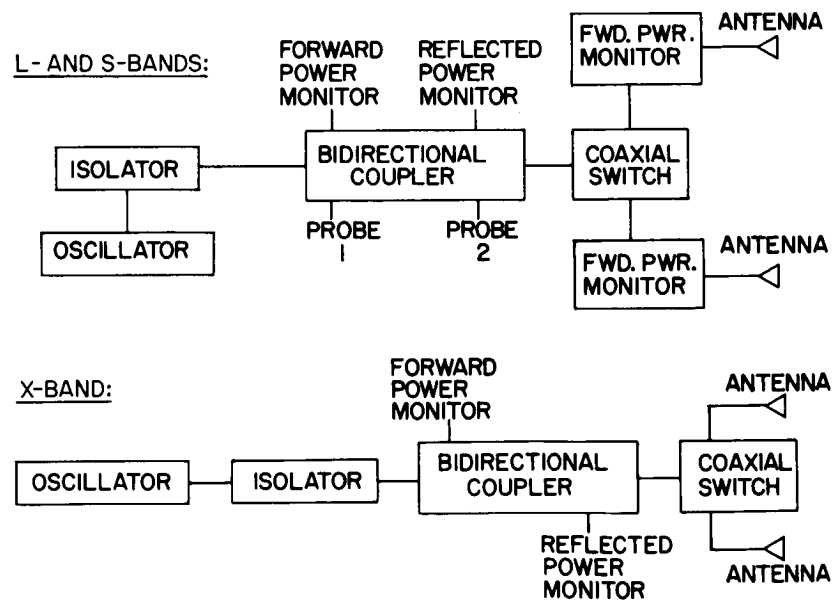


Figure 6

SECRET

REFLECTOMETER ANTENNA LOCATIONS

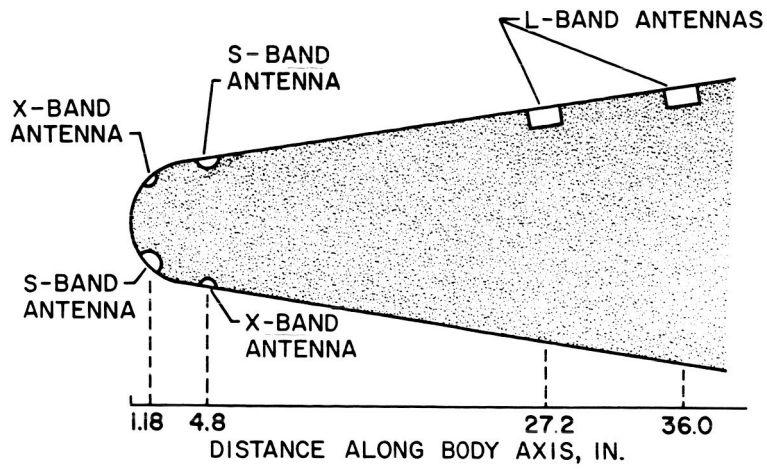


Figure 7

S- AND X-BAND FLIGHT ANTENNAS RAM B 3

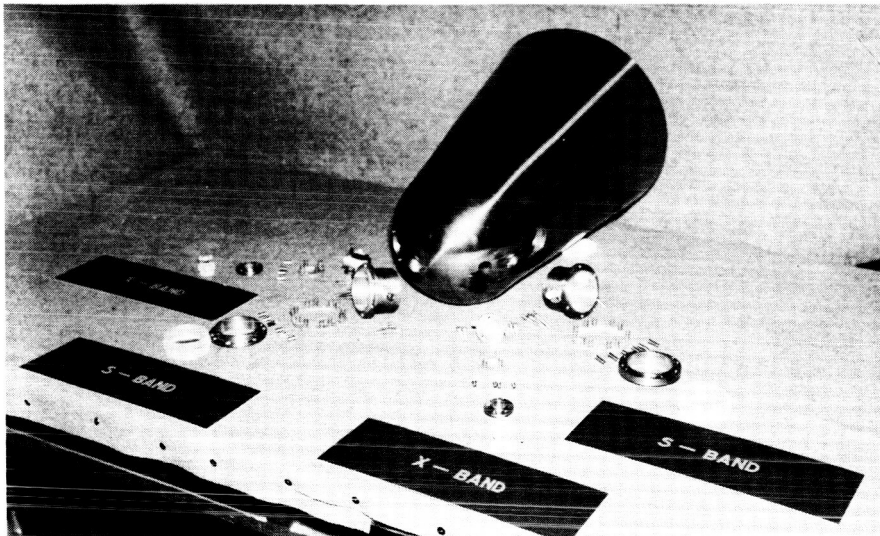


Figure 8

L-2171-3

SECRET



GRADIENT OF ELECTRON DENSITY SEEN BY EACH ANTENNA
ALTITUDE, 180,000 FT ; VELOCITY, 20,000 FT/SEC

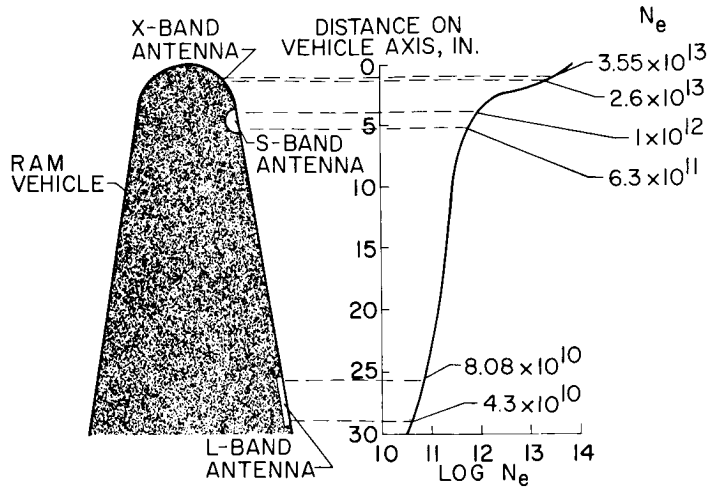


Figure 9

REFLECTOMETER ROCKET-EXHAUST MODEL

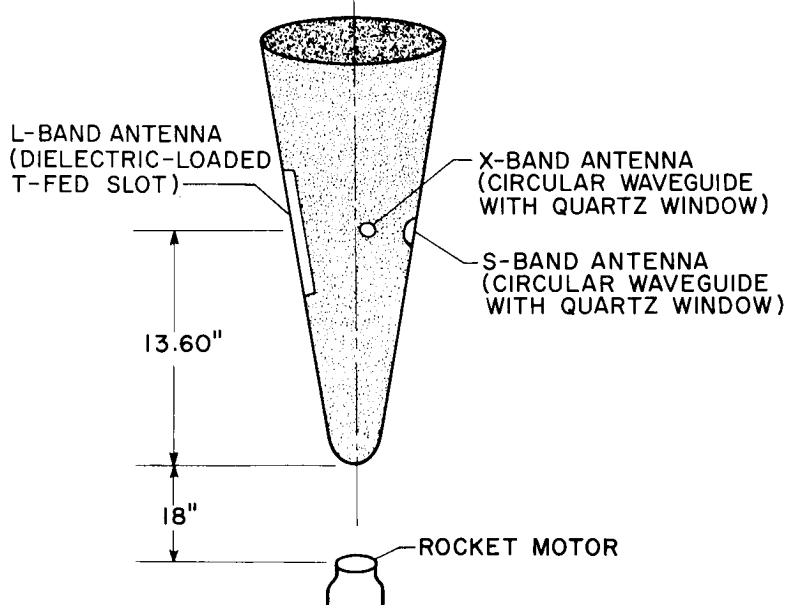
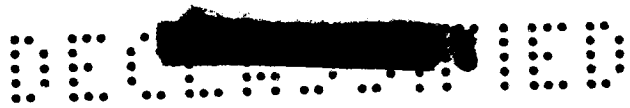


Figure 10





TYPICAL ANTENNA RESPONSE TO DIELECTRIC REFLECTORS

$f_3 = 10,044$ mc

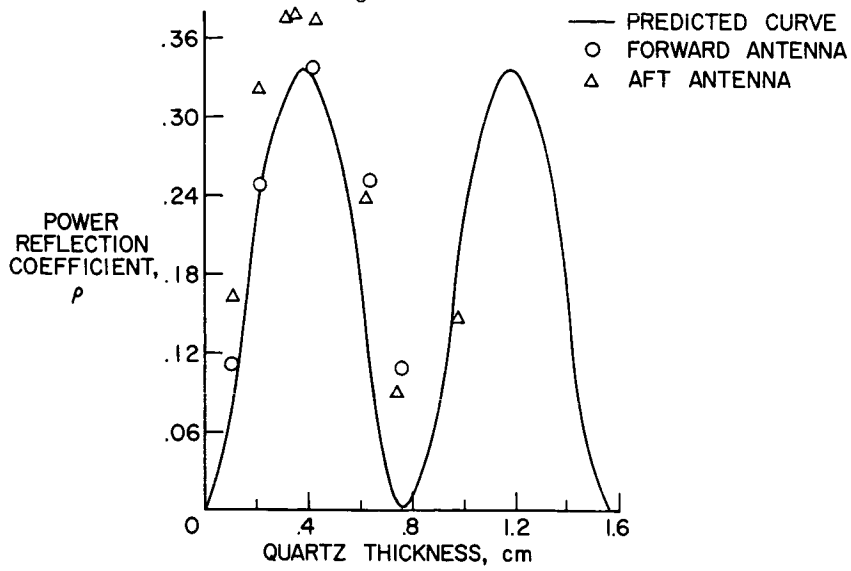


Figure 11

RAM B3 TRAJECTORY

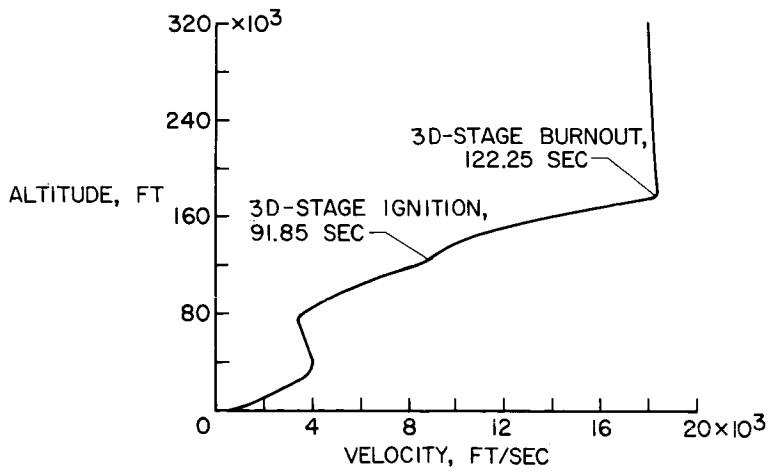


Figure 12



CALCULATED ELECTRON DENSITY FOR RAM TRAJECTORY

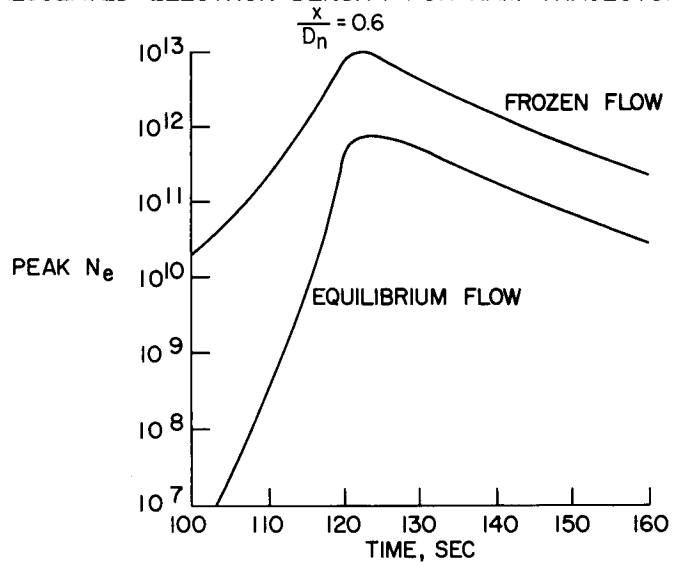


Figure 13

[REDACTED]

19. RAM FLIGHT-TEST RESULTS AND CONCLUSIONS

By Lyle C. Schroeder
Langley Research Center

SUMMARY

A summary of the Project RAM flight-test results is presented. Included are results of RAM A1 (aerodynamic shaping experiment), RAM A2 (magnetic field experiment), and RAM B2 (multifrequency and material-addition experiment). A brief description of each experiment is given, followed by data such as flight trajectory, attenuation level, and selected antenna impedance and VSWR. Conclusions drawn from the results are also presented.

INTRODUCTION

Three of the flight experiments in conjunction with the Langley Research Center Project RAM have been flown. They are (in chronological order) RAM A1 (aerodynamic shaping experiment), RAM A2 (magnetic field experiment), and RAM B2 (multifrequency and material-addition experiment). (See refs. 1 to 3.) This presentation summarizes the results of these tests and conclusions drawn from this program.

EXPERIMENT DESCRIPTION

Trajectory

The RAM trajectory was designed to place an ascending probe deeply within the VHF blackout region at about burnout. Plots of the variation of altitude with velocity for the three RAM flights are almost identical, with burnout occurring at an altitude of approximately 170,000 feet and a velocity of 17,700 ft/sec. In other words, the velocity-altitude conditions were about the same during the "data period" of all three completed RAM flights. The attenuation period lasted about 5 seconds on the RAM A flights, and about 60 seconds on the RAM B flights, due to a much shallower flight-path angle on the RAM B flight.

Configuration

The basic probe configuration used in the RAM flights was a slender, hemisphere-nose 9° half-angle cone, followed by a cylindrical section and a flare. The two probes used are shown in figure 1. The RAM A probe is shown in the upper portion and the RAM B probe is shown in the lower. It is evident



from this figure that the main difference is that the B probe is scaled up from the A probe by a factor of four.

Transmission Systems

Two VHF transmission systems were flown on each of the RAM flights. A signal was transmitted from a sharply tuned forward slot antenna at 244.3 mc, and a telemetry signal in the 240-mc range was transmitted from an aft antenna. The RAM B2 payload also transmitted signals at 30.8 mc, 9,210 mc, and 5,600 mc. (See fig. 1.)

Ground Stations

The ground stations used for the RAM launchings are shown in figure 2. Signal strength for the RAM flights was recorded at Wallops, Virginia; Langley Field, Virginia; Coquina Beach, North Carolina; a ship downrange; and Bermuda. The flight path of RAM B2 is also shown in this figure. The RAM A flights, which had a much shorter range, did not require the use of the Bermuda station.

Instrumentation and Measurements

In addition to measuring signal attenuation, impedance and VSWR were monitored on the forward slot antenna to provide an indication of antenna operation. Also, VSWR was measured at all frequencies except C-band on the RAM B2 probe. Antenna impedance changes were determined by sampling fixed probe positions on a coaxial line feeding the antenna, whereas VSWR was detected with a bidirectional coupler indicating the forward and reflected power of the antenna.

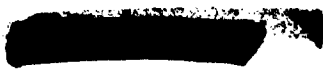
Instrumentation aboard RAM A2 and B2 (which were coning and spinning during flight) allows the determination of the exact look angle from a ground receiver to an antenna on the vehicle during flight. These data make it possible to correlate preflight antenna patterns with flight data.

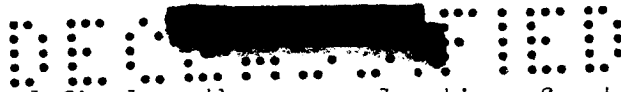
OBJECTIVES OF THE RAM FLIGHTS

The general objective of all the RAM flights is to determine how well attenuation can be predicted and how these predictions can be improved, and to find methods to control attenuation. However, before the results of the flights are discussed, it is necessary to point out the specific objectives of each experiment.

RAM A1 Objectives

RAM A1 used aerodynamic shaping to make a significant penetration into the blackout region with only a moderate signal loss. For the RAM flights,





aerodynamic shaping is defined as the proper location of antennas and the use of sharp-nose vehicles to keep the ionization levels low over these antennas, and the resulting attenuation levels low.

RAM A2 Objectives

In addition to being a followup aerodynamic shaping experiment, the RAM A2 experiment was designed to examine the effect of static magnetic fields as an aid to transmission through the plasma sheath. Basically, free electrons which cause signal attenuation are rendered immobile in the presence of a magnetic field. This immobility effectively causes a decrease in electron concentration and a corresponding decrease in attenuation. A magnetic field of 750 gauss was switched between off, half-strength, and full-strength, and corresponding levels and changes in signal strength were to be noted.

RAM B2 Objectives

RAM B2 carried on board two experiments: a multifrequency experiment and a material addition experiment. The material addition experiment is the subject of paper no. 17 by William F. Cuddihy and will not be discussed herein. The purpose of the multifrequency experiment was to examine attenuation as a function of transmitter frequency over a wide range of frequencies (30.8 mc to 9,210 mc). Theory says that plasma attenuation is not appreciable if transmitted frequency exceeds plasma frequency, but flight data for signals at either SHF (X-band and C-band) or HF under carefully controlled conditions were not available.

RESULTS OF RAM FLIGHTS

The results of the three flight experiments measuring the effect of plasma attenuation are presented in table 1.

RAM A1 Results

Figure 3 is a plot of relative signal strength against time after launch for the RAM A1 flight as recorded at Coquina Beach. Maximum signal losses recorded were 25 dB for the 244.3-mc system and 5 dB for the 240.3-mc system during the 5-second data period. The technique of aerodynamic shaping was verified since the signals survived the blackout environment, and signal losses encountered were within predicted limits. It is believed that the difference in flow-field chemistry existing between the forward slot antenna station and the ring antenna station caused some, but not all, of the resulting greater attenuation on the forward antenna. A VSWR of 8:1 and an impedance shift on the forward slot antenna, which was a narrowband antenna, indicate that some signal loss on this system was due to detuning.





RAM A2 Results

Figure 4 shows the variation of signal strength with time during the RAM A2 data period as recorded at Langley Field. The trajectory and configuration for RAM A2 were almost the same as those for RAM A1. The maximum signal loss on both the 244.3-mc and the 240.2-mc system was 5 dB. Paper no. 3 by John S. Evans and Calvin T. Swift and paper no. 4 by Francis P. Russo have indicated that the signal loss recorded on the 244.3-mc system was greater during the RAM A1 flight because of detuning of the more sharply tuned antenna flown on A1. Because of low signal loss on the RAM A2 flight, the magnetic field experiment was inconclusive, but as paper no. 12 by J. K. Hughes has shown, ground tests in the 60-foot-diameter vacuum sphere at the Langley Research Center have shown that this technique is very effective.

RAM B2 Results

RAM B2, which was four times larger than the A probes, transmitted signals at five frequencies: 30.8 mc, 225.7 mc, 244.3 mc, 5,600 mc (C-band), and 9,210 mc (X-band). Of these, X-band and C-band signals were not affected, 225.7-mc and 30.8-mc signals were moderately attenuated, and 244.3-mc signals were blacked out. See figure 5. The 244.3-mc slot antenna, which was purposely chosen as a narrow bandwidth antenna to insure a significant amount of attenuation, suffered an impedance shift and a high VSWR, indicating that some of the signal lost is due to detuning. The 225.7-mc systems, using a broadband antenna, recorded a 20-dB signal loss. This is more loss than was recorded on the aft antennas of the RAM A flights; however, this loss was expected because of the increased payload scale. The 30.8-mc system recorded a maximum signal loss of 15 dB. The loss recorded on this system was less than losses on the forward and aft VHF systems; however, a direct comparison cannot be made because of design differences. Rocket exhaust attenuation is evident on the 225.7-mc system record and the effect coincides with third-stage rocket burning. The prime experiment on RAM B2, which was to overcome attenuation by water addition to the flow field, was very successful; almost complete recovery for flows as low as 0.1 lb/sec existed.

CONCLUSIONS

The results of three flight experiments measuring the effect of plasma attenuation over a wide range of altitude, velocity, and frequency have been analyzed, and the following conclusions have been made:

1. Detuning of narrowband antennas in plasmas is a first-order cause of signal loss.
2. The technique of aerodynamic shaping is an effective means of signal survival.

SECRET

3. The magnetic field flight experiment was inconclusive because of low attenuation; however, tests in a simulated flight environment have shown that this technique is very effective.

4. In the RAM altitude-velocity regime, X-band and C-band signals were not attenuated, and 30.8-mc signals were moderately attenuated.

5. Water addition to the flow field is a very effective means of overcoming blackout.

REFERENCES

1. Sims, Theo E., and Jones, Robert F.: Flight Measurements of VHF Signal Attenuation and Antenna Impedance for the RAM A1 Slender Probe at Velocities up to 17,800 Feet Per Second. NASA TM X-760, 1963.
2. Russo, F. P., and Hughes J. K.: Measurements of the Effects of Static Magnetic Fields on VHF Transmission in Ionized Flow Fields. NASA TM X-907, 1964.
3. Cuddihy, William F., Beckwith, Ivan E., and Schroeder, Lyle C.: RAM B2 Flight Test of a Method for Reducing Radio Attenuation During Hypersonic Reentry. NASA TM X-902, 1963.

SECRET

TABLE 1

PROJECT RAM FLIGHT RESULTS

Flight	Date	Prime experiment	Nose radius, in.	Velocity at burnout, ft/sec	Altitude at burnout, ft	Frequency, mc	Antenna bandwidth	Maximum attenuation, dB	VSWR	Impedance changes
A1	8/30/61	{ Aerodynamic shaping	} 1	17,800	176,000	{ 244.3 240.3	Narrow Broad	25 5	8:1 -----	Inductive shift
A2	2/21/62	{ Magnetic field	} 1	17,200	157,000	{ 244.3 240.2	Broad Broad	5 5	No change -----	No change -----
B2	5/28/63	{ Multifrequency and material addition	} 4	17,800	162,200	{ 244.3 225.7 30.8 9,210 5,600	Narrow Broad ----- ----- -----	{ >30 Blackout 20 15 None None	} 10:1 No change 6:1 No change -----	{ Inductive shift ----- ----- -----

RAM FLIGHT CONFIGURATIONS

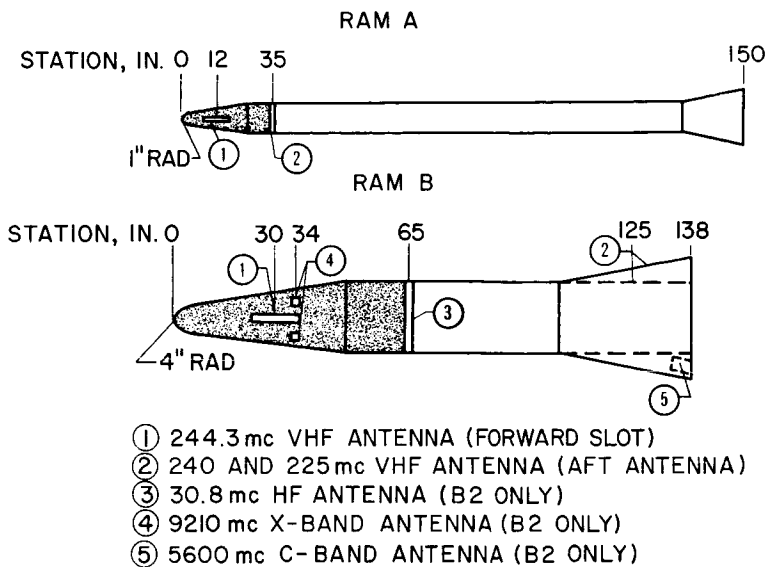


Figure 1

RAM B2 GROUND RANGE

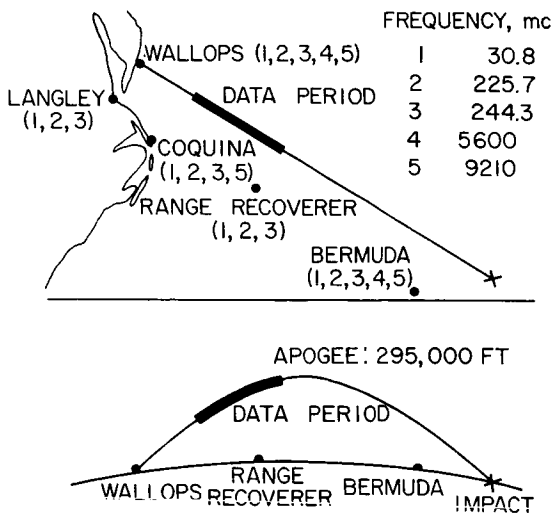
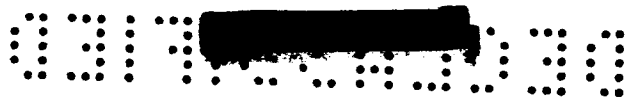


Figure 2



RAM A1 SIGNAL STRENGTH
COQUINA BEACH

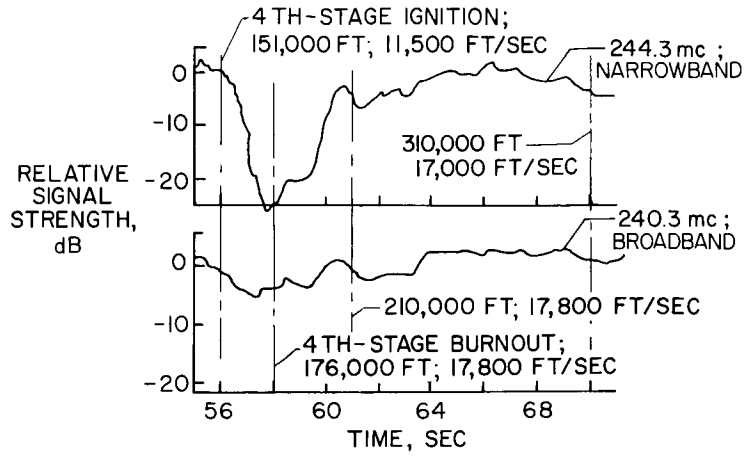


Figure 3

RAM A2 SIGNAL STRENGTH
LANGLEY FIELD

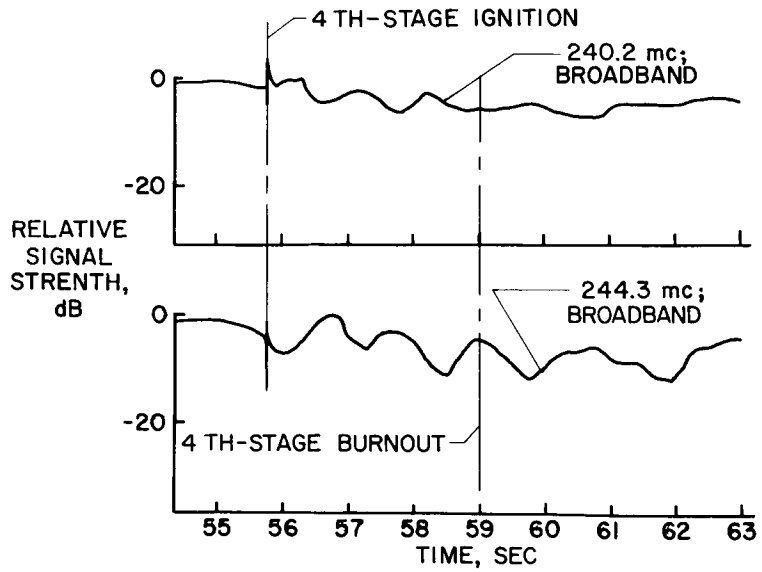
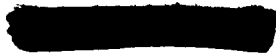


Figure 4



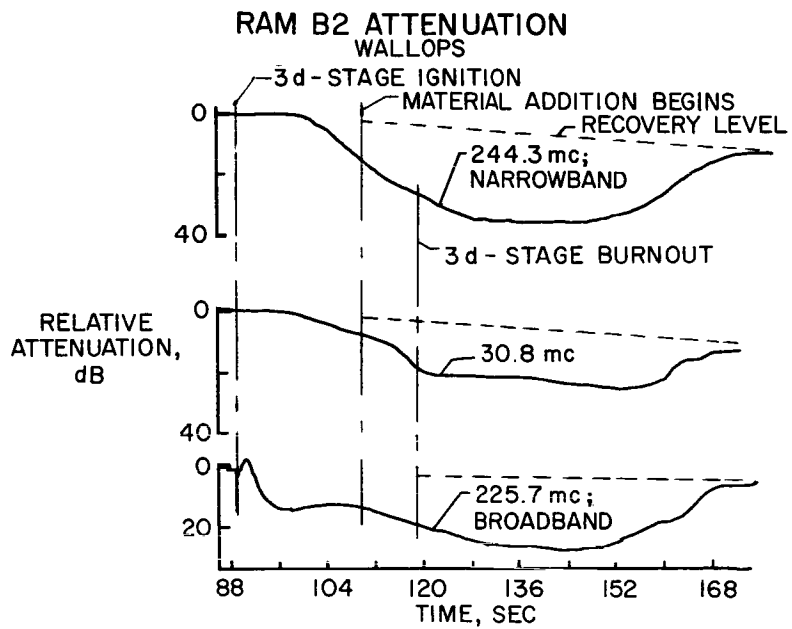


Figure 5